Alcohol Synthesis From Carbon-monoxide And Hydrogen Over Molybdenum-disulfide Based Catalysts.

Order Number 8921639

Alcohol synthesis from carbon monoxide and hydrogen over MoS_2-based catalysts

Santiesteban, José Guadalupe, Ph.D.

Lehigh University, 1989

U·M·I
300 N. Zeeb Rd.
Ann Arbor, MI 48106

ALCOHOL SYNTHESIS FROM CARBON MONOXIDE AND HYDROGEN OVER MoS_2-BASED CATALYSTS

by

José Guadalupe Santiesteban

A Dissertation

Presented to the Graduate Committee

of Lehigh University

in Candidacy for the Degree of

Doctor of Philosophy

in

Chemistry

Lehigh University

May 1989

CERTIFICATE OF APPROVAL

Approved and recommended for acceptance as a dissertation in partial fulfillment of the requirements for the degree of Doctor of Philosophy

Dr. Kamil Klier
Advisor and Committee Chairman

Special Committee Directing
The Doctoral Work of
José Guadalupe Santiesteban

Dr. Russell R. Chianelli

Dr. Richard G. Herman

Dr. Charles E. Lyman

Dr. Gary W. Simmons

May 17, 1989
(Date)

Dedicated with love, to

my parents

José Guadalupe and Guadalupe

my wife

Patricia Eugenia

and my son

Uriel

ACKNOWLEDGMENTS

I would like to express my sincere thanks and gratitude to my research advisor, Professor Kamil Klier, who through his commitment to excellence and concern for intellectual growth made my learning experience truly unique and rewarding.

I am extremely grateful to Dr. Richard G. Herman, member of my research committee, for his helpful discussion, criticism, and time in the preparation of this dissertation. The willingness of the other research committee members, Russell R. Chianelli, Charles E. Lyman, and Gary W. Simmons, to assist me in their personal fields of expertise is greatly appreciated.

Many other people have contributed to my education and social happiness during my studies at Lehigh, and I acknowledge with appreciation their friendship: Prof. G. Doyle Daves, Prof. Robert S. Sprague, Prof. Leonard Klebanoff, Rangasamy Pitchai, Paul Himelfarb, Kevin Smith, John Nunan, Donna and John Mitko, Vic Kuzmicz, David Cole, Chyi-Woei Young, Mark Reuter, Jiann Lin, Roy Bastian, Robert Bronson, Yarw-Nan Wang, Juan and Nora Marcos, Chuck Bogdan, Michelle Richards, Jana Klier, and Marge Sawyers.

My deepest thanks and friendship go to Ricki Grant for her skillful typing of the dissertation.

Finally, I thank my parents, wife, son, brothers, and sisters for their love, understanding, support, and many sacrifices. Without you I could not have achieved my Ph.D.

TABLE OF CONTENTS

LIST OF FIGURES

LIST OF FIGURES (cont'd)

LIST OF TABLES

LIST OF TABLES (cont'd)

ABSTRACT

The synthesis of linear C_1-C_4 alcohols from synyhesis gas (CO + H_2) over alkali-promoted MoS_2-based catalysts has been studied. A large doping level of alkali was essential for the formation of alcohols rather than hydrocarbons over these catalysts. The indispensable presence of the alkali salt promoter for alcohol synthesis was due to the bifunctionality of the catalyst in which the alkali activates CO and MoS_2 activates H_2. Injection of ^{13}C-labeled CH_3OH into the synthesis gas stream over alkali-promoted MoS_2-based catalysts and analysis by ^{13}C NMR spectroscopy of the condensable products, accompanied by mass spectrometric analysis of light gaseous products, demonstrated that the alcohol chain growth occurred via a *classical* CO insertion mechanism, and that methane is a secondary product that is formed from an alkyl moiety generated from a C_1-oxygenated precursor. The addition of cobalt to the alkali-doped MoS_2 catalyst greatly enhanced the rate of the $C_1 \rightarrow C_2$ growth step so that ethanol became the dominant product. The alkali-doped MoS_2 catalysts prior to and after attaining their working state were fully characterized by XPS, XRD, STEM, and surface area measurements. Electron microscopy results indicated that the MoS_2 portion of the catalyst consists of a semicrystalline hexagonal structure with regular lattice spacings (d(002) = 6.15 Å) that indicate no intercalation of the alkali. The cesium salt in the best catalysts (10-20 wt% CsOOCH) is distributed as ≈200 Å diameter particles and

also as a fine surface dispersion. The cesium particle agglomeration results from the low surface energy of MoS_2 and is the cause of the large levels of cesium required for the optimal functioning of the catalyst. Pretreatment (400 °C, 2% H_2/N_2, 1 h) of the catalysts induces not only reduction of surface species such as Mo(VI) and SO_4^{2-} detected on the fresh catalysts, but also dispersion of the cesium on the MoS_2 surface. The oxidation states of S and Mo in the tested catalysts correspond to those of MoS_2, i.e. Mo(IV) and S^{2-}. XPS intensity equations were derived from geometrical models of the catalyst surface to determine the degree of dispersion and/or segregation of Cs on the MoS_2 surface.

OBJECTIVE AND SCOPE OF THE WORK

The objective of this research was to generate the scientific knowledge that may lead to improvements of the process for the synthesis of C_1-C_4 alcohols from synthesis gas ($CO + H_2$) over MoS_2-based catalysts, which was recently disclosed by the Dow Chemical Company and Union Carbide. The approach was to perform both solid state studies of the MoS_2-based catalysts and mechanistic investigations of the synthesis of alcohols. The former will allow us to gain insight into the nature of active sites on the catalyst, while the latter will elucidate the reaction pathway of alcohol formation. The information obtained from these studies can be used to optimize the activity of the catalyst and control the selectivity to a desired product.

The first goal in this research was to verify the alkali promotion effect over the MoS_2 catalysts for the synthesis of alcohols. The issue of the nature of the alkali promotion was explored in this part of the research. After reaching this goal, the concentration of the alkali promoter in the catalyst was optimized to produce high yields of C_1-C_4 alcohols.

The second goal was to elucidate the reaction pathway of alcohol formation over the alkali-doped MoS_2 and alkali-doped Co/MoS_2 catalysts. This was achieved by injecting ^{13}C-labeled methanol into the synthesis gas feedstream and analysis of the products by ^{13}C NMR spectroscopy and mass spectrometry.

The third goal was to characterize the alkali-doped MoS_2 catalysts in terms of alkali distribution, chemical state, and structural features of their components at different stages of preparation and testing of the catalysts. This was accomplished using various techniques such as: X-ray diffraction (XRD), BET surface area measurements, X-ray photoelectron spectroscopy (XPS), and scanning transmission electron microscopy (STEM). The key questions answered by this dissertation are the following:

1. Are alcohols and hydrocarbons formed by separate reaction pathways or is one the precursor of the other?

2. What is the mechanism of C-C bond formation for the alcohols and of the formation of simultaneously produced hydrocarbons and methyl esters?

3. How is the alcohol product selectivity affected by reaction conditions?

4. What is the mechanistic function of MoS_2 and of the alkali metal? What is the mechanistic function of Co, which has been demonstrated to promote the formation of ethanol?

5. Is the alkali promotion effect for the synthesis of alcohols over the MoS_2-based catalyst alkali-ion specific?

6. How does alkali concentration affect catalyst activity and selectivity?

7. What are the structural features of the alkali-doped MoS_2 catalysts?

8. What is the chemical composition and the oxidation state of the different elements (Cs, Mo, and S) present on the catalyst surface?

This dissertation is divided into six chapters. Chapter 1 presents an extensive review of the synthesis of alcohols and of the role of alkali metals in CO/H_2 reactions. In the last section of this chapter, the crystal structure and nature of the active sites of MoS_2

are discussed. In Chapter 2, the preparation of the catalysts as well as the experimental methods involved in the catalytic testing are described. Catalytic activity results obtained over the alkali/MoS_2 and alkali/(Co/MoS_2) catalysts at different operating conditions are discussed in detail in Chapter 3. The mechanism of C-C bond formation of alcohols, and of the simultaneously produced hydrocarbons and methyl esters, is given in Chapter 4. Characterization studies of the alkali/MoS_2 catalysts are presented in Chapter 5. Chapter 6 summarizes the conclusions reached in this research.

Chapter 1

1.1 Introduction

The history of research and development in the area of direct catalytic synthesis of alcohols from synthesis gas (CO + H_2) is a classic example of how raw material availability, economic needs, and changing technology have evolved over the years. Currently, many research organizations are involved in alcohol synthesis projects due to an increasing demand for octane booster components since the U.S. Environmental Protection Agency (EPA) mandated an accelerated schedule for removal of lead alkyls from gasoline (1) and reduction of volatile compounds (2). Other factors such as octane upgrade, which is expected to increase substantially by 1995, will also contribute to the need of octane boosters (see Table 1-1). Alcohols such as methanol, ethanol, propanol, and butanol not only can be mixed with gasoline to enhance the octane rating but also can be used as a whole motor-fuel and as base chemicals (3,4).

The main limitation for the industrial synthesis of higher alcohols from CO and H_2 has, until recently, been the lack of a selective and durable catalyst that allows an efficient production of the alcohols, although advances have been made in the development of different catalytic systems. These catalytic systems can be classified into three groups:

(1) Modified high pressure methanol synthesis catalyst, alkali-doped ZnO/Cr_2O_3 (5-7).

TABLE 1-1

Estimation of the Total Octane Demand[a]

	1990	1995
Estimated Gasoline Demand (million bbl/day)	7.12 (7.04 in 1987)	7.40
Total Octane Demand[b]	2.80	6.50
Due to:		
* Lead Demise	0.30	0.30
* Octane Upgrade	0.50 (88.90)	1.20 (89.50)
* Reduced Volatility		
- Phase 1	2.00	2.00
- Phase 2	--	3.00

[a] Data taken from A. El Sawy and D. Gray, U. S. DOE Indirect Liquefaction Contractors' Review Meeting, Pittsburgh, PA, Nov. 15-17, 1988.

[b] 1 Octane Demand = 5 MM gal MTBE(methyltertiarybutyl ether)/year

(2) Modified low pressure methanol synthesis catalyst, alkali-doped $Cu/ZnO/Al_2O_3$ (8-10).

(3) Modified Fischer-Tropsch catalysts, alkali-doped $CuO/CoO/Al_2O_3$ (11-14) and alkali-doped MoS_2 (15-17).

These three types of catalysts are currently used in processes offered by different companies, as discussed in Section 1.3. However, as mentioned above, the present technologies to manufacture higher alcohols from synthesis gas ($CO + H_2$) still do not fulfill the requirements needed to make a process for the synthesis of higher alcohols economically attractive. There is every reason to believe that the future of such processes depend upon improvements of the preparation of highly selective and longevous catalysts. Solid state studies of the catalysts combined with mechanistic investigations of the synthesis of alcohols need to be performed in order to achieve these improvements.

All the catalysts mentioned above, with the exception of MoS_2-based catalysts, have been extensively studied in academic, as well as industrial, laboratories, and interesting results have been achieved in the interpretation of reaction mechanism and in the understanding of the catalytic systems. However, very little has been published in the scientific literature (18-20) about the MoS_2-based catalysts that were recently discovered by The Dow Chemical Company and Union Carbide Corporation (15-17). This novel MoS_2-based catalyst is of both industrial and academic interest in C_1 chemistry due not only to its longevity and resistance to sulfur, and iron carbonyl poisoning, but also for its activity and selectivity for the synthesis of C_1-C_4

alcohols. The objective of the present research is to provide a scientific understanding of the synthesis of alcohols over MoS_2-based catalysts.

In the next sections of this chapter, a literature review of the synthesis of alcohols from CO and H_2 is presented, followed by a discussion of the crystal structure and nature of the active sites of MoS_2.

1.2 Historical Review of Higher Alcohol Synthesis

The production of higher alcohols from hydrogen and carbon monoxide has been known since the beginning of this century. In 1913, Badische Anilin and Soda Fabrik (BASF) patented a process to manufacture a mixture of alcohols, aldehydes, ketones, acids and other organic compounds (21). In this process, the reaction between CO and H_2 occurred in the presence of alkalized oxide of cobalt or osmium and at 100 to 200 atm and 300 to 400°C. In 1923-1924 Fischer and Tropsch developed the "synthol" process to produce higher alcohols (22). This process used an alkalized iron catalyst to convert synthesis gas to alcohols at pressures above 100 atm and at temperatures of 400 to 450°C. An important step in the selective synthesis of alcohols from CO and H_2 was the discovery of the ZnO and Cr_2O_3-base catalyst by BASF (23). The first high yields of methanol were obtained at relatively high pressures in the presence of these catalysts. A few years later, in 1928, several researchers (24-27) discovered that mixtures of

methanol and higher alcohols were obtained when ZnO/Cr_2O_3 catalysts were doped with alkali salts. From 1935 to 1945, plants using these types of catalysts to produce higher alcohols were in operation in Europe. Natta et al. (6) mentioned that process conditions in these plants were severe with high pressure and very short catalyst life. In the 1940's, I.G. Farbenindustrie and the Ruhrchemie in Germany developed the "synol" process (28), which was based on medium-pressure (20 atm) Fischer-Tropsch iron catalysts with operating conditions optimized to enhance the production of higher alcohols. After 1945, with the growing availability of petroleum and the increasing demand for pure alcohols for chemical uses, these plants became economically unattractive and consequently were demolished. In contrast, in the 1950's the industrial development of high pressure methanol synthesis was well established and zinc chromite a "satisfactory" catalyst. While research activity on higher alcohols synthesis was absent during the 1950's and 1960's, the research on methanol synthesis continued, and this culminated with the discovery, pioneered by ICI, of the low-pressure methanol synthesis process that utilized ternary catalysts based on copper, zinc oxide, and chromia or alumina. This new low-pressure process was considered a dramatic industrial breakthrough. Currently, almost all the world's methanol production is based on this low pressure methanol catalyst.

In the early 1970's there was renewed interest in the synthesis and use of higher alcohols as a synthetic fuel which was initiated by the Arab oil embargo that created an energy shock in the Western

World. There was an intensive world-wide research effort on the production and use of synthesis gas ($CO + H_2$) derived from coal as an alternative to crude oil. This research effort was reflected by the numerous papers published in the syngas field. In the early 1980's, with oil prices going down as well as the fact that governments and companies tend to forget troublesome times rapidly, research on alcohol synthesis was tended to decline in importance. Currently, the main driving force for the synthesis of alcohols from synthesis gas ($CO + H_2$) is an environmental one. Mixed alcohols (C_1-C_4) are thought to be a feasible alternative, along with MTBE (methyltertiarybutyl ether) and other ethers, to meet the increasing demand for octane (see Table 1-1).

1.3 Present Technology

In this section, the processes for obtaining higher alcohols from CO and H_2 that have been demonstrated on at least a pilot plot scale will be summarized. These processes are based on (i) modified high pressure methanol technology utilizing alkalized zinc oxide-chromia catalysts, (ii) modified low pressure methanol technology utilizing alkalized copper-zinc oxide catalysts, (iii) combined methanol Fischer-Tropsch technology utilizing alkalized copper-cobalt-oxide catalysts and (iv) the Dow-Union Carbide technology utilizing alkalized molybdenum sulfide catalysts.

Figure 1-1 shows the temperature and pressure ranges under which these types of catalysts will operate, along with those for typical

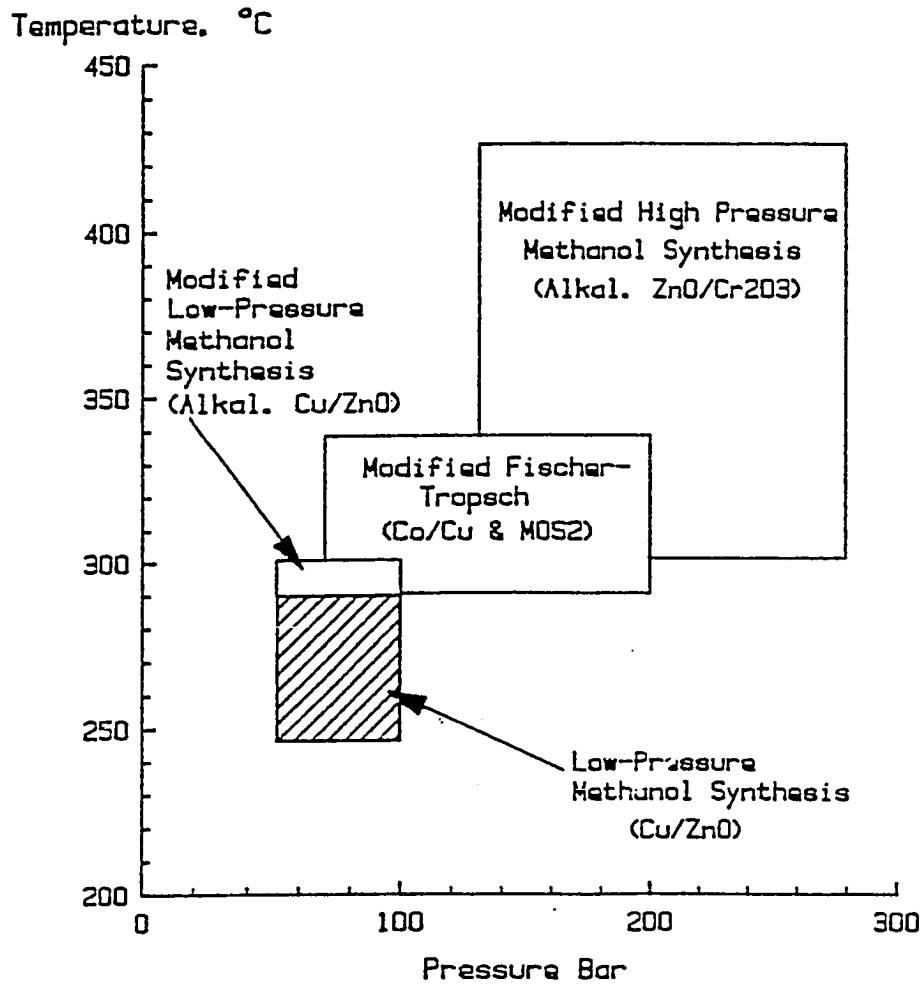

Figure 1-1 Pressure-temperature regions for higher alcohol synthesis processes (from Reference 1).

Table 1-2

Basic Operating Characteristics of Higher Alcohol Synthesis Technologies (from Reference 32).

Process / Main Characteristics	1 SEHT (MAS) Process	2 IFP (Substifual) Process	3 Dow HAS Process	3 UCC HAS	3 LU[a] HAS	4 Dow HAS	4 Lurgi OCTAMIX Process	5 LU[a] HAS Process	5 LU[a] HAS
Main Constituents of Catalyst	K/Zn/Cr	K/Cu/Co/Al	K/Co/MoS_2	Cs/MoS_2	Cs/MoS_2	K/MoS_2	Alkali/Cu/Zn/Cr Promoters	Cs/Cu/ZnO	Cs/Cu/ZnO/Cr_2O_3
Catalyst Stability (life), h	8,000	~2,000	>8,000	n.a.	>200	n.a.	8,000	>1,200[b]	>750[b]
Operating Temperature, °C	350-420	260-320	306	300	295	255	285-300	300	300
Operating Pressure, MPa	10-18	6-10	10.3	2.75	8.2	10.3	6-9	9.1	9.1
Syngas Space Velocity, 1000 h^{-1}	3.0-8.0	3.0-6.0	3.8	12.0	7.8	3.2	3.0-6.0	3.265	3.255
Syngas Feed H_2/CO Ratio	2-3	1-2	1[c]	1	0.96	1.02[c]	0.5-1.0	0.7	0.7
Syngas CO_2 Content, vol.%	1.0-6.0	2.5-3.5	0.0	0.0	0.0	0.0	1.0	0.0	0.0
Performance Characteristics									
Thermal Efficiency, %	56	-	-	-	-	-	60	-	-
CO Conversion Per Pass[d], %	14	12-15	16	4.8	9.1	12.3	13-30	22	25.5
Liquid Product Selectivity, %	90	70-75	88	80	77	85	95	>96	>96
C_2^+OH Selectivity, %	20-30	25-50	51.6	32.8	37.3	32.2	20-30	31.3	36.5
Alcohol Space Time Yield, kg/ℓ cat/hr[e] or kg/kg cat/hr[f]	0.21[e]	0.1-0.15[e]	0.23-0.30[f]	0.256[f]	0.32[f]	0.19-0.32[f]	0.46[e]	0.373[f]	0.46[f]

a Lehigh University
b Deactivation data in Reference 32
c Contained 50 p.p.m. H_2S
d CO conversion exclusive of CO_2
e STY in kg oxygenate product per hour per ℓ catalyst
f STY in kg oxygenate product per hour per kg catalyst

low pressure methanol synthesis catalysts. Table 1-2 summarizes the different processes and their basic operating characteristics offered by several companies for the synthesis of higher alcohols in the presence of the catalysts mentioned above. Results obtained on a bench scale at Lehigh University are also presented in Table 1-2 for the sake of comparison. All these processes have been discussed in detail in the literature (13,15,29-32). Recent evaluations of these systems by both industrial (2) and academic researchers (32,33) concluded, among other things, that improvements in the performance of these catalysts are needed for more efficient conversion of synthesis gas to alcohols.

1.4 Methanol Synthesis

Methanol synthesis is a major industrial process which is made catalytically from CO, CO_2, H_2 mixtures that are produced by steam reforming of natural gas or other hydrocarbons. The reactions involved in the synthesis of methanol are:

$$CO + 2H_2 = CH_3OH \qquad \Delta G_{600K} = +45.36 \text{ kJ/mol} \qquad [1.1]$$

$$CO_2 + 2H_2 = CH_3OH + H_2O \qquad \Delta G^\circ_{600K} = +61.80 \text{ kJ/mol} \qquad [1.2]$$

Simultaneously occurring with catalytic methanol synthesis is the water gas shift (WGS) reaction

$$CO + H_2O = CO_2 + H_2 \qquad \Delta G^\circ_{600K} = -16.5 \text{ kJ/mol} \qquad [1.3]$$

There are two industrial processes for the methanol synthesis:

(i) a high-pressure process that operates at P = 250-300 atm and T = 330-400°C and uses a ZnO/Cr_2O_3 catalyst and (ii) the ICI low-pressure process that operates at P = 50-100 atm and T = 200-270°C and uses a $Cu/ZnO/Al_2O_3$ catalyst. Currently, most of the methanol production is performed using the ICI low-pressure process. Although the synthesis of methanol is a well established industrial process and the reactions [1.1] and [1.2] that give rise to methanol appear rather simple, the exact mechanistic pathway that leads to the formation of methanol and the active sites of the Cu/ZnO based catalyst are still unknown and the subject of many controversies. In the next section the different mechanisms proposed in the literature are summarized. Interested readers should refer to references (34-39) and references therein for details.

1.4.1 Mechanism of Methanol Synthesis

The reaction pathway of methanol synthesis has been attempted to be solved by following two approaches. The first is the old fashioned method which consists of assuming the elementary steps of methanol formation and testing the derived rate equation by kinetic measurements of the overall reaction. This method has been shown to give ambiguous results, since several kinetic models will usually fit the experimental data. The second approach, which is currently widely used, consists of identifying the different intermediate species using spectroscopic, chemical trapping and isotopic tracer techniques. The

proposed reaction mechanisms for the formation of methanol over the Cu/ZnO catalyst have been reviewed in detail by Klier (36) and more recently by Bart and Sneeden (38) and by Kinnemann and Hindermann (39). The mechanisms proposed for the synthesis of methanol are either based on formyl or on formate species. The reaction schemes are:

I. Formyl species mechanism

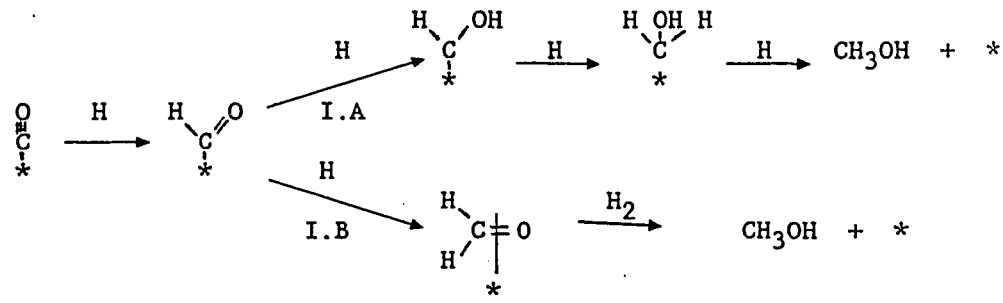

II. Formate species mechanism

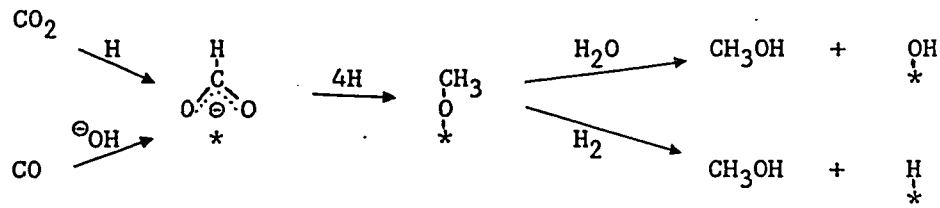

In Mechanism I the first step of the reaction is the formation of a formyl group which can be hydrogenated to produce either hydroxycarbene (route I.A) or formaldehyde (route I.B) which are further hydrogenated to produce methanol. In Mechanism II the first

step of the reaction is the insertion of CO into a surface hydroxyl to form a surface formate. This is followed by subsequent hydrogenation and dehydration to form a surface methoxide and then methanol. Klier (36) summarized the thermodynamic energies of the various intermediates involved in Mechanisms I and II. His results are presented in Figure 1-2 that shows enthalpies and Gibbs free energies at 250°C which would be required for noncatalyzed reactions that involve a particular set of intermediates. Klier concluded from his thermodynamic analysis that the catalyst would have to lower the 200 kJ/mol thermodynamic barrier of hydroxycarbene formation (route I.A), while the pathway of Mechanism II would require destabilization of the surface formate and methoxide. The author pointed out that the removal of surface methoxide by hydrolysis would proceed with a lower thermodynamic barrier than by hydrogenation. Klier also mentioned that the formaldehyde pathway (route I.B) would seem to be a feasible one because the free energy of formaldehyde lies only 17 kJ/mol above that of methanol, although, he added, is likely that large kinetic barriers exist for the synthesis of formaldehyde that offset the thermodynamic feasibility of pathway I.B, since formaldehyde has never been observed as intermediate of methanol synthesis over the Cu/ZnO catalyst. The identification of intermediates present on the catalyst surface during methanol synthesis has been the subject of great interest as evidenced by the number of publications on this matter.

The evidence for aldehydic type intermediates such as formyl, formaldehyde, or hydroxycarbene comes from isotopic tagging,

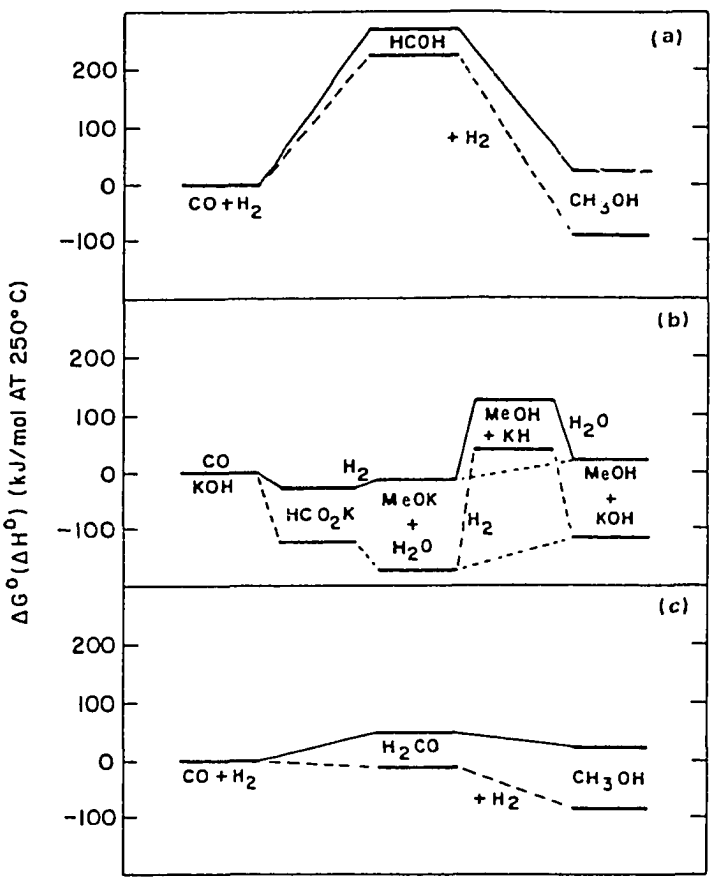

Figure 1-2 Standard enthalpy (dashed lines) and Gibbs free-energy (full lines) changes for intermediates in methanol synthesis; (a) hydroxycarbene route, (b) formate-methoxide route, and (c) formaldehyde route (from Reference 36).

spectroscopic, and chemical trapping studies. Formyl species were identified by chemical trapping on Ni, Rh, and Pd (40). Their evolution was followed on Pd by Deluzarche et al. (40). Recently, Vedage and co-workers (41) reported the detection of C_1 intermediate of the type either of a formyl or a hydroxycarbene over the Cu/ZnO catalyst by trapping experiments with amine. Surface formyl complexes have been identified by IR (42,43) on ZnO and Cu/ZnO after co-adsorption of CO and H_2 at near ambient conditions. Takeuchi and Katzer (44) used a mixture of $^{13}C^{16}O$ and $^{12}C^{18}O$ and H_2 over a Rh/TiO_2 catalyst that produced $^{13}CH_3{}^{16}OH$ and $^{12}CH_3{}^{18}OH$, but not $^{13}CH_3{}^{18}OH$ and $^{12}CH_3{}^{16}OH$. This result indicated that methanol is produced through the formyl path (Mechanism I) and excludes the formate path in which the two equivalent oxygens would result in isotopic scrambling to produce $^{13}CH_3{}^{18}OH$ and $^{12}CH_3{}^{16}OH$.

Evidence for Mechanism II, which involves formate and methoxide species, has been obtained using a great variety of techniques. Surface formate and methoxide species have been detected by IR spectroscopy in methanol decomposition over ZnO by Veno et al. (45). The authors concluded that by invoking the principle of microscopic reversibility these intermediate species must also participate in the synthesis reaction. The surface methoxide was also detected in IR spectra of methanol chemisorbed on iron, nickel, and cobalt (46), magnesia (47), and alumina (48). Amenomiya et al. (49) studied methanol synthesis from CO_2 and H_2 over $Cu/ZnO/Al_2O_3$ catalysts with the aid of a high pressure-temperature IR cell incorporated into a

continuous flow high pressure reaction system. They accompanied their in-situ spectroscopic investigation with a simultaneous kinetic study. The authors concluded that the formate ion is directly involved in the reaction path of both methanol synthesis and reverse water-gas shift reaction, and added that the rate-determining steps of the reactions are the hydrogenation and decomposition of formate, respectively. Edwards and Schrader (50) also performed high pressure IR studies and confirmed that the formate species should be considered as a reaction intermediate in both CO_2 and CO hydrogenation to methanol. More recently, Bogdan (51) showed by in situ IR studies that contacting Cs/ZnO or Cs/Cu/ZnO catalysts with CO + H_2 led to the formation of a unique CsOOCH species on the catalyst surface. In chemical trapping experiments with $SO_4(CH_3)_2$ and $SO_4(C_2H_5)_2$, formate and methoxide species have been detected during methanol synthesis from H_2/CO or H_2/CO_2 over Cu/ZnO catalysts (52,53). The synthesis of methanol through the formate mechanism was supported by Klier et al. (54) who injected D_2O into the CO/H_2 mixture to obtain methanol singly deuterated on the CH_3 group, $CH_2DO(H,D)$. These authors mentioned that quantitative evaluation of the isotope flow led to the conclusion that the formate mechanism accounted for at least 65% of the methanol synthesis from $CO/H_2 + D_2O$.

To conciliate the fact that experimental evidence supported the presence of aldehydic, formate, and methoxide species on the Cu/ZnO catalyst surface, Kinnemann and Hindermann (39) proposed the mechanism of methanol synthesis shown in Scheme 1-1.

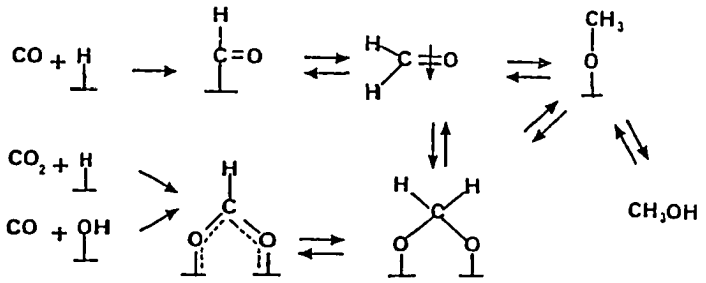

Scheme 1-1

The dioxymethylene species shown in this scheme has been observed over the Cu/ZnO catalyst by FT-IR (55) and in chemical trapping experiments (55) according to reaction:

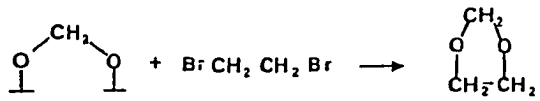

[1.4]

Very recently, Nunan et al. (56) also proposed a mechanism shown in Scheme 1-2, that encompasses both the formyl and formate intermediates over the Cs-doped Cu/ZnO catalyst.

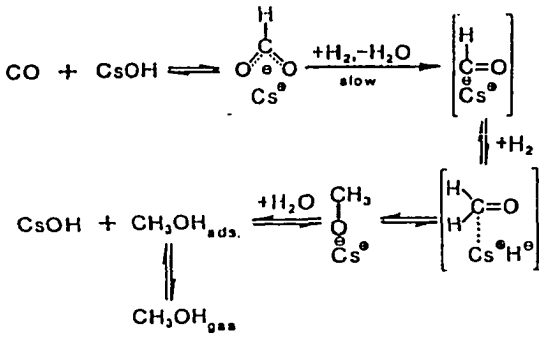

Scheme 1-2

In conclusion, there is a general agreement among various researchers that on nobel metal catalysts, e.g. Pd and Rh, the main route to methanol seems to be the formyl pathway, while on Cu/ZnO the

formation of methanol goes through formyl and formate intermediates

1.5 Higher Alcohol Synthesis

Aliphatic alcohols are synthesized from synthesis gas ($CO + H_2$) by the following over-all reaction

$$nCO + 2nH_2 = C_nH_{2n+1}OH + (n-1)H_2O \ . \qquad [1.5]$$

Simultaneously occurring is the water gas shift reaction

$$CO + H_2O = CO_2 + H_2 \ . \qquad [1.6]$$

Secondary reactions produce light hydrocarbons according to reactions

$$2nH_2 + nCO \rightarrow C_nH_{2n} + nH_2O, \text{ and} \qquad [1.7]$$

$$(2n+1)H_2 + nCO \rightarrow C_nH_{2n+2} + nH_2O \qquad [1.8]$$

Thermodynamic considerations of the above reactions, which have been discussed in detail by Natta (6) and Klier (36) and summarized in Figure 1-3, indicate that hydrocarbon formation is accompanied with a more negative free-energy change than for the formation of alcohols, as shown in Figure 1-3. To minimize or avoid the formation of hydrocarbons and allow the selective formation of alcohols, it is necessary to use a catalyst that will promote the formation of surface intermediates that give rise to the production of alcohols. In other words, the catalyst should be able to change the thermodynamically controlled process, which favors the production of hydrocarbons, to a

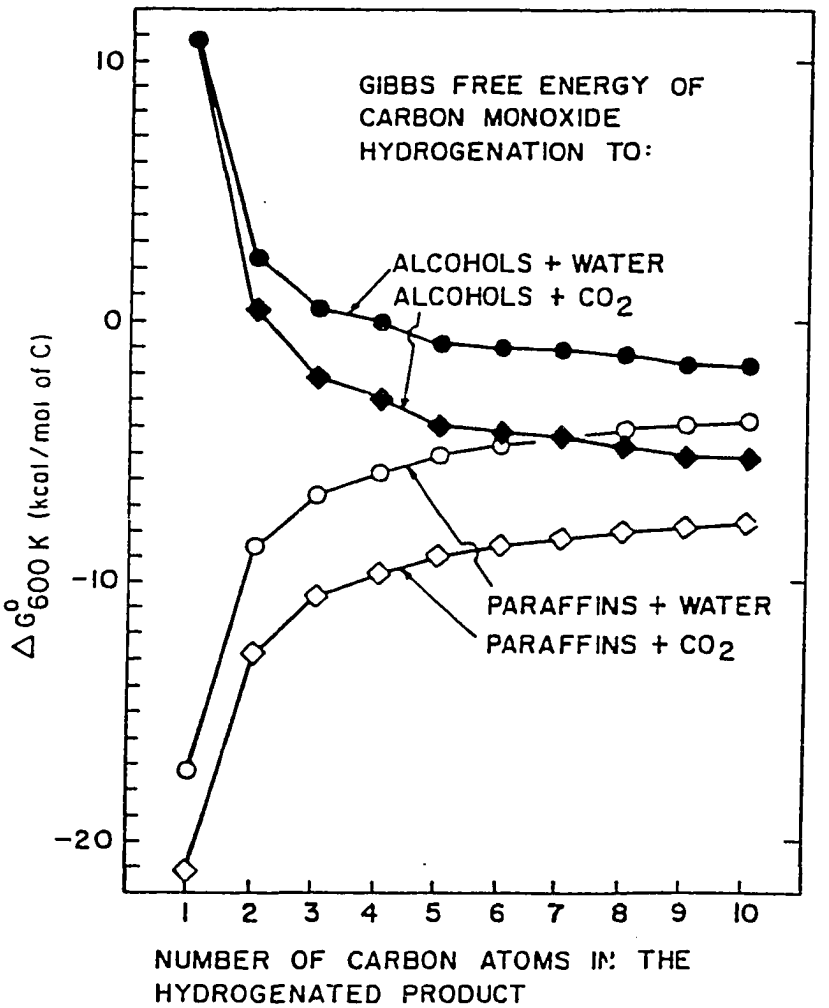

Figure 1-3 Gibbs free energies, $\Delta G°$, at 600K (kcal/mol of carbon) for the formation of alcohols and hydrocarbons from synthesis gas (from Reference 36).

kinetically controlled process, which would favor the production of alcohols. The distribution of the products obtained in higher alcohol synthesis depend upon the catalyst used and the operating conditions. Linear and branched higher alcohols are obtained over the alkali modified methanol synthesis catalysts, which typically contain Cu and ZnO with a Cr_2O_3 or Al_2O_3 support (8-10), while mainly linear alcohols are produced over alkali promoted Group VIII metals (28,57,58). Catalysts having both Fischer-Tropsch and methanol synthesis components, namely iron and copper (59,60) or cobalt and copper doped with alkali salts (11-14) produce significant yields of linear alcohols. The newly developed alkali-doped MoS_2 catalysts (15-17) also produce mainly linear alcohols. Formation of linear alcohols over some catalysts while branched alcohols are formed over other indicates that at least two different mechanisms are operable in alcohol synthesis.

1.5.1 Mechanism of the Higher Alcohol Synthesis

Many mechanistic pathways for the formation of higher alcohols over different catalysts have been postulated. The various early hypotheses, as well as current views, are described below.

(I) CO Insertion Mechanisms

The first hypothesis of a mechanism for the formation of higher alcohols from CO/H_2 was advanced by Fischer and Tropsch (22), who

suggested that higher alcohols are formed from methanol and carbon monoxide through the following consecutive reactions:

$$CH_3OH + CO \rightarrow CH_3COOH \quad [1.9]$$

$$CH_3COOH + H_2 \rightarrow CH_3CHO + H_2O \quad [1.10]$$

$$CH_3CHO + H_2 \rightarrow C_2H_5OH \quad [1.11]$$

and so forth for primary linear higher alcohols. This reaction sequence involves CO insertion into the C-O bond to form the C-C bond, followed by sequential hydrogenation to give the next higher alcohol. Natta et al. (6) proposed that the catalyst (KOH/ZnO) participated directly in the mechanism of the synthesis through the formation of an alkali alkoxide, which reacted with CO followed by rearrangement to give alkali carboxylate that is subsequently hydrogenated to the corresponding alcohol. Recently, this mechanism was also invoked to account for the formation of linear alcohols over the Cs/Cu/ZnO catalyst (10). More recently, Kiennemann and Hindermann (39) pointed out that the major drawback of this hypothesis is however the CO insertion into a carbon-oxygen bond for which no model is known in homogeneous catalysis, whereas the insertion into a metal carbon linkage is well documented by experiments. Wender et al. (61) were among the first researchers to suggest that carbon-carbon bond formation occurred via the insertion of CO in metal-carbon bonds as originally proposed for homogeneous organometallic CO catalysis (61). Later Pichler and Schulz (62), as well as Henrici-Olivé and Olivé

(63), proposed detailed reaction mechanisms involving CO insertion into metal-H bonds (initiation) and metal-alkyl bonds (chain growth) to account for the formation of alcohols and hydrocarbons during the catalyzed reaction between CO and H_2. The reaction mechanism proposed by Henrici-Olivé and Olivé is shown in Scheme 1-3. More recently, several researchers (64-66) have employed this CO insertion mechanism to describe the carbon chain growth over Group VIII metals. CO insertion into the M-C bond of a surface bound aldehyde forming a symmetric glycolate that is subsequently hydrogenated to ethanol was proposed by Mazanec (67) and described in Scheme 1-4.

(II) Enol Condensation Mechanism

This hypothesis is based on the work of Anderson et al. (68,69) and Emmett et al. (70,71), and may be written as follows:

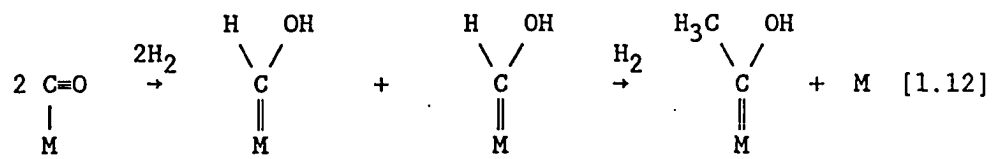

[1.12]

In this mechanism, the methanol precursor is the chain initiator and the synthesis of C_2^+ alcohols would occur via hydroxycarbene intermediates. The reaction is terminated by hydrogenolysis of the M-C bond and formation of the corresponding alcohol. The authors mentioned that the chemisorbed alcohol can be dehydrated to hydrocarbons that would in this case have the same growth probability

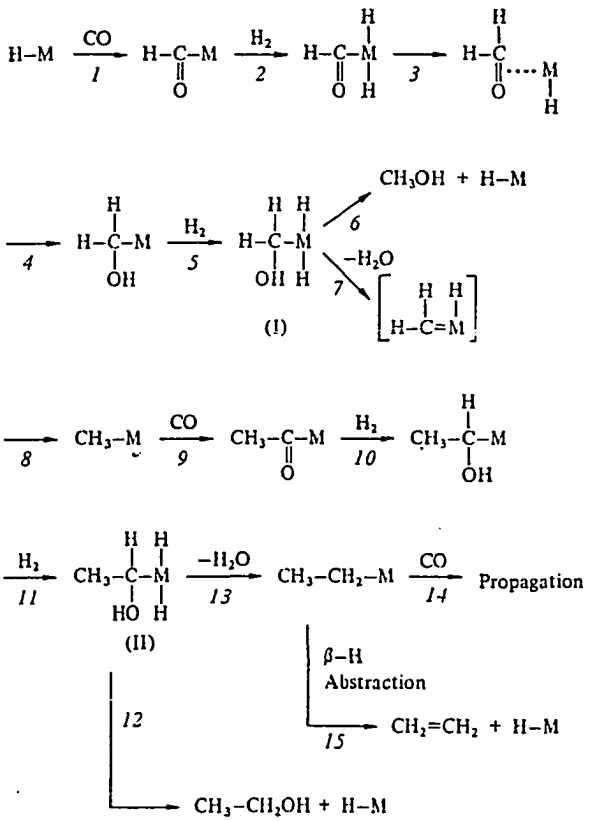

Scheme 1-3

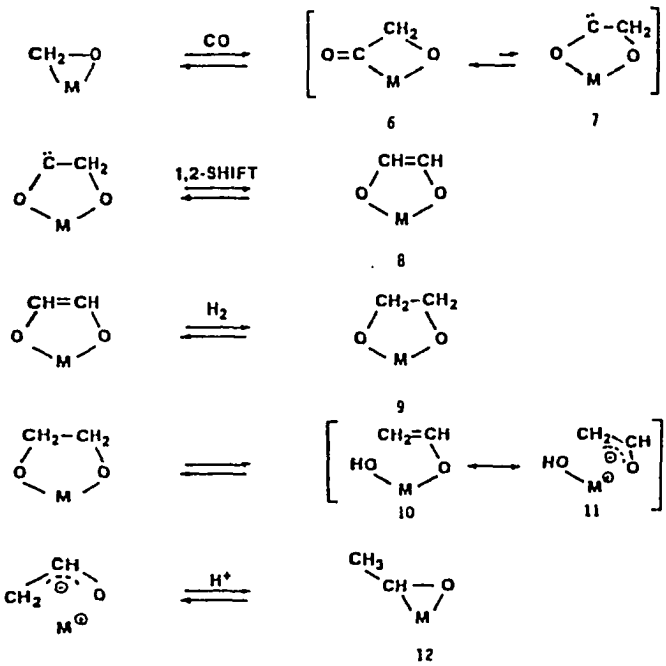

Scheme 1-4

as the alcohols.

(III) Condensation of Alcohols

Frolich and Cryder (72) and later Graves (73) proposed that higher alcohols are formed via condensation of lower alcohols according to reactions:

$$2CH_3OH \rightarrow CH_3CH_2OH + H_2O \quad [1.13]$$

$$CH_3OH + CH_3CH_2OH \rightarrow CH_3CH_2CH_2OH + H_2O \quad [1.14]$$

(IV) Aldol Condensation of Aldehydes

The formation of higher alcohols was postulated by Morgan et al. (74) and Taylor (75) to take place through aldol condensation of formaldehyde with other aldehydic species according to the reaction sequence

$$HCHO + RCH_2\text{-}CHO \rightarrow \underset{\substack{| \quad | \\ OH \quad R}}{CH_2\text{-}CH\text{-}CHO} \rightarrow \underset{\substack{| \\ R}}{CH_2{=}CCHO} \rightarrow \underset{\substack{| \\ R}}{CH_3\text{-}CHCH_2OH} \quad [1.15]$$

This mechanism was adopted by Vedage et al. (10) to explain the formation of higher alcohols, especially the branched 2-methyl-1-propanol product, over the Cs-doped Cu/ZnO catalyst. Fox et al. (76) also invoked this mechanism to account for the formation of higher alcohols from methanol in the presence of metal acetylides. Very recently, Nunan et al. (56) performed isotopic labeling experiments

during the synthesis of C_2^+ alcohols over the Cs/Cu/ZnO catalyst and concluded that "adsorbed formyl is a reactive nucleophile that forms the C-C bond by attacking the electropositive carbon of adsorbed formaldehyde or methanol." The authors proposed the mechanisms depicted in Schemes 1-5 and 1-6.

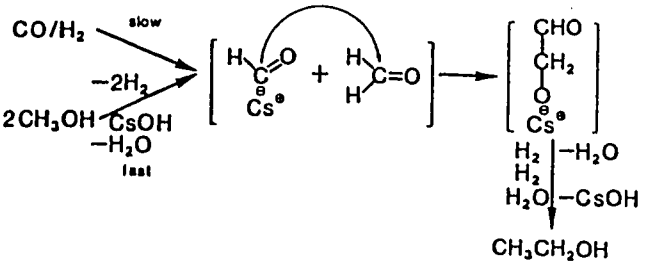

Scheme 1-5

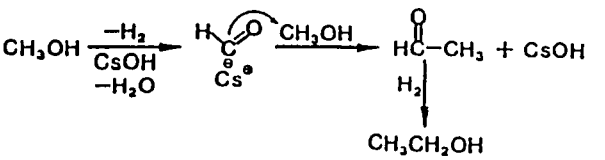

Scheme 1-6

1.6 Alkali Promotion on Alcohol Synthesis

The promotional effect of alkali in heterogeneous catalysis was first described more than 100 years ago by Döbereiner (77) when he observed that contacting platinum sponge with NaOH or KOH greatly increased its oxidation power. The positive effect of alkali doping has long been known for a great variety of reactions, which include coal gasification, alcohol synthesis, ammonia synthesis, and the oxidation of ethylene to ethylene oxide. Mross (78) has listed at least 30 industrial catalytic processes in which alkali-promoted catalysts are employed, and mentioned that the effect of alkali doping was evidently not restricted to particular types of reactions. The effect of the alkali can manifest itself in a number of ways, e.g. (i) increase or decrease of the selectivity, (ii) increase or decrease of the activity, and (iii) increase of catalyst lifetime. Fischer and Tropsch (22) were probably the first researchers that reported the promotional effect of alkali in the yield of higher alcohols obtained from CO and H_2 over an alkali-promoted iron-base catalyst. They mentioned that the promotional effect increases with the basic character of the promoters. Later, Natta and Strada (79) obtained similar results with ZnO-based catalysts and reported that the highest yields of higher alcohols were obtained by the use of catalysts containing K, Rb or Cs ions. In the following years, Morgan et al. (74) performed a systematic investigation of the influence of the addition of five different alkali ions to a Cr_2O_3/MnO catalyst used

for the synthesis of alcohols. They concluded that the yield of higher alcohols increased with the addition of alkaline promoters in the order: Li, Na, K, Rb, Cs. These results were confirmed later by Taylor (75). These early observations led to the use of alkali metals as promoters for the synthesis of higher alcohols over different catalytic systems that are used currently, namely, alkalized zinc-chromium catalysts (5-7), alkali-doped Cu/ZnO catalysts (8-10), alkali-doped copper-cobalt catalysts (11-14) and the recently developed alkali-doped MoS_2 catalysts (15-17). One can conclude that the promotional effect of alkali metals on certain CO/H_2 reactions, as well as on many other important catalytic reactions, is well established. However, the nature of the promotion is not well understood. The theories that have been proposed to explain the role of alkali as a promoter in CO/H_2 reactions are briefly discussed below.

(I) Electronic Effect

The promotional effect of alkali upon semiconductor and metallic catalysts is often explained based on electron-donation processes. Dry et al. (80) interpreted the change of catalytic performance of an iron catalyst upon addition of K_2O or K_2CO_3 based on the electron-donor capacity of K_2O. Electrons donated to the metal are assumed to enhance the adsorption of CO while reducing that of H_2. Charge transfer into CO from alkali via a transition metal is a well accepted

phenomenon (78), and it has been suggested that electrons transfer into the antibonding molecular orbital $2\pi^*$ of the adsorbed CO, thereby weakening the CO bond and strengthening the transition metal-CO bond. The reduced availability of H_2 has been explained (78) to be due to H_2 becoming chemisorbed and transferring electrons to the metal; thus the electron-donating alkali weakens the M-H bond. As a consequence of these events the chain growth is accelerated, and the formation of olefins and oxygenated products is expected to increase. However, a completely different interpretation of the effect of alkali on oxide catalysts used for the CO/H_2 reaction has been given and is discussed below.

(II) Chemical Effect

Natta (6) was the first researcher to suggest that the alkali compound participates directly in the carbon-carbon bond formation of alcohol synthesis by forming kinetically significant intermediates (details are given in Section 1.5.1). More recently, Klier et al. (10,56,81) have proposed that the alkali compound present on the Cu/ZnO catalyst is directly involved in the synthesis of methanol, activating CO through the formate mechanism (56), and also in the synthesis of higher alcohols through base-catalyzed reactions (56,81), as discussed in Section 1.5.1.

Henrici-Olivé and Olivé (82), based on organometallic chemistry results, proposed that the role of alkali promoters in the Fischer-Tropsch reactions is to promote the insertion of CO into a metal-

carbon bond. It was suggested that transition metal carbonylates, as well as donor (e.g. alkyl) substituted neutral carbonyl complexes, interact with an electron acceptor (Mg^{2+}, K^+, Na^+, Li^+, AlX_3, etc.) through the electron-rich oxygen of the carbonyl group (83). This interaction strengthens the metal-carbon bond and weakens the carbon-oxygen bond of the involved carbonyl ligand, as shown by various X-ray diffraction and IR studies (82). Henrici-Olivé and Olivé made reference to the studies performed by Collman et al. (84,85), who showed that the close interaction of an alkali cation with a carbonyl ligand of the alkyliron carbonyl $Na^+[RFe(CO)_4]^-$ greatly favors the migratory insertion of the CO ligand into the metal alkyl bond, according to reaction:

$$Na \ldots OC - Fe(CO_3)R \rightarrow R - \overset{\overset{Na^+}{O^-}}{\overset{|}{C}} - Fe(CO)_3 \qquad [1.16]$$

Collman and co-workers found that the Li^+ or Na^+ cations cause the insertion reaction to occur 2 to 3 orders of magnitude faster than the rate observed when the cation was trapped in a crown ether. Henrici-Olivé and Olivé (82) added that the interaction of an alkali cation with the oxygen of a carbonyl group leads to a lowering of the energy of the lower unoccupied orbital of the carbonyl group (86), which contributes to facilitating the insertion reaction.

(III) Geometric Effect

It has been suggested by several authors (87-89) that the role of alkali metals as catalytic modifiers in the CO/H_2 reactions over Group VIII metals is that of a selective poison. The depression of the rate of hydrogenation of the surface species was explained by invoking site blocking by the alkali metal adatoms rather than by an electronic effect (87).

1.7 Molybdenum Disulfide

Transition metal sulfide catalysts, mainly MoS_2, have played an important role in many important technological processes. These catalysts were originally used in the hydrogenation of coal and tar and later became essential catalysts in the field of petroleum processing (hydrodesulfurization, hydrodenitrogenation, hydrorefining, hydrocracking, etc.). Recently, sulfide catalysts are beginning to be used outside the petroleum industry. Their application is being considered in many processes where the raw materials processed contain substances, especially sulfur compounds, that are catalytic poisons to other types of catalysts. There are only a limited number of substances, for instance arsenic compounds, that cause efficient deactivation of sulfide catalysts (90). Weisser and Landa (90) have summarized the great variety of processes in which sulfide catalysts are being used or have shown potential to be used. Recently, Newsome (91) reviewed the water-gas shift reaction catalysts and concluded

that the alkali-doped cobalt-molybdenum disulfide catalysts are not only sulfur tolerant, but their activity is competitive with the best industrial water-gas shift catalysts (Fe-Cr, Zn-Cu-Cr). More recently, it was reported that molybdenum disulfide-based catalysts show good activity and selectivity for the synthesis of alcohols from synthesis gas (CO + H_2) (15-17). In the following sections, the crystal structure and nature of the active sites of these industrially important molybdenum disulfide catalysts are described.

1.7.1 Crystal Structure of MoS_2

Molybdenum disulfide exists in the two crystalline forms of hexagonal (a = 3.16; c = 12.19Å) and rhombohedral (a = 3.16; c = 18.38Å). The hexagonal form is reported to be the MoS_2 phase present in the catalytic systems. Catalytic properties of the rhombohedral form, which is obtained at high pressure (> 47 kbar) and high temperature (> 1050 °C), are not known.

The crystal structure of MoS_2 was first investigated with natural molybdenite in 1923 by Dickinson and Pauling (92). They reported that the compound is hexagonal and characterized by MoS_2 layers in which the Mo atoms have trigonal prismatic coordination of six sulfur atoms, with two molecules per unit cell. In this structure, single layers of Mo^{4+} cations are sandwiched between two layers of close-packed S^{2-} anions as shown in Figure 1-4. Crystals with layers having antiparallel orientation represent the hexagonal form, while those of parallel orientation yield the rhombohedral form (see Figure 1-5).

Within these layers, each S^{2-} anion is equidistant from three Mo^{4+} cations, and each Mo^{4+} cation is bounded to six S^{2-} anions at the corners of a trigonal prism with altitude and edge dimensions of 3.17 Å and 3.15 Å, respectively, where the Mo to S spacing is 2.41 Å as shown in Figure 1-6. The two vicinal sulfur layers are bound by van der Waals forces. The strong bonding along two dimensions and the weak bonding between layers in MoS_2 give rise to two major types of exposed planes for MoS_2 crystallites; i.e. the (0002) basal plane and the two most stable edge planes, $(10\bar{1}0)$ and $(11\bar{2}0)$. These planes are shown in Figure 1-7(a-c). The MoS_2 basal plane is more stable than the edge plane because the S^{2-} anions located on the basal plane are coordinately saturated. Each S^{2-} anion has three bonds to Mo^{4+} cations and each Mo^{4+} is coordinated to six S^{2-}, while S^{2-} anions located on the edge plane are coordinately unsaturated. The latter anions have either one or two bonds to Mo^{4+} cations. It is interesting to point out that only sulfur atoms are exposed on the basal plane, while both sulfur and molybdenum atoms are exposed on the edge planes.

1.7.2 Nature of the Active Sites on MoS_2

As with most heterogeneous catalysts, the catalytic activity of MoS_2 is related to defect sites in its crystal lattice. These defects sites or active sites have been shown to be present at the edge planes of MoS_2 crystals and not at ordered basal planes. The activity of the edge planes of MoS_2 towards hydrogenation reaction has been

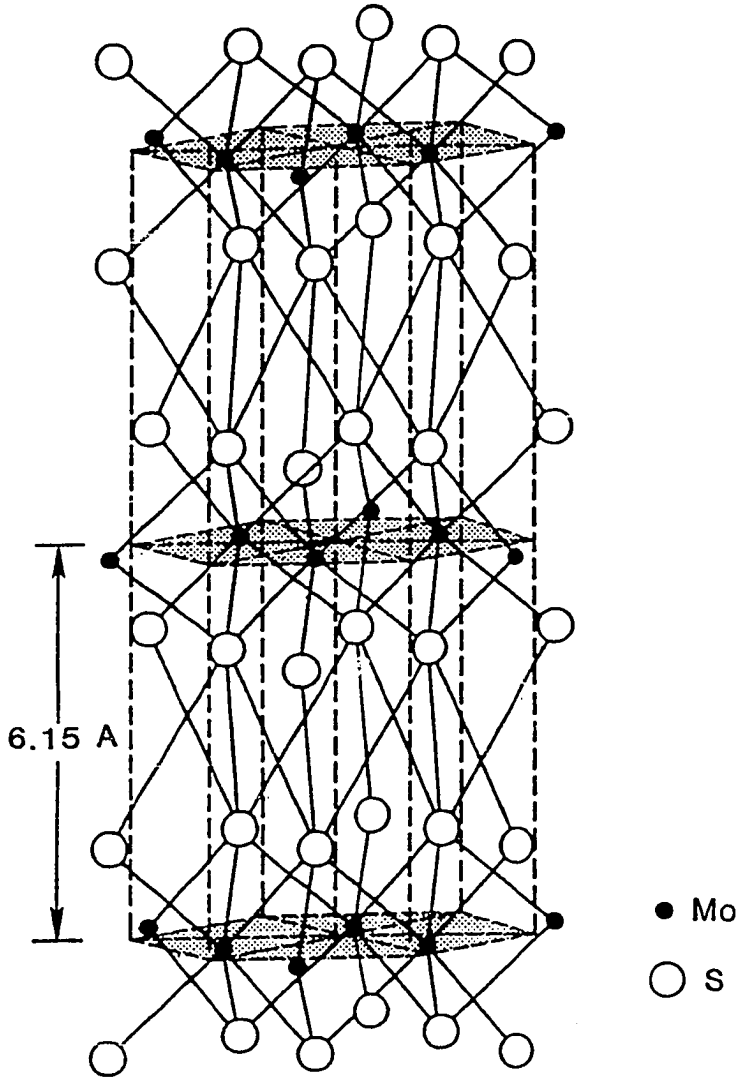

CRYSTAL STRUCTURE OF MoS_2

Figure 1-4 The hexagonal crystal structure of MoS_2.

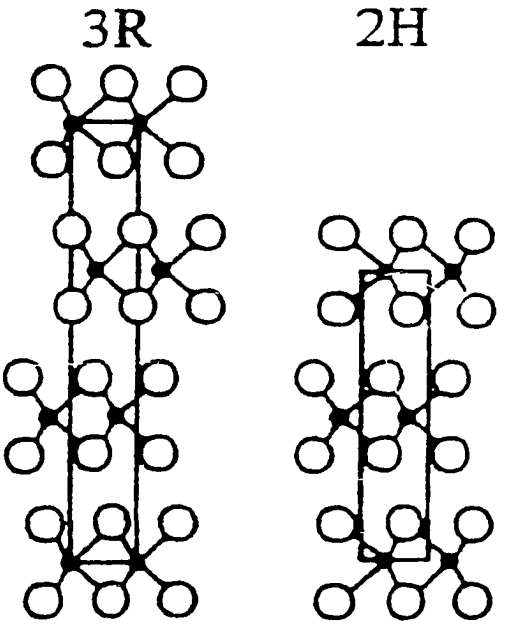

Figure 1-5 Rhombohedral (R) and hexagonal (H) structures projected along the a axis. The coefficient represents the number of molecules per unit cell.

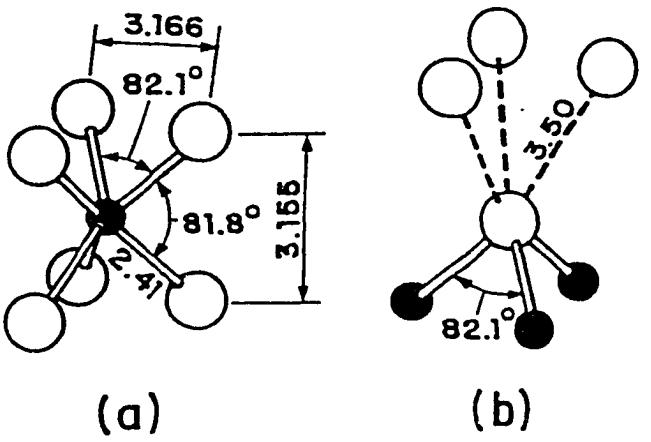

Figure 1-6 Atomic coordination in MoS_2: (a) configuration of the MoS_6 trigonal prism and (b) surroundings of the sulfur atom. Mo and S are respectively shown by solid and open circles.

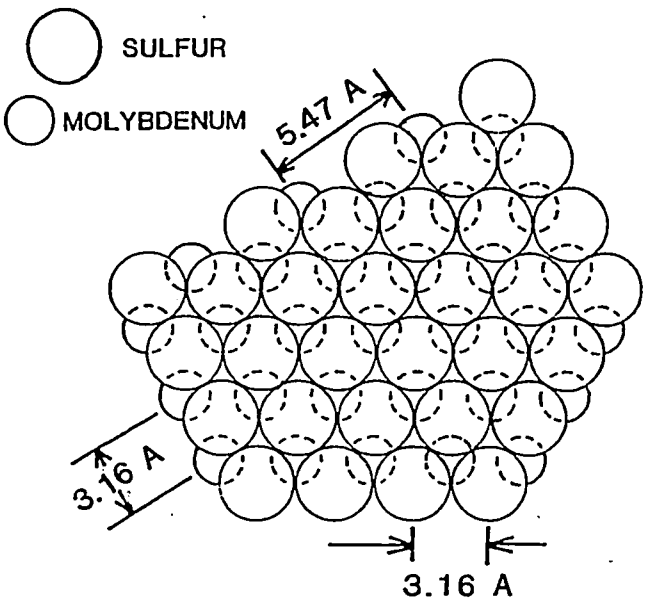

(a) (0002)

Figure 1-7 (a) The (0002) basal plane of MoS_2.

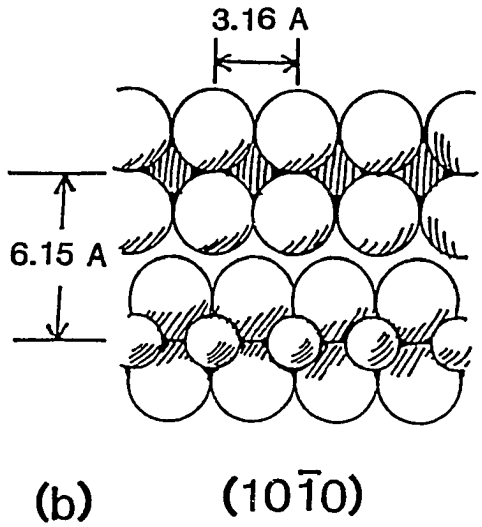

(b) $(10\bar{1}0)$

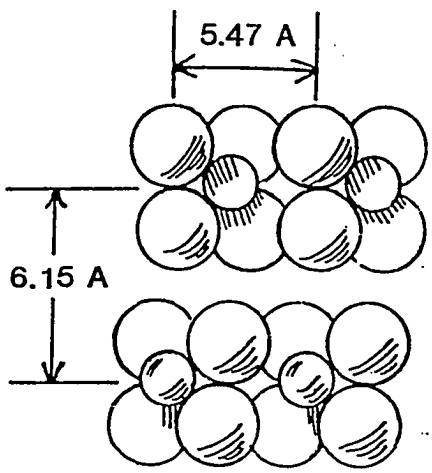

(c) $(11\bar{2}0)$

Figure 1-7 (b) The $(10\bar{1}0)$ edge plane of MoS_2 and (c) The $(11\bar{2}0)$ edge plane of MoS_2.

demonstrated by Tanaka and Okuhara (93), who compared the activity of edge planes and basal planes of MoS_2 by cutting single crystals into pieces and comparing the rates of cut and uncut crystals. These authors reported that the H_2-D_2 equilibration reaction, hydrogen exchange of ethylene, and hydrogenation reactions took place preferentially on the edge surface of MoS_2. Earlier, Stevens and Edmonds (94) had suggested that the edge planes promote the hydrogenation reactions.

The inertness of the basal planes has been shown by using modern surface science techniques (95). In such studies, adsorption of thiophene, hydrogen sulfide, and other molecules indicated that only physical adsorption occurs on the basal plane of MoS_2. Further studies showed that the basal plane of MoS_2 was inert to O_2 exposure at 247°C (96). This latter study was in accord with the results reported earlier by Bahl et al. (97) who studied the oxidation of single crystals of MoS_2 at 500-600°C and found that the edge planes oxidized preferentially. More recently, oxygen enrichment at edge planes of MoS_2 single crystals has been shown to occur by scanning Auger studies (98). This preferential interaction between O_2 and edge planes was used by Chianelli et al. (99) to determine the edge plane area of MoS_2. In their study, it was reported that the total surface areas of the MoS_2 catalysts gave no correlation with hydrodesulfurization (HDS) activity. However, a linear relationship was found when activities were plotted against O_2 chemisorption capacities. Chianelli and co-workers concluded that their results

supported the hypothesis of Voorhoeve and Stuiver (100) who proposed that the edge planes in MoS_2 and WS_2 were the sites of their catalytic activity. The reader is referred to extensive reviews (101-105) regarding the nature of the active sites for hydrodesulfurization (HDS) reactions. Recently, Concha and Bartholomew (106) found a good correlation of O_2 adsorption uptake with CO hydrogenation activity for MoS_2 catalysts and concluded that O_2 adsorption, which, as discussed above, occurs on edge planes, is a measure of active sites for CO hydrogenation.

From the above discussion, it is clear that the active sites for hydrogenation reactions are located on the edge planes of MoS_2. However, the local environment of the active sites is unclear. It is common to find in the literature that these active sites are related to sulfur vacancies or degrees of coordinative unsaturation of molybdenum, but their exact structure is unknown. Voorhoeve and Stuiver (100) found that the activity for the hydrogenation of benzene correlated with the ESR signal W^{3+} (W^{3+} is isoelectronic with Mo^{3+}) for unsupported NiS/WS_2 catalysts. They reported in the same study that cyclohexene hydrogenation activity did not correlate with the ESR W^{3+} signal, demonstrating that these reactions take place on different sites. They also proposed that olefin hydrogenation takes place on both four- and five-coordinate W^{3+} and W^{4+} edge plane sites that contained sulfur vacancies. Tanaka and Okuhara (93) studied hydrogenation and isomerization reactions of olefins using a deuterium tracer over MoS_2 single crystals and concluded that the active sites

for these two reactions were entirely different. It was proposed that the hydrogenation reaction would require three degrees of coordinative unsaturation (^{3}M-sites) and the isomerization reaction would take place on sites having two degrees of coordinative unsaturation (^{2}M-sites). Scheme 1-7, according to Tanaka and Okuhara, describes the reactions of alkyl species coordinated to ^{2}M-sites and to ^{3}M-sites. Roxlo et al. (107) combined optical absorption studies with catalytic properties of MoS_2 edge planes to gain insight into the electronic nature of the active sites. They found that the optical absorption observed below 1.2 eV in the MoS_2 microcrystals is due to the exposed edge planes, and mentioned that "dangling bonds," vacancies, or other similar surface defects would be expected to contribute to the optical absorption in this region. The authors reported a good correlation between the optical absorbance, which they attributed to edge site defects, and catalytic activity. Further studies by Roxlo et al. (108) showed that edge defects of MoS_2 crystals contained molybdenum that is reduced (Mo^{3+}) relative to the bulk (Mo^{4+}). They mentioned that the presence of Mo^{3+} would imply a deficiency of sulfur at the surface relative to the bulk.

It is interesting to point out that despite the fact that MoS_2 has been studied extensively because of its technological importance as a hydrodesulfurization and hydrogenation catalyst, there is no experimental evidence that would indicate how H_2 chemisorbs on MoS_2. Very recently, Anderson et al. (109) performed a theoretical study using the atom superposition and electron delocalization molecular

orbital (ASED-MO) theory of the chemisorption of H_2 on MoS_2 and concluded that their calculations support the formation of heterolytic H_2 adsorption products at 5-coordinate Mo^{4+} edge sites. They added that if lower coordinated edge sites are present, a second heterolytic adsorption could lead to two H^- bonded to a single Mo cation and two neighboring SH^- ligands. These theoretical results have yet to be supported by spectroscopic evidence.

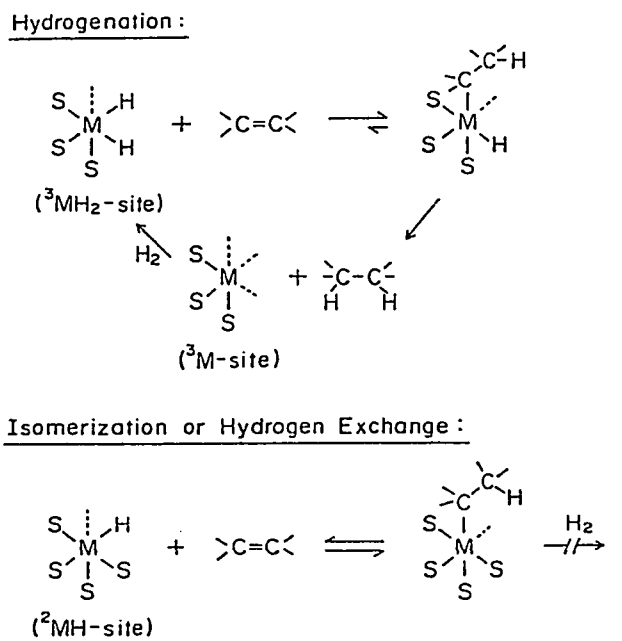

Scheme 1-7

Chapter 2

EXPERIMENTAL

2.1 CATALYST PREPARATION

2.1.1 Preparation of MoS_2

MoS_2 was prepared from thermal decomposition of molybdenum trisulfide (MoS_3), which was made by acidification of an aqueous solution of ammonium thiomolybdate ($(NH_4)_2MoS_4$) that was obtained by reacting ammonium heptamolybdate ($(NH_4)_6Mo_7O_{24}\cdot 4H_2O$) with ammonium sulfide ($(NH_4)_2S$). The procedure was as follows: 100 ml of concentrated acetic acid diluted with 300 ml distilled H_2O were added to 106 ml of 22% aqueous $(NH_4)_2S$ solution containing 15 g $(NH_4)_6Mo_7O_{24}\cdot 4H_2O$ at 60°C. The dark-brown residue (MoS_3) obtained by precipitation was washed with distilled H_2O and then placed in an evaporating dish and dried at 120°C overnight. MoS_3 was transferred into a quartz tube reactor and the decomposition $MoS_3 \rightarrow MoS_2 + S$ was carried out at 450°C for 2 hours in flowing nitrogen (60 ml/min). A heating rate of about 10°C/min was used. The resultant MoS_2 had a BET surface area of 63 m^2/g. The surface area of MoS_2 obtained by this procedure depends on the final temperature and heating rate (110,111). This dependence has been explained in terms of the competition between the rate of nucleation of MoS_2 and that of sintering of MoS_2 (111).

2.1.2 Preparation of Alkali-Doped MoS_2 Catalysts

Doping of MoS_2 with an aqueous solution of the alkali salt (CsOOCH or KOOCH) was performed under vacuum using the apparatus shown in Figure 2-1. The following is the procedure: MoS_2 was first evacuated at about 10^{-4} torr and heated to 100 - 110°C for 2 hours, and then allowed to cool down to room temperature before an aqueous solution of the alkali formate was introduced with a syringe onto the MoS_2 through a septum located in the attached side arm. The catalyst was allowed to dry under vacuum at 60°C before more solution was added. These two last steps, drying under vacuum and addition of solution, were repeated until the desired alkali concentration of the catalyst was reached.

2.1.3 Preparation of Alkali-Doped Co/MoS_2 Catalysts

The cobalt-molybdenum sulfide catalysts were prepared by adding an aqueous solution containing 10.583 g of $Co(CH_3COO)_2 \cdot 4H_2O$ to 400 ml of 25% acetic acid, the resultant solution was added to 120 ml of 22% aqueous $(NH_4)_2S$ solution containing 15 g of $(NH_4)_6Mo_7O_{24} \cdot 4H_2O$ at 60°C. The solution was stirred vigorously for 1 hour and cooled down to ambient temperature. The resultant precipitate was suction filtered through a Whatman #42 filter paper supported on a fitted glass filter and washed with distilled water. The solid was then placed in an evaporating dish and air dried overnight at 120°C. The dried black precipitate was loaded into a quartz tube reactor to perform the calcination, which was carried out at 450°C for 1 hour in flowing

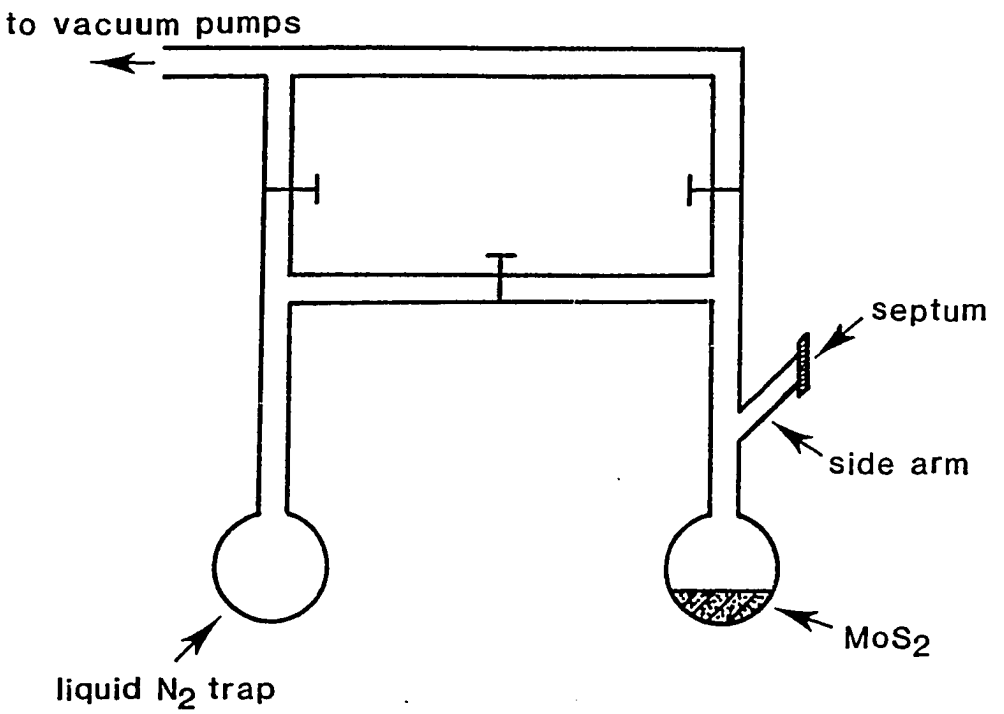

Figure 2-1 Diagram of the vacuum apparatus used in the preparation of alkali-doped MoS_2 catalysts.

nitrogen (60 ml/min). The atomic ratio Mo:Co was equal to 2 in the resultant catalyst.

The K_2CO_3-doped Co/Mo sulfide catalyst was prepared by simply grinding in an N_2-filled glove bag a mixture containing 10 wt% K_2CO_3 and 90 wt% of the Co/MoS_2 sample in a mortar.

2.2 TESTING APPARATUS

The catalyst activities and selectivities were evaluated in pressure units (Figures 2-2 and 2-3) equipped with flow reactors and with pressure, flow rate, and temperature controllers. The reactors used were single pass fixed bed tubular flow reactors. The units were designed for a maximum operating pressure of 100 atm. The desired pressure in the system was regulated by a Tescom back-pressure regulator and obtained from pressurized cylinders of the reactant gases, hydrogen and carbon monoxide (MG Scientific Gases, hydrogen-99.999%, carbon monoxide - 99.5%). Molecular sieves were used to trap any water in the feed gases to keep the moisture levels to a minimum. An activated charcoal trap was used to purify the feed gases from iron carbonyls. Both units were provided with mass flow controllers capable of operating at high pressures (Union Carbide Corp., Model FM-4550-6C-6C-6C) and regulating separately the H_2 and CO input streams. Therefore, a wide range of compositions and gas hour space velocities (GHSV), defined as liters of the feed gas per kg of catalyst per hour at 25°C, of the reaction stream could be utilized.

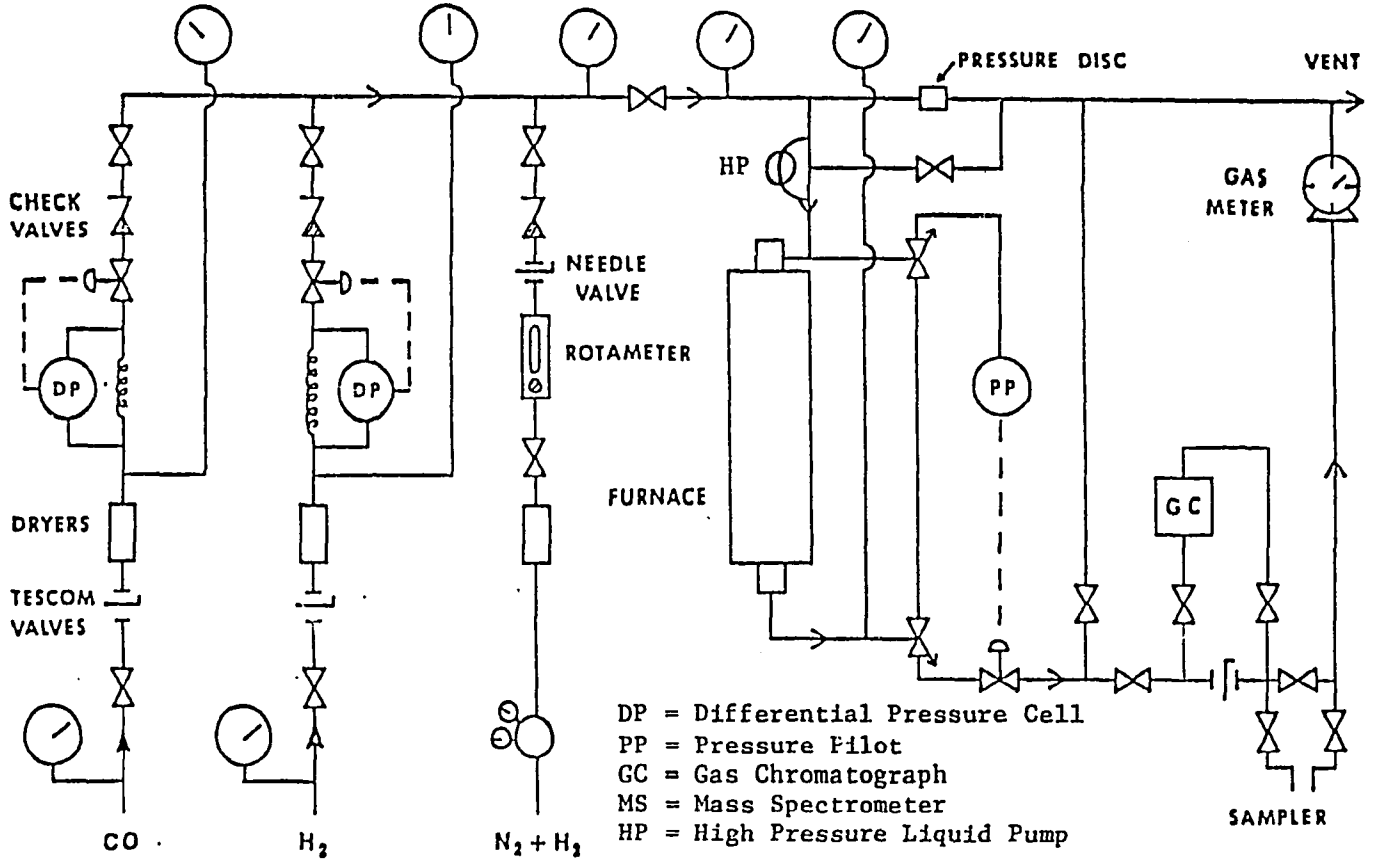

Figure 2-2 Catalyst testing unit I.

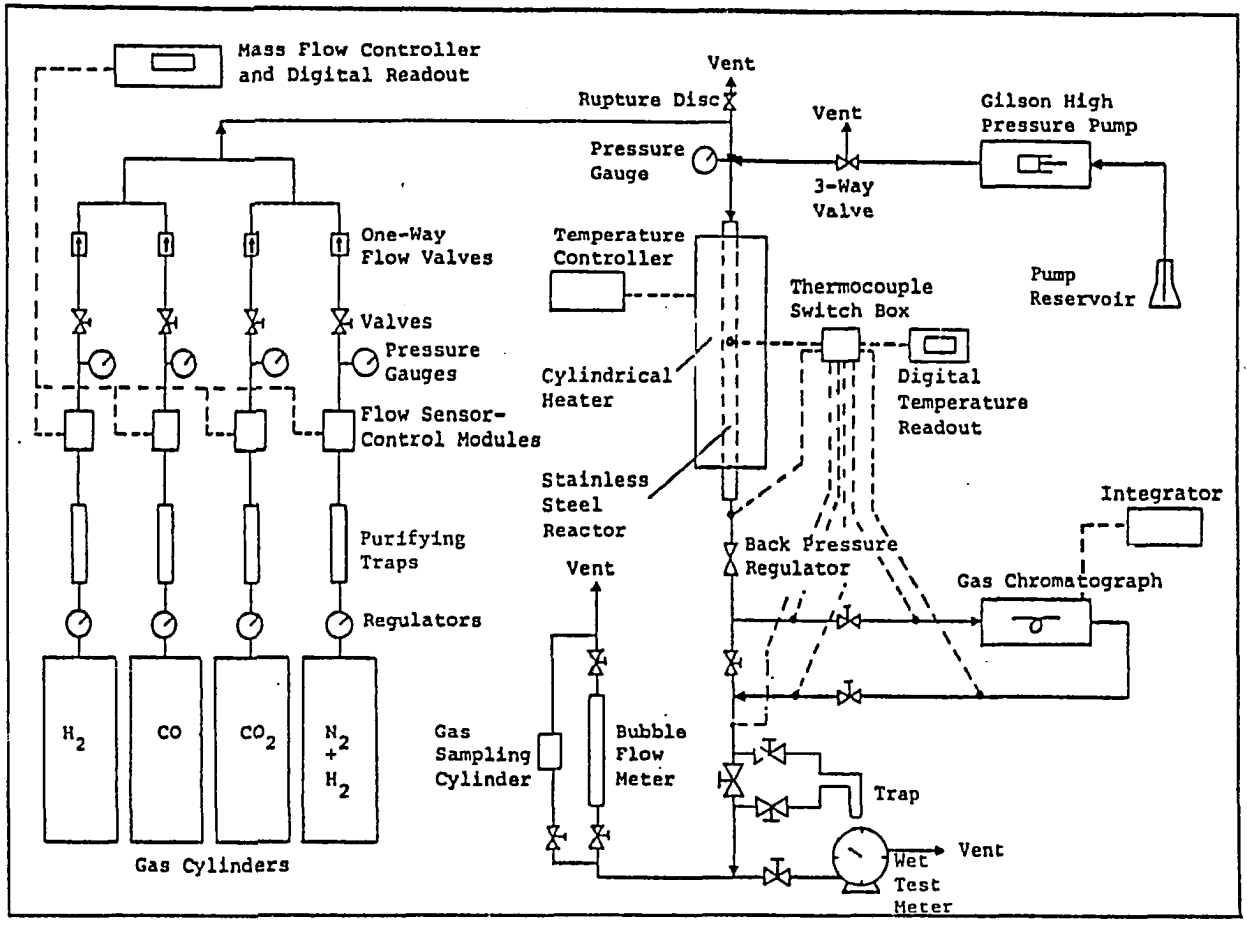

Figure 2-3 Catalyst testing unit II.

Although the basic principles involved in the operation of units I and II were the same, there were some significant differences between these two units. Unit I consisted of a stainless steel reactor 64 cm long with a 1.8 cm inside diameter and 0.3 cm wall thickness. The reactor was heated using a split tube furnace (S. B. Lindberg Co.) and was regulated by a proportional temperature controller (Theall Engineering Co., Model TC-1000-T1-P2). The catalyst bed temperature was measured using a 0.1 cm O.D. stainless steel clad thermocouple incorporated into a thermowell along the center line of the reactor. The catalytic reactor in Unit II consisted of 1.27 cm I.D., schedule 40, 316 stainless steel tubing, and was fitted with a 0.32 c.m. O.D. thermowell of the same material. The temperatures of the top, middle, and bottom section in the catalyst zone were measured by a vertically sliding thermocouple. The reactor furnace had three separate heat zones individually controlled by Electron Control System (ECS) power supplies of a silicon control rectifier (SCR) with proportional control and reset circuits, which allowed control of the catalyst bed temperature usually to within ± 1°C. Further, a provision was made for the fast cooling of the reactor by a manually controlled valve that allowed a stream of compressed air to flow directly over the reactor tube.

A back pressure regulator (Tescom Corp., Model 26-1725-24-070) was used to reduced the downstream pressure to atmospheric while maintaining the upstream pressure at the desired level. Heating and insulating tapes were wrapped around the stainless steel exit lines of

both units to maintain temperatures around 200 - 250°C on the high pressure side and 130 - 150°C on the low pressure side to avoid the condensation of the exit components in the lines.

The exit gases from the reactors were sampled every 15 - 60 min using an on-line Hewlett Packard Model 5730A Gas Chromatograph (one for each reactor), with computer control of the heated in line sampling valve and the employed temperature programming. Prior to entering the exhaust system, the exit gas flow rates were measured through a wet test meter (GCA/Precision Scientific Co., stainless-steel Model).

For safety purposes, a CO alarm (Model 701 from Mine safety Appliances Co., Pittsburgh, PA.) was in continual use when the testing unit was in operation. A hand-held gas leak detector (Model BT-44 from Quantum Inst. Inc., Garden City, L.I., N.Y.) was used to spot check for hydrogen leaks.

2.3 CATALYST TESTING

In each test, a 2.0 g (~2 c.c.) portion of powdered catalyst diluted with 6 c.c. of Pyrex beads were centered in either one of the fixed bed single pass tubular reactors shown in Figures 2-2 and 2-3. Before being subjected to the reaction conditions, the catalysts were pretreated at 400°C and 1 atm with a H_2/N_2 = 2/98 vol% gas mixture flowing at a rate of 60 ml/min (STP). The catalyst was then cooled to ambient temperature prior to pressurizing the reactor to 81.6 atm with

the $CO/H_2 \approx 1$ mixture.

The mechanism of the formation of C_2 - C_4 alcohols over the MoS_2-based catalysts was studied by the use of ^{13}C-enriched methanol that was injected continuously into the synthesis gas flowing over the catalyst operating under steady state conditions. The methanol was enriched by a factor of 21.69% over the natural ^{13}C abundance of 1.11 at%. The enriched methanol was introduced into the synthesis gas feed at the inlet of the reactor using a high-pressure Gilson Model 302 pump. The liquid ^{13}C-enriched methanol vaporized in the top of the reactor (preheater section) in which the temperature was always greater than 200°C. The injection rate, 6.0×10^{-4} ℓ/h, was such that the ^{13}C introduced as methanol did not exceed 5% of the total carbon introduced as carbon monoxide, and the concentration of injected methanol was substantially less than the equilibrium methanol concentration for the operating conditions used, T = 245 - 325°C; P = 81.6 atm, GHSV = 3540 - 7470 ℓ(STP)/kg cat/h; and $H_2/CO = 0.96$. Under these conditions, methanol decomposition, and thus scrambling of the ^{13}C label between methanol and the reactant carbon monoxide, was suppressed and the system was not expected to be perturbed by the injected methanol. Control experiments using methanol containing natural abundance (1.11 at%) ^{13}C were carried out under identical conditions. The isotopic product composition was determined by ^{13}C NMR and mass spectroscopy. The liquid reaction products were collected using a liquid nitrogen trap placed downstream from the back-pressure regulator and transferred to NMR tubes that were

subsequently sealed. The gaseous reaction products were collected using a gas syringe downstream from the liquid nitrogen trap.

2.4 THE ANALYTICAL PROCEDURES

Identification of the reaction products and quantification of reactants and products leaving the reactor were achieved by gas chromatography. An on-line Hewlett-Packard 5730A gas chromatograph (GC) equipped with an automatic gas sampling valve, a thermal conductivity detector, and a 6' x 1/8" column packed with 80/100 mesh Poropak Q was used to identify the components by comparing the retention times with those of known standards and also from their mass spectroscopic fragmentation patterns, as determined using a Finnegan-Nova 4000 GC/MS spectrometer. Coupled to the chromatograph was a Hewlett-Packard Model 3388A integrator-controller unit that provided the quantitative information by determining the areas under the peaks in the chromatogram. A set of typical GC operating conditions used during the catalytic testing is given in Table 2-1.

Since hydrogen has a higher thermal conductivity than the helium carrier gas, a negative signal was obtained. This signal was not integrated and, therefore, hydrogen was excluded from analysis. The relative molar concentration of each compound in the exit stream was obtained by dividing the integrated areas by the respective thermal response factors (112) followed by normalization. These molar concentrations were then used in the determination of conversions,

TABLE 2-1

Standard Gas Chromatograph Operating Conditions of GC-HP 5730A

Carrier gas	Helium
Carrier gas flow	20-30 cc/min
Oven	90-190°C
Injection port	150°C
Detector	200°C
Sensitivity	4
Attenuation	1
Temperature program[a]	90°C-2 min, 16°C/min, 190°C-8 min

a This temperature program was used to separate all the exit products except carbon monoxide and methane. Resolution of carbon monoxide and methane was achieved by using a column temperature of 25°C for 2 minutes followed by the regular temperature program to separate the other components.

product yields, selectivities, and mass balances. An example is given in Appendix 2.A.

The analysis of the products obtained during the ^{13}C-enriched methanol pumping experiments was also performed by the on-line Hewlett-Packard 5730A gas chromatograph. To determine the isotopic product distribution, the liquid reaction products were collected using liquid nitrogen traps placed downstream from the back pressure regulator and transferred to NMR tubes that were subsequently sealed. The gaseous reaction products were collected using a gas syringe downstream from the liquid nitrogen traps. The ^{13}C spectra of the liquid samples were obtained on a JEOL FX90Q Fourier Transform NMR spectrometer using broadband proton decoupling. The gas sample was analyzed by a Finnegan-4000 GC/MS spectrometer.

2.5 SAMPLE HANDLING

The handling of fresh catalysts was carried out under normal conditions, i.e. exposure to air was not excluded during catalyst preparation and loading of the reactor. Tested catalysts, however, were handled in such a way to air was eliminated. After catalytic testings were made, the reactor was cooled down to ambient temperature in the CO/H_2 mixture and depressurized. The catalyst was then removed in a nitrogen-filled glove bag and stored in sealed Pyrex vacuum tubes for later characterization studies.

APPENDIX 2.A

Example of the Determination of Product Yields, Selectivities, Conversion, and Balance Material from Gas Chromatographic Data

The results obtained on the 20.0 wt% CsOOCH catalyst are used to illustrate the procedure involved in the determination of product yields, selectivities, conversion, and mass balance. The operating conditions under which the data were obtained were: T = 275°C, P = 81.6 atm, H_2/CO = 0.95, GHSV = 7736.4 ℓ/kg cat/h, 2.0 g of catalyst.

1) **Relative Molar Concentration.** The relative molar concentration of each component (i) was obtained by dividing the integrated areas (A) by the respective thermal response factor (TRF) followed by the normalization of these values to give the percent molar concentration (C_i) (see Table 2A-1).

$$C_i = \frac{A_i/TRF}{\sum_i (A_i/TRF)} \qquad [2.A\text{-}1]$$

2) **Material Balances.** The material balances were based on the number of carbon and oxygen atoms entering and leaving the reactor at steady state. The number of mols of CO entering the system (CO in) was determined from the product of the inlet flow rate and the concentration of that component. For the present example in which an inlet flow rate = 15.473 ℓ/h (measured at 25°C and 1 atm) and a gas composition of H_2/CO = 48.72/51.28 vol% were used, the number of mols

TABLE 2.A-1

Example of the Determination of the Molar Concentrations from Gas Chromatographic Data

Compound	Integrated Area (%)	Thermal Response Factor (TRF)[a]	Area/TRF	Relative Molar Conc. (%)
CO	91.008	42	2.1686	92.4540
CO_2	2.649	48	0.0552	2.3533
H_2O	0.13	33	0.0039	0.1663
CH_4	1.024	35.7	0.0287	1.2236
C_2H_4	0.016	48	0.0003	0.0128
C_2H_6	0.142	51.2	0.0028	0.1194
C_3H_8	0.040	64.5	0.0006	0.0256
CH_3OH	3.532	55	0.0642	2.7370
C_2H_5OH	1.203	72	0.0167	0.7120
C_3H_7OH	0.301	83	0.0036	0.1535
CH_3OOCH	0.027	72	0.0004	0.0171
CH_3OOCCH_3	0.047	83	0.0006	0.0256

[a] TRF were obtained from Dietz, W. A., J. Gas Chromatogr., 5 (1967) 68

is calculated as follows:

CO in = (15.473 ℓ/h)(0.5128)/(24.45 ℓ/mol) = 0.3245 mol/h

CO in = C in = O in = 0.3245 mol/h.

The exit concentration of the total gas mixture was unknown, due to hydrogen not being included in the GC analysis. Hydrogen has a higher thermal conductivity than the carrier helium gas and therefore, its integrated peak resulted in a negative value. What is known is that it is the relative molar concentration of the products. Thus, if one assumes that all the inlet oxygen is distributed among the products, one can calculate that total number of mols leaving the reactor. The procedure is as follows:

(i) Calculate the percent distribution of oxygen atoms among the products containing oxygen using the relative molar concentration values, e.g.

$$\% \text{ O from CO} = \frac{C_{CO}}{\sum_i (nC_i)} \times 100 \qquad (2.A\text{-}2)$$

where n is the number of oxygen atoms in each component.

% O from CO = 91.5252.

(ii) Since it is assumed that all the inlet oxygen is distributed among the products, one can calculate the absolute mols of oxygen containing compounds, e.g.

Oxygen atoms in CO out = (O in) x (fraction of oxygen as CO)

= (0.3245 mol/h) x (0.915252)

= 0.297 mol/h.

(iii) The number of mols of the compounds containing only carbon and hydrogen can be calculated by comparing the relative molar concentration with the calculated number of an oxygen containing compound, e.g.

$$CH_3OH \text{ out} = (C_{CH_3OH}/C_{CO}) = (\text{Oxygen atoms in CO out})$$

$$= (2.7370/92.4540) \times (0.297 \text{ mol/h})$$

$$= 0.0088 \text{ mol/h}.$$

(iv) Calculate the number of mols of carbon out and compare with that entering the reactor.

(v) Calculate error on carbon balance

$$\% \text{ Error on C balance} = \frac{C_{in} - C_{out}}{C_{in}} \times 100$$

3) **Calculation of Conversions.** CO conversions were expressed as mols of CO converted to products exclusive of CO_2

$$\text{(i)} \quad CO \text{ (\% mol)} = \frac{CO_{in} - CO_{out} - CO_{2out}}{CO_{in}} \times 100$$

$$\text{(ii)} \quad CO \text{ (mol/kg cat/h)} = \frac{CO_{in} - CO_{out} - CO_{2out}}{\text{kg cat}} \times 100$$

4) **Calculation of Product Yield (Y).** The yields were based on the weight of the product formed per hour per weight of catalyst:

$$Y_i = \frac{N_i M_i}{W} \qquad [2.A\text{-}3]$$

where: N_i is the molar flow rate of the i^{th} component expressed in mol/h, M_i is the molecular weight of the i^{th} component (g/mol), W is the weight of the catalyst (kg) present in the reactor, and Y_i is the product yield of the i^{th} component expressed in g/kg cat/h.

5) Calculation of Selectivities (S). The selectivities were based on carbon mol selectivity on a CO_2 free basis.

$$S_i = \frac{nN_i}{\sum_i (nN_i)} \qquad [2.A\text{-}4]$$

where: S_i is the selectivity of the i^{th} component, n is the number of carbon atoms in the i^{th} component, and N_i is the molar flow rate of the i^{th} component.

Table 2.A-2 shows the program output of the calculations discussed above.

TABLE 2.A-2

Example of the Calculations to Determine Product Yields, Selectivities, Conversions, and Material Balances from GC Data

NAME	#O	#C	#W	TRF	M.W.	%VOL
CO	1	1	0	42	28	91.00801
CO2	2	1	0	48	44	2.649
H2O	1	0	0	33	18	.013
CH4	0	1	0	35.7	16	1.024
C2H4	0	2	0	48	28	.0157
C2H6	0	2	0	51.2	30	.142
C3H8	0	3	0	64.5	44	.04
MEOH	1	1	0	55	32	3.532
ETOH	1	2	0	72	46	1.203
1PROH	1	3	0	83	60	.301
CH3OOCH	2	2	0	72	60	.027
CH3OOCCH3	2	3	0	83	74	.047

NAME	%MOLE	MOLES*	YIELD**	SELECT***
CO	0.9259E+02	0.2974E+00	4164.26	0.0000
CO2	0.2358E+01	0.7576E-02	166.66	0.0000
H2O	0.1683E-01	0.5408E-04	0.49	0.0000
CH4	0.1226E+01	0.3937E-02	31.50	19.4190
C2H4	0.1398E-01	0.4490E-04	0.63	0.4429
C2H6	0.1185E+00	0.3807E-03	5.71	3.7553
C3H8	0.2650E-01	0.8513E-04	1.87	1.2596
MEOH	0.2744E+01	0.8815E-02	141.04	43.4764
ETOH	0.7139E+00	0.2294E-02	52.75	22.6234
1PROH	0.1550E+00	0.4978E-03	14.93	7.3656
CH3OOCH	0.1602E-01	0.5148E-04	1.54	0.5078
CH3OOCCH3	0.2420E-01	0.7773E-04	2.88	1.1501

* MOLES - MOLES/HOUR
** YIELD - G/KG CAT/HOUR
*** SELECTIVITY - %MOLE OF C ATOM

REACTION CONDITIONS:
TEMPERATURE (C) - 275
PRESSURE (ATM) - 81.6
FLOW RATE (SCCM) - 257.88
H2/CO (%VOL) - 48.72 / 51.28

CATALYST :
ID - JS3
WT.- .002 KG

MATERIAL BALANCES (MOLE/HOUR) :
O IN-O OUT - .3245174
CO IN - .3245174
C FROM P IN - 0
C IN - .3245174
C OUT - .3252987
ERROR IN C BAL - -.2407476 %

CONVERSIONS :
CO (%MOLE) - 6.007324
CO (MOLES/KG CAT/HOUR) - 9.747406

Chapter 3

ALCOHOL SYNTHESIS OVER ALKALI-DOPED MoS_2-BASED CATALYSTS

3.1 Introduction

In 1984, the Dow Chemical Company and Union Carbide Corporation separately disclosed a novel catalytic system for the production of linear alcohols from synthesis gas ($CO + H_2$) (15-17). This novel catalytic system consists of supported or unsupported alkali-doped MoS_2 or alkali-doped Co/MoS_2, and much interest has been subsequently generated in both industrial and academic fields. Various patent applications related to this process have been filed (15-17) and publications are now beginning to appear in the scientific literature (18-20), but a lack of systematic study on this catalytic system can be sensed from reading this literature. With this in mind, a systematic study of the effect of alkali doping of MoS_2 as a function of reaction temperature and flow rate on the activity and selectivity, not only for alcohols but also for the undesirable side products, mainly hydrocarbons, was performed. In the first section of this chapter the activity and selectivity of the undoped, K-doped, and Cs-doped MoS_2 catalysts will be compared. In the following sections cesium concentration dependence studies at different reaction temperatures, as well as the effect of total flow rate on the product distribution will be discussed. In the last section of the chapter the results obtained with the cobalt-containing alkali/MoS_2 catalyst

will be presented. The results obtained from the experiments described above allow optimization of the catalyst for high yields and selectivities of alcohols and set the stage for performing the mechanistic investigation that will be presented in the next chapter.

3.2 RESULTS

3.2.1. Effect of Alkali Doping of MoS_2 on the Activity and Selectivity for Alcohol Synthesis

The preparation and testing of undoped MoS_2, K-doped MoS_2, and Cs-doped MoS_2 were performed to study the effect of alkali doping of MoS_2 on the activity and selectivity for alcohol synthesis. Table 3-1 shows the composition of the catalysts. The testing of the catalysts was carried out under identical operating conditions; 295°C, 81.6 atm, H_2/CO = 0.96 and a gas hourly space velocity (GHSV) of 7787 ℓ(STP)/kg cat/h. The results of the product selectivity obtained under these conditions are tabulated on Table 3-2, and shown schematically in Figure 3-1. It is clear that practically only hydrocarbons are produced over undoped MoS_2, and that the selectivity is dramatically altered toward alcohols upon promotion of the MoS_2 with either potassium or cesium. The product yields obtained for each of the catalysts are presented in Table 3-3. The alcohol yields are illustrated in Figure 3-2. Table 3-4 shows the product yields obtained over the Cs-doped and K-doped MoS_2 catalysts at 256°C. From inspection of Tables 3-3 and 3-4, it is apparent that at identical

TABLE 3-1

Composition of the Alkali-Doped MoS_2 Catalysts[a]

MoS_2	$CsOOCH/MoS_2$		$KOOCH/MoS_2$	
--	CsOOCH wt%	CsOOCH mol%	KOOCH wt%	KOOCH mol%
	20.00	18.36	10.36	18.03

[a] 0.22 mol alkali/mol MoS_2

TABLE 3-2

Product Selectivities Obtained over Undoped MoS_2, 0.22 mol K/mol MoS_2, and 0.22 mol Cs/mol MoS_2 Catalysts. Experimental Conditions are given in Table 3-3.

	Selectivity[a]		
Product	MoS_2	K/MoS_2	Cs/MoS_2
Hydrocarbons			
C_1	43.64	17.80	17.88
C_2	25.24	3.31	3.73
C_3	16.98	-	1.17
C_4	8.92	-	-
C_5	3.86	-	-
Alcohols			
C_1	0.67	45.15	38.34
C_2	-	26.14	26.85
C_3	-	5.32	8.98
C_4	-	tr	1.43
Esters			
Methyl Formate	-	1.25	0.54
Methyl Acetate	-	1.03	1.07

[a]Selectivity is based on carbon mol selectivity on a CO_2 free basis.

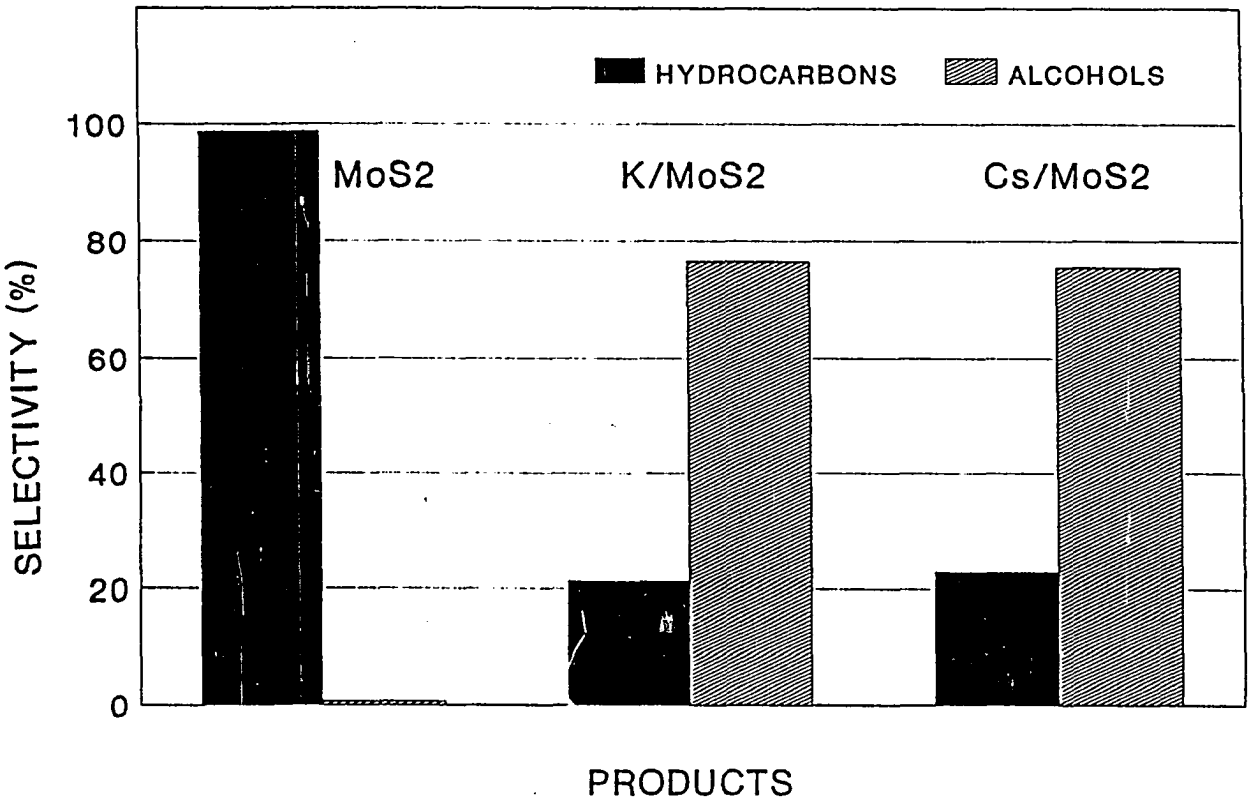

Figure 3-1 Product selectivity obtained over undoped MoS_2, 0.22 mol K/mol MoS_2, and 0.22 mol Cs/mol MoS_2 catalysts. Experimental conditions are given in Table 3-3.

TABLE 3-3

Product Yields Obtained over Undoped MoS_2[a], 0.22 mol K/MoS_2[b], and 0.22 mol Cs/mol MoS_2[c] at 295 °C, 81.6 atm and with a H_2/CO = 0.96.

Product	Yield (g/kg cat/h)		
	MoS_2	K/MoS_2	Cs/MoS_2
CO	4050.16	4086.92	3966.86
CO_2	235.81	199.89	259.59
H_2O	135.69	4.65	2.82
CH_4	89.11	27.00	44.65
C_2H_6	48.33	4.64[d]	8.63[d]
C_3H_8	31.79	tr	2.68[e]
C_4H_{10}	16.51	-	-
C_5H_{12}	7.11	-	-
CH_3OH	2.75	136.95	191.44
C_2H_5OH	-	56.99	96.34
C_3H_7OH	-	10.08	28.00
C_4H_9OH	-	tr	4.13
CH_3OOCH	-	3.55	2.52
CH_3OOCCH_3	-	2.41	4.11
CO converted to products exclusive of CO_2 (mol/kg cat/h)	13.06	10.67	14.85

[a]GHSV = 7775.4 l(STP)/kg cat/h [b]GHSV = 7803.5 l(STP)/kg cat/h
[c]GHSV = 7786.8 l(STP)/kg cat/h
[d]ethane + ethylene [e]propane + propylene

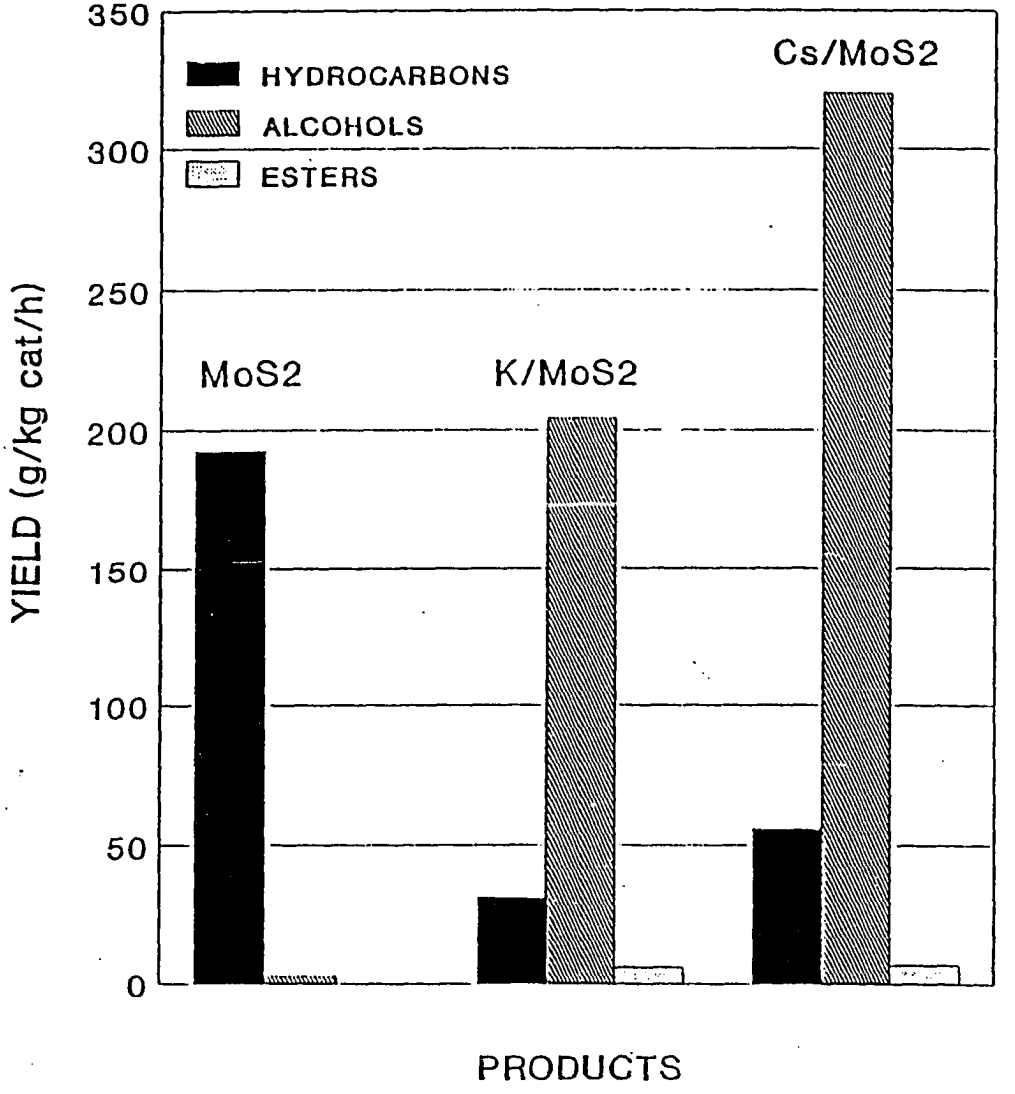

Figure 3-2 Alcohol yields obtained over undoped MoS_2, 0.22 mol K/mol MoS_2, and 0.22 mol Cs/mol MoS_2 catalysts. Experimental conditions are given in Table 3-3.

TABLE 3-4

Product Yields Obtained over 0.22 mol K/MoS_2[a], and 0.22 mol Cs/mol MoS_2[b] at 256°C, 81.6 atm and with $H_2/CO = 0.96$.

Product	Yield (g/kg cat/h)	
	K/MoS_2	Cs/MoS_2
CO	4349.51	4358.69
CO_2	72.60	63.87
H_2O	1.63	-
CH_4	11.27	12.40
C_2H_6	2.82[c]	1.97[c]
C_3H_8	tr	tr
CH_3OH	66.44	94.18
C_2H_5OH	16.07	32.37
C_3H_7OH	1.23	7.39
C_4H_9OH	-	-
CH_3OOCH	-	1.32
CH_3OOCCH_3	tr	1.47
CO converted to products exclusive of CO_2 (mol/kg cat/h)	4.18	5.30

[a]GHSV = 7803.5 ℓ(STP)/kg cat/h
[b]GHSV = 7786.8 ℓ(STP)/kg cat/h
[c]Ethane + Ethylene

molar concentrations (0.22 mol alkali/mol MoS_2) and regardless of the reaction temperature the Cs-doped catalyst is more active for the synthesis of alcohols than the K-doped catalyst. X-Ray photoelectron spectroscopy (XPS) analysis of the alkali-doped MoS_2 tested catalysts indicated that the surface concentrations of Cs and K were identical (see Table 3-5). Thus, the enhanced promotion by Cs, relative to K, appears to be a real effect and is consistent with the results obtained by researchers at Union Carbide (16), as indicated in Table 3-6.

The carbon number distribution of both hydrocarbons and alcohols followed the Anderson-Schulz-Flory distribution, as depicted in Figure 3-3 for the case of the Cs-doped MoS_2 catalyst. The chain growth probability (α) values obtained for each of the catalysts are tabulated in Table 3-7. It is interesting to note that α decreased upon addition of the alkali metal to the MoS_2 catalyst. This negative effect of the alkali metal on the α value is different from that reported in the Fischer-Tropsch literature that established that the addition of alkali to a Fischer-Tropsch catalyst promoted the selectivity to higher hydrocarbons, i.e. promoted an increase in the α value (113). This difference can be understood if one accepts that two different catalytic systems are being considered. Under our operating conditions, the addition of alkali to MoS_2 is opening a new reaction pathway by promoting the formation and/or concentration of intermediate species that give rise to the dramatic shift in selectivity from hydrocarbons to oxygenates, while under the operating

TABLE 3-5

X-Ray Photoelectron Spectroscopy Analysis of the 0.22 mol K/mol MoS_2 and 0.22 mol Cs/MoS_2 Catalysts.

Catalyst	Element	Photoelectron	Sensitivity Factor[a]	I_A/I_{Mo}[b]	X_A/X_{Mo}[c]
$KOOCH/MoS_2$	K	$2p_{3/2}$	0.55	0.1749	0.38
$CsOOCH/MoS_2$	Cs	$3d_{5/2}$	5.5	1.8455	0.40

[a] Sensitivity factor of $Mo(3d_{5/2})$=1.2. Sensitivity factors taken from Ref. (153)

[b] Integrated photoelectron intensity ratio of the alkali, A, and $Mo(3d_{5/2})$ photoelectrons.

[c] The relative atomic surface concentration of the alkali with respect to molybdenum, X_A/X_{Mo}, was calculated assuming homogeneity in the surface analysis volume. Models to account for heterogeneity are discussed in Appendix 5.C.

TABLE 3-6

Alcohol Yields and Selectivities Obtained over Alkali-doped MoS_2 Catalysts at 300°C, 27.2 atm, H_2/CO = 1.0, and GHSV = 12000 h^{-1}. Data taken from Reference (16).

Catalyst	Selectivity to Alcohols	Alcohol Yield (g/l cat/h)
0.85-0.9 mol Cs acetate/ mol MoS_2	80	256.0
0.85-0.9 mol K acetate/ mol MoS_2	81	144.0
0.616 mol Rb acetate/ mol MoS_2	66	100.8
0.616 mol Li nitrate/ mol MoS_2	24	12.8
0.616 mol Na nitrate/ mol MoS_2	53	19.2

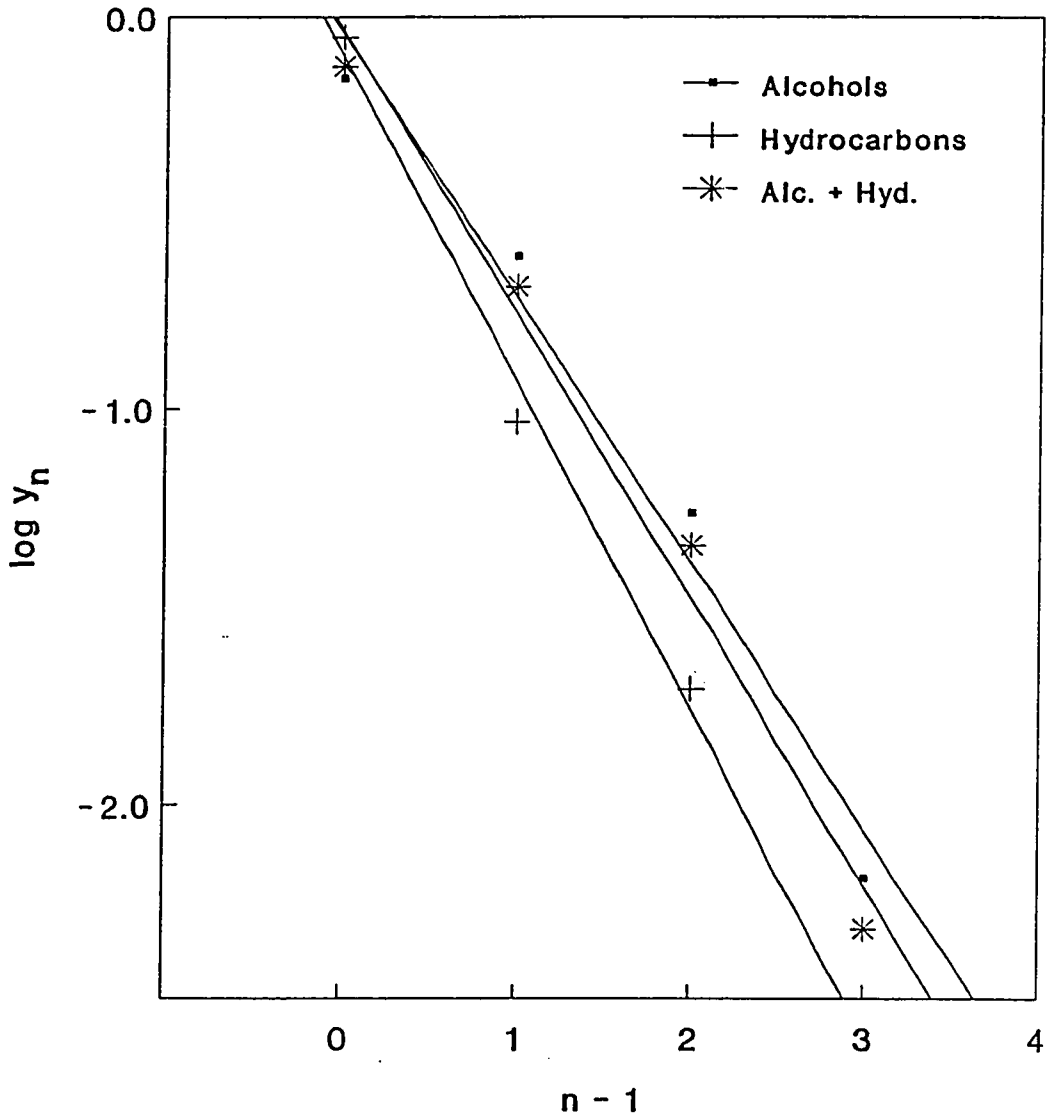

Figure 3-3 Carbon number distribution for the alcohols and hydrocarbons formed over the Cs-doped MoS_2 catalyst at 295°C, 81.6 atm, H_2/CO = 0.96, and GHSV = 7787 ℓ(STP)/kg cat/h. The α values given in Table 3-7 were obtained by linear regression analysis of the data points.

TABLE 3-7

Chain Growth Probability (α) Values Obtained over MoS_2-Based Catalysts at 295 °C and 81.6 atm, with H_2/CO = 0.96 and GHSV = 7787 l(STP)/kg cat/h.

Catalyst	Chain Growth Probability (α)		
	Alcohols	Hydrocarbons	Alcohols + Hydrocarbons
MoS_2	____	0.38	0.38
Cs/MoS_2 (.22 mol Cs/ mol MoS_2)	0.21	0.15	0.19
K/MoS_2 (.22 mol K/ mol MoS_2)	0.19	0.09	0.17

The chain growth probability (α) value was calculated from the Anderson-Schulz-Flory distribution

$$y_n = \alpha^{n-1}(1 - \alpha)$$

where y_n is the mol fraction of the product with n carbon atoms and α is the chain growth probability or chain growth parameter.

conditions of a typical Fischer-Tropsch synthesis the addition of alkali to the Fischer-Tropsch catalyst does not change the nature of the intermediates, but only their surface concentration, and therefore the selectivity to total hydrocarbons (olefins + alkanes) is conserved.

It should be mentioned that in the present study the distribution of the sum of hydrocarbons and alcohols fits the Schulz-Flory distribution better than those of individual products. This might be an indication that the paths of chain growth are the same for hydrocarbons and alcohols over the alkali-doped MoS_2 catalyst. This will be discussed in detail in the next chapter.

3.2.2 Effect of Cesium Concentration on the Activity and Selectivity of Alcohol Synthesis

Once the superior promotional effect of cesium was confirmed, the next step was to perform cesium concentration dependence studies. A series of CsOOCH/MoS_2 catalysts with different CsOOCH concentrations was prepared according to the procedure given in Chapter 2. Table 3-8 shows the composition of the catalysts. The catalysts were pretreated at 400°C for 1 h under 2%H_2/98%N_2 flow (60 ml/min), before they were tested under alcohol synthesis conditions in the temperature range of 245-295°C. The product yields and CO conversion obtained for each of the catalysts are presented in Table 3-9. The products reported in this table are those determined by GC using a packed column of Poropak

Table 3-8

Composition of the Cs-doped MoS_2 Catalysts

CsOOCH/MoS_2		
CsOOCH wt%	CsOOCH mol%	mol Cs/mol MoS_2
2.5	2.25	0.023
5.3	4.77	0.05
10.0	9.09	0.10
20.0	18.36	0.22
25.0	23.07	0.30
30.0	27.83	0.38

Table 3-9

Effect of Cs Loading on the Product Yields and CO Conversion at Different Temperatures, 81.6 atm, H_2/CO = 0.96, and GHSV ≈ 7750 ℓ(STP)/kg cat/h.

CsOOCH LOADING (wt%)	TEMP. (°C)	PRODUCT YIELD, g/kg cat/hr													CO CONVERSION (mol/kg cat/hr)
		CO_2	H_2O	CH_4	C_2H_4	C_2H_6	C_3H_8	C_4H_{10}	Methanol	Ethanol	Propanol	1-Butanol	Methyl Formate	Methyl Acetate	
2.5	245	39.59	1.34	12.67	-	2.11	0.79	-	57.82	11.82	2.65	-	-	1.30	3.13
	256	68.03	2.05	17.66	-	3.90	1.71	-	76.05	16.56	3.75	-	-	1.59	4.50
	265	124.36	6.29	28.12	-	8.39	4.63	1.90	79.53	22.97	6.13	tr	-	1.58	6.33
	275	186.51	8.65	39.14	-	15.44	7.67	3.19	84.83	25.93	7.49	tr	-	3.56[a]	8.15
	295	424.00	18.75	81.81	-	30.12	20.24	11.75	70.31	24.80	9.00	3.93	-	10.08[a]	13.89
5.3	245	43.50	tr	10.97	0.57	1.20	-	-	82.35	17.55	4.71	-	-	3.15	4.10
	256	68.75	tr	15.91	0.68	2.16	0.37	-	118.43	25.46	6.01	-	tr	4.67	6.04
	265	103.26	tr	22.03	0.68	3.68	0.88	-	135.28	33.46	8.68	tr	tr	5.65	7.59
	295	423.24	5.13	85.27	0.87	19.23	12.05	5.50	136.56	52.19	21.97	8.08	-	9.22[a]	16.03

[a] Methyl acetate + pentane

Table 3-9 (Continued)

CsOOCH LOADING (wtX)	TEMP. (°C)	PRODUCT YIELD, g/kg cat/hr													CO CONVERSION (mol/kg cat/hr)
		CO_2	H_2O	CH_4	C_2H_4	C_2H_6	C_3H_8	C_4H_{10}	Methanol	Ethanol	Propanol	1-Butanol	Methyl Formate	Methyl Acetate	
10.0	245	52.47	tr	12.75	0.28	0.92	-	-	85.32	24.12	5.06	-	0.86	1.30	4.53
	256	79.74	tr	16.73	0.76	2.01	0.28	-	106.22	32.96	7.54	tr	1.30	1.96	6.06
	265	136.83	tr	26.31	0.68	4.18	1.03	-	132.71	48.87	12.71	tr	1.03	2.63	8.63
	275	166.66	0.49	31.50	0.63	5.71	1.87	-	141.04	52.75	14.93	tr	1.54	2.88	9.74
	295	317.10	3.66	62.00	0.92	13.52	6.77	2.76	152.86	62.70	22.23	3.63	tr	1.33	14.09
20.0	245	37.77	tr	9.22	0.48	0.48	-	-	64.86	19.19	4.41	-	-	0.86	3.39
	256	63.87	tr	12.40	0.88	1.09	-	-	94.18	32.37	7.39	tr	1.32	1.47	5.30
	265	100.72	tr	18.49	0.68	1.73	-	-	124.82	48.45	12.60	tr	1.60	2.64	7.57
	275	146.96	tr	26.01	0.92	3.07	tr	-	152.91	65.71	16.79	tr	1.84	3.31	9.97
	295	259.59	2.82	44.63	1.49	7.14	2.68[b]	-	191.44	96.34	28.00	4.13	2.52	4.11	14.85

[b] propane (mainly) + propylene

Q. It should be noted that olefins and methyl formate were produced over the high Cs-content catalysts. Also note that the yield of water is quite low since most of the water formed as the by-product of hydrocarbon and higher alcohol synthesis was converted to carbon dioxide through the water-gas shift reaction catalyzed by the CsOOCH/MoS_2 catalyst. The sum of the yields of CO_2 and water detected is close, within the experimental error, to the amount of water expected from the production of hydrocarbons and alcohols. Schematic representations of the yields of methanol, ethanol, and hydrocarbons as a function of the CsOOCH loading are given in Figures 3-4 (a)-(e). These figures show a maximum in the methanol yield as the concentration of cesium on the catalyst increased, while the production of hydrocarbons was progressively suppressed. The formation of ethanol also goes through a maximum, although much broader than that shown by methanol formation. The suppression of the formation of hydrocarbons by the addition of CsOOCH to the MoS_2 catalysts is apparent in Figure 3-5, which shows the hydrocarbons yield as a function of the CsOOCH loading at different reaction temperature.

3.2.3 Effect of Reaction Temperature on the Selectivity to Alcohols at Different Cs Loadings

The selectivity to alcohols and hydrocarbons as a function of temperature at different loading of cesium is shown in Figure 3-6. It is evident that at a given temperature, the selectivity to alcohols

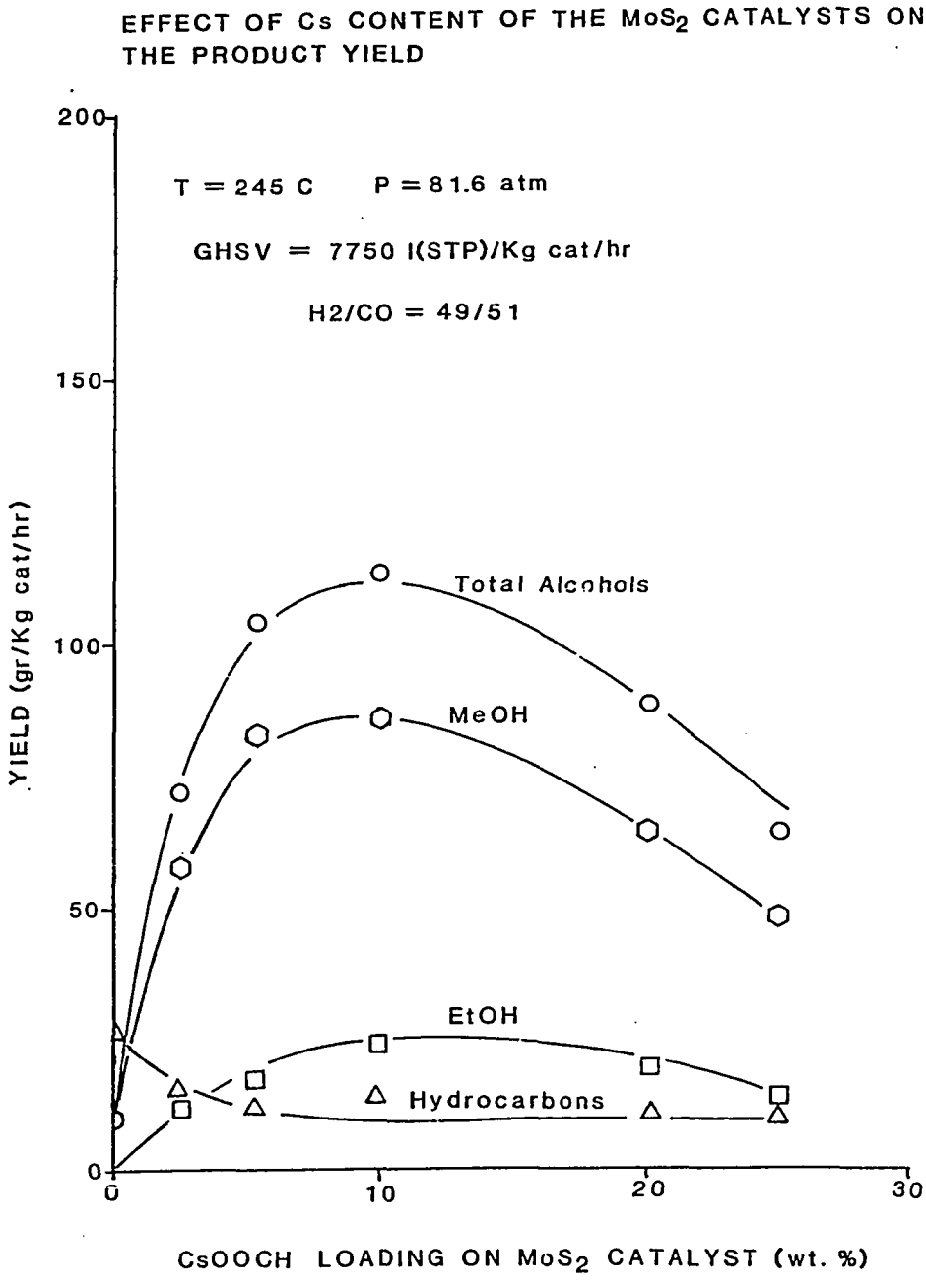

Figure 3-4 (a)-(e) Yields of methanol (?), ethanol (□), total alcohols (o) and hydrocarbons (Δ) as a function of cesium loading of the MoS_2 catalysts at 81.6 atm H_2/CO = 0.96, GHSV = 7750 ℓ(STP)/kg cat/h, and (a) 245°C, (b) 256°C, (c) 265°C, (d) 275°C, and (e) 295°C.

EFFECT OF Cs CONTENT OF THE MoS_2 CATALYSTS ON THE PRODUCT YIELD

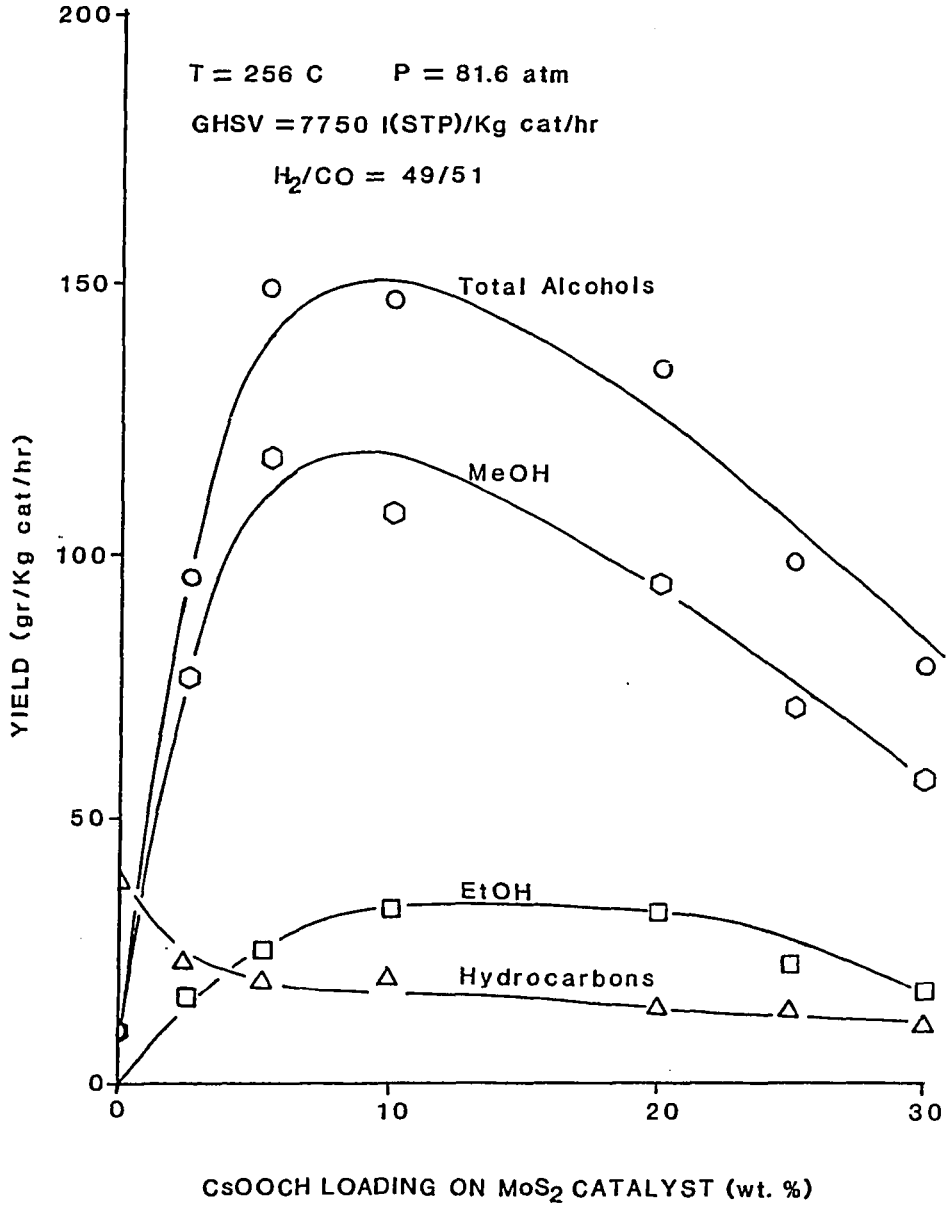

(b)

EFFECT OF Cs CONTENT OF THE MoS_2 CATALYSTS ON THE PRODUCT YIELD

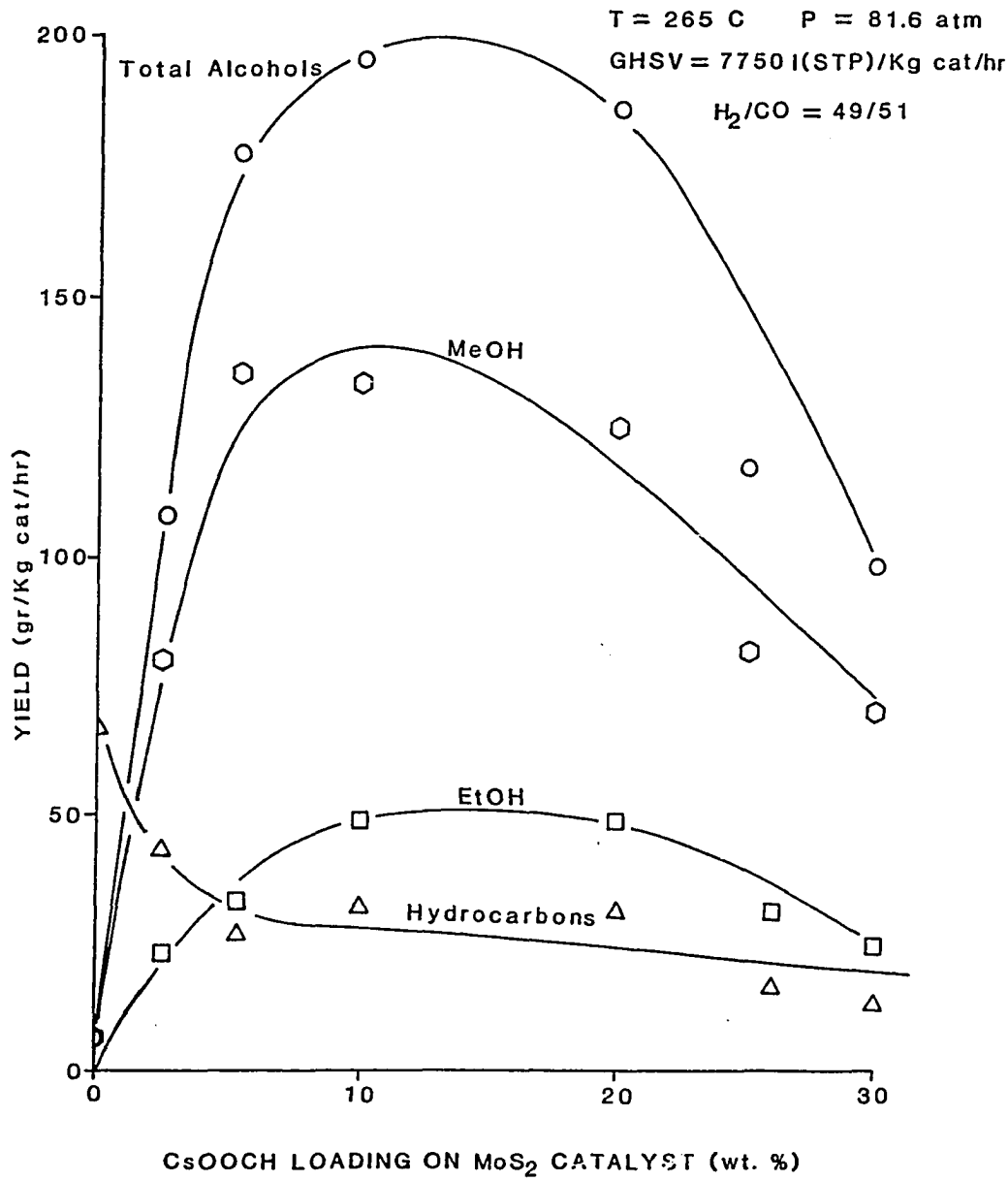

(c)

EFFECT OF Cs CONTENT OF THE MoS_2 CATALYSTS ON THE PRODUCT YIELD

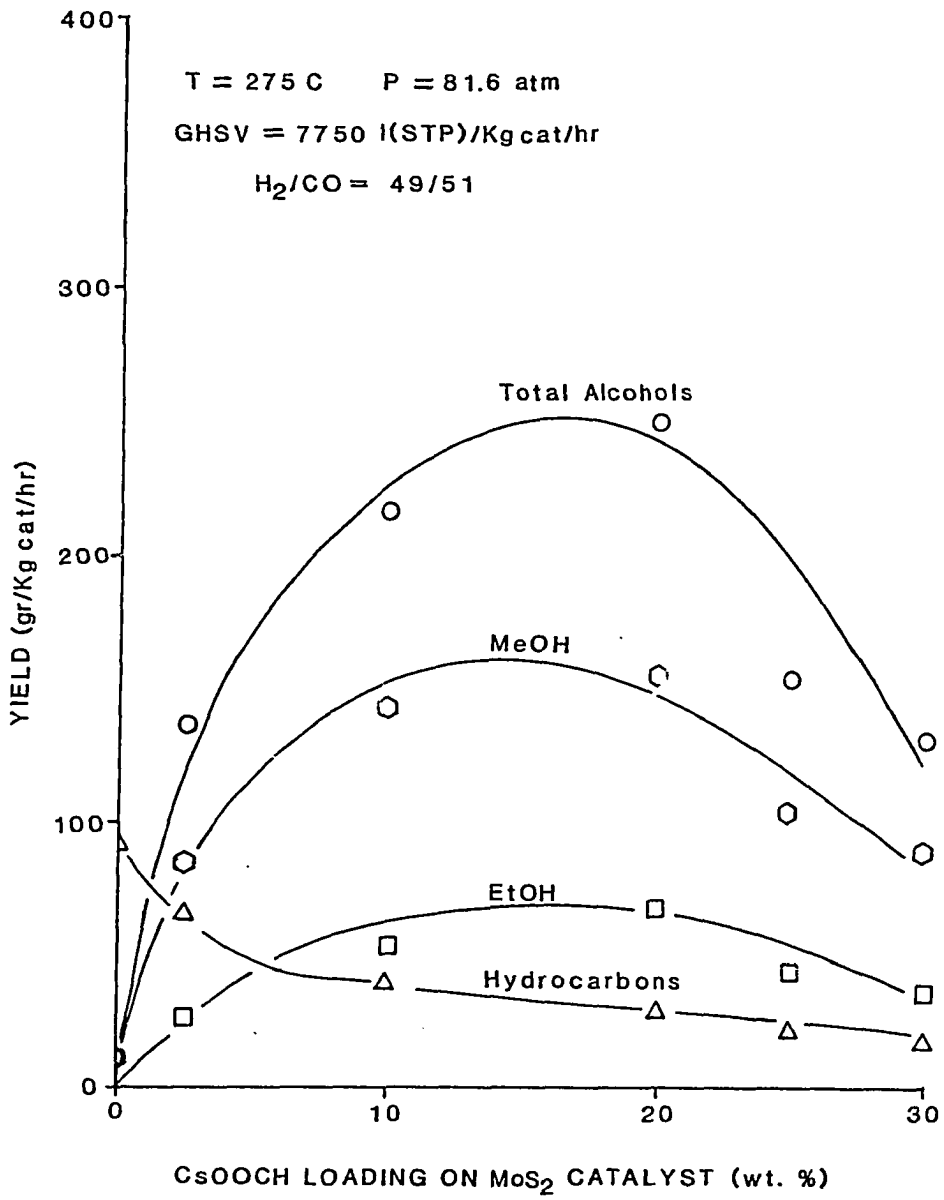

(d)

EFFECT OF Cs CONTENT OF THE MoS_2 CATALYSTS ON THE PRODUCT YIELD

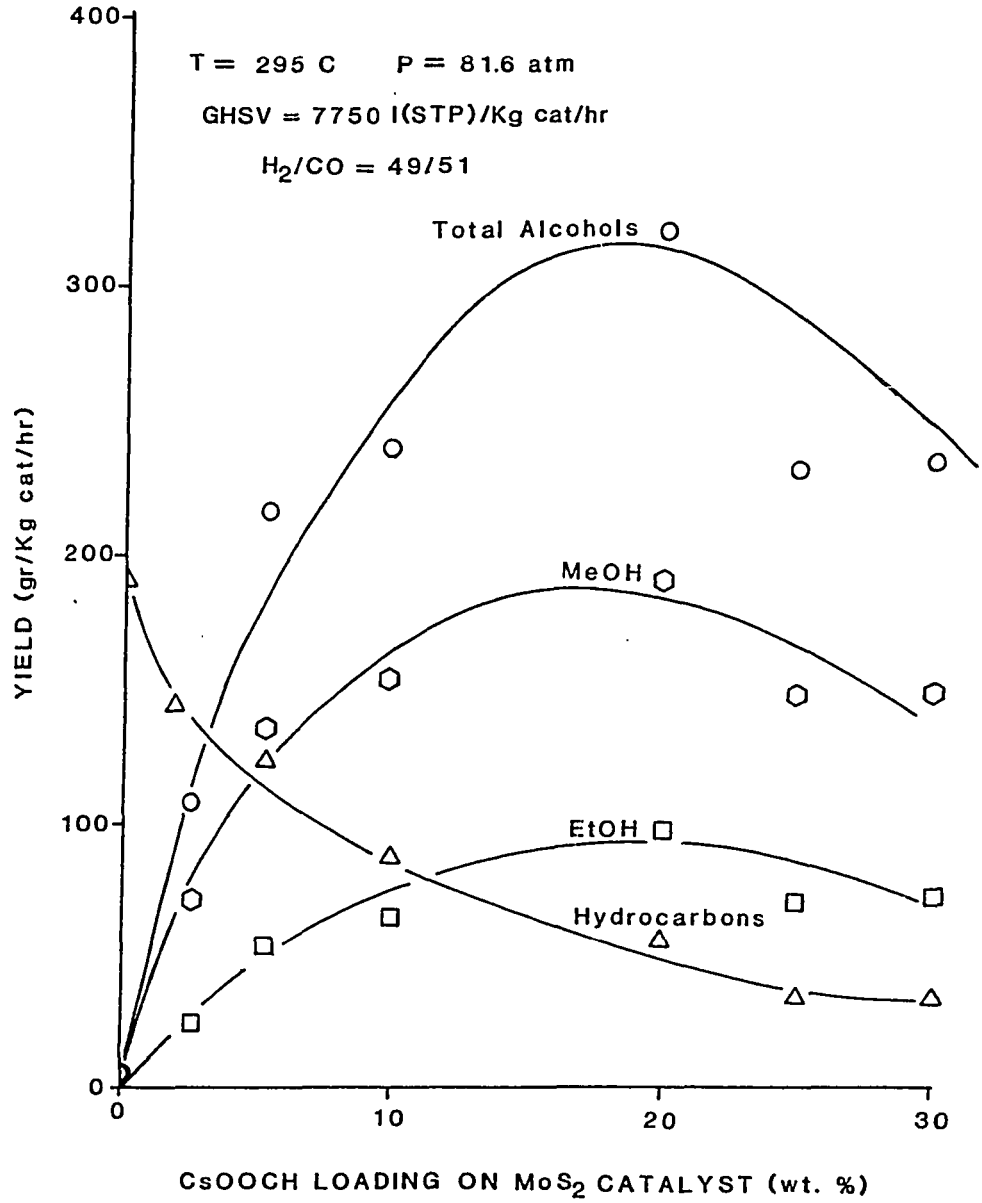

(e)

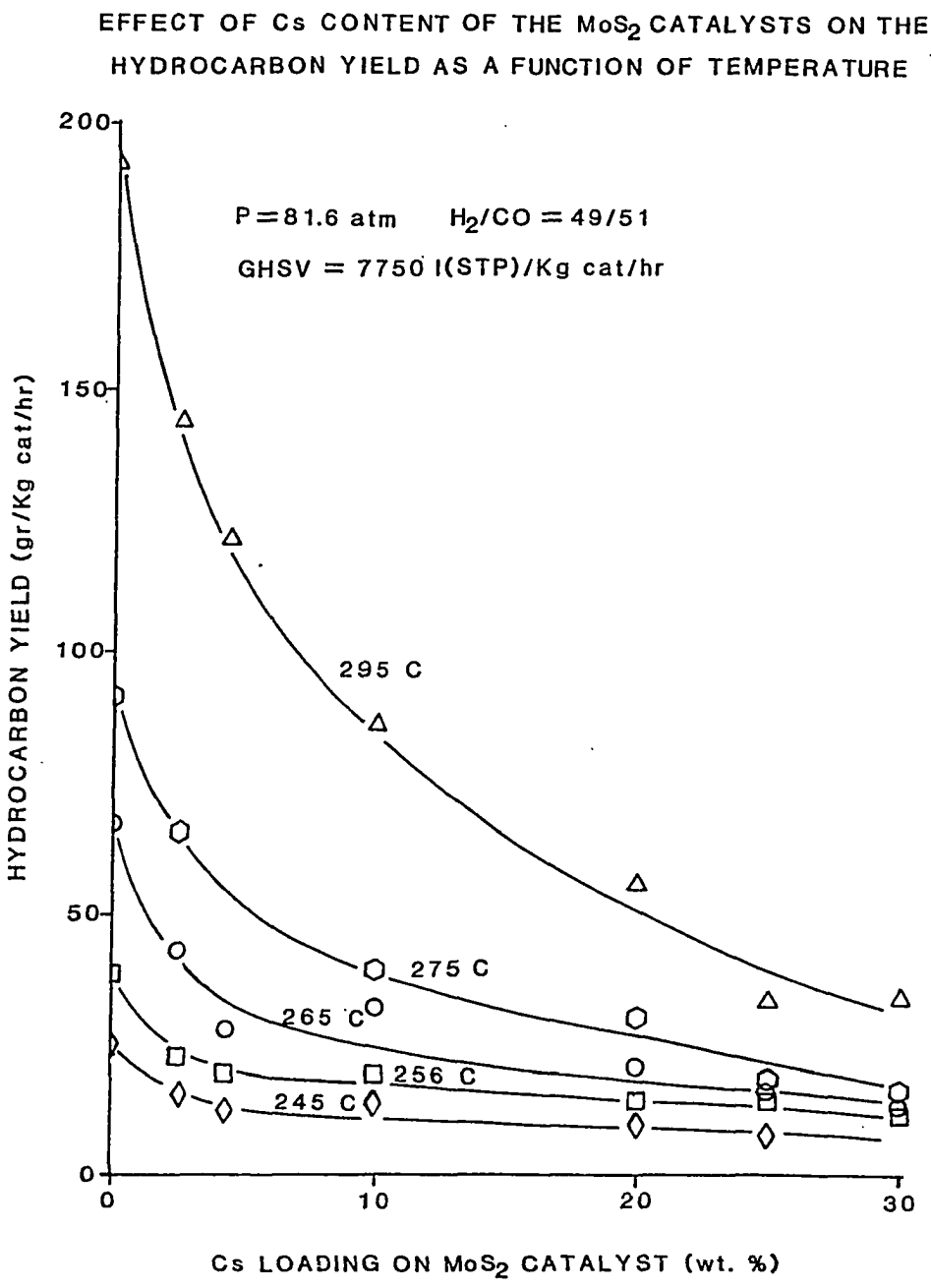

Figure 3-5 Effect of cesium loading of the MoS_2 catalysts on the hydrocarbon yield as a function of temperature at 81.6 atm, H_2/CO = 0.96, and GHSV = 7750 ℓ(STP)/kg cat/h.

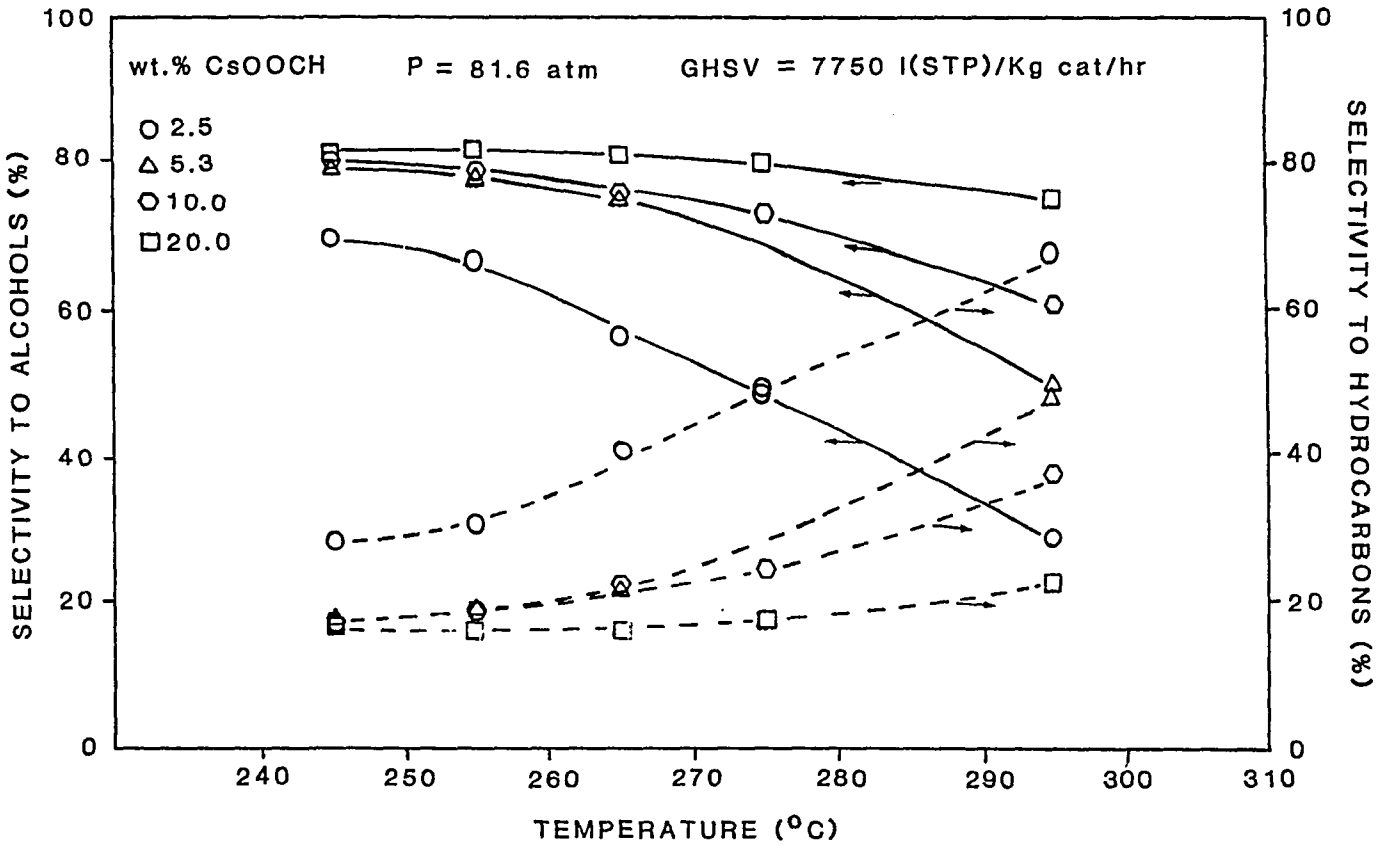

Figure 3-6 Effect of cesium loading of the MoS_2 catalysts on the selectivity to alcohols and hydrocarbons as a function of temperature. Reaction conditions are given in Figure 3-4.

increased with increasing cesium content in the catalyst. Increasing the reaction temperature, however, led to a decrease in the selectivity for alcohols, and this effect was more noticeable over the 2.5 wt% CsOOCH catalyst in which the selectivity was dramatically altered from alcohols to hydrocarbons above 275°C. Over the 20 wt% CsOOCH catalyst, increasing the reaction temperature from 245 to 295°C only led to a moderate decrease in the selectivity for alcohols. The selectivity to alcohols for catalysts containing 25 and 30 wt% CsOOCH is practically constant (≈80%) in the temperature range studied. At a given temperature, an increase in the selectivity to C-C bond formation (C_2-C_4 alcohols) was observed with increasing cesium content on the catalyst, as shown by the results in Figure 3-7. The observed decrease in selectivity for C_2-C_4 alcohols over the 2.5 wt% CsOOCH catalyst when the temperature was raised from 275 to 295°C is related to the dramatic shift in selectivity from total alcohols to hydrocarbons observed over this catalyst (see Figure 3-6).

Apparent activation energies were obtained from linear Arrhenius plots (see Figure 3-8) for undoped MoS_2 for methane, ethane, and propane under conditions in which the selectivity to hydrocarbons was ≥96%. The results are given in Table 3-10 along with the apparent activation energies for methanol, ethanol and propanol obtained from linear Arrhenius plots (see Figure 3-9) for the 20 wt% CsOOCH catalyst. It is interesting to note that the activation energies for ethanol and propanol formation are similar and higher than that for methanol formation. Thus, high reaction temperatures will favor

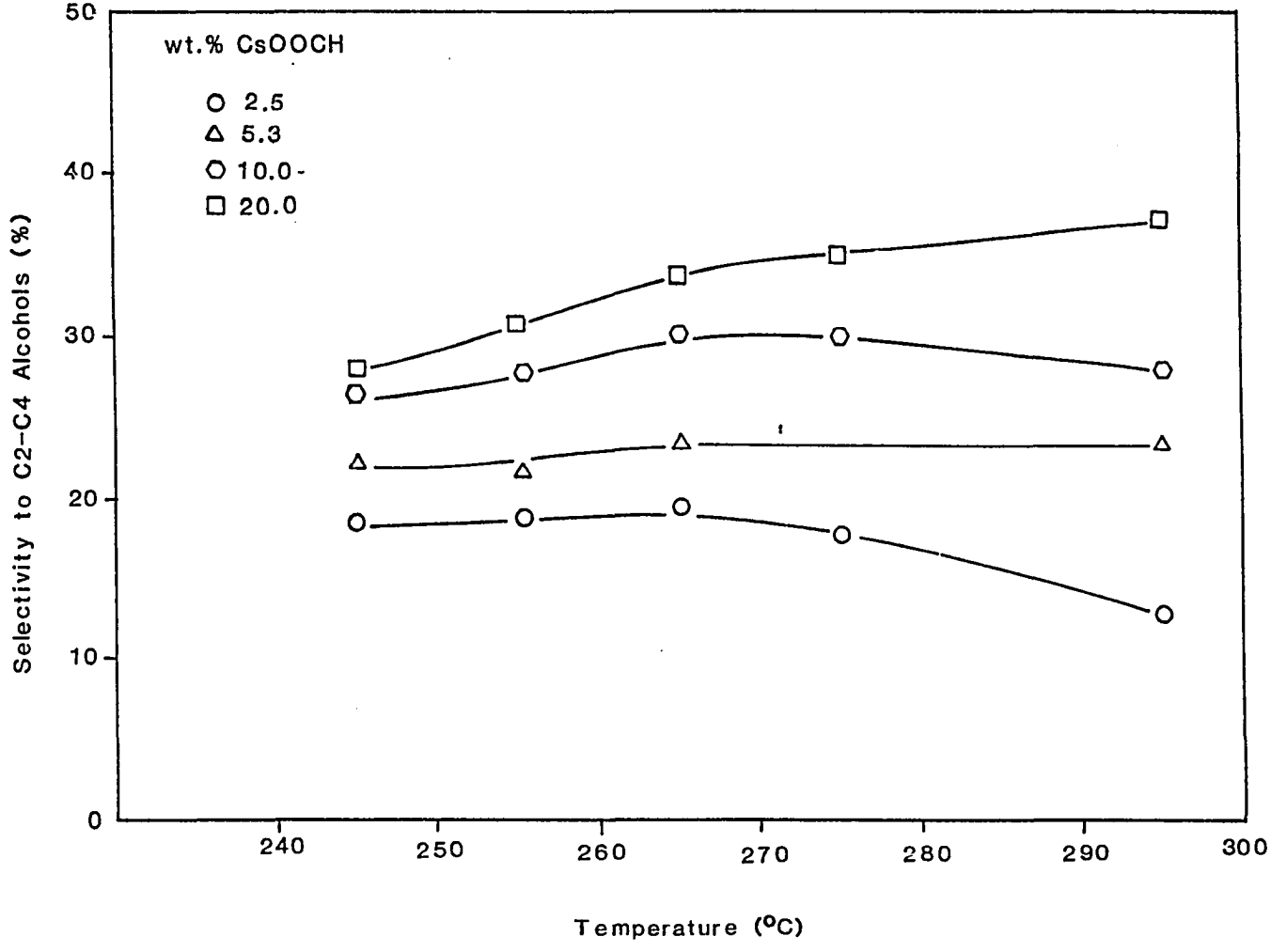

Figure 3-7 Selectivity to C_2-C_4 alcohols as a function of temperature for the Cs-doped MoS_2 catalysts. Reaction conditions are given in Figure 3-4.

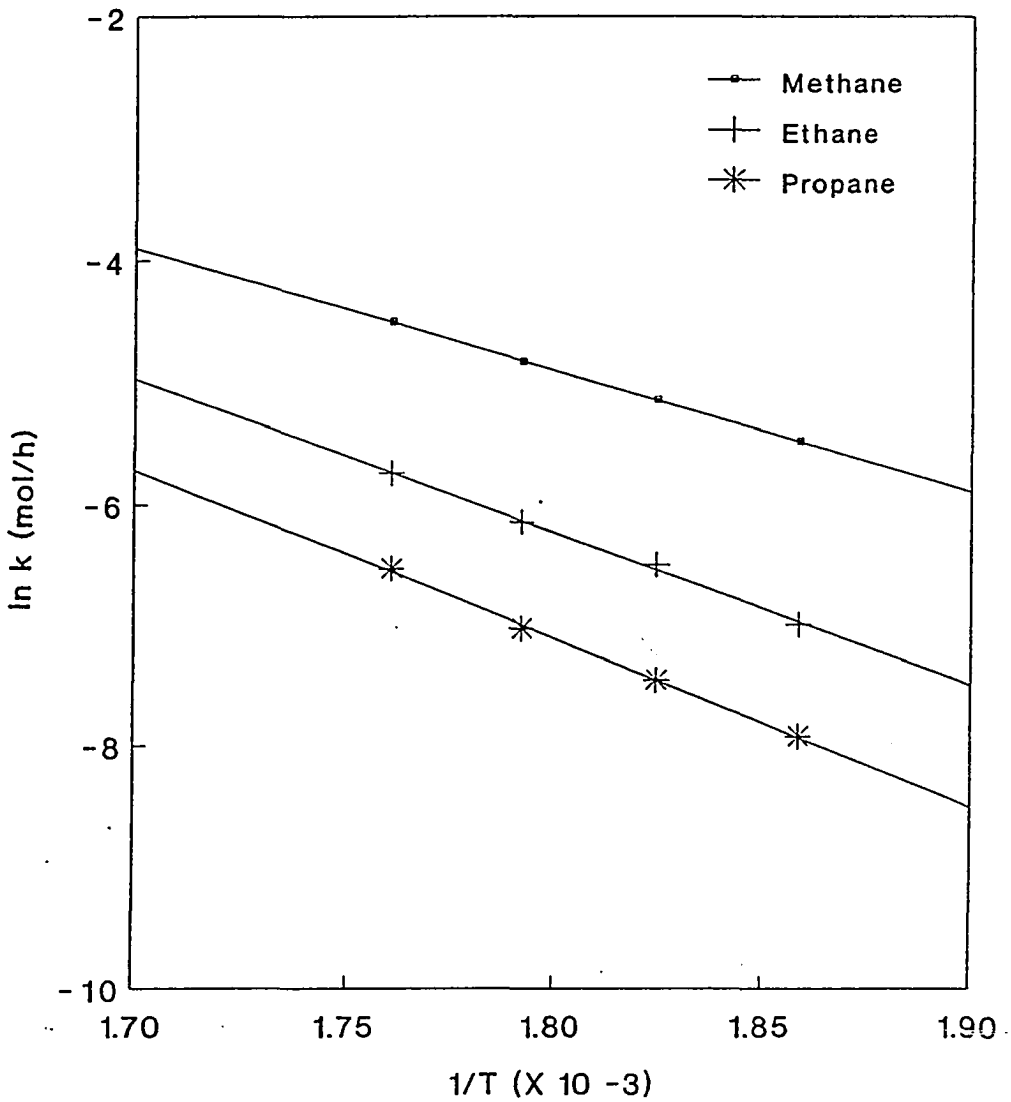

Figure 3-8 Arrhenius plots for the formation of methane (□), ethane (+), and propane (*) over undoped MoS_2 catalyst. Reaction conditions are given in Figure 3-14. The apparent activation energies were obtained by linear regression analysis of the data points and are given in Table 3-10.

TABLE 3-10

Apparent Activation Energies for Alcohols and Hydrocarbons Formation Obtained over the Cs-doped and Undoped MoS_2 Catalysts. Experimental Conditions are given in Figure 3-2.

Product	$CsOOCH/MoS_2$=20/80 wt% Temp. range (235-275°C) Ea_{app}(KJ/mol)	MoS_2 Temp. range (265-295°C) Ea_{app}(KJ/mol)
Methanol	68.0	--
Ethanol	94.9	--
Propanol	98.5	--
Methane	--	90.1
Ethane	--	114.3
Propane	--	127.5

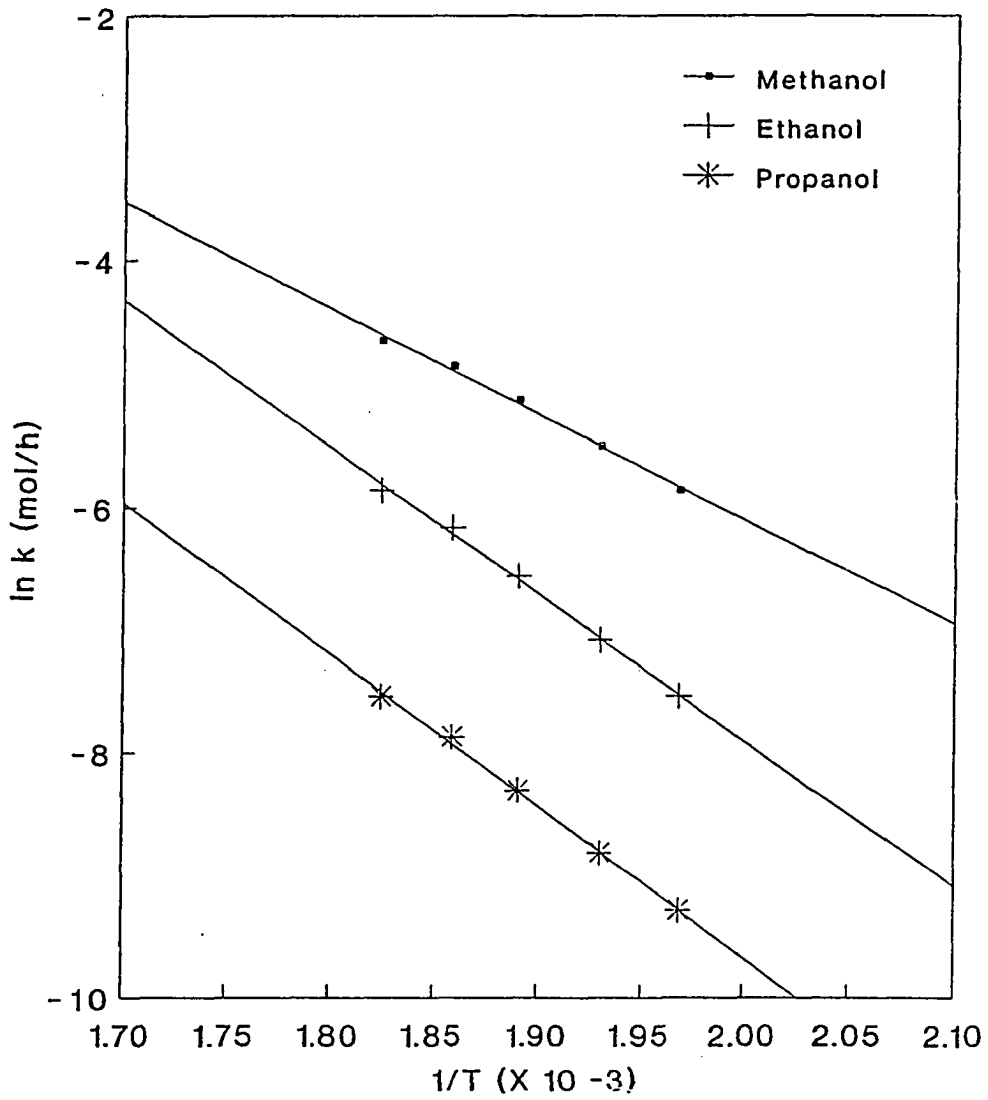

Figure 3-9 Arrhenius plots for the formation of methanol (□), ethanol (+), and propanol (*) over the $CsOOCH/MoS_2$ = 20/80 wt% catalyst. Reaction conditions are given in Figure 3-14. The apparent activation energies were obtained by linear regression analysis of the data points and are given in Table 3-10.

ethanol and propanol formation. The activation energies for hydrocarbon formation determined over the undoped MoS_2 are higher than those for the corresponding alcohols, therefore, high reaction temperatures will not only favor C_2^+ alcohols but also the formation of hydrocarbons.

3.2.4 Effect of Total Flow Rate

The flow rate dependence of the selectivities for alcohols and hydrocarbons was studied over the 5.3 wt% CsOOCH catalyst at 256°C, 81.6 atm, and with $H_2/CO = 0.96$. The results are presented in Figure 3-10. From this figure it is apparent that the selectivity for alcohols was increased at high flow rates, while the selectivity towards hydrocarbon synthesis was increased by decreasing the flow rate. This behavior shown by the hydrocarbon is that expected from secondary products.

3.2.5 Effect of Adding Cobalt to the Alkali-Doped MoS_2

The objective of this study was to verify the promotional effect of cobalt on the selectivity for ethanol over the MoS_2-based catalyst (17). The effect of operating conditions such as temperature and flow rate on the product distribution were also studied. The ultimate goal of this study was to prepare a reliable cobalt-containing catalyst and optimize the operating conditions to perform mechanistic investigations of alcohol formation over this catalyst. With this in

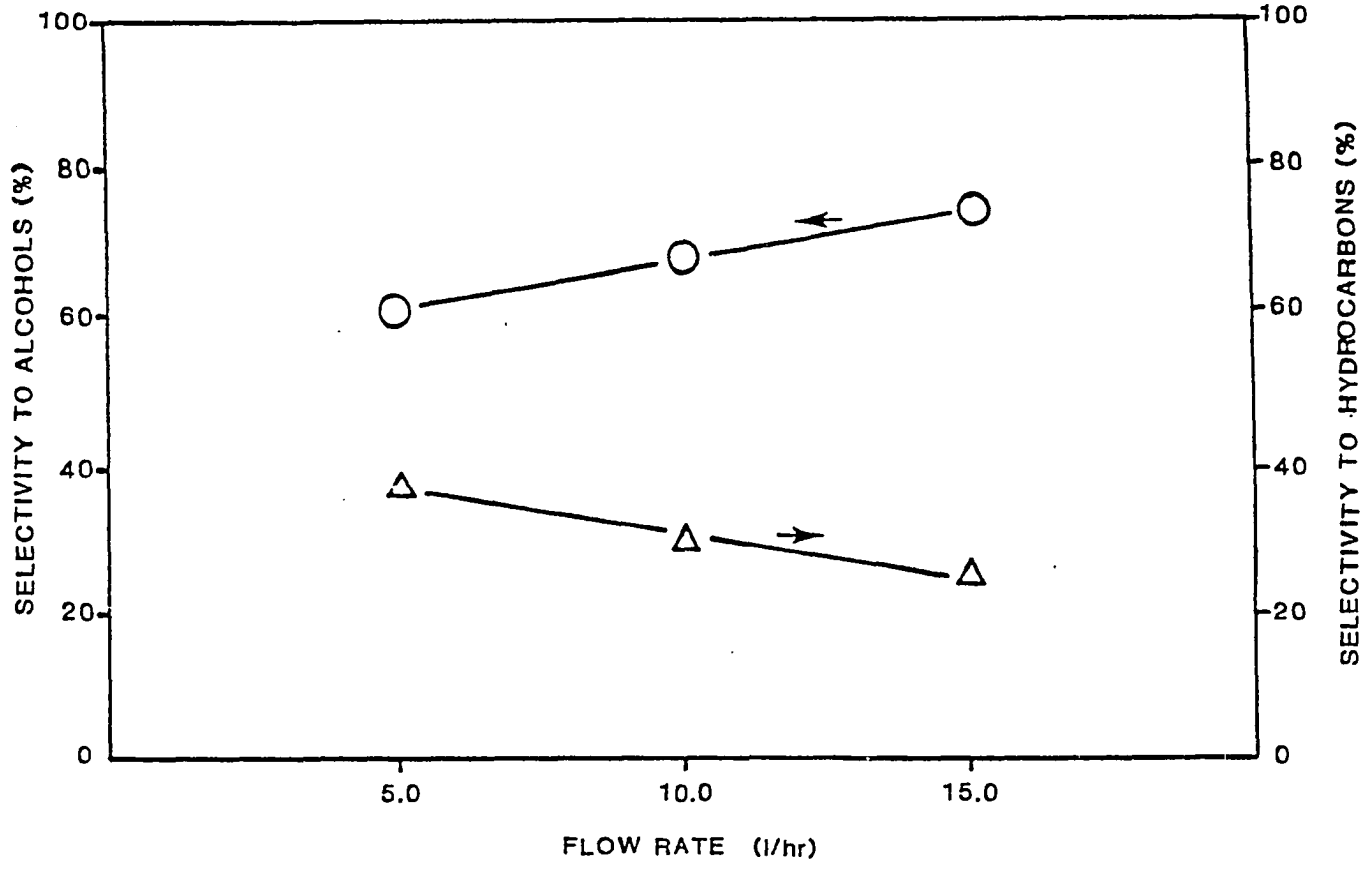

Figure 3-10 Effect of flow rate on the selectivity of the 5.3 wt% $CsOOCH/MoS_2$ catalyst for alcohols and hydrocarbons at 256°C and 81.6 atm with H_2/CO = 0.96 synthesis gas.

mind, a $K_2CO_3/(Co/MoS_2)$ = 10/90 wt% catalyst was prepared according to the procedure described in Chapter 2, Section 2.1.3, and tested at 81.6 atm, H_2/CO = 0.96, 304°C, and GHSV = 1940 ℓ(STP)/kg cat/h. The product distribution obtained over this catalyst is given in Figure 3-11 along with that obtained over the cesium-doped MoS_2 catalyst. It is apparent that the addition of cobalt to the catalyst shifted the selectivity in favor of ethanol, as was reported previously by Dow Chemical researchers (17,20). It should be mentioned that the ratio of methanol to C_2^+ alcohols over this catalyst varies considerably with reaction conditions, e.g. temperature and flow rate. This is discussed below.

3.2.5.1 Effect of Total Flow Rate

The selectivity ratio of ethanol to methanol as a function of the flow rate was studied over the $K_2CO_3/(Co/MoS_2)$ = 10/90 wt% catalyst in the range of GHSV = 1900 to 7600 ℓ(STP)/kg cat/h at 303°C and 81.6 atm with H_2/CO = 0.96 synthesis gas. The results are presented in Figure 3-12. From this figure, it is apparent that the ethanol/methanol selectivity ratio increased as the flow rate was decreased. At the same time, a decrease in the total selectivity to alcohols and an increase in the selectivity to hydrocarbons was observed with lowering of the flow rate, as indicated in Figure 3-13. These results suggest that: (i) ethanol is being formed from an intermediate species produced from methanol. This result is opposite to that found in Rh-

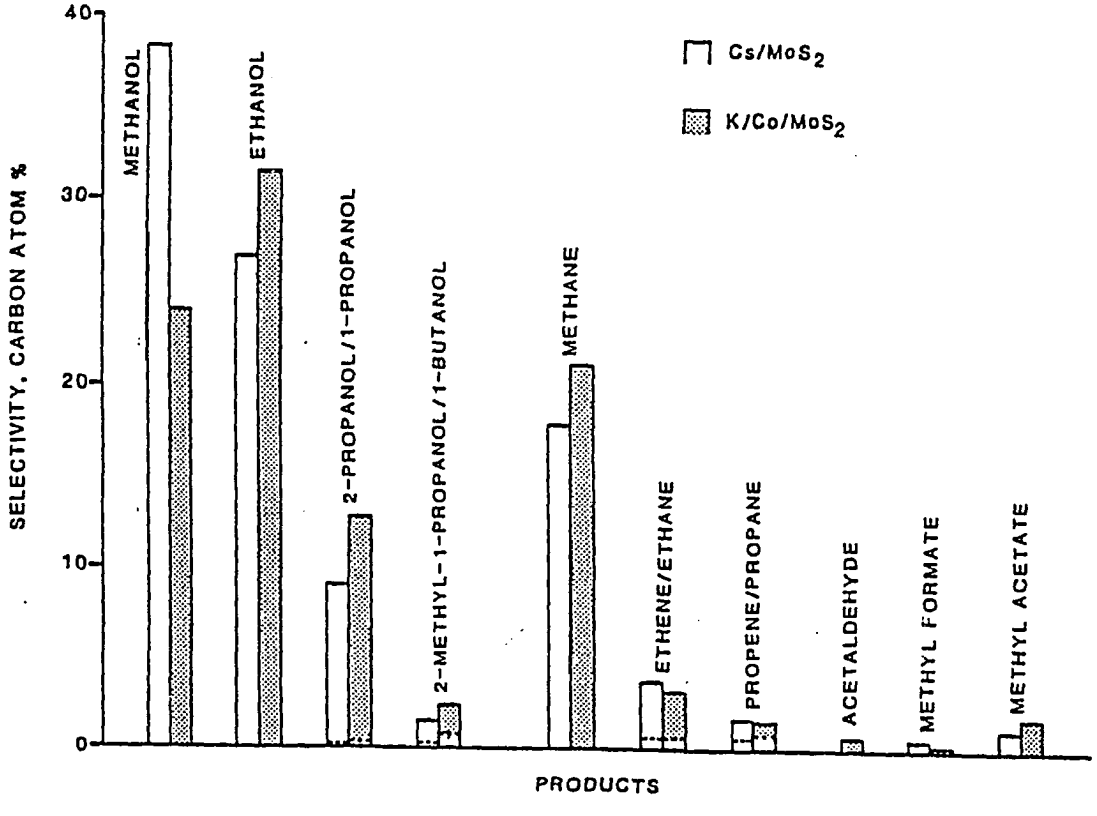

Figure 3-11 Product distributions obtained at H_2/CO = 0.96 and 81.6 atm over the $CsOOCH/MoS_2$ = 20/80 wt% catalyst (295°C, GHSV = 7790 ℓ(STP)/kg cat/h) and the $K_2CO_3/(Co/MoS_2)$ = 10/90 wt% catalyst (304°C, GHSV = 1940 ℓ(STP)/kg cat/h).

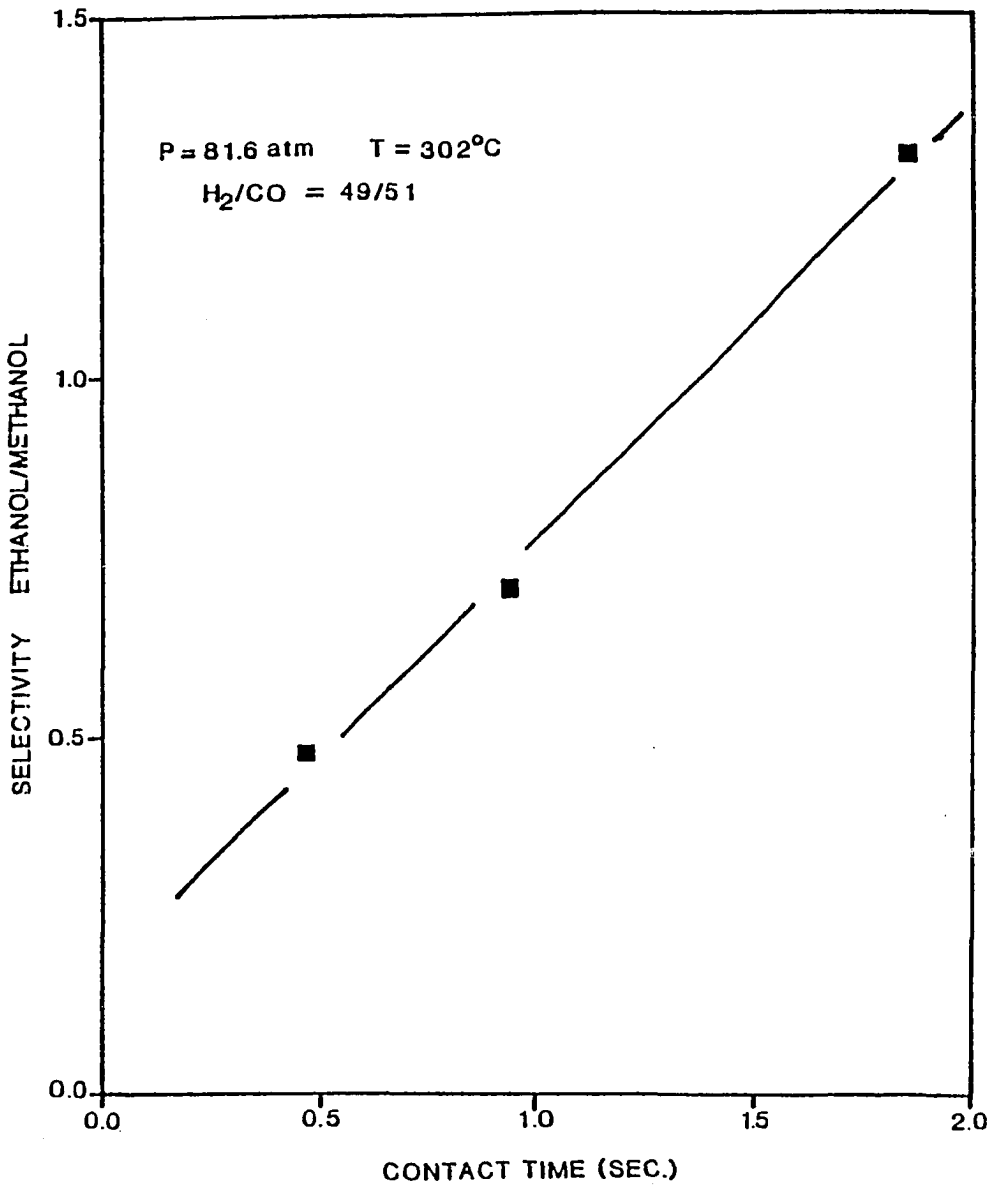

Figure 3-12 Effect of flow rate on the selectivity ratio of ethanol to methanol over the $K_2CO_3/(Co/MoS_2)$ = 10/90 wt% catalyst at 303°C, 81.6 atm, and with a H_2/CO = 0.96 synthesis gas.

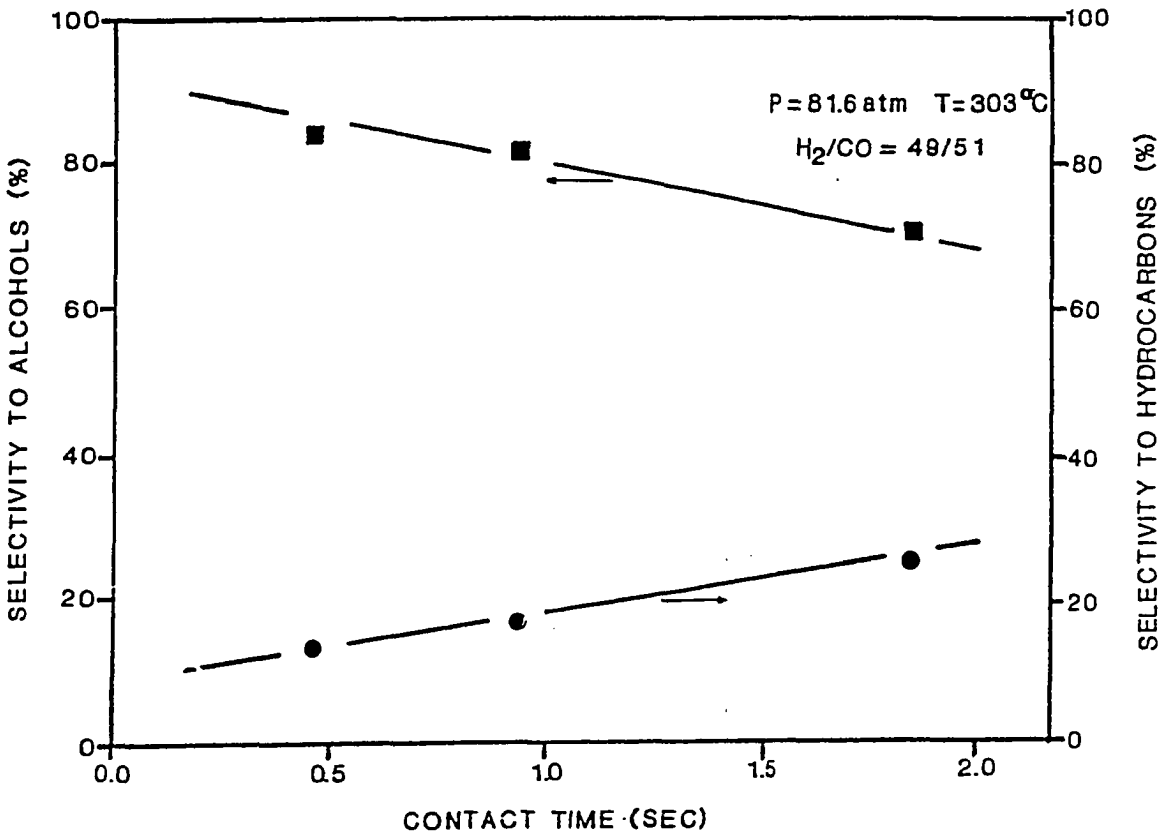

Figure 3-13 Effect of flow rate on the selectivity of the $K_2CO_3/(Co/MoS_2)$ - 10/90 wt% catalyst for alcohols and hydrocarbons at 303°C, 81.6 atm, and with a H_2/CO = 0.96 synthesis gas.

based catalysts, in which methanol is not an important intermediate in ethanol synthesis (114); (ii) hydrocarbons are produced at least in part from secondary reactions involving alcohols. This result is similar to that found on the alkali-doped MoS_2 (see Section 3.2.4 in this chapter).

3.2.5.2 Effect of Reaction Temperature

The effect of reaction temperature on the rate of formation of methanol, ethanol, and propanol was studied over the $K_2CO_3/(Co/MoS_2)$ = 10/90 wt% catalyst at 81.6 atm, H_2/CO = 0.96 and GHSV = 3600 ℓ/kg cat/h. Linear Arrhenius plots were obtained in the temperature range of 270-303°C for the alcohols mentioned above, and the resultant apparent activation energies are given in Table 3-11. The activation energies for alcohol formation follow the order propanol > ethanol > methanol, which indicates that high temperatures favor C_2^+ alcohol formation. Also in Table 3-11, the apparent activation energies obtained over the Cs-doped MoS_2 and Cs-doped Cu/ZnO catalysts are shown for the sake of comparison. The apparent activation energy for methanol formation is similar in the three different catalytic systems, this implies that the methanol formation over these catalysts is proceeding through similar pathways. The activation energy for ethanol formation is comparable on the MoS_2-based catalysts, but lower than that obtained over the Cs/Cu/ZnO catalyst, thus indicating that higher selectivity to C_2^+ catalysts can be achieved on the MoS_2-based catalysts at lower temperatures than that obtained on Cs/Cu/ZnO. In

TABLE 3-11

Comparison of the Apparent Activation Energies for Methanol, Ethanol, and Propanol Formation over K-doped Co/MoS_2, Cs-doped MoS_2 (Experimental Conditions are given in Figure 3-11), and Cs-doped Cu/ZnO (cf. Ref.117) Catalysts.

Product	K-doped Co/MoS_2 Temp. range (270-303°C) Ea_{app}(KJ/mol)	Cs-doped MoS_2 Temp. range (235-275°C) Ea_{app}(KJ/mol)	Cs-doped Cu/ZnO Temp. range (210-250°C)[a] (258-289°C)[b] Ea_{app}(KJ/mol)
Methanol	66.8	68.0	76.6
Ethanol	104.2	94.9	148.5
Propanol	132.1	98.5	--

[a] Temperature range for methanol
[b] Temperature range for ethanol

addition the formation of ethanol over the MoS_2-based catalysts takes place through an energetically more favorable pathway. In Chapter 4, it will be shown that this pathway is related to CO insertion into a methyl group to produce an acyl group that is subsequently hydrogenated to ethanol. In contrast, the formation of ethanol over the Cs/Cu/ZnO catalyst has been shown to occur through coupling of the C_1 surface intermediates originating from methanol (56).

3.3 DISCUSSION

3.3.1 Effect of Alkali Doping

The results obtained in this work regarding the effect of alkali doping can be summarized as follows:

(i) The selectivity was shifted dramatically from hydrocarbons to alcohols upon doping of MoS_2 with the alkali compound.

(ii) The promotional effect of cesium for alcohol synthesis was greater than that shown by potassium.

(iii) The alcohol yields passed through a maximum, while the hydrocarbon formation is suppressed, as the content of cesium in the catalyst increases.

(iv) Olefins and methyl formate were observed to be formed only over the high cesium content catalysts.

(v) At a given temperature, an increase in the selectivity to C_2-C_4 alcohols was observed with increasing the amount of cesium in the catalyst.

(vi) Promotion of the water-gas shift reaction was observed.

The most striking effect observed upon addition of the alkali salt to MoS_2 is the dramatic shift in selectivity in favor of alcohol formation, for which the Dow Chemical Company and Union Carbide Corporation are filing for patents. The question to be discussed here is the following: what is the mechanistic role of the alkali compound that induces the formation of alcohols rather than hydrocarbons from synthesis gas ($CO + H_2$) over MoS_2-based catalysts? The promotional effect of alkali doping has long been known in heterogeneous catalysis, and several theories have been proposed to explain the role of alkali as a promoter in a great variety of reactions (78). In the present work, the role of the alkali compound on the activity and selectivity of the MoS_2-based catalysts is proposed to be two-fold. It is responsible (i) for the presence of basic centers capable of associatively activating CO and thus opening a new pathway to form alcohols, and (ii) for the reduced availability of active hydrogen. Our experimental observations and those reported in the literature on different alkali-doped catalysts for the synthesis of alcohols support these suggestions. The superior promotional effect of cesium compared to that of potassium indicates that base-catalyzed reactions are being promoted in the system. The superior promotional effect of Cs is by no means unique to MoS_2. This effect has been observed on different catalytic systems. It was noticed initially by Fischer and Tropsch (22) on the alkali-activated iron-base catalysts, and later systematic studies in catalysts such as Cr_2O_3/MnO (74,75), ZnO/Cr_2O_3 (6), and

Cu/ZnO (10) concluded that the promotion of alcohol synthesis by alkali metals is ion specific as Cs>Rb>K>Na>Li, in the same order of their basicity. Activation of CO by alkali hydroxides is known to occur under mild conditions (115). Details of this reaction have recently been investigated by reaction path calculations (116) with the result that a facile nucleophilic attack of CO by $^{\ominus}OH$, which, needless to say, is favored by the basicity of $OH^{\ominus}$,

$$HO^{\ominus} + CO \rightarrow \underset{H\text{-}O\text{-}C\text{-}O}{\overset{\ominus}{\overline{\quad\quad}}}$$

The formation of this intermediate is followed by an activated hydrogen transfer to produce formate

$$\underset{H\text{-}O\text{-}C\text{-}O}{\overset{\ominus}{\overline{\quad\quad}}} \rightarrow HCOO^{\ominus}$$

The energetics along the reaction coordinate for the above steps are shown in Figure 3-14. It has been reported (56) that formate species are subsequently hydrogenated to produce methanol.

Another indication that the basic centers created by cesium are participating actively in the system is the fact that the formation of methyl formate and the water-gas shift reaction are being promoted. These two reactions are known to be associated with the presence of basic centers.

The maximum in alcohol yields as a function of cesium content observed in this study was also observed by Nunan and co-workers (117) with the Cs-promoted Cu/ZnO catalyst, although at much lower loadings of cesium, e.g. 0.45 wt% Cs. It was reported (56,118) that the latter

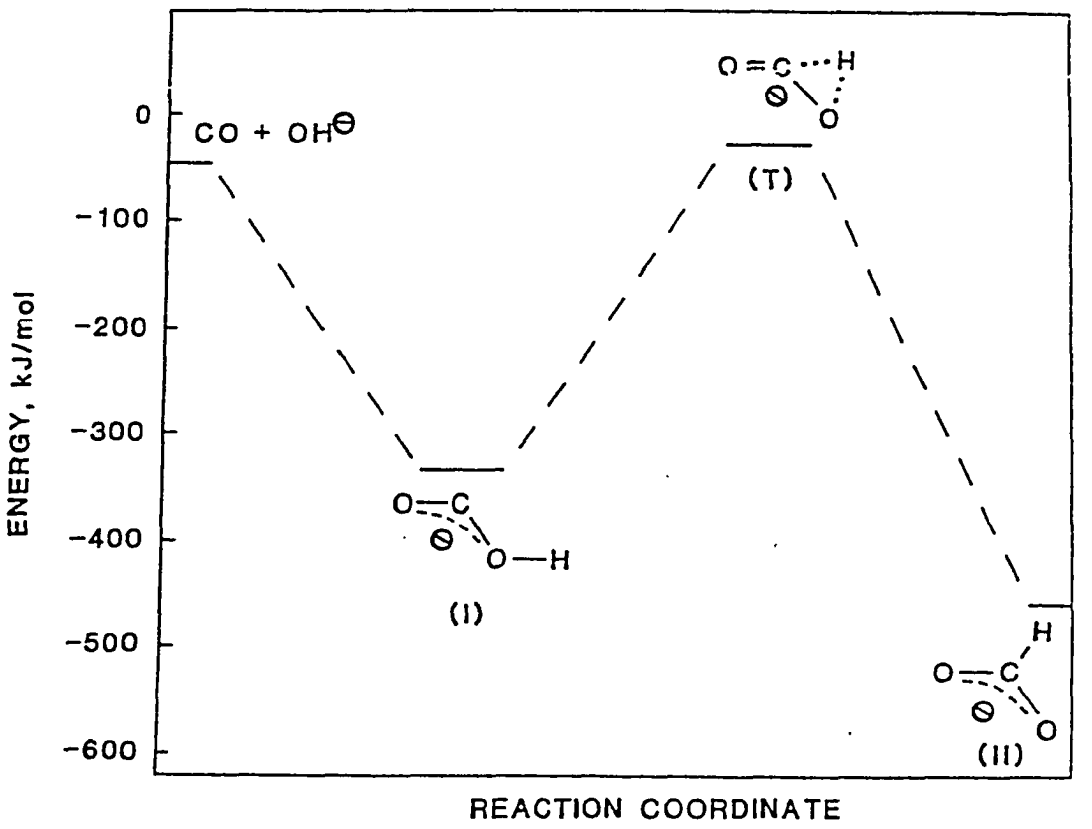

Figure 3-14 MNDO energy diagram for the reaction of carbon monoxide with hydroxide to form formate (from Reference 116).

catalyst was bifunctional, in which the cesium component associatively activated CO and the Cu/ZnO matrix provided the hydrogenation function necessary for the synthesis of alcohols. This picture can be applied to the Cs/MoS_2 catalyst. The basic component (Cs) contributes the active sites to activate CO in such a way that a new reaction pathway for the formation of alcohols rather than for the formation of hydrocarbons is open. The hydrogenation function necessary for the synthesis of alcohols is supplied by MoS_2. It is well known that MoS_2 dissociatively activates H_2 and that its active sites are edge-like defects (see Chapter 1, Section 1.7 for details). The increase in the total product yield is due to the introduction of cesium to the catalyst which increases the number of CO activation sites. The maximum activity is achieved when the CO and H_2 activating components, Cs^+ and MoS_2, respectively, are balanced. Details of the mechanism of alcohols formation is offered in Chapter 4. It should be mentioned that MoS_2 is also capable of activating CO, although this activation is through a reaction pathway that leads to the formation of hydrocarbons, as evidenced by the fact that undoped MoS_2 produces mostly hydrocarbons.

The reduced availability of active hydrogen is reflected in the suppression of hydrocarbon formation, the production of olefins over the high Cs content catalysts, and also by the increase in the selectivity to C_2-C_4 alcohols with increasing quantity of cesium. This last point is explained as follows: in Chapter 4, it will be shown that the formation of methane and ethanol go through a common

intermediate, namely the methyl group. If the hydrogenation function of the catalyst is reduced, one would expect that the CO insertion rate (k_{CO}) would be favored, i.e. $k_{CO} > k_H$, thus giving rise to C_2^+ oxygenated compounds. On the other hand, if there is an abundant supply of active hydrogen available, the hydrogenation rate (k_H) would be favored ($k_H > k_{CO}$), and therefore the hydrogenation of the methyl group to produce methane will take place. Scheme I illustrates these two pathways.

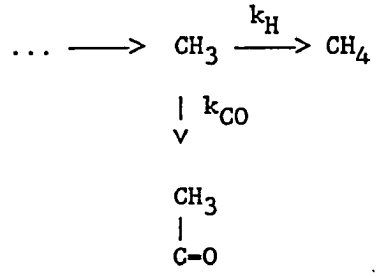

Scheme 3-1

3.3.2 Effects of Reaction Temperature and Flow Rate on the Synthesis of Hydrocarbons and Alcohols

The results shown in Figure 3-10 demonstrate that the selectivity to alcohols and hydrocarbons is affected by the flow rate. Hydrocarbon selectivity is favored at low space velocity. This suggests that hydrocarbons are produced by decomposition of alcohols. This was later confirmed (see Chapter 4) by injection of ^{13}C-labeled methanol into the synthesis gas. Mass spectroscopic analyses indicated that the methane formed contained appreciable amounts of

^{13}C. Furthermore, it was also shown that the methane yield was considerably increased during the methanol pumping experiments. Based on these results one can conclude that the changes in selectivity for alcohols and hydrocarbons observed over the cesium-doped MoS_2 catalysts as a function of temperature, as shown in Figure 3-6, are associated with secondary reactions of alcohols to produce hydrocarbons. This decomposition of alcohols is suppressed over the catalysts with high content of cesium compound, in which less surface of MoS_2 is exposed (see Chapter 5). Presumably, active sites on the MoS_2 are responsible for the decomposition of alcohols. It has been shown with labeled alcohols added to the system that Fischer-Tropsch catalysts have C-O bond rupture capability not only for carbon monoxide but also for alcohols (119). As discussed above, ^{13}C-labeled methanol experiments demonstrated that MoS_2-based catalysts certainly have this capability of breaking the C-O bond of alcohols.

Another plausible explanation for the change in selectivity in favor of hydrocarbons upon increasing the reaction temperature, is that the activation energy for hydrocarbon formation over the bare MoS_2 surface is higher than that for alcohols (see Table 3-10), and therefore an increase in reaction temperature would favor the hydrocarbon formation. However, since the values of the apparent activation energies for hydrocarbons, e.g. methane = 90.1 kJ/mol, are slightly higher than those for alcohols, e.g. methanol = 68.0 kJ/mol, this explanation cannot account fully for the change in selectivity. Therefore, it is proposed that secondary reactions are mainly

responsible for the change in selectivity in favor of hydrocarbons at high temperature.

3.3.3 Effect of Cobalt

The promotional effect of cobalt toward ethanol formation has been known since the early investigations of Taylor (75) who obtained an ethanol selectivity of 22% with respect to the condensate product using a catalyst containing CoS/CuO/MnO. Also in the 1930's, high yields of ethanol were reported to have been obtained over a CoO/ZnO catalyst (6). Later, Wender et al. (120) studied the reaction between methanol and synthesis gas ($CO + H_2$) in the presence of dicobalt octacarbonyl, $[Co(CO)_4]_2$, and concluded that cobalt catalyzed to a great extent the homologation reaction of methanol to produce ethanol. Recently, researchers from the French Petroleum Institute (IFP) disclosed a copper-cobalt based catalyst for the production of linear alcohols (11,12). More recently, Dow Chemical researchers reported that the addition of cobalt to the alkali-doped MoS_2 catalyst shifted the selectivity in favor of ethanol (17,20). In the present study, it was confirmed that the addition of cobalt to the alkali-doped MoS_2 catalyst has the effect of changing the selectivity in favor of ethanol under certain operating conditions, as shown in Figure 14. Thus, it is clear that cobalt promotes the $C_1 \rightarrow C_2$ homologation step. This promotional effect of cobalt is a well accepted phenomenon in heterogeneous catalysis, but the nature of its promotional effect is unknown. Very recently, Dianis (19) performed CO Temperature Program

Desorption (TPD) studies on the MoS_2-based catalysts, and reported the existence of two forms of CO on the cobalt-containing MoS_2 catalyst. Dianis proposed that "the more strongly bound CO is less readily hydrogenated directly to methanol, and therefore, the cobalt molybdenum sulfide shows better selectivity toward higher alcohols," but no details were given (19).

In homogeneous catalysis, the promotional role of cobalt on the methanol homologation reaction to form ethanol is better understood. Recently, Röper and Loevenich (121) reviewed in detail the homologation of methanol catalyzed by cobalt, and based on literature data and on their own work they suggested that the rate-determining step is the oxidative addition of methanol to a cobalt center by scission of the carbon-oxygen bond, and that this step can be promoted by iodine compounds. The authors proposed the mechanism shown in Scheme 3-2, which they explain as follows: oxidative addition of methyl iodide to the coordinatively unsaturated cobalt (I) species (1) gives the methyl complex (2) which undergoes CO insertion, probably via methyl migration. Elimination of iodine from the acetyl complex (3) and oxidative addition of hydrogen gives (5). Reductive elimination of the primary product acetaldehyde leads to the unsaturated complex (6) that oxidatively adds iodine. The catalytic cycle is closed by elimination of hydrogen iodide from (7), which is consumed by reaction with methanol to give methyl iodide. The primary product acetaldehyde is hydrogenated to give ethanol (8).

As mentioned above, the most crucial step of the reaction cycle

THE HOMOLOGATION OF METHANOL

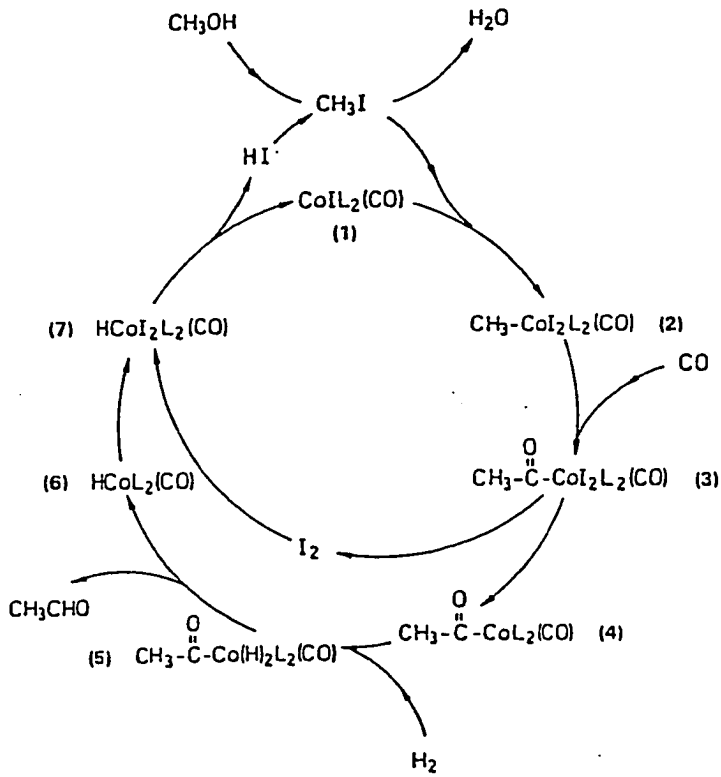

Scheme 3-2

is thought to be the oxidative addition of methanol to a cobalt center by scission of the C-O bond. In Chapter 4 of this thesis, it is shown that MoS_2-based catalysts have the capability of breaking the C-O bond of methanol to produce a methyl group, thus overcoming this crucial step. Based on this result, it is proposed here that this methyl group, produced from methanol, can migrate toward the strongly bound CO found on the cobalt-containing MoS_2 catalyst to produce an acyl group that is subsequently hydrogenated to form ethanol. Sakari et al. (124) performed ab initio Hartree-Fock MO calculations to show that methyl migration is an easy reaction path. Experimental evidence supporting the reaction between a methyl group and CO over the MoS_2-based catalysts is discussed in Chapter 4.

Chapter 4

MECHANISM OF C_1 - C_4 ALCOHOL SYNTHESIS OVER ALKALI/MoS_2 AND ALKALI/Co/MoS_2 CATALYSTS

4.1 Introduction

The mechanism of methanol and higher alcohols formation have been subject of intense debate in the literature. The large number of papers published supporting different mechanisms indicate that the reaction pathway of products formation may not be identical for different catalysts. A summary of the numerous reaction mechanisms proposed in the literature is given in Chapter 1, Sections 1.4 and 1.5.

The objective of this chapter is to provide insight into the mechanism of alcohols synthesis and of the formation of simultaneously produced hydrocarbons and methyl esters over the MoS_2-based catalysts.

Injection of ^{13}C-labeled CH_3OH into the synthesis gas feedstream over $CsOOCH/MoS_2$ = 20/80 wt% and $K_2CO_3/(Co/MoS_2)$ = 10/90 wt% catalysts, and analysis of the products by ^{13}C NMR and mass spectroscopy provided details of the stepwise pathways involved in the synthesis of products via C-C and C-O bond formation. It is shown that over the MoS_2-based catalysts the alcohol chain growth ocurred by stepwise CO insertion into adsorbed alkyl species. It is also demonstrated that methane is a secondary product that is formed from an alkyl moiety generated from a C_1-oxygenated precursor, and that

methanol is the source of the methyl group of the methyl esters. The formation of methanol is also discussed based on the experimental data obtained on this study as well as those reported in the literature in similar syngas catalytic reactions.

4.2 Results

4.2.1 Injection of Native and ^{13}C-Enriched Methanol over the $CsOOCH/MoS_2$ Catalyst.

The effect of injecting methanol and ^{13}C-enriched methanol into the synthesis gas over the 20 wt% $CsOOCH/MoS_2$ catalyst under steady state conditions was determined at different reaction temperatures by analyzing the reaction rates and the isotope distribution in the liquid and gaseous products by on-line GC analysis, ^{13}C NMR and mass spectroscopy. A 2.0 g portion of the catalyst was centered in the reactor using and upper and lower glasswool bed to contain the catalyst and pretreated in a manner described in Chapter 2, Section 2.3. After cooling to ambient temperature, the reactor was pressurized to 81.6 atm with a H_2/CO = 0.96 synthesis gas. After a gas flow of 7465 ℓ(STP)/kg cat/h was set, the reactor was heated to the reaction temperature and methanol was injected continuously into the gas stream at the reactor inlet using a high-pressure Gilson Model 302 pump. The methanol was enriched by a factor of 21.69 over the natural carbon-13 abundance of 1.11 at%. The ^{13}C-enriched methanol injection rate was 14.81 mmol/2.0 g cat/h (238.96 g methanol/kg

cat/h).

Table 4-1 shows steady state rates of formation of methane, ethanol, propanol, methyl formate, and methyl acetate obtained with and without injection of methanol at two different temperatures. Comparison of these two experiments at given temperatures demonstrates that the rate of formation of the products mentioned above increased upon injection of methanol.

GC/MS analyses of the gaseous products collected during injection of ^{13}C-enriched methanol are shown in Table 4-2 for different reaction temperatures. It is apparent that methane contained appreciable amounts of ^{13}C indicating that methane formation occurred via intermediates derived from ^{13}C-methanol. The ^{13}C enrichment factor of methane given in Table 4-2 was defined as the ratio of $\%^{13}CH_4$ determined during the isotope experiments to that of the $\%^{13}C$ natural abundance (1.11%). The observed decrease of the ^{13}C enrichment factor of CH_4 upon increasing the reaction temperature (from 245°C to 295°C) is due to dilution of the ^{13}C-enriched methanol with native methanol synthesized over the catalyst.

Figure 4-1 shows spectra of the liquid product collected during injections of the native and ^{13}C-enriched methanol for the reaction temperature of 295°C. Comparison of the peak heights of the carbons of the products formed during the native ^{13}C and ^{13}C-enriched methanol experiments clearly showed that (i) preferential enrichment of the terminal carbons of the C_2 - C_4 alcohols occurred and (ii) the methyl group of the methyl esters was preferentially enriched relative to the

TABLE 4-1

Effect of Methanol Injection on the Product Yields Obtained over the CsOOCH/MoS_2 = 20/80 wt% Catalyst at 81.6 atm, H_2/CO = 0.96 Synthesis Gas, and GHSV = 7465 l(STP)/kg cat/h. Methanol Injection Rate = 238.96 g methanol/kg cat/h.

		Yield of Products (g/kg cat/h)					
Temp.(°C)		Methanol	Ethanol	1-PrOH	Methyl Formate	Methyl Acetate	Methane
245	a	280.7	22.1	3.8	4.1	4.3	7.3
	b	75.1	15.7	3.8	0.7	tr	0.3
295	a	280.0	91.3	27.8	0.8	5.9	65.9
	b	201.7	81.4	24.4	tr	3.6	43.5

[a] With methanol injection

[b] Without methanol injection

TABLE 4-2

Mass Spectroscopic Analyses of the Methane Produced During Injection of ^{13}C-Enriched Methanol over the $CsOOCH/MoS_2$ = 20/80 wt% Catalyst at 81.6 atm, H_2/CO = 0.96 Synthesis Gas, and GHSV = 7465 l(STP)/kg cat/h.

Temperature (^oC)	^{13}C Enrichment Factor of CH_4
245	25.7
265	14.2
285	10.9
295	9.6

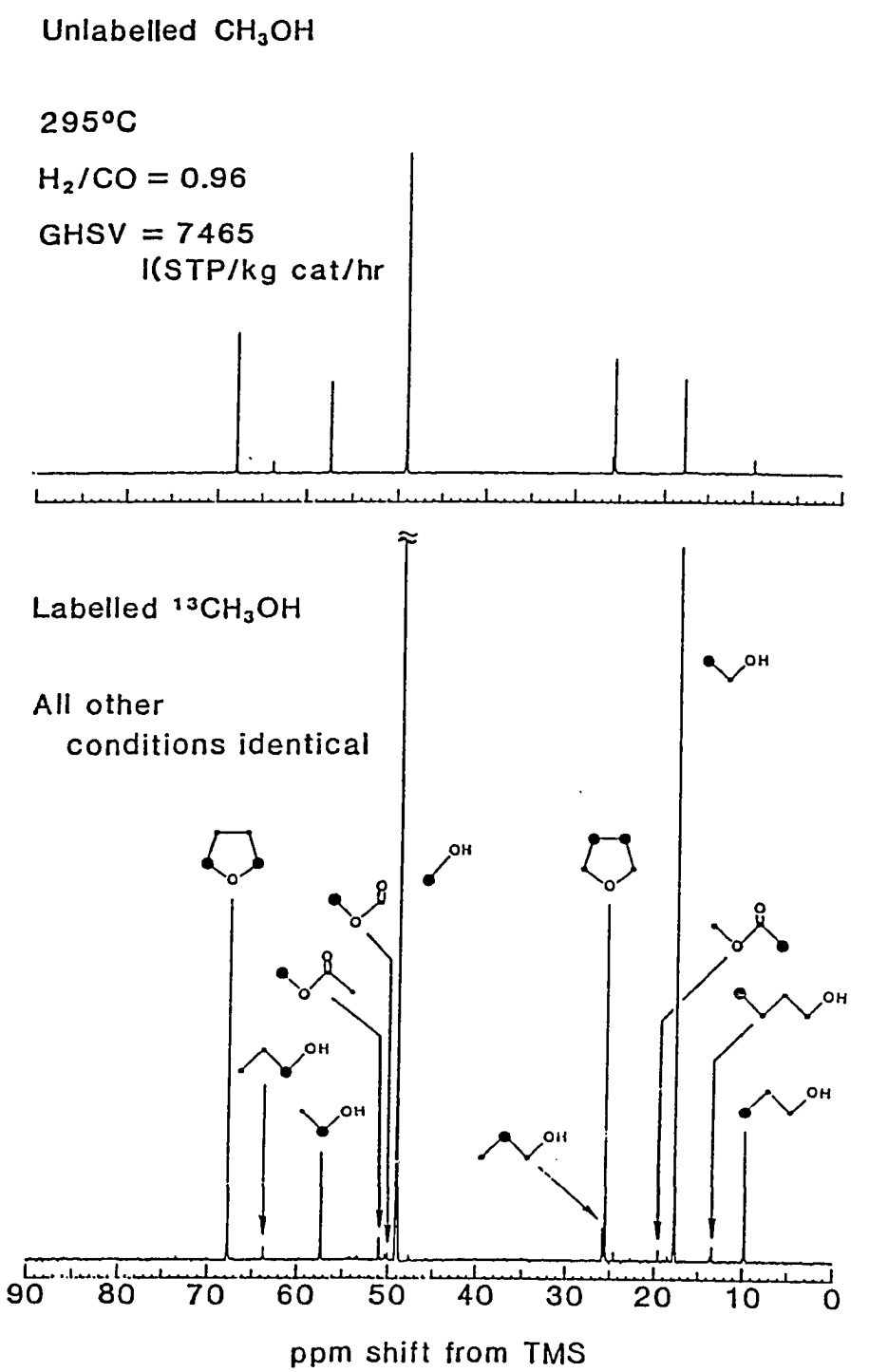

Figure 4-1 ^{13}C-NMR spectra of the liquid product obtained upon injection of native methanol and ^{13}C-enriched methanol into the synthesis gas feedstream over the $CsOOCH/MoS_2$ - 20/80 wt% catalyst at 295°C, 81.6 atm, H_2CO - 0.96, and GHSV - 7465 ℓ(STP)/kg cat/h. Methanol injection rate - 238.96 g methanol/kg cat/h, ^{13}C enrichment - 21.69.

carbonyl carbon.

The degree of enrichment of the oxygenated products was calculated by combining GC analyses and NMR analyses. The carbons of tetrahydrofuran (THF), which was added after the products were collected, were used as an internal standard to calculate the enrichment of each carbon center observed by NMR. The procedure was as follows:

(i) Calculate (C at% THF/C at% X prod.) using GC;

(ii) Calculate (C at% THF/C at% X prod.) using NMR;

(iii) Divide (i) by (ii). If the result is equal to 1, it indicates that there was no enrichment; if the result is larger than 1, it indicates enrichment.

The magnitude of the experimental error was determined by calculating the enrichment of each carbon atom of the products collected during the non-enriched methanol injection experiment. The values obtained varied from 0.9 to 1.5. Based upon this reference analysis, a carbon was assumed to be enriched as a result of ^{13}C-enriched methanol injection when the enrichment factor was > 2. Table 4-3 shows the degree of enrichment of the oxygenated products collected during the ^{13}C-enriched methanol injection experiment. It is evident that the methanol had retained the ^{13}C label. The decrease of the enrichment factor for methanol and the other products upon increasing the reaction temperature from 245°C to 295°C is due to dilution of the ^{13}C-enriched methanol with native methanol synthesized over the catalyst. Calculation of the thermodynamic equilibrium constant based on the reaction conditions used and exit gas

Table 4-3

Carbon Labeling of the Products Formed During Injection of ^{13}C-Enriched Methanol into the Synthesis Gas Feedstream under Steady State Conditions as a Function of Reaction Temperature over the $CsOOCH/MoS_2$ - 20/80 wt% Catalyst. Reaction Conditions are given in Table 4-2.

	^{13}C ENRICHMENT OF CARBON ATOMS			
Temperature (°C)	245	265	285	295
CH_3OH	17.7	14.2	11.9	7.4
CH_3	11.6	12.0	10.7	7.5
CH_2OH	1.3	1.4	1.5	1.1
CH_3	9.8	9.1	9.6	6.6
CH_2	-	-	2.4	1.8
CH_2OH	-	-	1.5	0.7
CH_3	-	-	9.0	5.9
CH_2	-	-	-	-
CH_2	-	-	-	-
CH_2OH	-	-	-	-
CH_3	21.8	26.2	18.9	25.7
O				
HC=O	-	-	-	-
CH_3	12.6	15.9	9.8	9.7
O				
C=O	-	-	-	-
CH_3	-	6.3	5.2	5.0

composition indicated that no substantial methanol decomposition to CO and H_2 occurred, even at the highest temperature employed, 295°C (see Table 4-4). The calculated enrichment factors presented in Table 4-3 again clearly demonstrated that preferential enrichment of the terminal carbons of the C_2-C_4 alcohols and of the methyl group of the methyl esters occurred. This results suggests that C_1 species gives rise to the chain growth of C_2^+ alcohol synthesis and to the methyl group of the methyl esters is originated from methanol rather than from CO.

4.2.2 Injection of Native and ^{13}C-Enriched Methanol over the $K_2CO_3/Co/MoS_2$ Catalyst.

The effect of injecting methanol and ^{13}C-enriched methanol into the synthesis gas over the $K_2CO_3/(Co/MoS_2)$ = 10/90 wt% catalyst under steady state conditions was determined at different reaction temperatures by on-line GC and ^{13}C NMR analyses of the reaction products. A 2.0 g portion of powdered catalyst was centered in the reactor using an upper and lower glasswool bed to contain the catalyst. The reactor was pressurized to 81.6 atm with a H_2/CO = 0.96 synthesis gas. After a gas flow of 3535 ℓ(STP)/kg cat/h was set, the reactor was heated to the reaction temperature and methanol was injected continuously into the gas stream at the reactor inlet using a high pressure liquid pump. The methanol was enriched by a factor of 21.69 over the natural carbon-13 abundance of 1.11 at%. The ^{13}C-enriched methanol injection rate was 14.81 mmol/2.0 g cat/h (238.96 g

TABLE 4-4

Observed and Theoretical Equilibrium Constants K_{eq} of Methanol Formation During the ^{13}C-Enriched Pumping Experiment over the $CsOOCH/MoS_2$ = 20/80 wt% Catalyst at 295 °C, 81.6 atm, H_2/CO = 0.96, and GHSV = 7465 l(STP)/kg cat/h.

	Equilibrium Constant K_{eq}
Theoretical	4.078×10^{-4}
Observed	5.140×10^{-5}

K_{eq} is the equilibrium constant of the reaction $CO + H_2 = CH_3OH$ K_{eq} is related to the reaction equilibrium constant based on partial pressures of reactants (K_p) at a total pressure of one atmosphere through the fugacity ratios of the chemical reaction (K_ϕ)

$$K_{eq} = K_p/K_\phi$$

K_p is a function of temperature only, while K_ϕ is a function of both temperature and pressure. These P,T dependences of K_p and K_ϕ were taken from reference (Strelzoff,S., Chem. Eng. Prog. Symp. Ser. 66(98) (1970) 54) in the form

$$K_p = 3.27 \times 10^{-13} \exp(11687/T)$$
$$K_\phi = 1 - A_1 P$$
$$A_1 = 1.95 \times 10^{-4} \exp(1703/T)$$

The theoretical K_{eq} was obtained using above equations with total pressure P = 81.6 atm and T = 568 K. The experimental or observed K_{eq} was obtained calculating K_p from the partial pressure of CH_3OH, CO, and H_2 at the exit of the reactor, and K_ϕ from above equation.

methanol/kg cat/h).

Spectra of the liquid product collected during injections of non-enriched and ^{13}C-enriched methanol over the $K_2CO_3/Co/MoS_2$ catalyst for the reaction temperature of 300°C are shown in Figure 4-2. The degree of enrichment of each carbon center was calculated by combining GC and NMR analyses. The results are summarized in Table 4-5. It is once again clearly seen that the terminal carbon of ethanol was exclusively enriched, and that the methyl group of methyl acetate was preferentially enriched relative to the carbonyl group, which was not detected in sufficient quantities that would allow reliable ^{13}C enrichment factors to be calculated from the observed ^{13}C-NMR spectra. Propanol was composed of the two isotopic species $^{13}CH_3CH_2CH_2OH$ and $CH_3{}^{13}CH_2CH_2OH$. The presence of $^{13}CH_3{}^{13}CH_2CH_2OH$ which would have been indicated by doublets produced from carbon-carbon coupling, was not detected. It should be noted that the enrichment factors of the C-2 and C-3 carbons of propanol are approximately equivalent and lower than that obtained for C-2 carbon of ethanol. This result may indicate that propanol is produced from a symmetric intermediate derived from ethanol.

Scheme 4-1 shows a summary of the location of ^{13}C, as determined by ^{13}C NMR and mass spectrometry, in the products obtained over the Cs-doped MoS_2 and K-doped Co/MoS_2 catalysts.

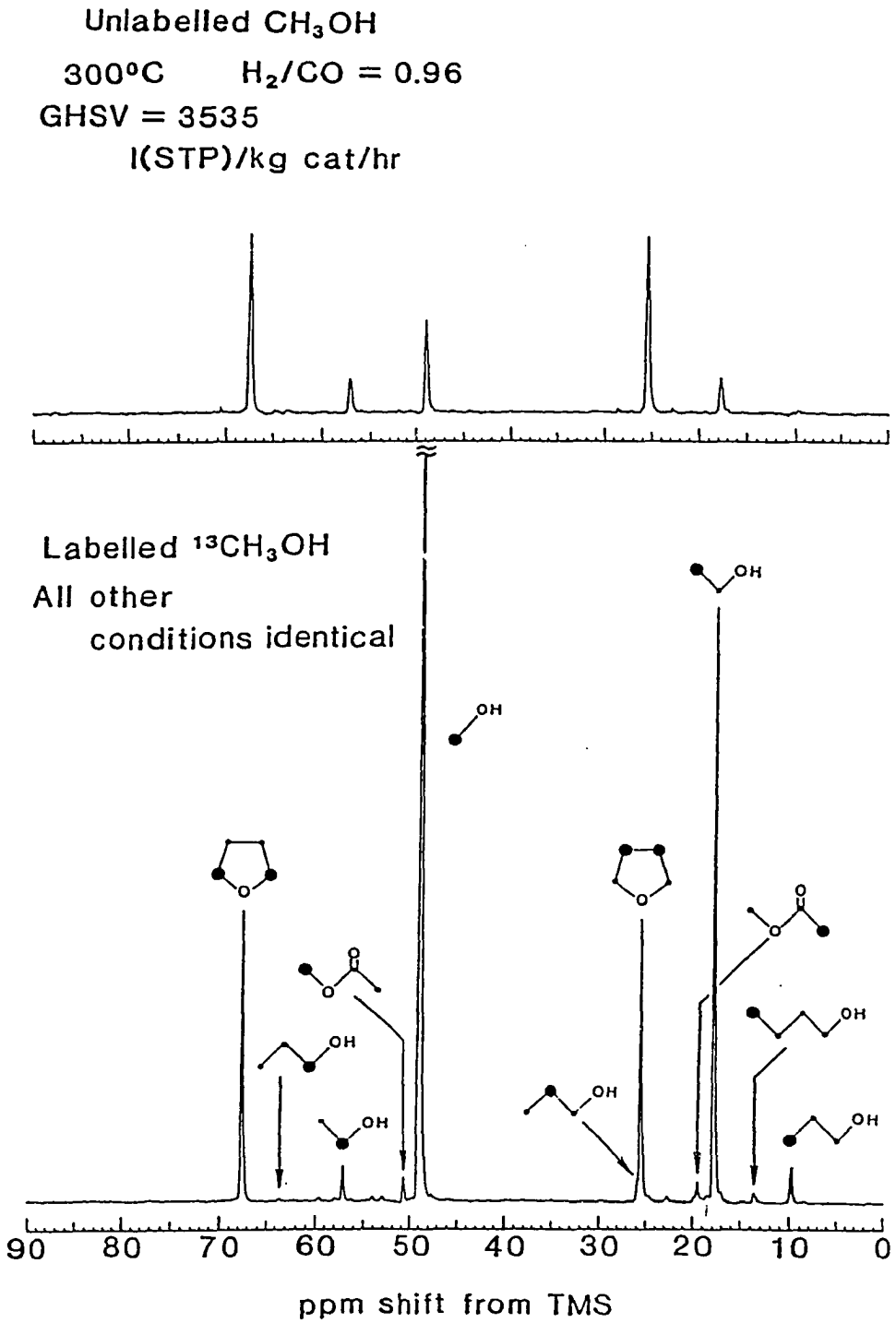

Figure 4-2 ^{13}C-NMR spectra of the liquid product obtained upon injection of native methanol and ^{13}C-enriched methanol into the synthesis gas feedstream over the $K_2CO_3/(Co/MoS_2)$ - 10/90 wt% catalyst at 300°C, 81.6 atm, H_2CO - 0.96, and GHSV - 3535 ℓ(STP)/kg cat/h. Methanol injection rate - 238.96 g methanol/kg cat/h, ^{13}C enrichment - 21.69.

Table 4-5

Carbon Labeling of the Products Formed During Injection of ^{13}C-Enriched Methanol into the Synthesis Gas Feedstream under Steady State Conditions as a Function of Reaction Temperature over the $K_2CO_3/(Co/MoS_2)$ - 10/90 wt% Catalyst. Reaction Conditions are given in Figure 4-2.

	^{13}C ENRICHMENT OF CARBON ATOMS			
Temperature (°C)	260	280	300	325
CH_3OH	27.5	26.9	22.2	12.5
CH_3	22.8	24.0	21.9	15.9
CH_2OH	1.0	1.2	1.3	1.8
CH_3	-	12.6	15.9	10.4
CH_2	-	10.9	13.5	11.3
CH_2OH	-	-	-	-
CH_3	17.8	23.4	12.2	8.7
O				
C=O	-	-	-	-
CH_3	10.6	14.6	9.1	-

ISOTOPIC SPECIES

(*CH_3OH INJECTED)

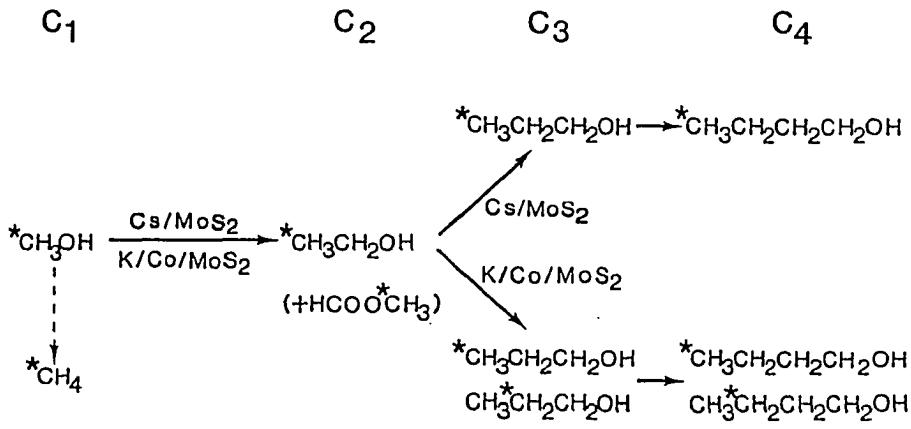

Scheme 4-1

4.3 DISCUSSION

4.3.1 Methanol Synthesis.

In order to discuss the mechanism of methanol synthesis over the alkali- doped MoS_2 catalyst, I shall briefly summarize some results obtained in Chapter 3.

(i) The presence of the alkali compound is indispensable for developing alcohol synthesis activity.

(ii) Promotional effect of Cs > K.

(iii) A maximum in methanol yield as a function of cesium was observed.

Result (i) indicates that the alkali compound promotes the formation of species intermediates that give rise to alcohols. Result (ii) is consistent with the results obtained on different catalytic systems, and has been explained in terms of the superior basicity of cesium counterions (6,10,56). Result (iii) is compatible with the concept of a bifunctional base-hydrogenation catalyst for methanol synthesis (118), where the basic component, in the present case Cs, activates CO and the hydrogenation component (MoS_2) activates H_2. The maximum in alcohol yield is obtained when the CO and H_2 activating components are balanced. Figure 4-3 shows a schematic representation of the methanol synthesis over the Cs/MoS_2 catalyst. The Cs^+ cation sitting on the edge plane of MoS_2 is to indicate that a close proximity of Cs^+ cations with the hydrogenation active site of MoS_2, which is thought to be an edge-like defect is required. The formate generated by the activation of CO by CsOH is subsequently hydrogenated

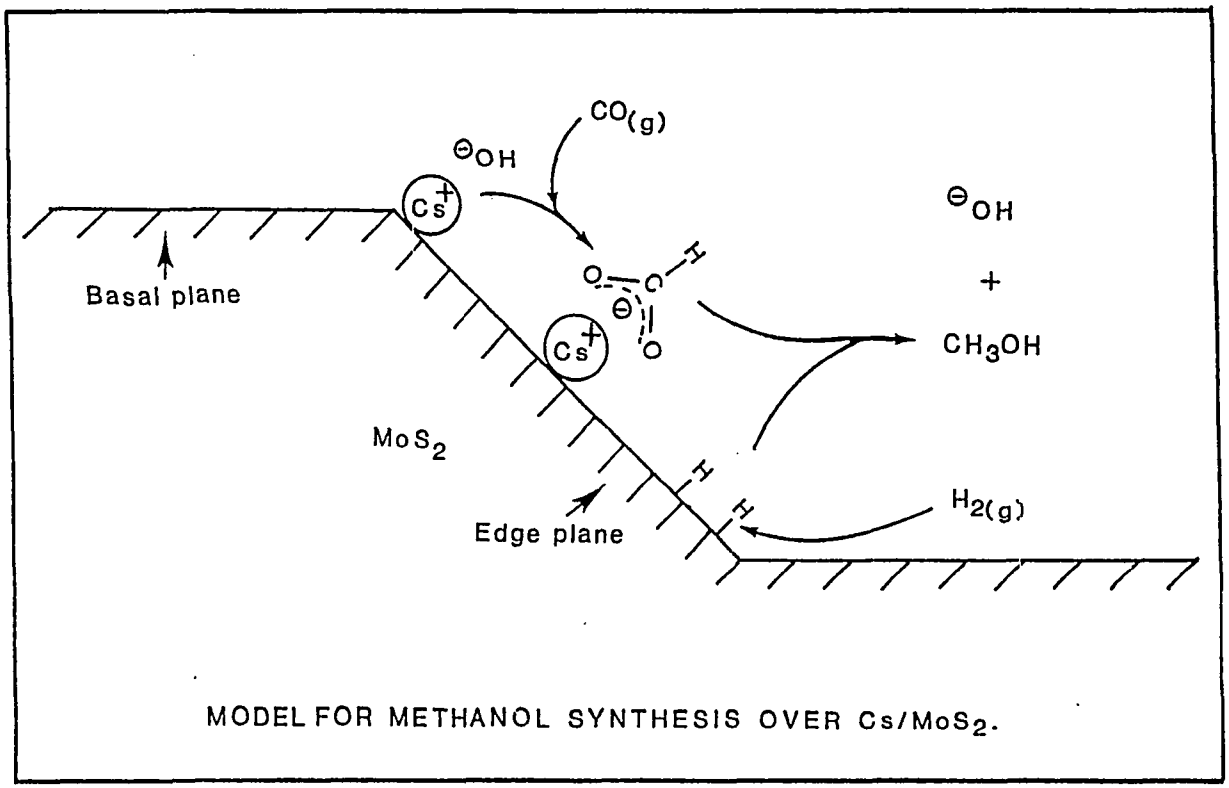

MODEL FOR METHANOL SYNTHESIS OVER Cs/MoS_2.

Figure 4-3 Schematic representation of the methanol synthesis over the Cs/MoS_2 catalyst.

to produce methanol.

4.3.2 Formation of C_2-C_4 Alcohols.

Numerous mechanisms have been proposed for the synthesis of alcohols over different catalytic systems. These mechanisms were discussed in Chapter 1, Section 1.5, and are summarized as follows:

(1) CO insertion mechanisms

  (1.1) insertion into the C-O bond of adsorbed alkoxides (6,10,22)

  (1.2) CO insertion into the M-C bond of adsorbed aldehydes (67)

  (1.3) CO insertion into the M-C bond of adsorbed alkyls (61-63)

(2) Enol condensation mechanism (68-71).

(3) Condensation of alcohols (72,73).

(4) Aldol condensation of aldehydes (56,74-76).

The results obtained from the reactions of isotopically labeled mixtures of $^{13}CH_3OH$ and $^{12}CO/H_2$ over the MoS_2-based catalysts indicated that the terminal carbon of ethanol was preferentially enriched with ^{13}C, $^{13}CH_3CH_2OH$. No enrichment of the oxygen containing carbon of ethanol was observed. This results suggests that methanol gives rise to active C_1 intermediates which react with CO to produce an ethanol precursor species. Although the intermediates cannot be identified by the present isotopic study, the results obtained in this study permit to propose a mechanism involving CO insertion into a methyl/intermediate bound to the surface for the formation of ethanol,

similar to the mechanism suggested by Pichler and Schulz (62), and exclude mechanisms that involve coupling of oxygenated intermediates, since these would give rise to a doubly ^{13}C-labeled ethanol molecule. Also excluded is the mechanism of CO insertion into adsorbed formaldehyde forming a symmetric glycolate that can be subsequently hydrogenated to ethanol as proposed recently by Mazanec (67). This mechanism would predict the ethanol to be composed of two isotopic species $^{13}CH_3CH_2OH$ and $CH_3{}^{13}CH_2OH$, due to the symmetry of the intermediate species, and this was not observed. The mechanism of CO insertion into the C-O of adsorbed alkoxides cannot be ruled out by the observed isotopic composition of ethanol. This mechanism, however, is less likely than the CO insertion into a methyl group, due to CO insertion into a carbon oxygen bond has a very high barrier and has not been known to occur over any system; another possibility within this mechanism would be the nucleophilic attack of CO by the methoxide anion with subsequent rearrangement of the intermediate species by methyl transfer that could lead to carbon-carbon bond formation, but, this mechanism was also ruled out, since its pathway has been reported to have a high activation energy (257 kJ/mol) (56). Therefore, the most feasible mechanism that would account for the observed isotopic composition of ethanol ($^{13}CH_3CH_2OH$) is the CO insertion into a methyl bound to the catalyst surface.

The mechanism of carbon chain growth to form C_3 and C_4 alcohols over the cesium-doped MoS_2 is similar to the one proposed for ethanol formation, i.e. through CO insertion into an alkyl-surface bond.

Scheme 4-2 illustrates the reaction pathway of alcohol formation that accounts for the observed isotopic product distribution. Scheme 4-2 is discussed in Section 4.3.2 along with the mechanism of hydrocarbons formation.

An interesting result is that over the K-doped cobalt molybdenum disulfide catalyst the mechanism of formation of C_3 and C_4 alcohols is different than that obtained over the Cs-doped molybdenum disulfide. This is indicated by the fact that over the cobalt-containing catalyst propanol was composed of two isotopic species; $^{13}CH_3CH_2CH_2OH$ and $CH_3{}^{13}CH_2CH_2OH$. The lower enrichment values of C-2 and C-3 carbons of propanol relative to ethanol and the approximate equivalence of the two carbons suggest that adsorbed symmetric C_2 species give rise to propanol. Species of the type " π-bonded ethylene" or "σ-di-bonded ethylene" have been suggested in homogeneously catalyzed reactions (122), and they are likely to exist on the surface of the catalyst, since olefins (C_2,C_3) were detected in appreciable amounts among the products. Thus, symmetric C_2 species are proposed to react with CO to form an acyl group that is subsequently hydrogenated to produce propanol according to the Scheme 4-3.

It is interesting to point out that Burns (123) studied the reaction of ^{14}C-labeled CH_3OH with CO and H_2 catalyzed by dicobalt octacarbonyl $[Co(CO)_4]_2$, and found the same isotopic composition for propanol ($^{14}CH_3CH_2CH_2OH$ and $CH_3{}^{14}CH_2CH_2OH$) as we did in the present study. Therefore, one can conclude that the intermediate species involved in both homogeneous and heterogeneous systems are identical.

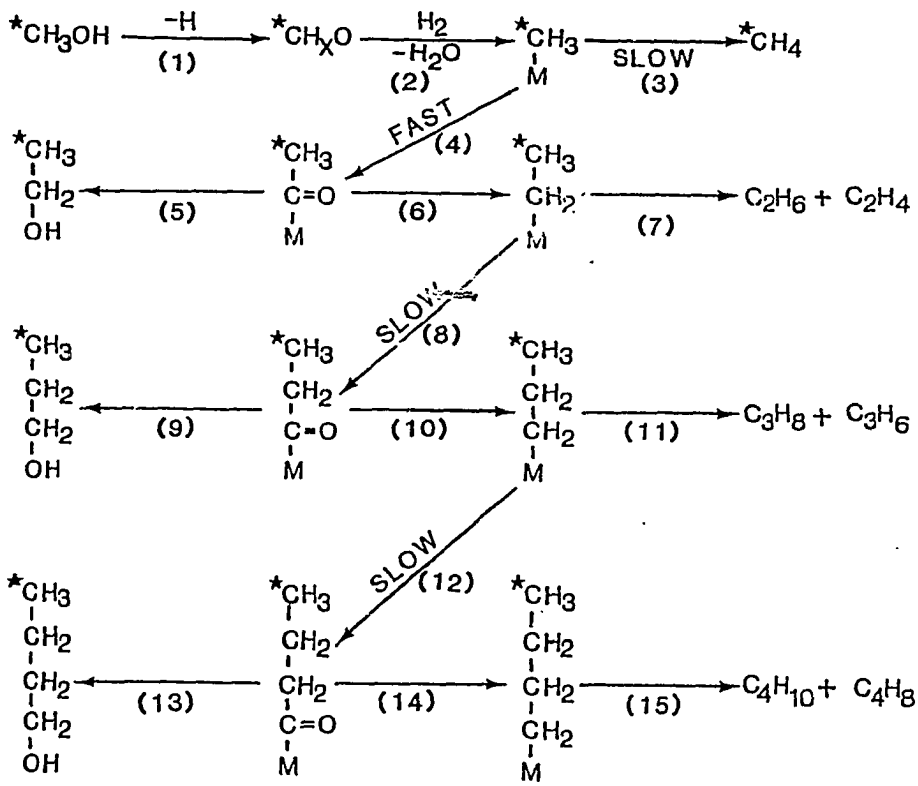

Scheme 4-2

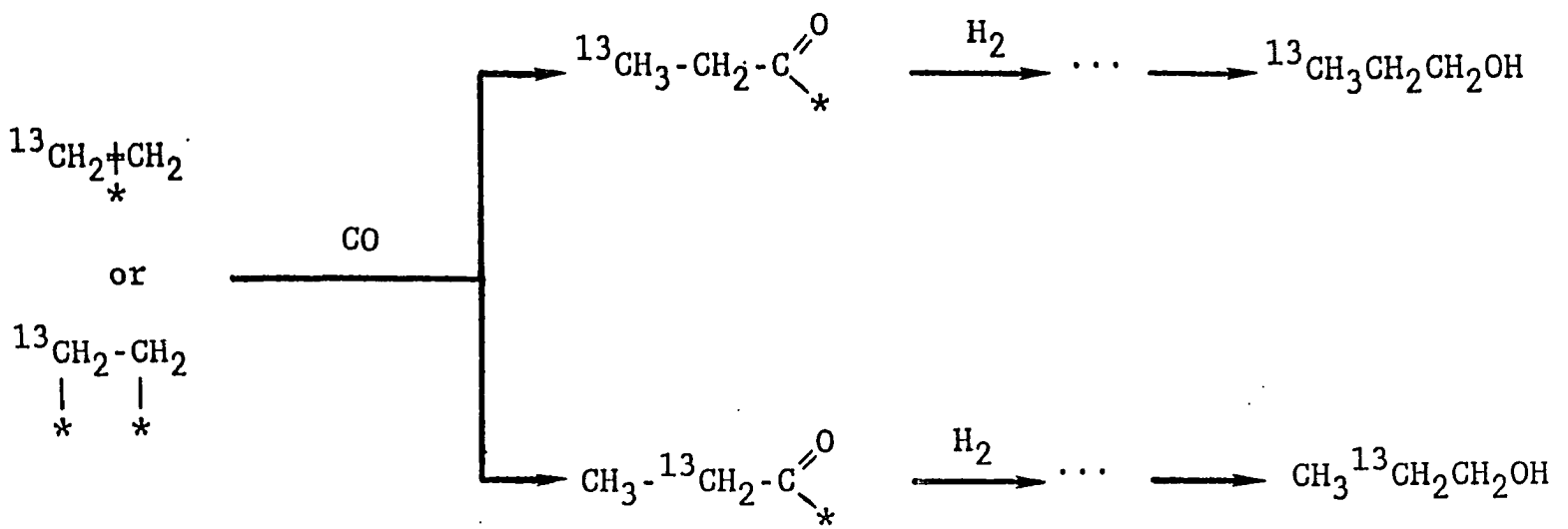

Scheme 4-3

4.3.3 Formation of Hydrocarbons

Several mechanisms have been postulated to account for the formation of hydrocarbons and alcohols from carbon monoxide and hydrogen over Fischer-Tropsch catalysts. The great variety of chemisorbed intermediates that have been observed and/or assumed over different catalytic systems indicates that the reaction mechanism of hydrocarbon formation may not be identical for different catalysts. Broadly speaking, the mechanisms of hydrocarbon formation reported in the literature can be divided into two categories; 1) those that propose oxygenated intermediates as precursors of hydrocarbons (57,62,63) and 2) those that suggest that hydrocarbons are formed through nonoxygenated intermediates (125-128).

Hou and Wise (129) studied the hydrogenation of CO to produce methane over undoped MoS_2 at atmospheric pressure, and based on isotopic studies concluded that the mechanism of methane synthesis involved dissociative chemisorption of carbon monoxide and hydrogen, i.e. methane was formed through nonoxygenated intermediates. In the present study, it was observed that the formation of methane over the alkali-doped MoS_2 catalyst under alcohol synthesis conditions is through oxygenated intermediates. The high enrichment of ^{13}C in methane synthesized from $^{13}CH_3OH$ and CO/H_2 (see Table (4-2) suggested that methane was a secondary product that was formed from an alkyl moiety generated from a C_1-oxygenated precursor. Furthermore, as shown in Table 4-1, the rate of methane formation was considerably

increased during the methanol pumping experiments. Another indication that the hydrocarbons were produced by secondary reactions involving alcohols was obtained from space velocity studies (see Chapter 3, Section 3.2.4). The formation of hydrocarbons through oxygenated intermediates was also reported to occur over the alkali-doped rhodium catalysts by Kagami et al. (130).

Scheme 4-2 illustrates the reaction pathway for the formation of linear alcohols and hydrocarbons over the MoS_2-based catalysts. The reductive adsorption of methanol on the catalyst surface is the first step of Scheme 4-2. The next step (2) is the oxidative addition of H_2 to the oxygenated intermediate followed by the reductive elimination of H_2O to give rise to a methyl group, perhaps bounded to a coordinatively unsaturated edge Mo cation. Methyl species can undergo two alternative reactions: (i) hydrogenation to produce methane (step (3)), and (ii) CO insertion to produce an acyl group (step (4)). Apparently, step (3) is suppresed partially by the presence of the alkali compound, which reduces the availability of active hydrogen, while step (4) is favored by alkali metals. The promotional effect of alkali metals on CO insertion reactions has been shown to occur in organometallic chemistry (82-85). Colleman et al. (84,85) reported that the close interaction of an alkali cation with a carbonyl ligand of the alkyliron carbonyl $Na^+(RFe(CO)_4)^-$ greatly favors the migratory insertion of the CO ligand into the metal alkyl bond:

$$Na \ldots OC\text{-}Fe(CO)_3R \text{ -----> } R - \overset{\overset{Na^+}{|}}{\underset{|}{\overset{O^-}{C}}} - Fe(CO)_3 \qquad [4.1]$$

This interaction between the alkali cation and the oxygen of a carbonyl group has been reported to give rise to a lowering of the energy of the lowest unoccupied molecular orbital (LUMO) of the carbonyl group (86), this would facilitate the insertion reaction (82).

The acyl group obtained from CO insertion into a methyl group can undergo two alternative reactions: (i) hydrogenation to produce ethanol (step (5)) and (ii) hydrogenation with subsequent dehydration to produce an ethyl group. This ethyl group can either add CO to form the next acyl and thus contribute to the chain propagation (step (8)) or, by β-H transfer, give ethylene or be hydrogenated to give ethane (step (7)).

The hydrogenation of the acyl group to produce ethanol is suggested to proceed in two steps, with an intermediate aldehyde bounded to molybdenum , according to reaction:

$$\begin{array}{l} CH_3 \\ | \\ C - O \\ | \\ * \end{array} \xrightarrow{H} H - \begin{array}{l} CH_3 \\ | \\ C \\ * \end{array} + O \xrightarrow{H_2} CH_3CH_2OH + * \qquad [4.2]$$

acetaldehyde has been found among the products in small quantities.

4.3.4 Formation of Methyl Esters

4.3.4.1 Formation of Methyl Formate

The different mechanisms that might give rise to methyl formate during hydrogenation of CO under alcohol synthesis conditions have been recently discussed in detail along with their thermodynamic features by Nunan et al. (56). These reaction pathways are summarized as follows:

1) Direct carbonylation of methanol

$$CH_3OH + CO \rightarrow HCOOCH_3 \qquad [4.3]$$

2) Dehydrogenative coupling of methanol

$$2CH_3OH \rightarrow HCOOCH_3 + 2H_2 \qquad [4.4]$$

3) Formaldehyde dimerization (Tischenko reaction)

$$2HCHO \rightarrow HCOOCH_3 \qquad [4.5]$$

4) Esterification of formic acid with methanol

$$HCOOH + CH_3OH \rightarrow HCOOCH_3 + H_2O \qquad [4.6]$$

The experimental results of this study (see Tables 4-3 and 4-5) show that the methyl group of methyl formate was selectively enriched by the ^{13}C from the injected $^{13}CH_3OH$, while the carbonyl group showed no enrichment. This result strongly suggests that CO was inserted into an intermediate, such as methoxy anion, derived from the labeled methanol. This reaction pathway is consistent with Reaction [4.3]. Thus, Reactions [4.4] and [4.5] are ruled out based on the isotopic composition observed for the methyl formate. Reaction [4.4] would

predict enrichment of both carbon atoms of methyl formate and Reaction [4.5] would predict no enrichment, if formaldehyde is produced from CO/H_2, or both carbon atoms enriched, if formaldehyde is formed from methanol, contrary to the experimental result, i.e. $HCOO^{13}CH_3$. Reaction [4.6] cannot be ruled out by the observed isotopic composition, since as discussed by Nunan and co-workers (56), who observed the same isotopic composition of methyl formate from labeled methanol and unlabeled CO experiments over Cs/Cu/ZnO, the esterification of an adsorbed formate by methanol

$$HCOO^{\ominus} + CH_3OH \rightarrow HCOOCH_3 + {}^{\ominus}OH \qquad [4.7]$$

coupled with a rapid regeneration of the formate

$$CO + {}^{\ominus}OH \rightarrow HCOO^{\ominus} \qquad [4.8]$$

gives the overall stoichiometry of Reaction [6] and would produce the observed isotopic composition of methyl formate ($HCOO^{13}CH_3$) from the reactant mixture labeled $^{13}CH_3OH$ and CO/H_2. Nunan and co-workers, however, concluded that this path is less likely than Reaction [4.3] due to steric hindrance in Reaction [4.7].

It is important to mention that the yield of methyl formate was considerably increased upon injection of methanol. As shown in Table 4-1, this increase was more dramatic at low temperature reaction where methyl formate is likely to be far from thermodynamic equilibrium (131).

Scheme 4-4 illustrates the suggested mechanism of methyl formate

formation over the alkali-doped MoS_2 catalyst.

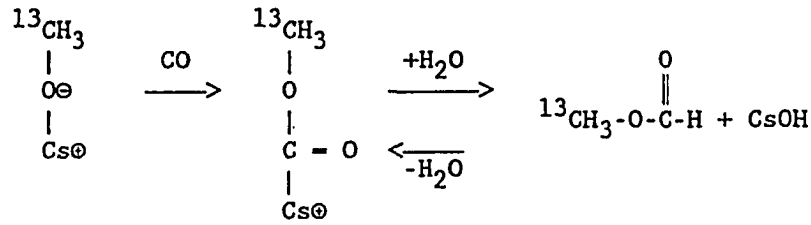

Scheme 4-4

The CO insertion into a methoxy species has been proposed in the homogeneous carbonylation of methanol catalyzed by sodium methoxide (132) and recently suggested to occur over the Cs/Cu/ZnO catalyst (56). Theoretical investigations performed by Klier et al. (116) using the MNDO method for electronic energy calculations and the McIver-Komornicki-Powell sigma method for geometry optimization of the transition state showed that there was no activation barrier for the nucleophilic attack of CO by the methoxide anion, (Equation [4.9]), and that the reaction is strongly exothermic.

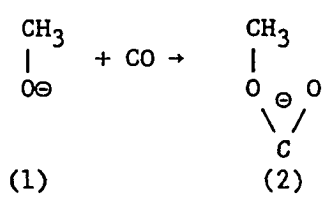

[4.9]

Klier and co-workers mentioned that the rearrangement of the intermediate species by methyl transfer that could lead to carbon-carbon bond formation, Equation [4.10], is unfavorable due to a high activation energy (257 kJ/mol) despite the reaction being exothermic

overall, see Figure 4-4. Instead, the authors mentioned that a more

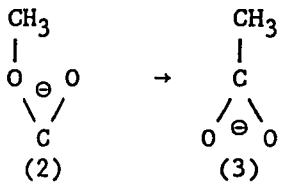

(2) (3) [4.10]

hydrolytic pathway, Equation [4.11], gives rise to the formation of methyl formate rather than the acetate ion, Equation [4.9].

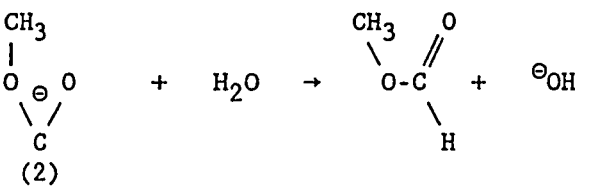

(2) [4.11]

4.3.4.2 Formation of Methyl Acetate

Two mechanisms leading to the formation of esters during alcohol synthesis conditions have been proposed: i) a Cannizzaro type condensation of two aldehydes (72) and ii) reaction of surface methoxide with aldehydic species, Tischenko reaction, (10,133). The isotopic distribution obtained for methyl acetate from the labeled $^{13}CH_3OH$ and CO/H_2 (see Tables 4-3 and 4-5) accounts for these two mechanisms. Scheme 4-5 illustrates the reaction pathway for the formation of methyl acetate through the Tischenko reaction that leads to the observed isotopic distribution.

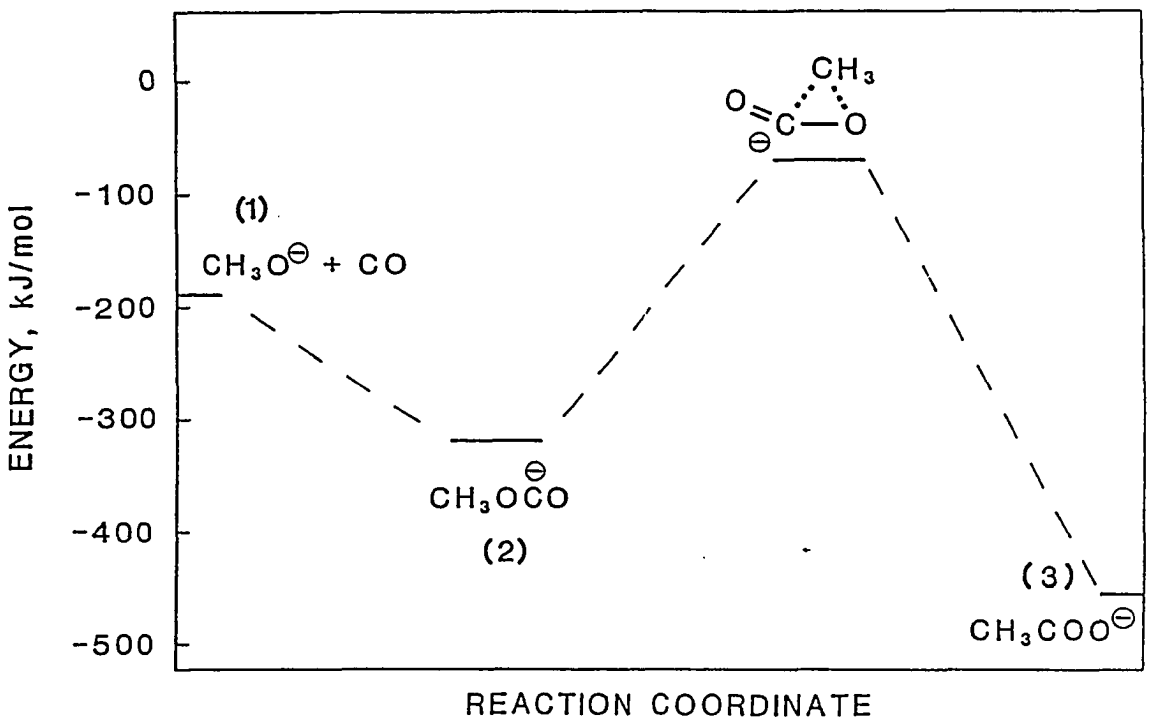

Figure 4-4 MNDO energy diagram for the reaction of carbon monoxide with methoxide to form methyl formate (from Reference 56).

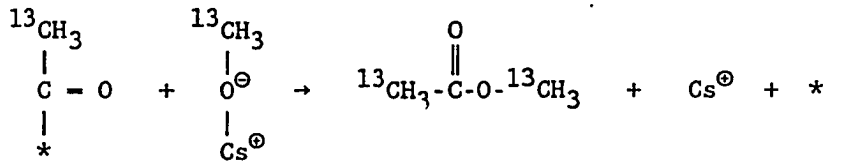

Scheme 4-5

The methoxy anion species are expected to be present on the surface of the catalyst. It has been reported that alcohols such as methanol readily react with basic surface sites to give adsorbed methoxides (134-136). In the present case, those basic sites are presented by the cesium surface cations. The acyl species are also expected to be present on the catalyst surface, and they may be produced from the CO insertion into adsorbed methyl groups.

Chapter 5

CHARACTERIZATION STUDIES ON Cs/MoS_2 CATALYSTS

5.1 Introduction

The purpose of these studies is to characterize the Cs/MoS_2 catalysts in terms of alkali distribution, chemical state of the catalyst surface, and structural features of their components. The structural features of interest include bulk and surface atomic arrangements and particle morphology. The ultimate aim of this or any catalyst characterization study is to identify the structure of the active sites that influence the activity and selectivity of the process. Knowledge of the nature of the active sites provides for the catalyst to be optimized in terms of stability and activity and control of the selectivity to a desired product.

Up until about a decade ago, kinetic studies were used extensively to interpret the nature of catalytic activity. The results were often contradictory and confusing, and they are summarized by Satterfield (137), when he describes the characteristic feelings of the typical scientist when he first encounters the world of the heterogeneous catalyst: "... his first impression ... is apt to be that of a vast and confusing field, replete with an enormous quantity of perhaps significant but empirical facts, interspersed with perhaps useful theories."

Currently, the feelings expressed by Satterfield are being

dispelled, thanks in part to the application of characterization techniques that have brought the catalysis field into a new dimension and have provided insight into the nature of the active surface of many catalytic svstems.

In this chapter, I shall discuss the results of the characterization studies obtained with the Cs/MoS_2 catalysts using various analytical techniques, such as X-ray photoelectron spectroscopy (XPS), X-ray diffraction (XRD), scanning transmission electron microscopy (STEM), and BET surface area measurements.

5.1 Surface Area Measurement

5.1.1 Experimental

The surface area of the fresh Cs/MoS_2 catalysts was determined using the conventional multi-point BET method (138). The measurements were performed in a Digisorb 2500 instrument using helium to calibrate the dead volume and nitrogen as the adsorbate. Prior to the analysis, the samples were evacuated overnight to approximately 10^{-4} torr and then outgassed for two hours at 110°C. The vacuum system for the sample preparation (degas) was separated from the vacuum system for the analysis. Both the volume and the surface area measurements were done with the sample vessel at liquid nitrogen temperature.

5.1.2 Results and Discussion

The results of the BET surface area measurements of the undoped

MoS_2 and cesium-doped MoS_2 catalysts are presented in Table 5-1. The preparation of MoS_2 and the cesium-doping procedure are described in detail in Chapter 2, Section 2.1. It is apparent from Table 5-1 that cesium doping caused a dramatic decrease of the surface area of MoS_2. This reduction of the surface area was a function of the doping level of CsOOCH. The larger the concentration of CsOOCH in the catalyst the lower the surface area. This effect was reported to occur over the potassium-doped MoS_2 (139) and also in a variety of oxide systems such as: MgO, SiO_2, Al_2O_3 and Cr_2O_3 (140).

The appreciable loss of MoS_2 surface area is proposed to be due to pore blockage by the cesium compound, rather than by an increase of the MoS_2 particle size. XRD and STEM studies indicated that the morphology and size of MoS_2 particles did not change upon cesium doping. Testing of the Cs/MoS_2 catalysts under alcohol synthesis conditions led to a slight drop in surface areas as shown in Figure 5-1.

5.2 X-Ray Diffraction (XRD)

5.2.1 Experimental

Powder diffraction patterns for the undoped and cesium-doped MoS_2 catalysts were obtained with a Philips Diffractometer consisting of a XRG 3100 x-ray generator coupled with an APO 3600 control unit using CuKα radiation. Scans were conducted with a step size of 0.02° in 2θ and a scan rate of 1.0°/min.

XRD was used for phase identification and for detecting possible

TABLE 5-1

Surface Areas of the Fresh Undoped and Cesium-Doped MoS_2 Catalysts

MoS_2 Catalysts CsOOCH Mol%	Surface Area (m^2/g)
0	63
2.25	42
4.77	27
9.10	17
18.36	13
23.07	10
27.83	11

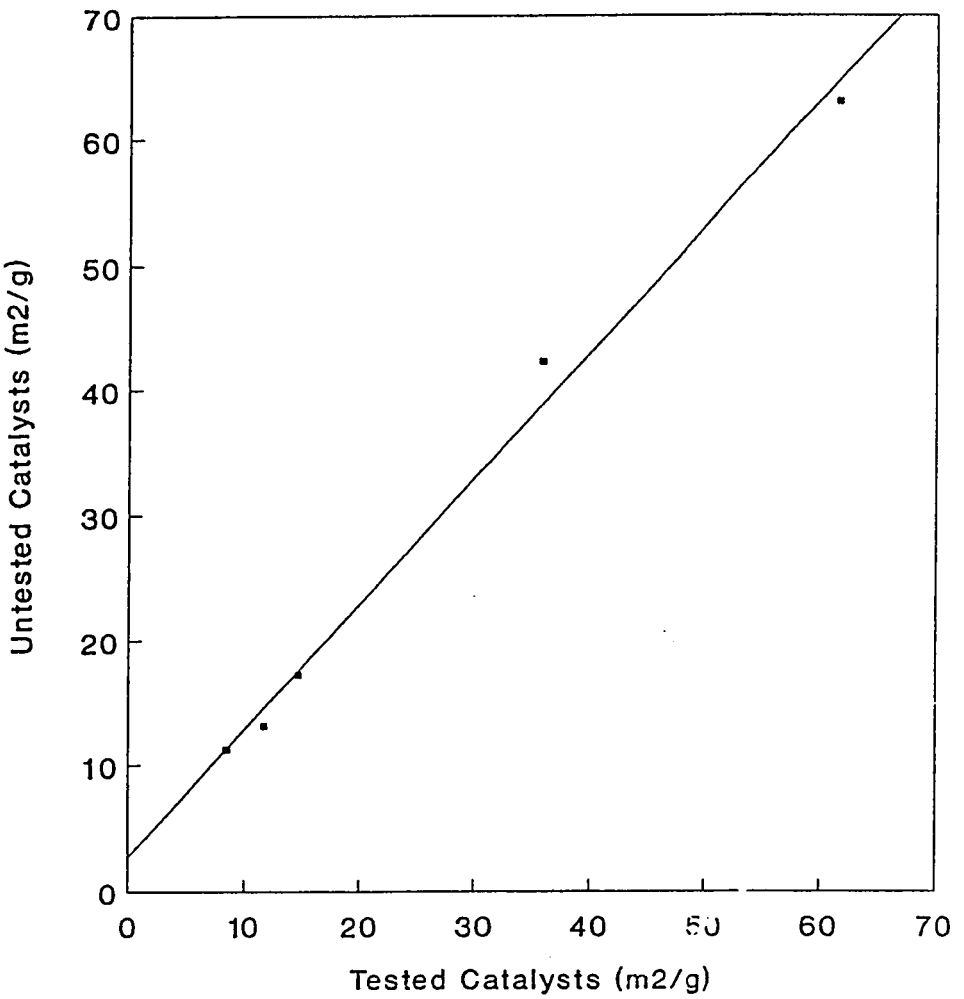

Figure 5-1 Relationship between the surface areas of fresh and tested Cs-doped MoS_2 catalysts.

lattice parameter changes. One has to bear in mind that the determination of MoS_2 particle size by line broadening analysis has to be taken with care since random stacking and folding of the MoS_2 layers also produce line broadening.

Air sensitive samples, tested catalysts, were loaded into an air-tight sample holder under dry nitrogen. The sample holder, shown in Figure 5-2, was equipped with mylar film for x-ray penetration. The mylar film, 3.6 μ thick, was attached to the sample holder using double stick tape.

5.2.2 Results and Discussion

Figure 5-3 shows a typical XRD spectrum of MoS_2 obtained from thermal decomposition of MoS_3. The X-ray powder diffraction pattern of MoS_2 presented in Figure 5-3 is characteristic of poorly crystalline hexagonal MoS_2 ($P6_3/MMC$, ASTM card number 6-0097), which has been discussed in detail in the literature (141-144). The (002) peak is one of the most intense. This indicates some stacking of the layers along the c axis. The number of stacked layers cannot be obtained from standard line broadening analysis due to the presence of stacking faults that produce additional line broadening. The stacking faults are evidenced by the asymmetric shape of the (100) peak (indicated in Figure 5-3) (143-145). Chianelli et al. (143) indicated that the strong intensity of the (103) diffraction line suggests that the two-layer molybdenite stacking sequence is maintained for at least two stacks. The number of stacked layers as well as the a-axis

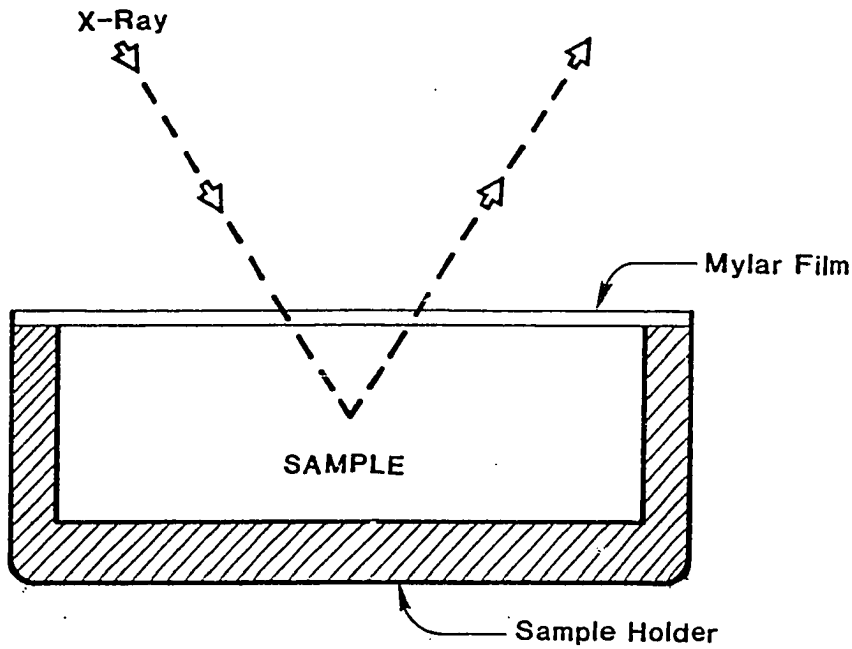

Figure 5-2 X-Ray diffraction sample holder for air sensitive samples.

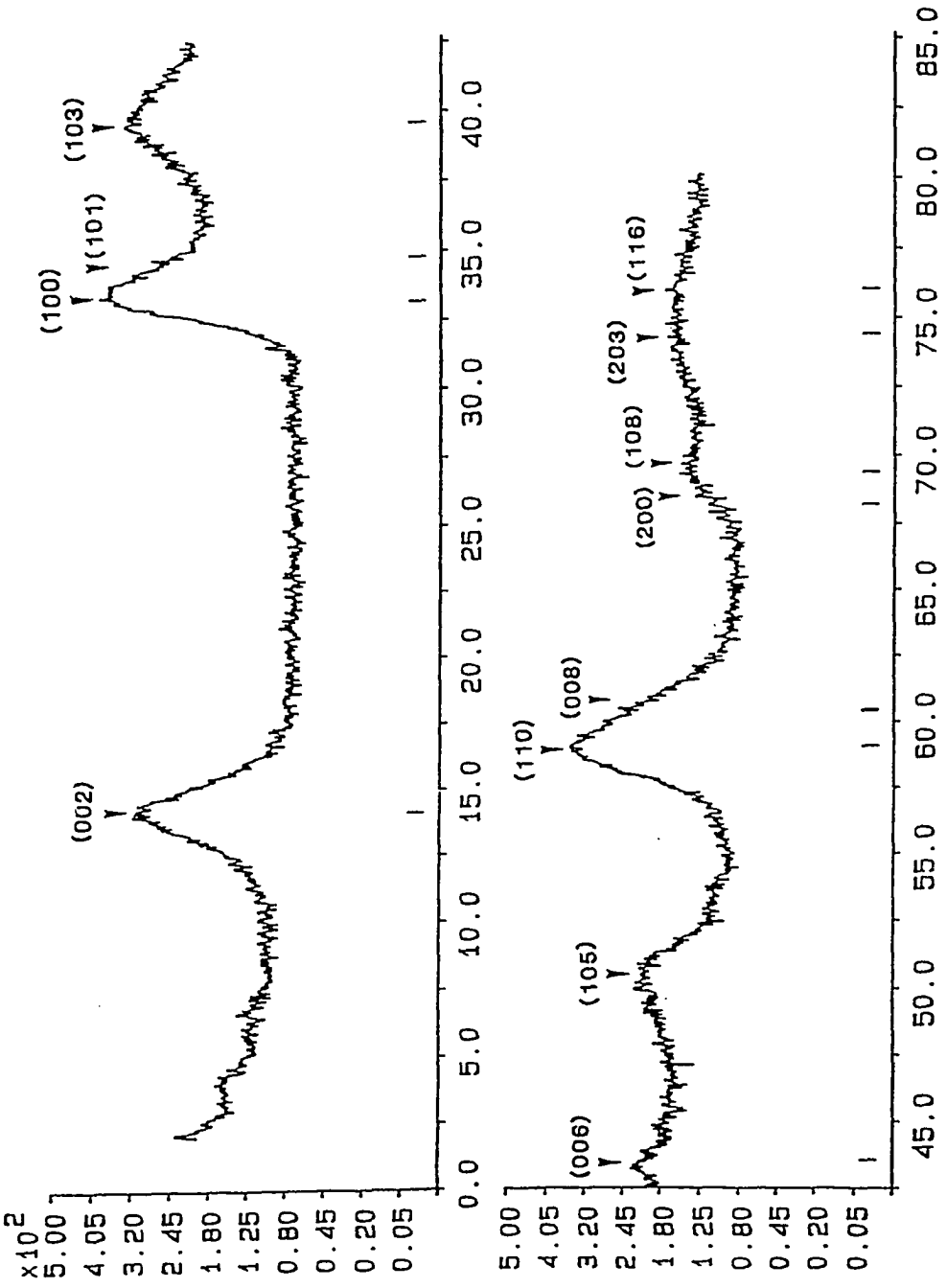

Figure 5-3 X-Ray Powder Diffraction Pattern of MoS_2 Obtained by Thermal Decomposition of MoS_3.

dimensions are determined later in Section 5.3.2 using high resolution transmission electron microscopy, since it is not possible to accurately extract the particle size dimensions by X-ray diffraction line broadening analysis because of random stacking and folding of layers in the MoS_2 structure.

Figure 5-4 illustrates the XRD patterns of the fresh CsOOCH/MoS_2 catalysts. The XRD spectra A, B, and C of the catalysts containing 2.5, 5.3, and 10.0 wt% CsOOCH, respectively, are very similar to the spectrum of pure MoS_2. The only difference is the very broad and weak peak, characteristic of an amorphous phase, beginning about 20° and continuing out to approximately 30°. This feature is easily observed in the 9.1 mol% Cs catalyst, spectrum C. In addition to the hexagonal MoS_2 phase and the broad weak peak, XRD spectra D, E, and F of the catalysts containing 20.0, 25.0 and 30.0 wt% CsOOCH, respectively, contain two well defined peaks at approximately 26.8° and 28.1° that correspond to d-spacings of 3.31 and 3.16 Å. These d-spacings match those obtained from the spectrum of pure CsOOCH. A third small peak was observed in spectra D, E, and F at 2θ = 24° (d-spacing = 3.70 Å). This small peak could not be accounted for by the CsOOCH phase, but rather was found to correspond to the Cs_2CO_3 phase (see Table 5-2).

It is interesting to point out that the MoS_2 diffraction lines did not change upon addition of CsOOCH. Thus, the decrease in surface area as a consequence of the addition of CsOOCH cannot be attributed to an increase in the MoS_2 particle size.

XRD patterns obtained for the tested Cs/MoS_2 catalysts indicated

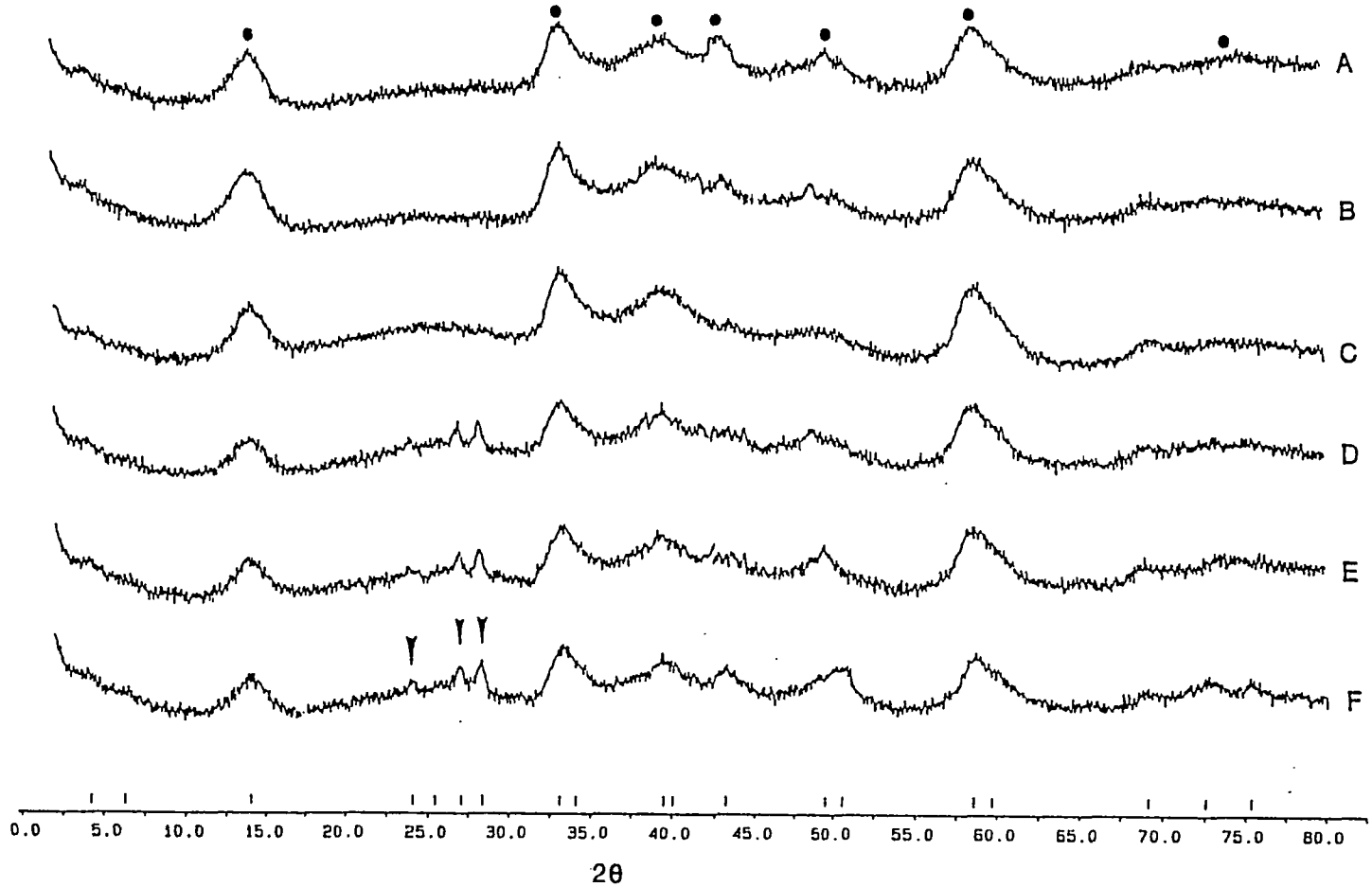

Figure 5-4 X-Ray Powder Diffraction Patterns of the Fresh $CsOOCH/MoS_2$ Catalysts. Patterns A, B, C, D, E, and F Correspond to Catalysts Containing 2.25, 4.77, 9.09, 18.36, 23.07, and 27.83 mol% CsOOCH, respectively. The Solid Dots Indicate Diffraction Peaks for the MoS_2 Phase and the Arrowheads Indicate Diffraction Peaks Assigned to the Cesium Compound.

TABLE 5-2

X-Ray Powder Diffraction Data for CsOOCH and Cs_2CO_3[a]

CsOOCH		Cs_2CO_3	
d(Å)	(I/I_o)	d(Å)	(I/I_o)
2.15	(9)	2.13	(2)
2.16	(6)	2.23	(7)
2.19	(15)	2.27	(6)
2.23	(41)	2.36	(3)
2.24	(36)	2.45	(2)
2.31	(3)	2.62	(3)
2.38	(4)	2.65	(3)
2.47	(2)	2.71	(18)
2.61	(3)	2.79	(4)
2.74	(19)	2.86	(24)
2.84	(8)	2.95	(1)
2.88	(69)	3.27	(23)
3.01	(12)	3.41	(100)
3.03	(13)	3.70	(19)
3.12	(25)	4.16	(18)
3.21	(34)	6.80	(5)
3.32	(80)		
3.42	(100)		
3.65	(26)		
3.82	(16)		
3.85	(14)		
3.89	(10)		
4.31	(26)		
5.34	(4)		
6.63	(51)		

[a] $CsOOCH \cdot xH_2O$ (99.9%) obtained from alfa products.
Cs_2CO_3 (99.995%) obtained from Aldrich Chemical Company.

that no changes in the structure of MoS_2 occurred. The broad weak peak observed for the fresh Cs/MoS_2 catalysts in the range between 20° to 30° tended to vanish upon testing of the catalysts. This is clearly demonstrated by comparing spectrum A in Figure 5-5, corresponding to the tested 10.0 wt% $CsOOCH/MoS_2$ catalyst, to spectrum C in Figure 5-4, which corresponds to the fresh 10.0 wt% $CsOOCH/MoS_2$ catalyst. XRD powder pattern B in Figure 5-5 was obtained from the tested 25.0 wt% $CsOOCH/MoS_2$ catalyst. In this pattern, in addition to the MoS_2 diffraction lines, indicated by dots, two small lines at 2θ = 26.8° and 28.1°, corresponding to d-spacings of 3.31 and 3.16 Å, respectively, were also observed. These d-spacings were also obtained with the fresh Cs/MoS_2 catalysts (see patterns D, E, and F in Figure 5-4) and were found to match those obtained from the diffraction pattern of pure CsOOCH (see Table 5-2). No lines related to the Cs_2CO_3 phase were observed in the tested catalysts.

An important observation made during the present XRD study of the Cs/MoS_2 catalysts was that the surface CsOOCH compound underwent dramatic changes after the catalysts were exposed to air for long periods of time. Figure 5-6 shows the XRD patterns of the Cs/MoS_2 catalysts after they were exposed to atmospheric conditions for weeks. From these diffraction patterns, it is apparent that agglomeration and crystallization of the CsOOCH compound took place. In addition, some of the new diffraction lines were found to match those of Cs_2CO_3, as indicated in Table 5-3. Therefore, it is essential to keep the Cs/Mos_2 catalysts protected from prolonged air exposure since this can

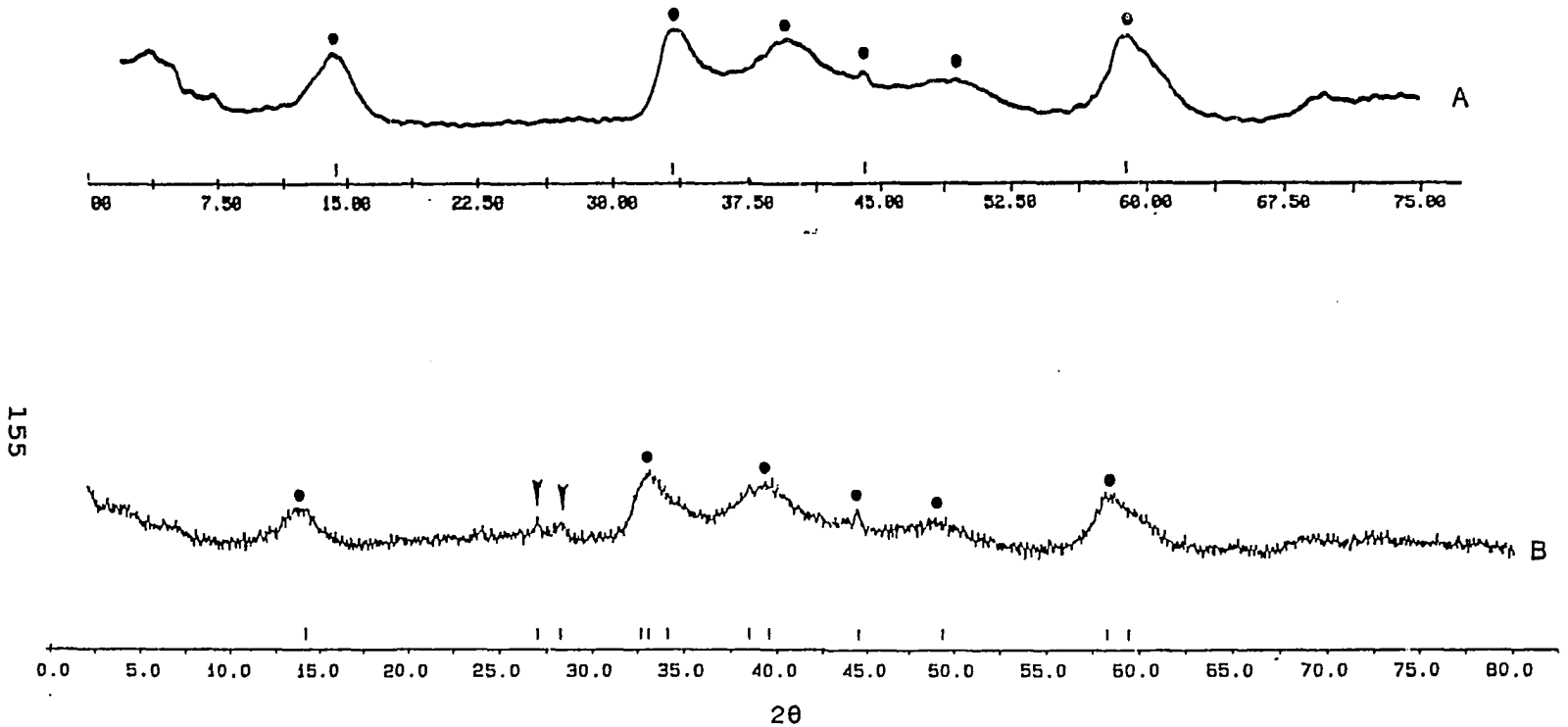

Figure 5-5 X-Ray Powder Diffraction Patterns of the Tested (A) 9.09 mol% $CsOOCH/MoS_2$ and (B) 23.07 mol% Catalysts. The Solid Dots Indicate Diffraction Peaks for the MoS_2 Phase and the Arrowheads Indicate Diffraction Peaks Assigned to the Cesium Compound.

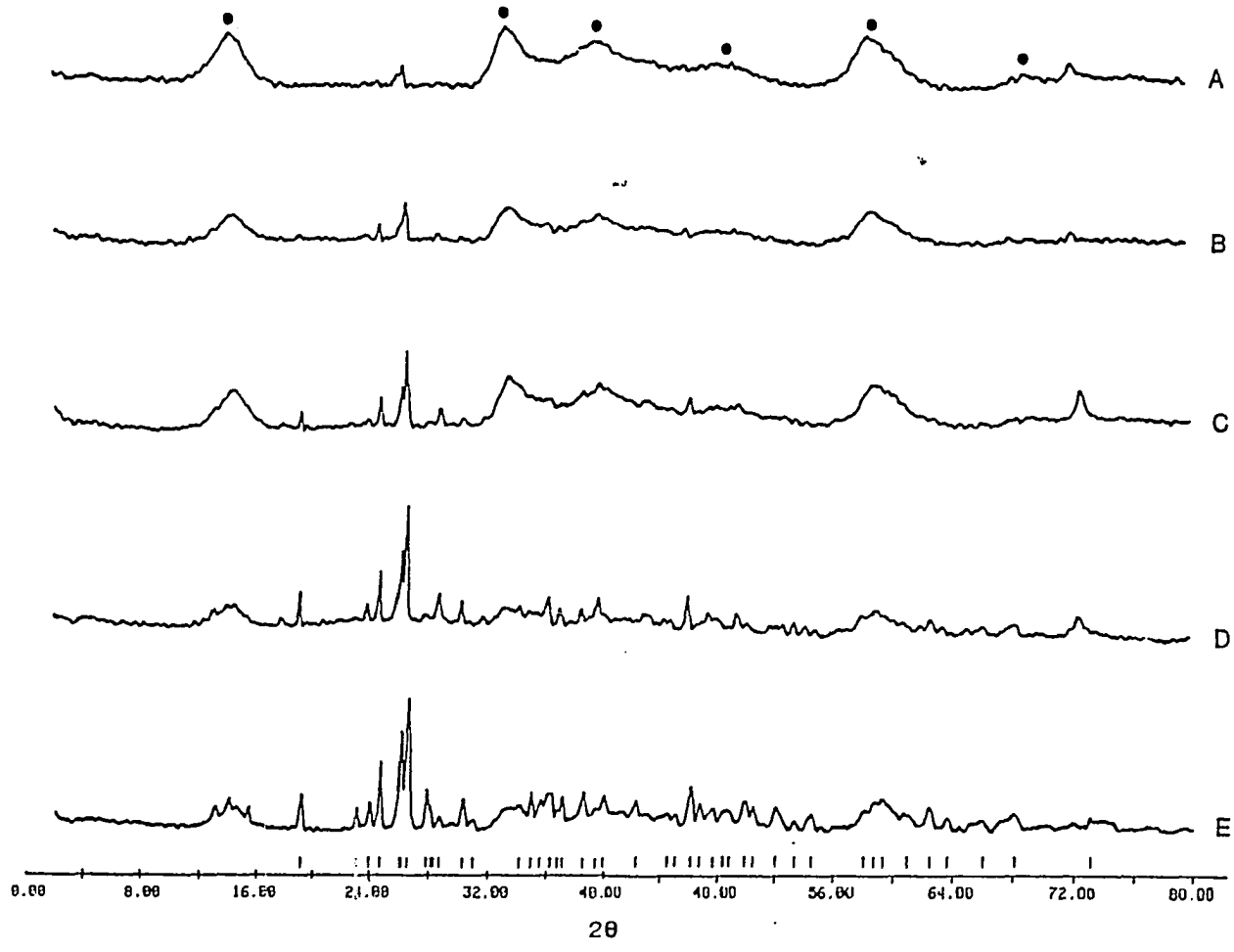

Figure 5-6 X-Ray Powder Diffraction Patterns of CsOOCH/MoS_2 Catalysts Exposed to Air for Long Periods of Time. Patterns A, B, C, D, and E Correspond to Catalysts Containing 2.25, 4.77, 9.09, 18.36, and 23.07 mol% CsOOCH, respectively.

TABLE 5-3

X-Ray Powder Diffraction Data for the 25.0 wt% $CsOOCH/MoS_2$ Catalyst Obtained after Long Exposure to Ambient Atmospheric Conditions (Figure 5-6, Spectrum E)[a]. Diffraction Lines of MoS_2 Phase are not Listed.

d(Å)	(I/I_o)	d(Å)	(I/I_o)
x 6.8	(8)	+x 2.63	(10)
? 6.36	(12)	? 2.57	(15)
? 5.78	(9)	? 2.53	(12)
? 4.65	(13)	+ 2.48	(16)
+ 3.86	(8)	x 2.45	(8)
x 3.71	(10)	+x 2.42	(14)
+ 3.61	(36)	+x 2.34	(15)
+x 3.42	(64)	+ 2.29	(9)
+ 3.36	(100)	x 2.26	(13)
+x 3.21	(87)	+ 2.24	(9)
? 3.18	(6)	+x 2.13	(11)
+ 3.11	(2)		
x 2.96	(12)		
+x 2.89	(2)		

[a]Diffraction lines obtained from $2\Theta = 2°$ to 44°
x; Reference compound = Cs_2CO_3 (see Table 20)
+; Reference compound = $CsOOCH$ (see Table 20)
?; Unidentified phase

alter the surface state of the prepared and tested catalysts and could lead to the wrong conclusions regarding the chemical and physical state of the cesium on the surface of the prepared, pretreated, and tested catalysts.

5.3 Electron Microscopy

Electron microscopy is a very useful technique for obtaining chemical and microstructural information for heterogeneous catalysts. Two types of instruments are usually used in catalyst characterization by electron microscopy; (i) the conventional transmission electron microscope (TEM) and (ii) the scanning transmission electron microscope (STEM). In the latter instrument, besides having all of the capabilities of a conventional TEM, the electron beam can be focused on a scale of nanometers (≥2 nm) and be scanned over the surface of the specimen. This electron probe can be used to obtain a microdiffraction pattern, obtain a scanning image of the specimen, or generate characteristic X-ray emission of the elements present in the small volume being analyzed.

Schematic diagrams of the operating principles of TEM and STEM are shown in Figures 5-7 and 5-8, respectively. In TEM, a static beam of electrons is focused by electromagnetic condenser lenses onto a small region of the specimen, which are immersed in the objective lens of the microscope. The transmitted and forward scattered electrons are recombined by the objective lens to form a diffraction pattern in the back focal plane and a magnified image in the image plane. The

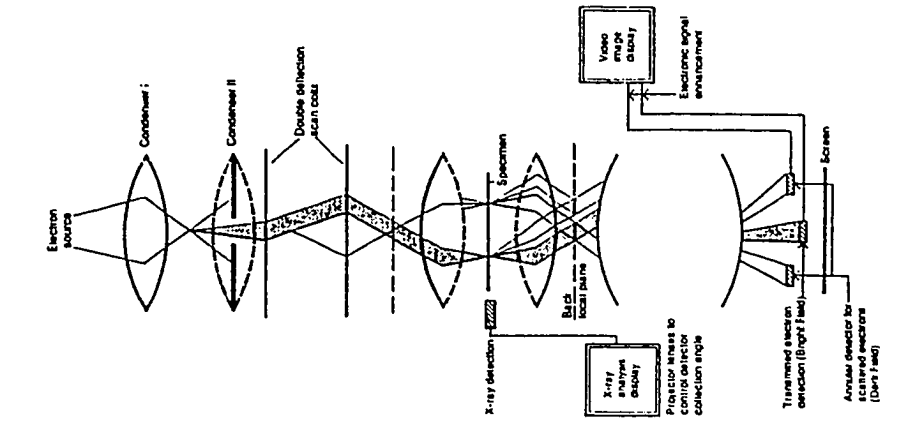

Figure 5-8

Electron Optical System and Signal Detectors in a STEM.

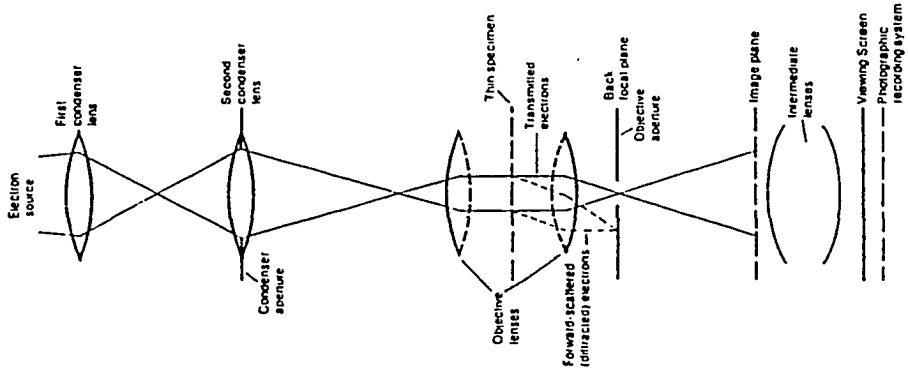

Figure 5-7

Electron Optical System of a TEM.

image or diffraction pattern undergoes further magnification by intermediate lenses and is projected onto a fluorescent screen or a photographic plate. In STEM, Figure 5-8, a probe of electrons is scanned by electromagnetic raster coils across the specimen. The optics are such that a stationary diffraction pattern is formed in the back focal plane of the objective lens, as in TEM. The intermediate and projector lenses are used to transfer this diffraction pattern to an electron detector that intercepts the transmitted beam and the signal is used to modulate a CRT display, producing the STEM equivalent of a bright field TEM image. While observing the scanning image, the electron probe can be stopped and electronically positioned at any point on the specimen. With a beam positioned at the point of interest, microanalytical and microdiffraction information can be obtained. The characteristic X-rays produced by the specimen can be detected and analyzed by a solid state energy dispersive spectrometer (EDS). In conventional scanning electron microscopy (SEM), although electron probe sizes of 5-10 nm can be used, the detected X-rays come from a region of 1-2 μm in diameter because of electron beam spreading in the specimen. In STEM, this beam spreading is minimized because the specimens are essentially transparent to the electron beam. Thus, the analyzed area in STEM is close to the size of the area covered by the electron probe (146,147).

The theory of imaging, electron diffraction, and microanalysis is well-established, and the interested reader is referred to References (146) and (147).

The objective of the present electron microscopy study was to determine the morphology, structure, and cesium distribution of the Cs/MoS_2 catalysts.

5.3.1 Experimental

Characterization studies on the Cs/MoS_2 catalysts were performed on a Phillips EM-400 (S)TEM equipped with an EDAX energy dispersive x-ray spectrometer (EDS). A 120 KeV accelerating voltage was used in all the analyses. For energy dispersive x-ray analysis, each energy spectrum was collected from 0-20 KeV, an electron probe size of ~10 nm and counting times of 100 sec were used.

The sample handling of tested catalysts was carried out in a nitrogen-filled glove bag. The samples were deposited on the carbon-coated grid by simply touching the sample with the grid. To eliminate air from the samples during the loading into the microscope chamber, a recently developed vacuum/inert atmosphere transfer specimen holder was used. This sample holder, which is depicted in Figure 5-9, consists of a specimen holder tip which retracts into the holder housing to seal off a vacuum or an inert gas, e.g. N_2.

5.3.2 Results and Discussion

5.3.2.1 MoS_2

High resolution electron microscopy studies showed that MoS_2

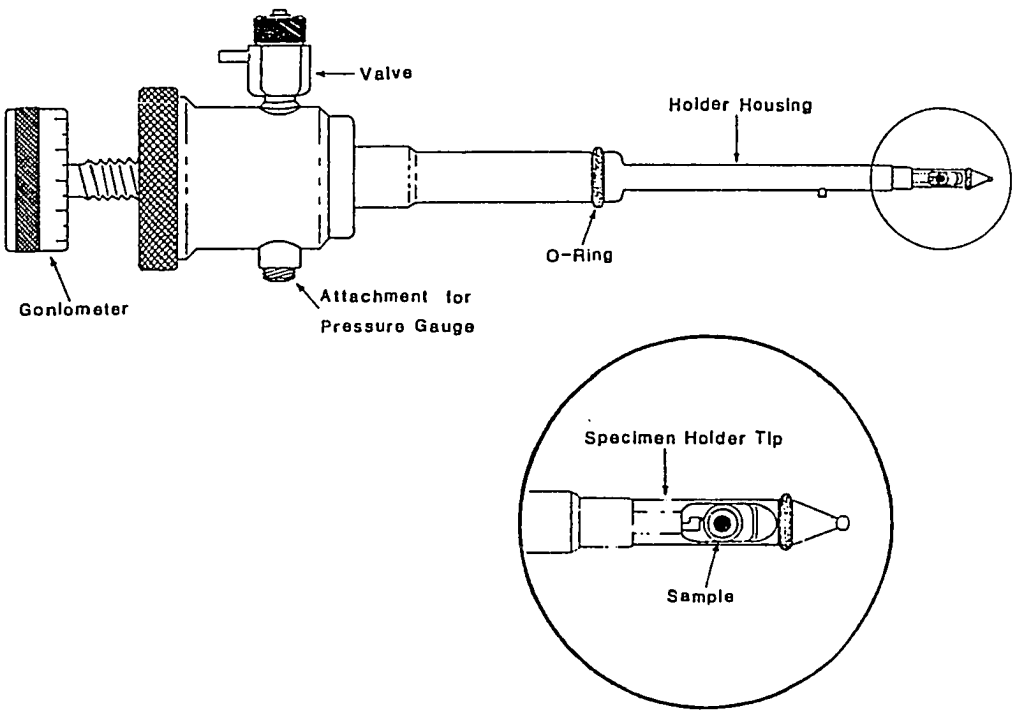

Figure 5-9 Electron microscope sample holder for air sensitive samples.

obtained from thermal decomposition of MoS_3, as described in Section 2.1, crystallized partially in what is called the "rag" structure (143). This structure, as shown in Figure 5-10, consists of several stacked, but highly folded and distorted MoS_2 layers. The lattice fringes (d-spacing equal to 6.15 Å) shown in Figure 5-10, correspond to the (002) planes of hexagonal MoS_2. Selected area electron diffraction pattern (Figure 5-11) obtained from this region also indicates the poor crystalline nature of the hexagonal MoS_2. The d-spacings calculated from the ring SAD pattern of Figure 5-11 are reported in Table 5-4.

The MoS_2 crystal size dimensions were determined from high resolution electron micrographs. The number of stacked layers usually observed varied between 8 and 10 layers which indicates that the crystal size in the c-axis was 49-62 Å. The a-axis dimensions observed were of the order of a few hundred angstroms.

5.3.2.2 Cs/MoS_2 Catalysts

The catalyst compositions used in this study are listed in Table 3-8, and their alcohol synthesis activity was discussed in detail in Chapter 3. Imaging studies and energy dispersive x-ray analysis (EDS) were used in order to determine the morphology and cesium distribution of the Cs/MoS_2 catalysts.

The results of this study indicated that the way in which cesium is distributed on the MoS_2 surface is a function of the cesium concentration in the catalyst. The general morphological features of

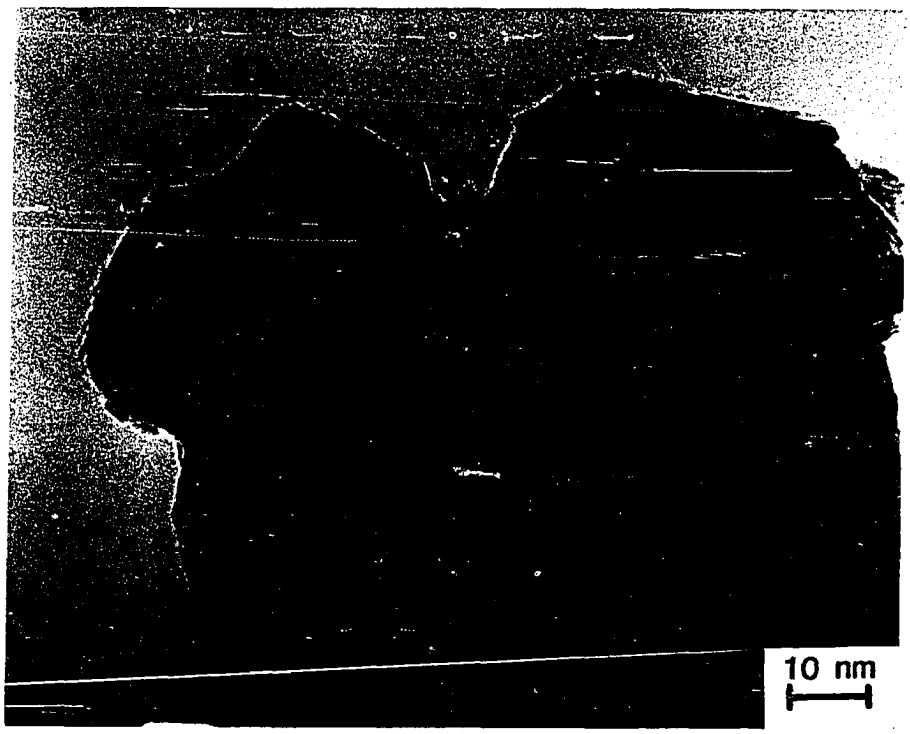

Figure 5-10 Lattice fringes in MoS_2 (interplanar spacing d(002) = 6.15 Å).

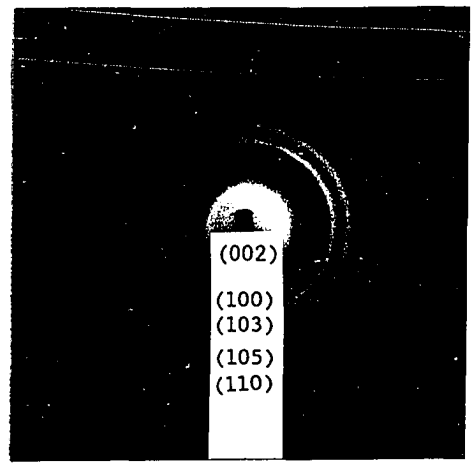

Figure 5-11 Selected area diffraction pattern (SADP) of the MoS_2 catalyst.

Table 5-4

d-spacings Calculated from Selected Area Diffraction Pattern (Figure 5-11).

(hkl)	d-spacing (Å)
(002)	6.15
(100)	2.74
(103)	2.28
(105)	1.83
(110)	1.58

the whole series of Cs/MoS_2 catalysts after testing under alcohol synthesis conditions are summarized as follows:

- There were no changes in either the morphology or the size of the MoS_2 particles in the whole range of different cesium concentrations.
- In the Cs/MoS_2 catalyst containing 2.5 wt% CsOOCH (2.25 mol% Cs), cesium was detected by EDS on some regions of the catalyst. Cesium particles were not observed.
- In the Cs/MoS_2 catalysts containing Cs in the range of 5.3-20.0 wt% CsOOCH (4.8-18.4 mol% Cs), it was found that the cesium is in the form of relatively uniform particles as well as finely dispersed on the MoS_2 surface.
- In the catalysts containing 25.0 and 30.0 wt% CsOOCH (23.1 and 27.83 mol% Cs), the cesium agglomerates into large particles.

Based on the morphological features mentioned above, and for the sake of clarity, the results and discussion of the Cs/MoS_2 catalysts will be divided into three groups: 1) low cesium loading (2.5 wt% CsOOCH) catalyst, 2) intermediate cesium loading (5.3 - 20.0 wt% CsOOCH), and 3) high cesium loading (25.0 and 30.0 wt% CsOOCH) catalysts.

1) Low Cesium Loading (2.5 wt% Cs) Catalyst.

The surface of this catalyst consists of a mixture of bare MoS_2 and cesium highly dispersed over the MoS_2 surface, as determined by energy dispersive X-ray analysis (EDS).

Figures 5-12A and 5-13A show typical TEM images of the 2.5 wt% CsOOCH (2.25 mol% Cs) catalyst. Microanalyses from those regions by energy dispersed X-ray analysis indicate the presence of cesium

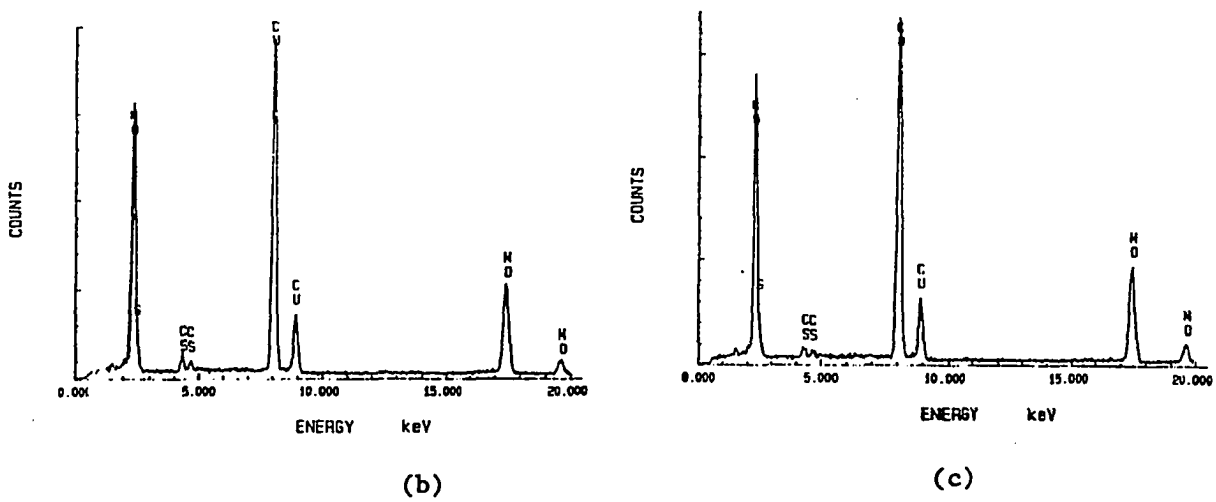

Figure 5-12 (a) Typical TEM image of the tested 2.5 wt% $CsOOCH/MoS_2$ catalyst. (b) and (c) Energy dispersive X-ray analysis (EDS) of regions shown in (a).

(a)

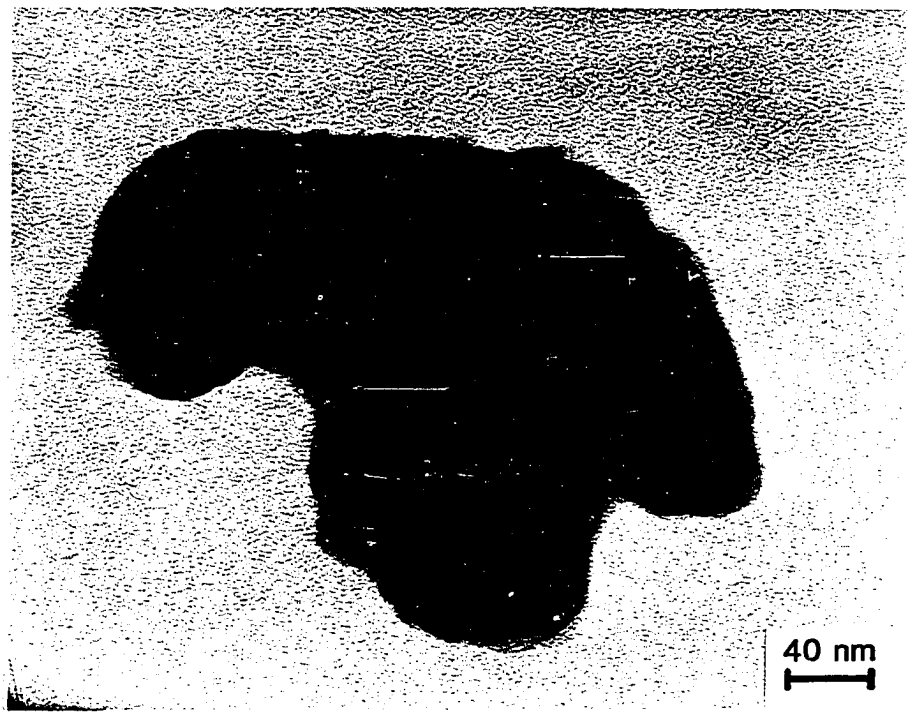

(b)

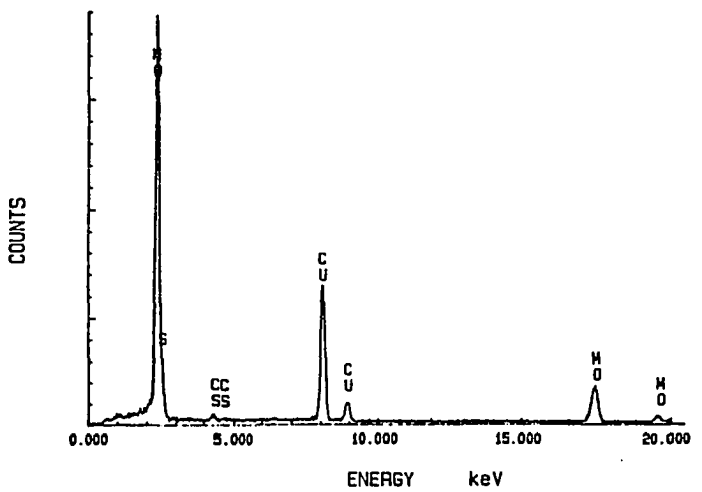

Figure 5-13 (a) Typical TEM image of the tested 2.5 wt% $CsOOCH/MoS_2$ catalyst. (b) Energy dispersive X-ray analysis (EDS) of region shown in (a).

(Figures 5-12B,C and 5-13B), which must be in a very finely dispersed state, since no cesium particles were readily observed despite the relatively high resolution of those electron micrographs.

The relative concentration of Cs in regions that were essentially transparent to the electron beam was obtained by using the Cliff-Lorimer ratio approach (148). This approach relates the characteristic X-ray peak intensities, I_A and I_B, to the actual concentration of the species in wt.%, C_A and C_B, according to the equation

$$\frac{C_A}{C_B} = k_{AB} \frac{I_A}{I_B} \qquad [5.1]$$

where k_{AB} is termed the Cliff-Lorimer k factor. Calculations from first principles of k factors for Cs, Mo, and S are presented in Appendix 5.A.

The results of the analyses over the 2.5 wt% CsOOCH (2.25 mol% Cs) catalyst indicate that in regions in which cesium was detected, its concentration was determined to be in the range 0.4 - 0.7 mol% Cs. This concentration of cesium determined by energy dispersive x-ray analysis should be considered an underestimate due to the high mobility of the cesium under the electron beam (see Figure 5-14), despite the low current density (<5 μA) and relatively low counting time (100 s) used to minimize beam damage. Semiquantitatively speaking, based on the fact that all analyses were performed under similar conditions (120 KeV beam, 100 s counting time, 100 Å probe diameter), the concentration of cesium was approximately similar in

(a)

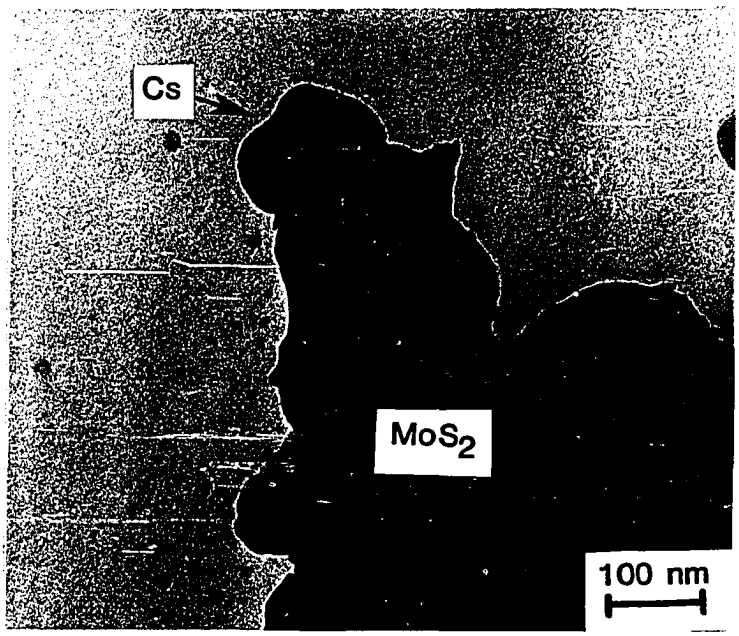

(b)

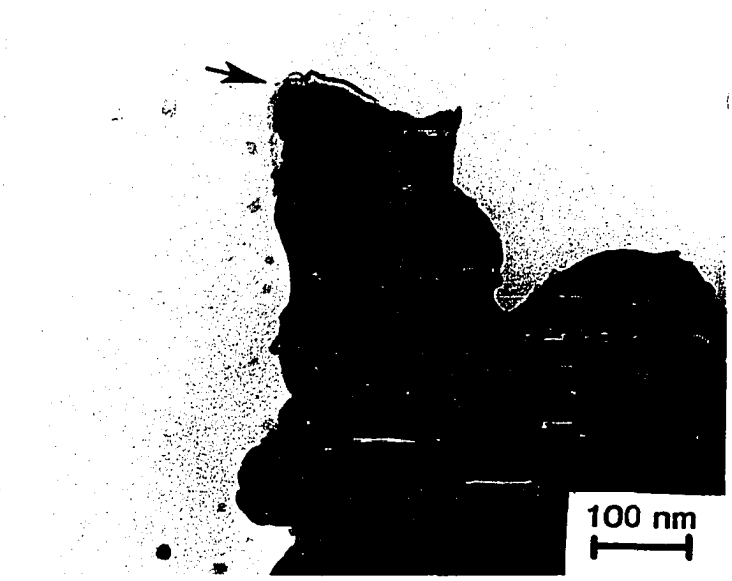

Figure 5-14 Electron micrograph showing electron beam damage to the cesium particle (a) before and (b) after energy dispersive X-ray analysis (EDS) was performed.

regions in which it was detected.

There were regions (>50% of the regions analyzed) in which cesium was not detected, within the experimental limits of the microanalysis. The minimum mass fraction (MMF) of cesium that can be detected in MoS_2 was calculated to be 0.24 wt% Cs (0.3 mol% Cs). Details of the MMF calculations are given in Appendix 5.B.

The question of interest at this point is: what is the driving force for the spreading of cesium rather than the formation of 3-dimensional particles on the mainly nonpolar and hydrophobic MoS_2 surface? The driving force for this phenomenon of dopant spreading may be a strong interaction between cesium and defects in the MoS_2 surface. These defects are expected to exist in the poorly-crystalline MoS_2 catalyst. On the other hand, in a well-crystallized MoS_2, most of the surface is the (002) basal plane that results from the anisotropic crystal structure. Therefore, the interaction between this nonpolar, hydrophobic MoS_2 surface and the ionic, hydrophilic cesium compound is expected to be minimal, giving rise to the formation of 3-dimensional cesium particles. Kennou et al. (152) studied the behavior of cesium on the basal plane of a MoS_2 single crystal and concluded that cesium tends to form 3-dimensional clusters on MoS_2, in contrast to the uniform adsorption exhibited on metals and other semiconductors.

2) Intermediate Cesium Loading (5.3, 10.0, and 20.0 Wt% CsOOCH) Catalysts.

The electron microscope results of the tested catalysts containing cesium in the range of 5.3 - 20.0 wt% CsOOCH indicated that these catalysts had similar morphological features. The cesium compound was found to be present on the surface of MoS_2 in the particle form as well as finely dispersed.

An electron micrograph of the 5.3 wt% CsOOCH (4.8 mol% Cs) catalyst is shown in Figure 5-15. In this figure, the presence of small cesium particles with a hemispherical shape can be observed. The identification of these particles was performed by energy dispersive x-ray analysis (EDS). Selected area diffraction of the region containing these cesium particles did not reveal any other phase other than polycrystalline MoS_2. Electron microdiffraction of the cesium particles was unsuccessful due to the high instability of the cesium compound under the electron beam. The cesium particle size distribution of the 5.3 wt% CsOOCH (4.8 mol% Cs) catalyst is summarized in the histogram shown in Figure 5-16. From this histogram, it can be seen that there is a maximum at 110 to 130 Å interval.

The concentration of cesium on regions in which cesium was not observed visually, i.e. cesium not in the form of particles, but detected by energy dispersive X-ray analysis, was determined to vary from 1.0 to 2.5 mol% Cs. It has to be pointed out, once more, that these values must be considered underestimated due to the instability

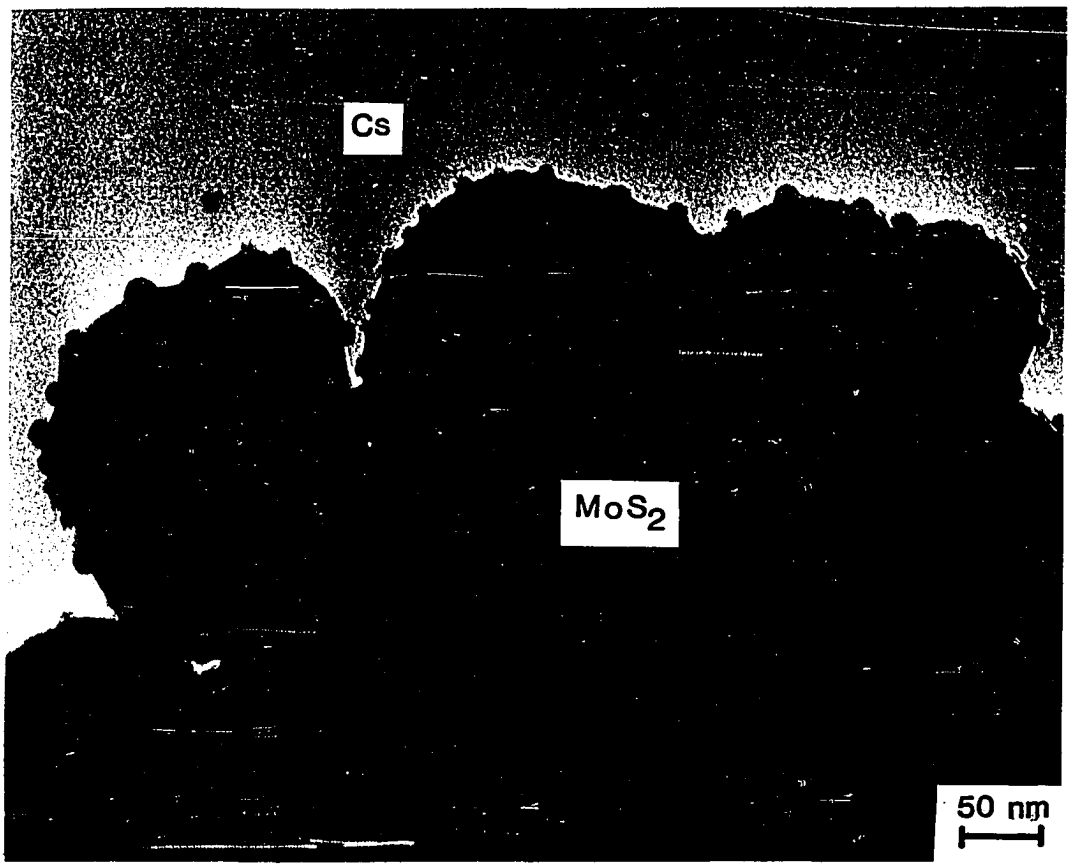

Figure 5-15 Electron micrograph of the tested 5.3 wt% (4.77 mol%) $CsOOCH/MoS_2$ catalyst showing the hemispherically shaped cesium salt particles.

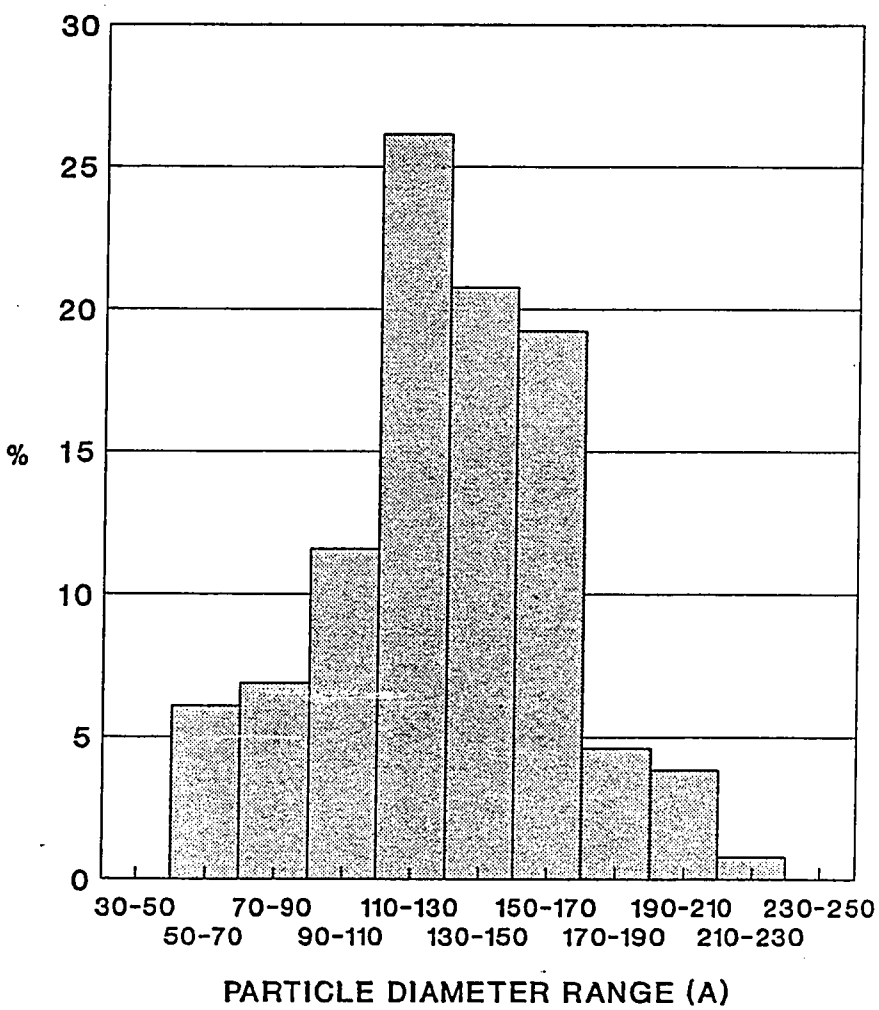

Figure 5-16 Cesium particle size distribution of the tested 5.3 wt% $CsOOCH/MoS_2$ catalyst.

of cesium under the electron beam. Figure 5-17 shows a typical region in which cesium particles were not observed, but cesium was detected by EDS. The results of the analyses obtained from different spots of the region shown in Figure 5-17 are summarized in Table 5-5.

Imaging studies on the 10.0 wt% CsOOCH (9.1 mol% Cs) catalyst indicated that the cesium particles had a hemispheric-like morphology similar to that found in the 5.3 wt% CsOOCH catalyst. This is clearly observed in Figure 5-18, which shows a topographical image (149) of the tested 10.0 wt% CsOOCH catalyst. Figure 5-19 shows the cesium particle size distribution of the tested 10.0 wt% CsOOCH catalyst. From this histogram it can be seen that the average size of the cesium particles found on this catalyst, ≈200 Å, is larger than that determined on the 5.3 wt% CsOOCH catalyst. In regions in which cesium particles were not observed, but a cesium X-ray signal was obtained, its concentration was determined to range between 1.0-3.0 mol% Cs. There were also regions in which cesium was not detected within the experimental limits of the technique, which was 0.3 mol% Cs (see Appendix 5.B for details).

Results obtained on the catalyst containing 20.0 wt% CsOOCH (18.4 mol% Cs) suggested that the cesium was distributed on the MoS_2 in a rather heterogeneous fashion. Based on imaging and EDS studies, one can classify the following regions on the 20.0 wt% CsOOCH (18.4 mol% Cs) catalyst:

1) Bare MoS_2 surface (cesium was neither observed nor detected).

Figure 5-17 Electron micrograph of the tested 5.3 wt% $CsOOCH/MoS_2$ catalyst showing the regions examined by EDS. The results of the EDS analyses are given in Table 5-4.

TABLE 5-5

Results of the Energy Dispersive X-Ray Analysis (EDS) Performed on the Region Shown in Figure 5-14.

Spot	mol% Cs
A	2.5
B	2.6
C	2.1
D	2.2
E	1.5
F	1.7
G	1.8
H	2.8

(a)

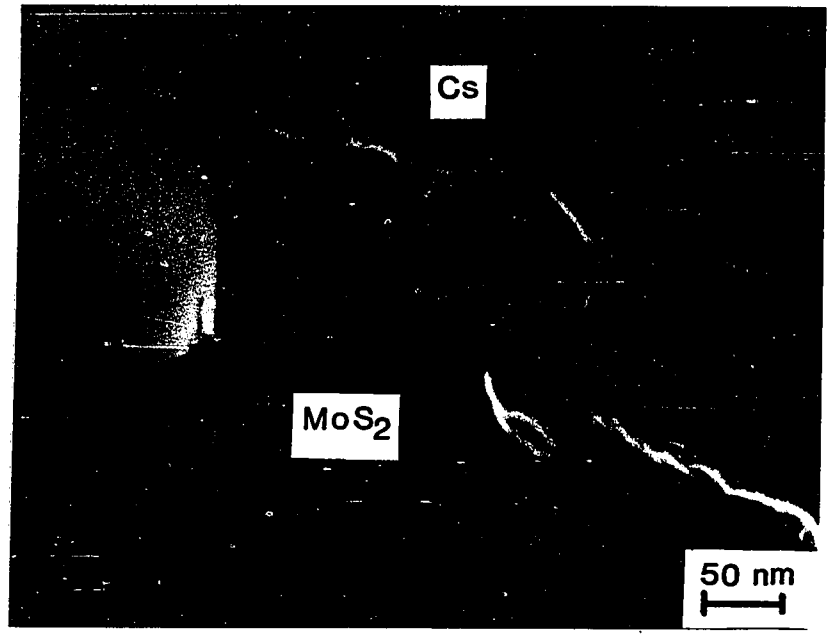

(b)

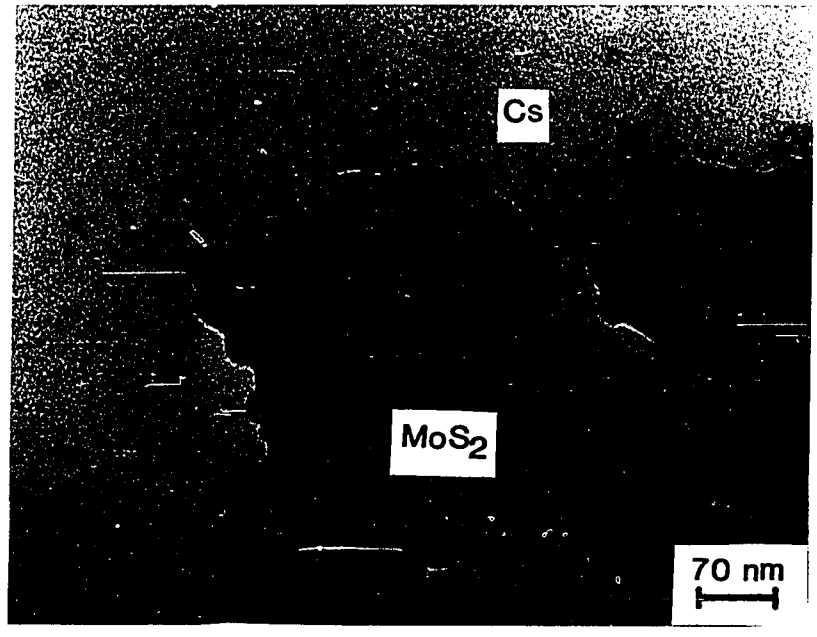

Figure 5-18 Electron micrographs of the tested 10.0 wt% $CsOOCH/MoS_2$ catalyst showing the hemispherical cesium particles on the surface of MoS_2. (a) Topographical image (b) bright field image.

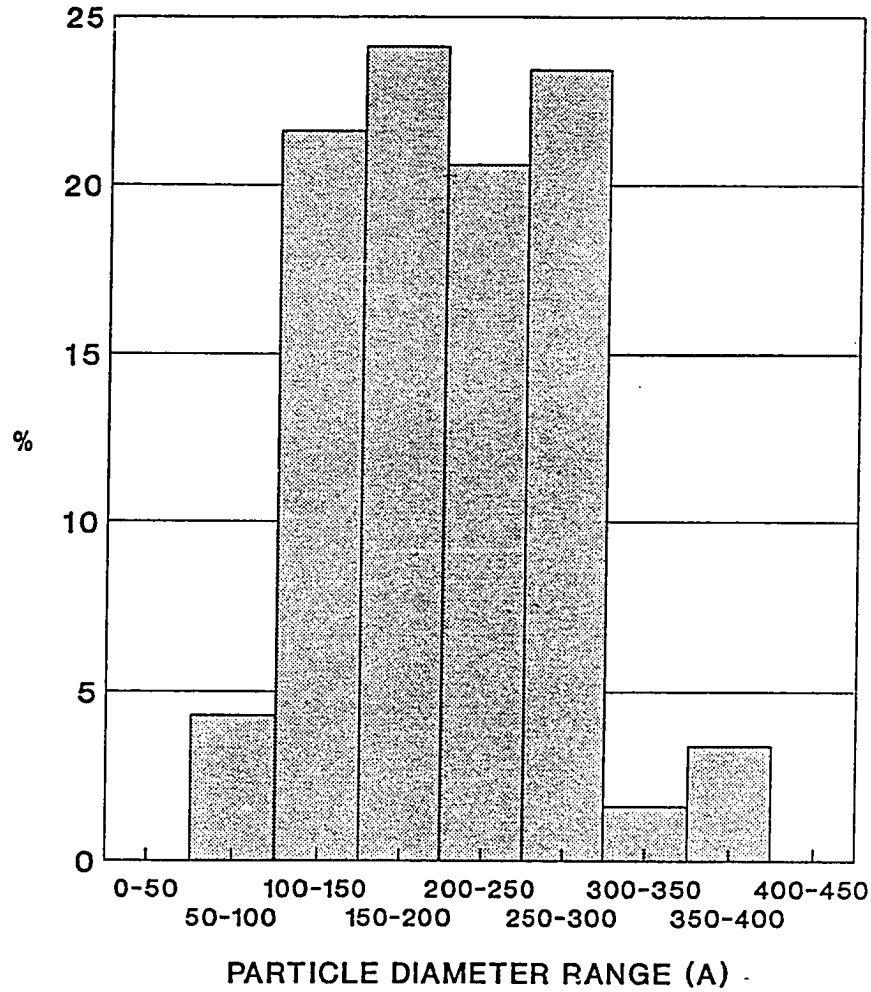

Figure 5-19 Cesium particle size distribution of the tested 10.0 wt% $CsOOCH/MoS_2$ catalyst.

2) Cesium was not observed visually, however, it was detected by EDS.

3) Cesium was observed in the form of hemispherical particles.

In regions in which cesium was detected by energy dispersive X-ray analysis, its concentration varied from 1.0 to 3.5 mol% Cs. This concentration range is similar to that found on the 10.0 wt% CsOOCH (9.1 mol% Cs) catalyst.

The cesium particle size distribution of the tested 20.0 wt% CsOOCH catalyst is summarized in the histogram shown in Figure 5-20. This histogram indicates a very broad cesium particle size distribution. A distinct maximum in the 250 - 300 Å range is present. This particle size range is larger than those obtained for the 5.3 and 10.0 wt% CsOOCH catalysts.

At this point, it is convenient to discuss in detail the factors that influence the spreading (cesium highly dispersed) and clustering (hemispherical particles) of cesium on the MoS_2 surface. The argument will be presented in terms of the surface (interface) tensions between the cesium compound and MoS_2.

The surface tension (δ) of the MoS_2 surface (s) and the cesium particle (p) are related via the contact angle (θ) and the interfacial surface tension (δ_{sp}) through Young's equation (see Figure 5-21),

$$\delta_{sg} = \delta_{sp} + \delta_{pg}\cos\theta \qquad [5.2]$$

where g represents the gas phase.

Effective nonwetting occurs for $\theta > 90°$; for values of $\theta < 90°$,

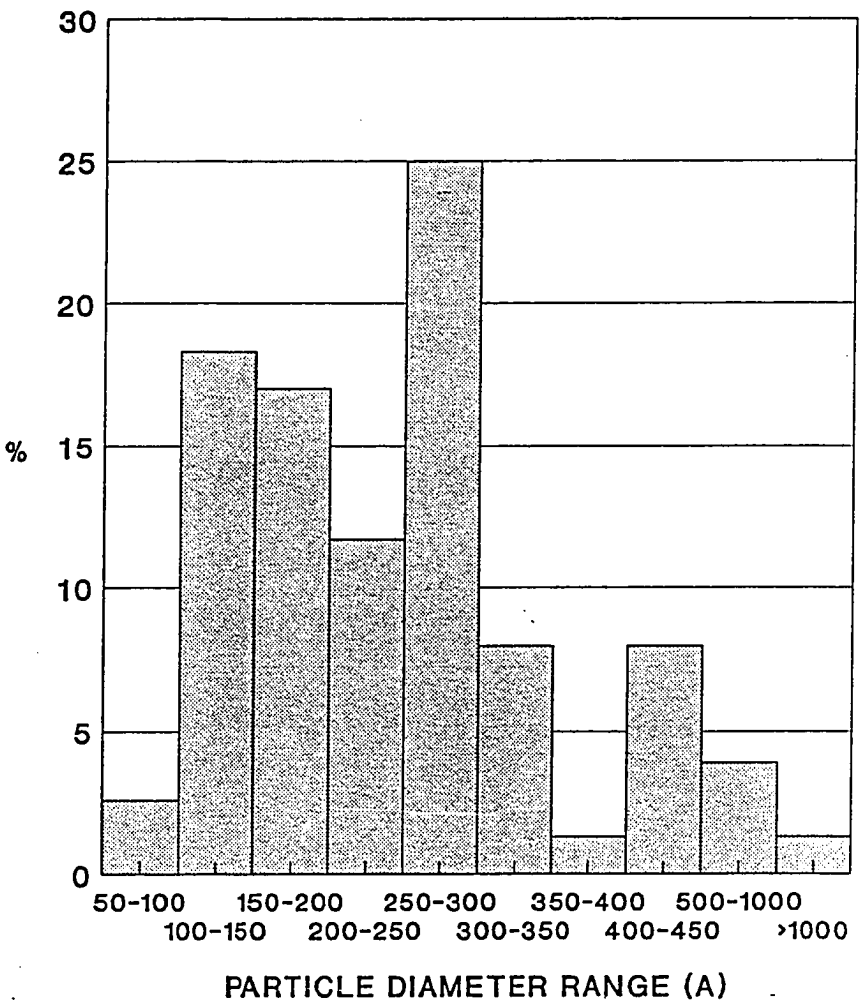

Figure 5-20 Cesium particle size distribution of the tested 20.0 wt% CsOOCH/MoS_2 catalyst.

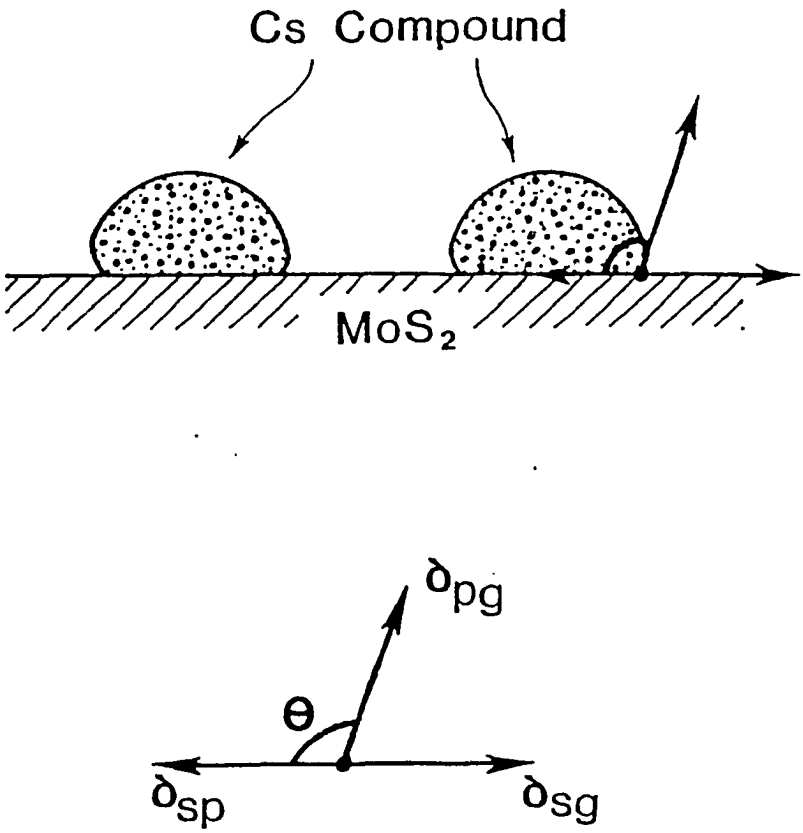

Figure 5-21 Equilibrium forces on the periphery of the cesium compound particle sitting on MoS_2. δ_{sg} is the surface tension of the MoS_2 surface, δ_{pg} is the surface tension of the cesium particle, and δ_{sp} is the interfacial surface tension between MoS_2 and the cesium particle.

partial wetting will be observed, and in the extreme that θ approaches 0° then complete wetting will occur. Factors which promote the attainment of wetting or spreading are those which result in high values of δ_{sg} and lower values for both δ_{sp} and δ_{pg}.

Because of the anisotropic nature of MoS_2, its surface energy as well as all its other physical chemical properties will depend on the crystallographic plane in which they are being obtained. The surface energy of MoS_2 (δ_{sg}) has been determined to be 24 erg/cm^2 on the nonpolar basal plane (002) and 700 erg/cm$_2$ on the edge planes (100) (150). From these values one would expect that the interaction of the cesium formate, whose surface energy (δ_{pg}) is estimated to be 50 erg/cm^2 (151), with MoS_2 will depend upon what crystallographic planes of MoS_2 are involved. For instance, cesium spreading is expected to be more favorable on the edge planes of MoS_2, which have higher surface energy (δ_{sg} = 700 erg/cm^2).

Results obtained on the Cs/MoS_2 catalysts indicated two different situations for the cesium: 1) cesium is dispersed on the MoS_2 surface, i.e. the contact angle, θ is 0°, and 2) cesium forms hemispherical particles. The contact angle, θ, obtained from measurements on the electron micrograph varied between 80 and 125°.

First, let us analyze the situation in which cesium is dispersed on the MoS_2 surface, i.e. θ = 0°, and consider the situations when cesium is on the basal plane (002) and on the edge plane (100). In the former case, solution of Young's equation gives

$$\delta_{sp} = \delta_{sg} - \delta_{pg}\cos\theta = 24 - 50(1) = -26 \text{ erg/cm}^2$$

where the negative value has no meaning. Therefore, one can conclude that complete wetting of the basal plane (002) of MoS_2 by cesium cannot take place. This result is in agreement with the experimental findings of Kennou et al. (152), who studied the behavior of cesium on the basal plane (002) of a MoS_2 single crystal and concluded that cesium tends to form 3-dimensional clusters on the basal plane (002) of MoS_2 in contrast to the uniform adsorption or spreading exhibited on metals and other semiconductors.

For the latter case with the (100) edge planes, solving Young's equation gives

$$\delta_{sp} = \delta_{sg} - \delta_{pg}\cos\theta = 700 - 50(1) = 650 \text{ erg/cm}^2.$$

The fact that δ_{sp} (650 erg/cm^2) is smaller than δ_{sg} (700 erg/cm^2) indicates that complete wetting, i.e. $\theta = 0°$, is likely to occur on the edge planes (100) of MoS_2.

The situation in which cesium would form hemispherical particles with a contact angle varying between 80 and 125° can also be analyzed. If one assumes that the cesium particles are sitting on the basal plane (002) of MoS_2, solution of Young's equation yields interfacial surface tension (δ_{sp}) values between 15 and 53 erg/cm^2. This upper limit value, corresponding to $\theta = 125°$, is 2.2 times greater than the surface tension of the basal plane of MoS_2 ($\delta_{sg} = 24$ erg/cm^2). On the other hand, if the Cs particles are sitting on the edge planes (100) of MoS_2, the interfacial surface tension is found to vary from 691 to 728 erg/cm^2. The upper limit value is just slightly higher than the

surface tension of the edge planes (δ_{sg} = 700 erg/cm^2). Thus, one can conclude that nonwetting, i.e. formation of 3-dimensional particles, will be more favorable on the basal plane than on the edge planes, since the interfacial surface tension (δ_{sp}) with these planes is much greater than the surface tension of the basal plane. The results are summarized in Table 5-6.

3) High Cesium Loading (25.0 and 30.0 wt% CsOOCH) Catalysts.

Figures 5-22 (a) and (b) show typical electron micrographs of the 25.0 wt% CsOOCH catalyst. In these figures it is apparent that the cesium tends to agglomerate into large particles. In addition to the large Cs particles, cesium was found to be in a film-like morphology as well as in the form of small particles. Regions in which cesium was detected by EDS, but not visually observed, were also found on the 25.0 wt% CsOOCH catalyst.

Figures 5-23 (a) and (b) show the morphology of the cesium particles frequently found in the 30.0 wt% CsOOCH catalyst. Cesium was also observed in a film-like morphology. Regions A and B of Figure 5-24A show this feature. The relatively poor contrast shown by the cesium compound film may be due to the fact that the cesium compound is not crystalline. Figure 5-24B shows the same region after microanalysis was performed to identify the presence of cesium, and loss of cesium from the surface is noticed, which was induced by the electron beam despite the fact that low beam current was used. It

TABLE 5-6

Surface Tensions for the CsOOCH/MoS_2 System

	δ_{sp} θ=0°	δ_{sp} θ=80°	δ_{sp} θ=125°	δ_{sg} (MoS_2)	δ_{pg} (CsOOCH)
CsOOCH/MoS_2(002)	-26[a]	15	53[b]	24	50
CsOOCH/MoS_2(100)	650	691	728	700	50

[a]A negative value is not possible, therefore wetting is favored on the edge plane (100).

[b]At θ = 125°, $\delta_{sp} > \delta_{sg}$(002) and $\delta_{sp} \sim \delta_{sg}$(100); therefore nonwetting is favored on the basal plane (002).

(a)

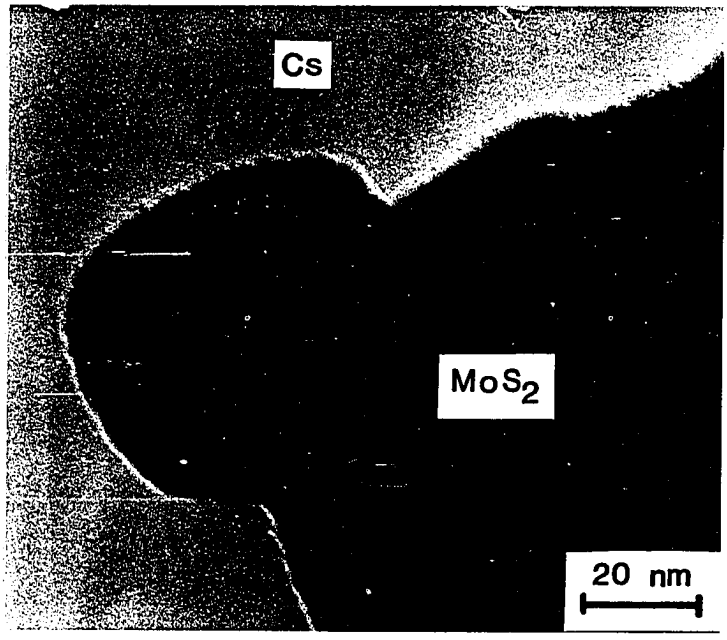

(b)

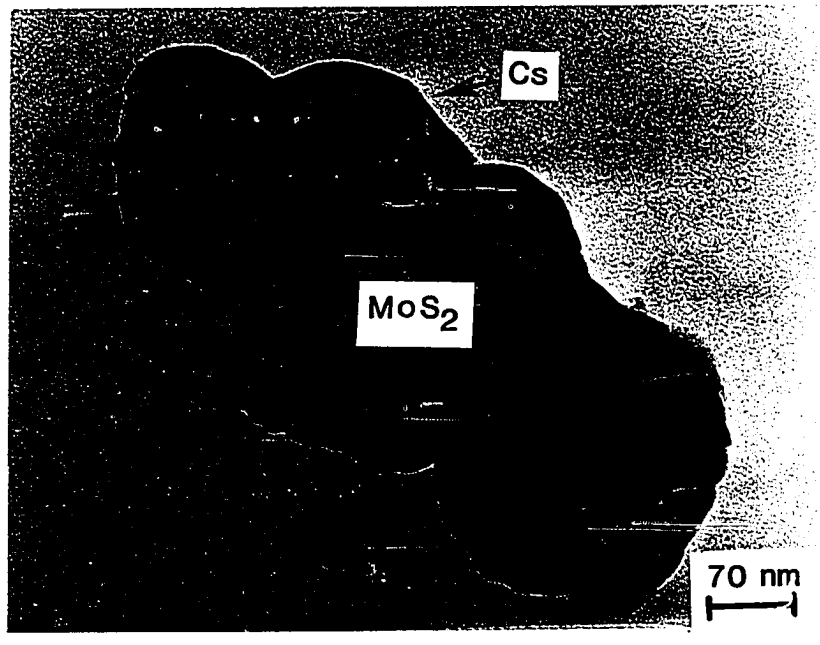

Figure 5-22 (a) and (b) Typical TEM images of the tested 25.0 wt% $CsOOCH/MoS_2$ catalyst.

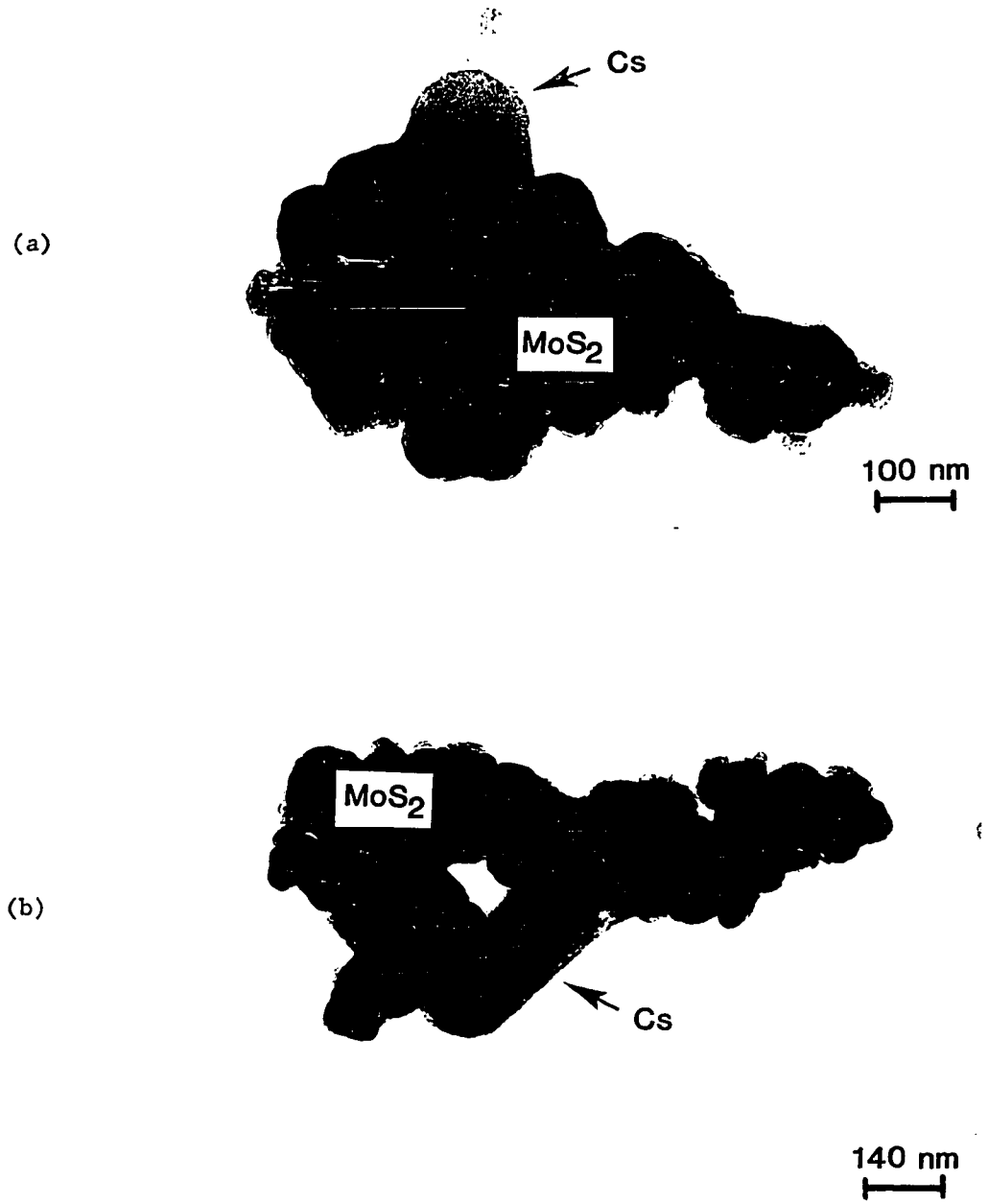

Figure 5-23 (a) and (b) Typical TEM images of the tested 30.0 wt% $CsOOCH/MoS_2$ catalyst.

(a)

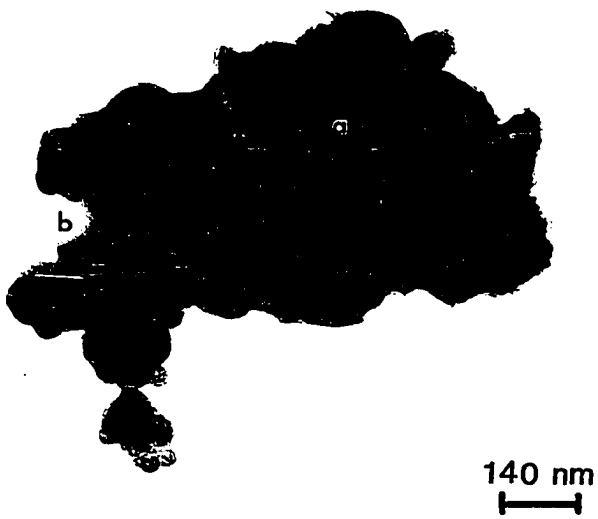

(b)

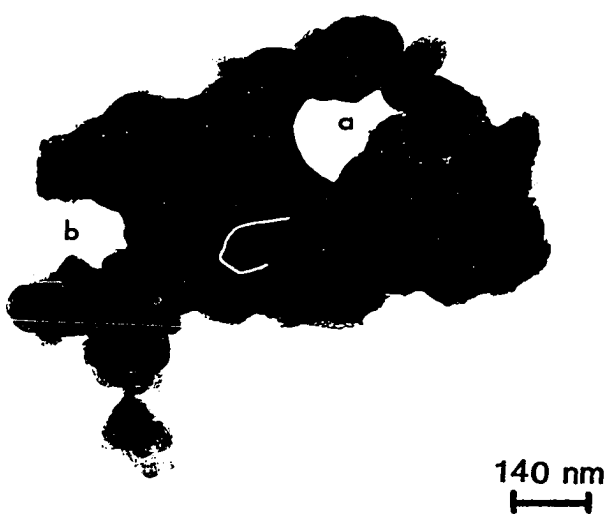

Figure 5-24 Electron micrographs of the tested 30.0 wt% CsOOCH/MoS_2 catalyst showing the film-like morphology and the instability of the cesium component. Micrograph (a) was obtained prior to EDS analysis, and micrograph (b) was obtained immediately after the analysis was performed.

should be pointed out that in the 30.0 wt% CsOOCH catalyst, there were regions in which cesium was not visually observed, but when microanalysis was performed a cesium signal was obtained. An example of these regions is depicted in Figure 5-25. The letters represent the regions in which the microanalysis was performed using a 10 nm electron beam diameter and 100 s counting time. As shown in Table 5-7, the concentration of cesium was approximately uniform over this particular region. In general, however, it can be concluded that cesium is heterogeneously distributed on the MoS_2 surface in the catalysts containing 25.0 and 30.0 wt% CsOOCH.

5.4 X-Ray Photoelectron Spectroscopy (XPS)

X-Ray photoelectron spectroscopy (XPS), which is also known as Electron Spectroscopy for Chemical Analysis (ESCA), is a surface sensitive technique for determining the chemical state and elemental composition of solids. This technique has become a nearly indispensable tool for catalyst characterization, since the behavior of catalysts is dictated by their topmost atomic layers. Besides the determination of binding energies, which provide information on the valence and chemical environment of the element studied, XPS is capable of giving quantitative information of the catalyst surface.

In this section, quantitative as well as qualitative results obtained over the Cs/MoS_2 catalysts using XPS are discussed.

The Cs promoted catalysts containing 2.5 - 30.0 wt% CsOOCH were

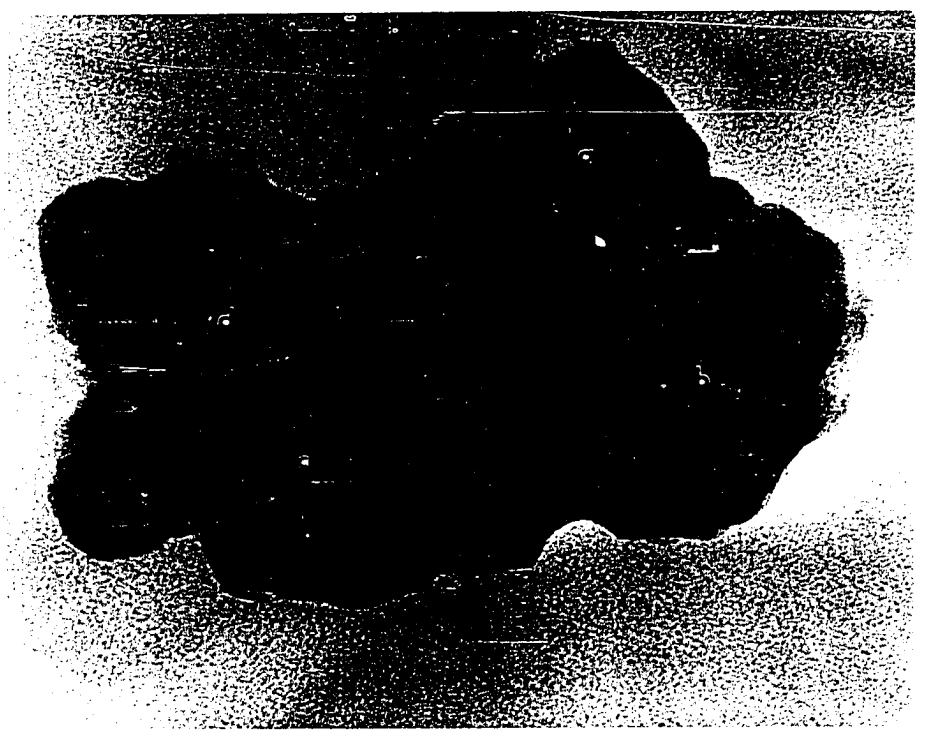

Figure 5-25 Electron micrograph of a region of the tested 30.0 wt% $CsOOCH/MoS_2$ catalyst in which no cesium particles were observed but where cesium was detected by EDS. The results of the EDS analyses are given in Table 5-7.

TABLE 5-7

Results of the Energy Dispersive X-Ray Analysis (EDS) Performed on the Region Shown in Figure 5-25.

Spot	mol% Cs
A	3.4
B	3.8
C	3.0
D	3.5

analyzed by XPS to determine the state of the surface for catalysts (i) as prepared, (ii) as pretreated in a 2% H_2/N_2 mixture at 400°C for 1 h prior to testing, and (iii) after testing.

5.4.1 Experimental

XPS spectra were recorded on a Physical Electronics 548 XPS/AES Spectrometer equipped with a double pass cylindrical mirror analyzer (CMA) using a 400 W Mg x-ray source. A schematic diagram of the spectrometer is shown in Figure 5-26. Survey scans were conducted between 0 and 1000 eV binding energy, with a 100 eV pass energy, 0.1 time constant, rate of 3 eV/sec, and sensitivities of 30K. Detail scans for intensity measurements were performed with a 50 eV pass energy, 0.1 sec time constant, rate of 0.08 eV/sec, and sensitivities of 10K. Multiple scans were signal averaged by a Nicolet Model 1072 Multichannel Analyzer. The measuring temperature was 20°C and the pressure did not exceed 1×10^{-8} torr.

XPS analyses of pretreated and tested catalysts were performed on samples loaded without exposure to air. This was accomplished through a N_2-filled glove bag attached to a side-arm which allows the sample to be transferred to the XPS spectrometer (see Figure 5-27). The samples were pressed into a cylindrical hole, 10 mm x 1 mm, bored in a titanium holder. The position of the sample with respect to the X-ray source and photoelectron detector is shown in Figure 5-26. The portion of photoelectrons detected and the size of the analysis area are strictly a function of the analyzer, which is a double pass,

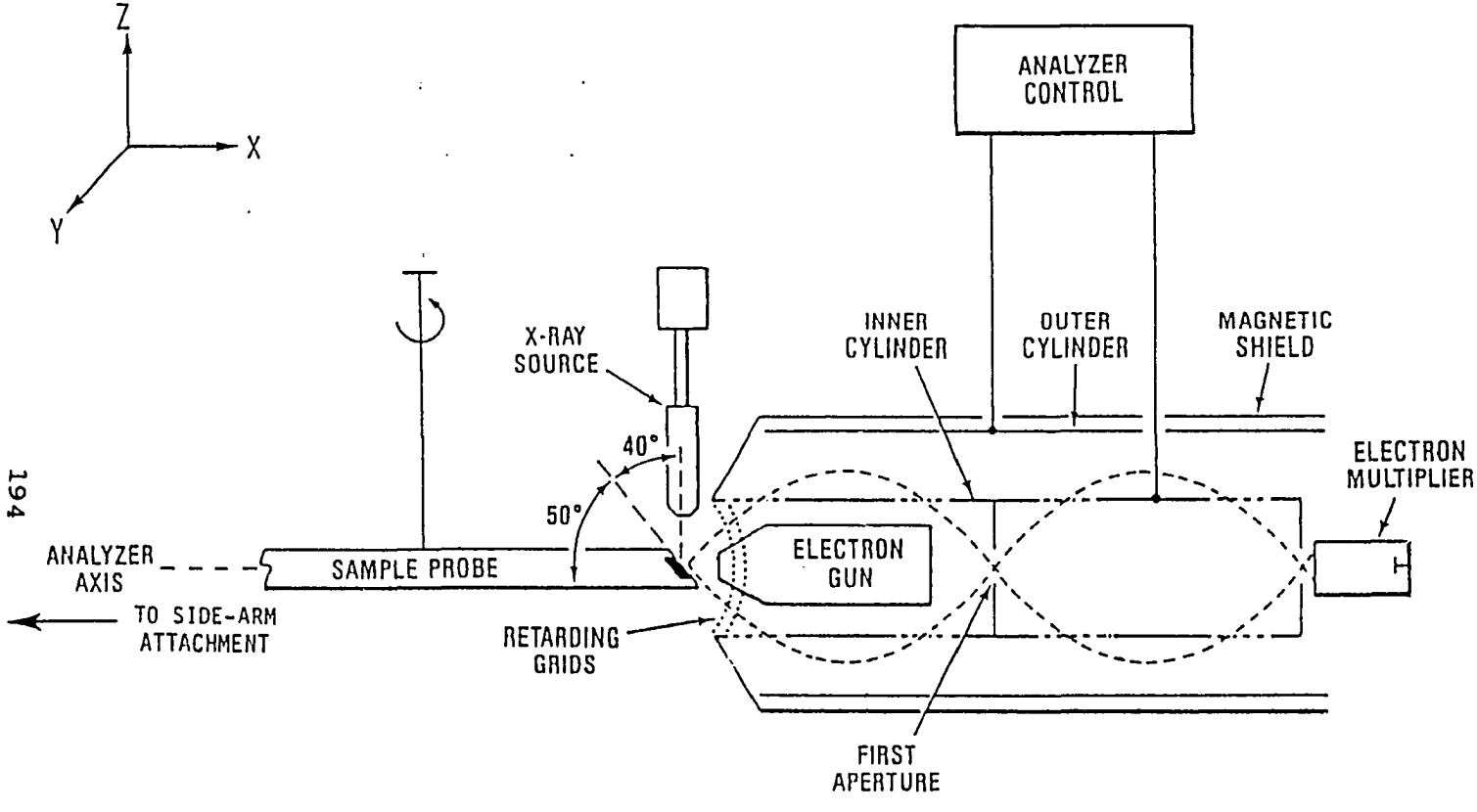

Figure 5-26 Schematic of Physical Electronics Model 548 Spectrometer showing sample location with respect to the X-ray source and cylindrical mirror electron analyzer (153). The X-ray source is rotated out of the plane of the paper, y direction, by 45°.

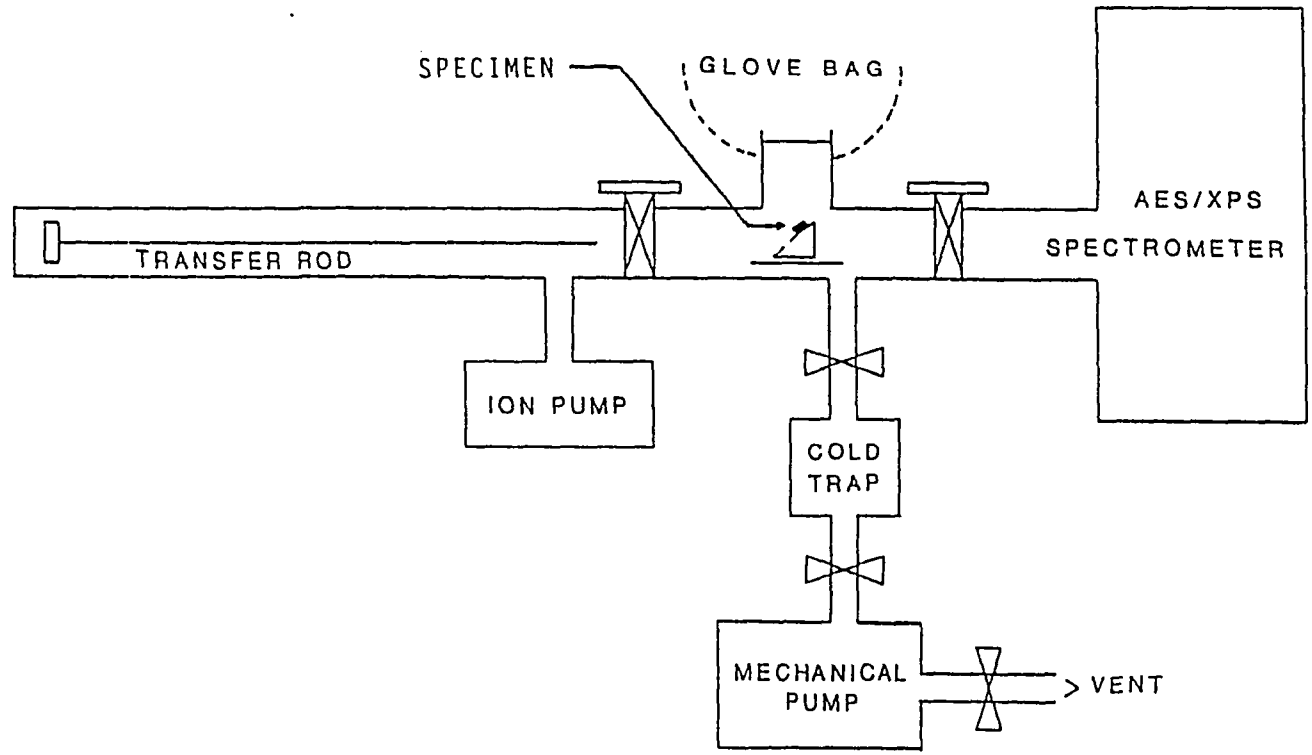

Figure 5-27 Side-arm attachment for loading of air-sensitive samples through a glove bag into the X-ray photoelectron spectrometer. The glove bag is attached to the side-arm by a rubber seal over the entrance port.

cylindrical-mirror analyzer (CMA). In order to obtain a constant energy resolution across the entire energy spectrum the CMA was operated in the retarding mode. The retarding grids are used to scan the spectrum while the CMA is operated at a constant pass energy. The size of the analysis area is defined by the size of the circular apertures at the output of the CMA stages, pass energy, and photoelectron energy and is given approximately by (5.3a):

$$\text{area analyzed} \propto \frac{\text{pass energy, eV}}{\text{photoelectron energy, eV}} \text{ (aperture area)}$$

and ranges from ~ 1 - 3 mm in diameter (153).

Initial sample alignment was made with a blank metallic sample holder by using an electron beam in the Auger analysis mode (153). The purpose of this procedure was to determine the sample height, Z, and direction along the X (analyzer) axes. These optimized positions were then used for all analyses of catalyst samples. After the sample positions were fixed along the X and Z axes, misalignment could only occur in the Y direction and rotation axis upon sample loading. The effects of sample position along these axes were determined by Himelfarb (154) using the single phase Cu/Zn catalyst precursor aurichalcite as the calibration compound. His results are presented in Figures 5-28 and 5-29. From these figures Himelfarb concluded that peak intensities varied considerably, but peak ratios are not sensitive to the possible variations in sample position. This holds true only if the initial sample position is close to the focal point

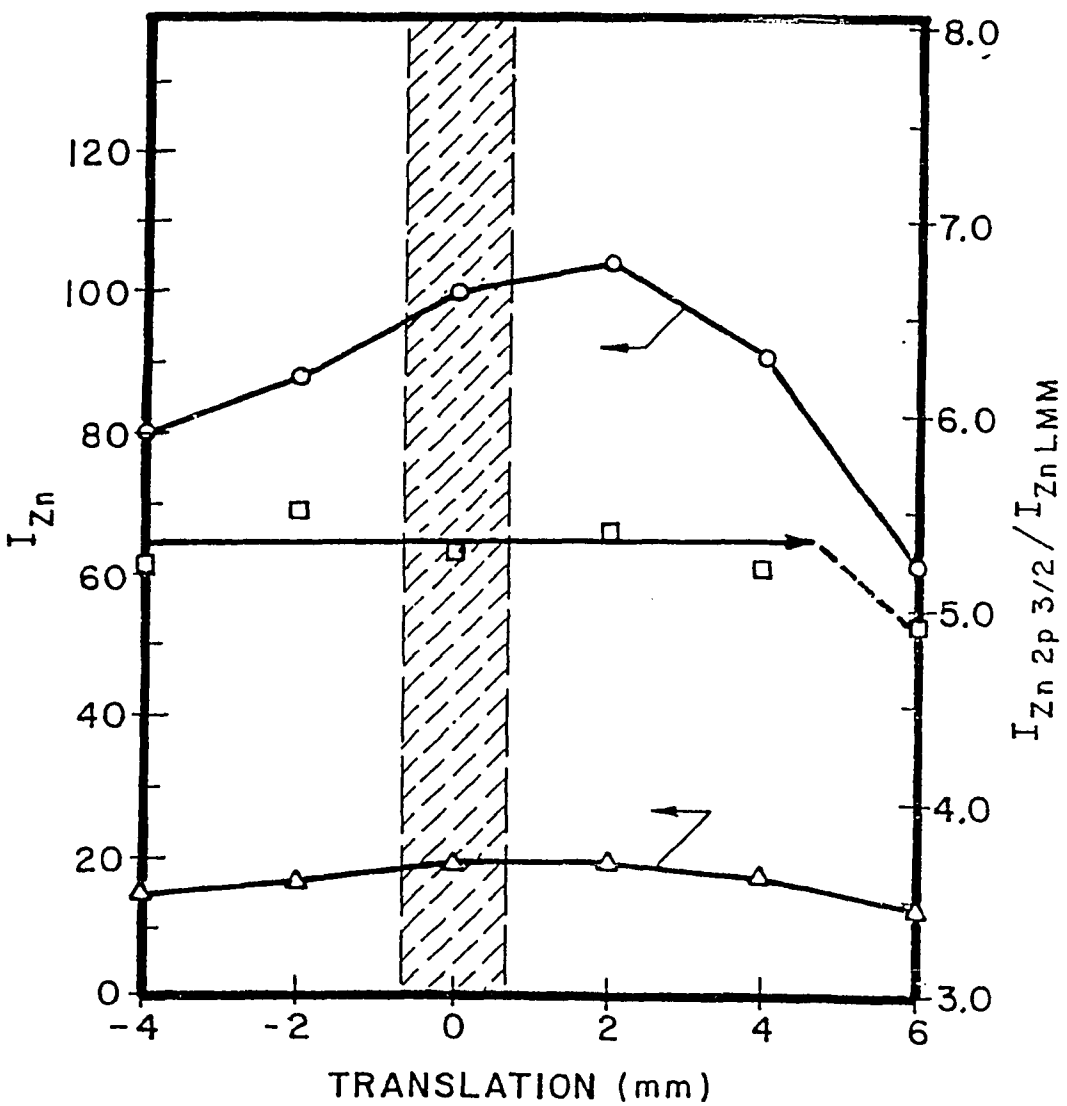

Figure 5-28 Photoelectron intensity variation as a function of sample translation along the y axis (Fig. 12). Intensities for the Zn $2p_{3/2}$ (KE = 232 eV) (O) and for Zn LMM (KE = 992 eV) (Δ) photoelectrons and ratio of these intensities are shown. The shaded area shows the uncertainty in sample position due to sample loading (from Reference 154).

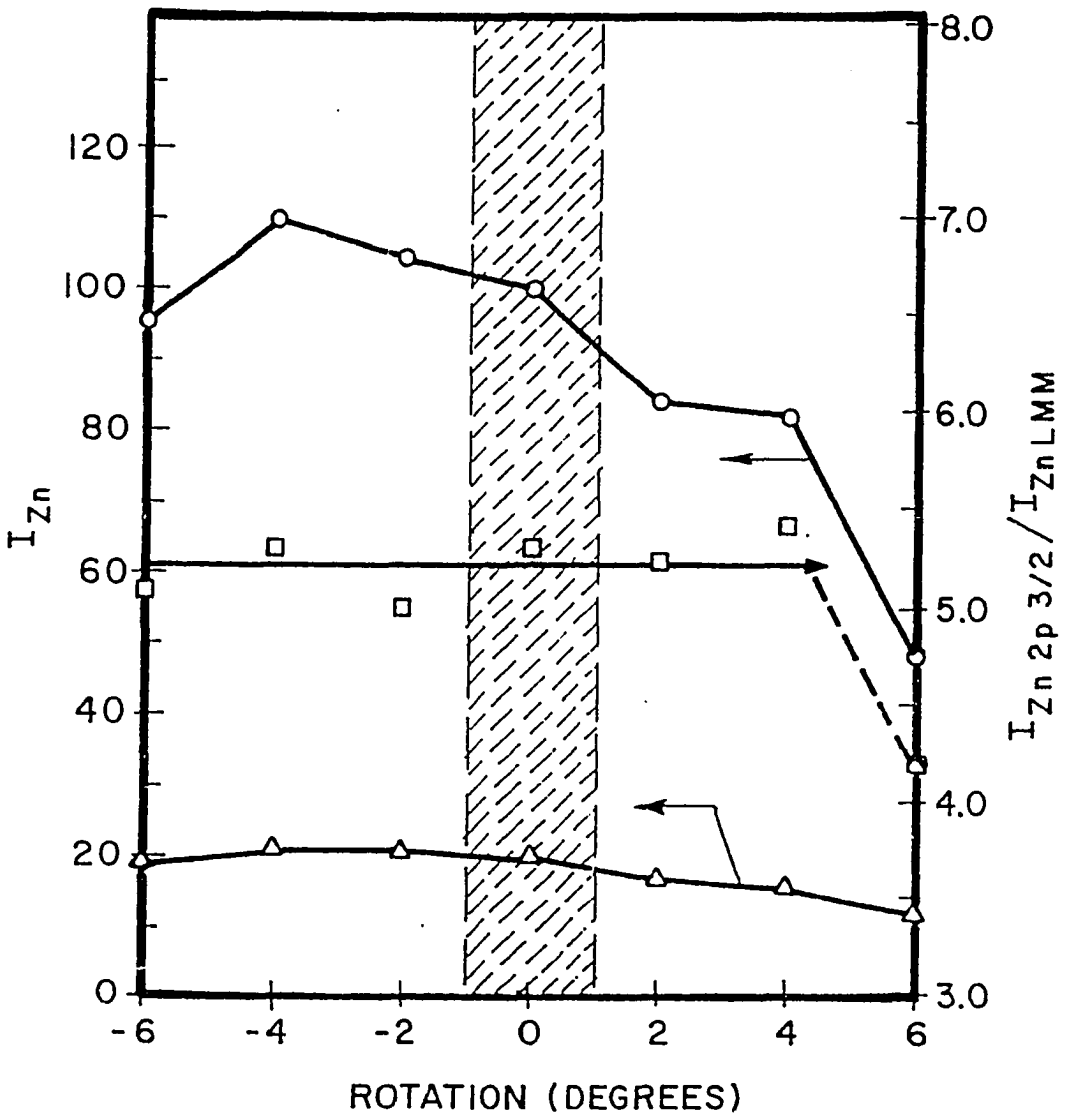

Figure 5-29 Photoelectron intensity variation as a function of sample rotation about the Z axis (Fig. 12). Intensities for the Zn $2p_{3/2}$ (KE = 232 eV) (O) and for Zn LMM (KE = 992 eV) (Δ) photoelectrons and ratio of these intensities are shown. The shaded area shows the uncertainty in sample position due to sample loading (from Reference 154).

of the CMA.

5.4.2 Results and Discussion

XPS Analyses of Fresh and Pretreated Cs/MoS_2 Catalysts

A representative XPS survey scan of the Cs/MoS_2 catalysts is shown in Figure 5-30. XPS analyses were performed on the fresh (before pretreatment) and pretreated catalysts in order to establish the effect of the pretreatment on the surface composition of the Cs-doped MoS_2 catalysts. The pretreatment of the catalysts was carried out in a quartz-tube reactor under identical conditions as those used in the testing unit (2% H_2/N_2, 400°C, 1h). The catalysts were cooled to room temperature under 2% H_2/N_2 flow, and subsequently transferred into a N_2-flushed glove bag to the XPS spectrometer according to the procedure described above. The pretreated samples were never exposed to air, while the fresh catalysts were handled without special care. XPS analyses of the fresh catalysts indicated the presence of small amounts of $SO_4^{=}$ and Mo^{6+} species. These species must have been reduced during the pretreatment process, since they were not observed on the pretreated catalysts. $SO_4^{=}$ and Mo^{6+} species were not detected on the surface of the tested catalysts either. Figure 5-31 shows typical S(2p) XPS spectra of the fresh, pretreated and tested catalysts.

Changes on the Cs surface concentration as a result of the pretreatment were determined by comparing the photoelectron intensity ratio of $Cs(3d_{5/2})/Mo(3d_{5/2})$ for the pretreated and fresh catalysts at

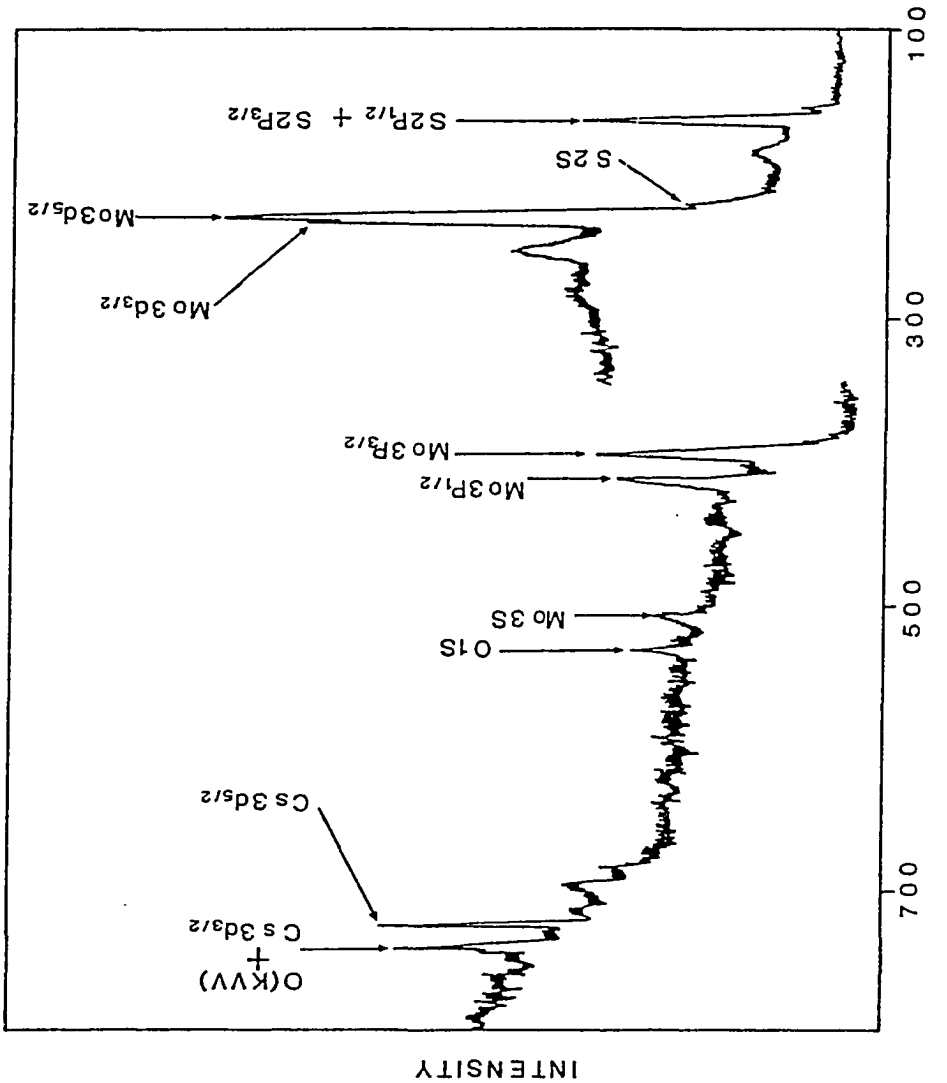

Figure 5-30 Typical XPS survey scan of the Cs/MoS_2 catalyst.

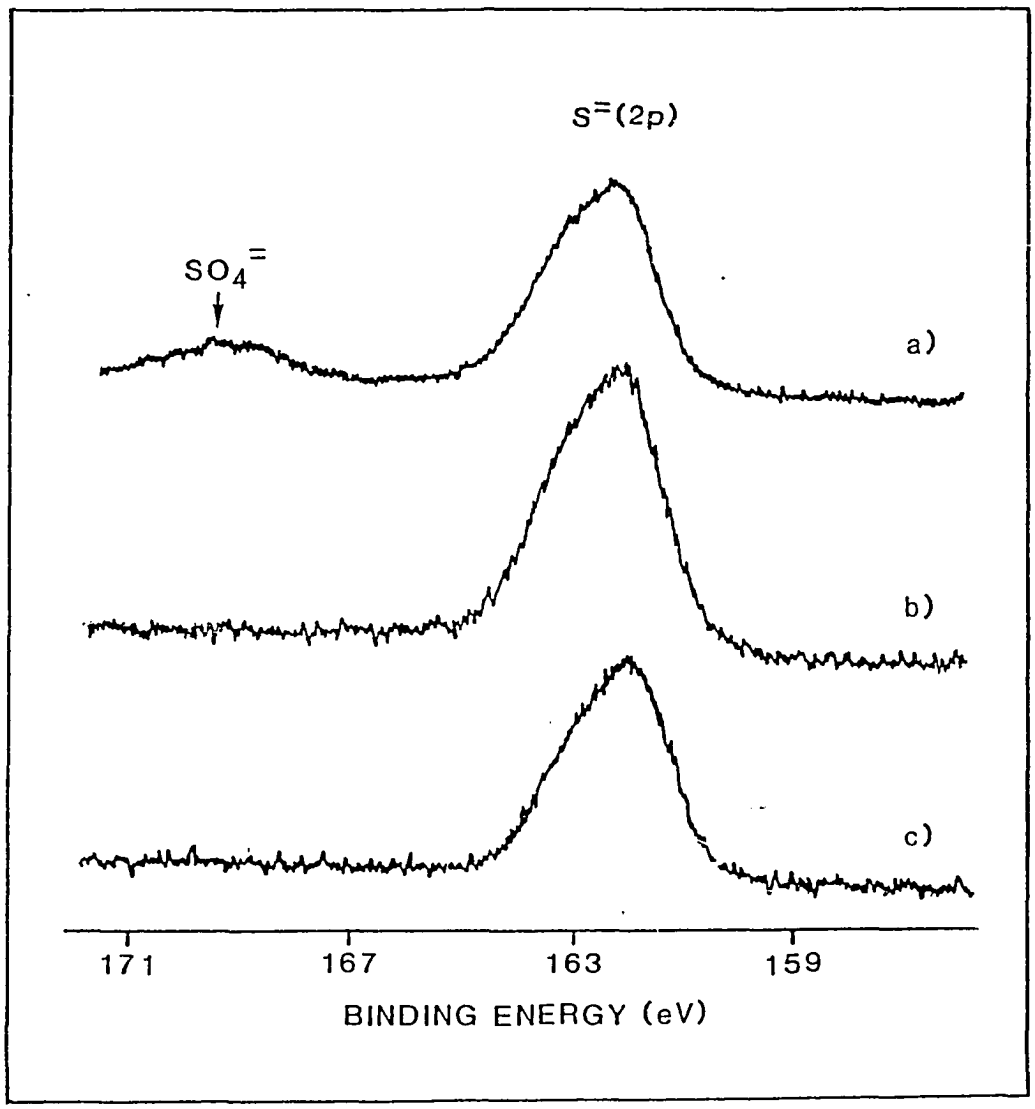

Figure 5-31 S(2p) XPS spectra of Cs/MoS_2 catalysts (a) fresh; (b) pretreated and (c) tested.

different CsOOCH concentrations. The results are shown in Figure 5-32. This figure shows that at given CsOOCH loadings, on the catalysts containing <20 wt% CsOOCH (18.36 mol% CsOOCH) the Cs/Mo photoelectron intensity ratio for the pretreated catalysts (P) is larger than that obtained for the fresh catalysts (F). On the catalysts containing >20 wt% CsOOCH (18.36 mol% CsOOCH), the Cs/Mo photoelectron intensity ratios for the pretreated (P) and fresh (F) catalysts are approximately the same. This is indicated by the fact that the ratio $(I_{Cs}/I_{Mo})_P$ to $(I_{Cs}/I_{Mo})_F$ is close to 1. Speaking in terms of cesium surface concentration, Figure 5-32 indicates that the pretreatment induces dispersion of the cesium compound on the MoS_2 surface on the catalysts that contain <20 wt% CsOOCH (18.36 mol% CsOOCH), and has little or no effect on the cesium surface concentration on the catalysts that contain > 20 wt% CsOOCH.

XPS Analyses of Tested Cs/MoS_2 Catalysts

After the catalysts were tested for alcohol synthesis activity, they were removed in a nitrogen-filled glove bag and store in a vacuum tube for later characterization. The handling of the samples to be analyzed by XPS was described in Section 5.4.1.

The XPS results obtained for the tested Cs/MoS_2 catalysts (2.5 - 30.0 wt% CsOOCH) indicated that the oxidation state of S and Mo correspond to those of MoS_2, i.e. $S^{2-}(2p)$ = 162.4 eV and $Mo^{4+}(3d_{5/2})$ = 229.4 eV. Detailed analysis of the S(2p) and Mo(3d) peaks indicated that neither oxisulfides species nor species containing Mo^{6+} were

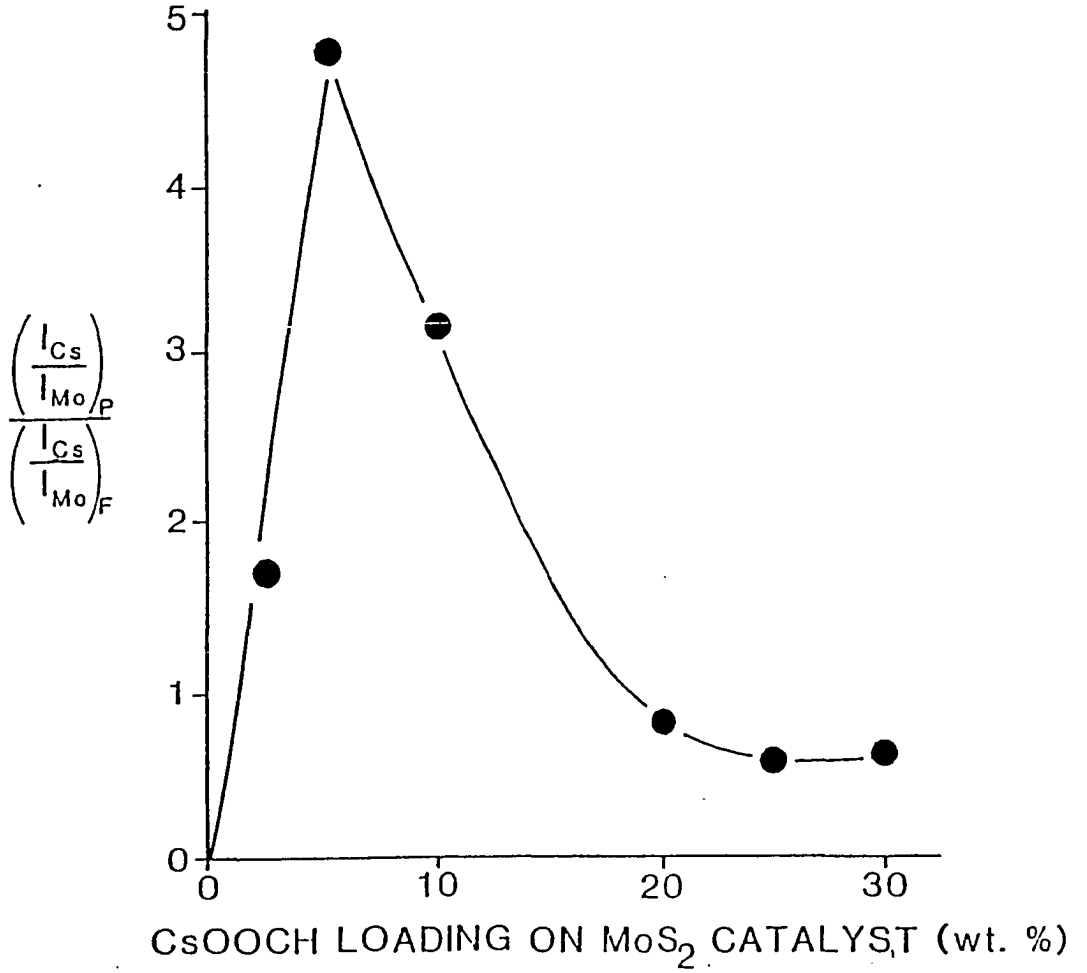

Figure 5-32 $Cs(3d_{5/2})$ over $Mo(3d_{5/2})$ XPS intensity ratio of the pretreated (P) catalysts over the same ratio for the fresh (F) catalysts.

present on the surface (within the detection limits of the XPS technique). It is interesting to note that despite the fact that carbon dioxide and water are being formed during the alcohol synthesis, these two products do not affect the oxidation states of sulfur and molybdenum, this at least applies to the catalyst compositions and operating conditions used in the present study.

In the next section, quantitative XPS analysis of the tested Cs/MoS_2 catalysts is discussed.

Quantitative Analyses of XPS Intensities for the Cs/MoS_2 Catalysts

The objective of the quantitative XPS analysis of the Cs-doped MoS_2 catalysts was to determine the degree of dispersion and/or segregation of the Cs compound on MoS_2. The Mo ($3d_{5/2}$) XPS signal was used as an internal reference for the Cs ($3d_{5/2}$) signal. Figures 5-33 and 5-34 show typical Mo(3d) and Cs($3d_{5/2}$) XPS spectra of a tested catalyst. Table 5-8 presents the experimental Cs($3d_{5/2}$) photoelectron intensity with respect to the Mo ($3d_{5/2}$) XPS signal. In this table it is shown that the (I_{Cs}/I_{Mo}) ratio increases with increasing the CsOOCH loading on the MoS_2 catalyst. (The same trend was observed when the S(2p) signal was taken as a reference).

The magnitude of the uncertainty regarding the reproducibility of XPS intensity ratios was determined by preparing and loading eight separate samples of a 5.3 wt% $CsOOCH/MoS_2$ catalyst, and then

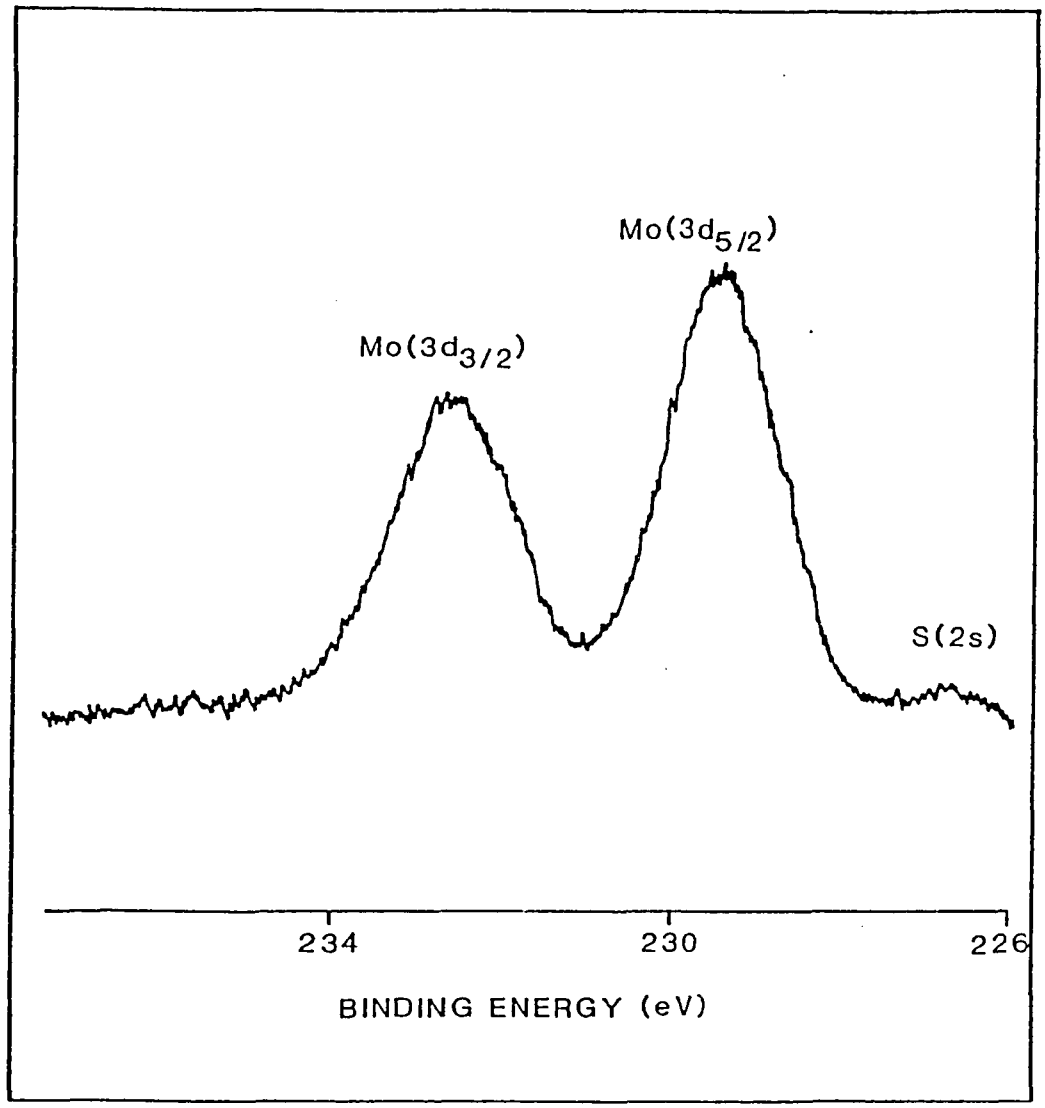

Figure 5-33 Mo(3d) XPS spectrum of a tested Cs/MoS_2 catalyst.

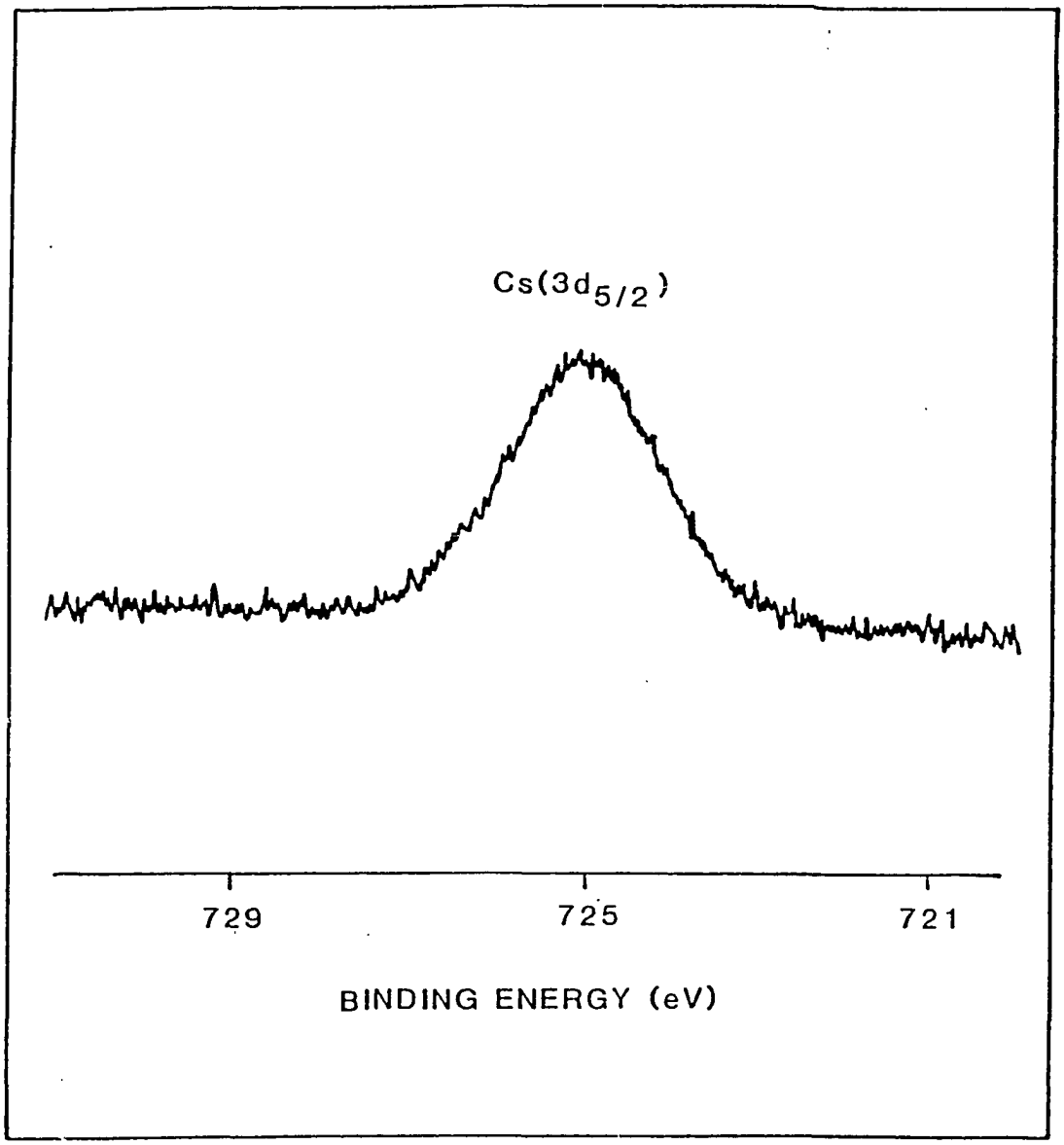

Figure 5-34 $Cs(3d_{5/2})$ XPS spectrum of a tested Cs/MoS_2 catalyst.

Table 5-8

XPS Results Obtained over the Tested Cs/MoS_2 Catalysts.

wt% CsOOCH	Binding Energies (eV)				Intensity ratios	
	Mo(3d) 3/2	5/2	S(2p)	Cs($3d_{5/2}$)	$\frac{I_{Cs}}{I_{Mo}}$	$\frac{I_{Cs}}{I_S}$
2.5	232.5	229.4	162.4	724.6	0.321	0.395
5.3	232.6	229.4	162.3	725.1	0.620	0.982
10.0	232.6	229.4	162.4	725.0	1.790	2.090
20.0	232.5	229.4	162.5	725.1	1.845	2.393
25.0	232.5	229.4	162.4	725.1	2.082	2.877
30.0	232.5	229.4	162.4	725.1	2.830	3.590

determining the standard deviation around the mean value of the Cs/Mo intensity ratio. The resulting mean value of the Cs/Mo intensity ratio was 0.6076 and the standard deviation that was calculated using the equation,

$$S_\chi = \frac{n\Sigma\chi^2 - (\Sigma\chi)^2}{n(n-1)}, \qquad [32]$$

was equal to ±0.082. This uncertainty corresponds to ±13.5% in the mean value.

XPS intensity equations have been developed in Appendix 5.C to determine the degree of dispersion and/or segregation of cesium on MoS_2. Based on STEM results regarding the morphology and distribution of cesium on the MoS_2 catalyst, three different geometric models of the catalyst surface were considered to develop the XPS intensity equations. The models were: 1) "Hemispherical-Particles Model," that assumes that cesium is agglomerated forming hemispheric-like particles (see Figure 5.C-2 in Appendix 5.C), 2) "Layer Model," based on that cesium is highly dispersed on the MoS_2 surface and/or forming a film-like morphology (see Figure 5.C-3 in Appendix 5.C), and 3) "Combined Model," that assumes that cesium is present on the MoS_2 surface in the form of hemispherical particles as well as in a film-like morphology. The experimental XPS intensity results, given in Table 5-8, will be discussed in terms of these models.

1) "Hemispherical-Particles Model"

The Cs/Mo intensity ratio determined from Equation [C-11], in Appendix C, for the Cs-doped MoS_2 catalysts with different cesium loading is plotted as a function of the particle size (r) in Figure 5-35. The particle size (r) determined by XPS for each catalyst is compared with the average particle size (r) determined by STEM in Table 5-9. This table indicates that there is a disagreement in the particle size determined by these techniques. This disagreement was expected since STEM results indicated that the cesium was present on the MoS_2 surface not only in the form of hemispherical particles but also highly dispersed and/or forming a film-like morphology.

2) "Layer Model"

Although STEM studies demonstrated clearly that part of the cesium is forming hemispherical particles, it is interesting to see how both the Cs/Mo intensity ratio and the surface coverage (f_ℓ) of MoS_2 by cesium behave if one assumes that cesium is just present on the MoS_2 surface in a film-like morphology.

The Cs/Mo intensity ratios determined from Equation [C-15] for the Cs-doped MoS_2 catalysts is plotted as a function of the number of cesium layers (n) in Figure 5-36. From this figure it can be seen that the model predicts that the intensity ratio of Cs to Mo changes a little as a function of the number of Cs layers in the catalysts containing 2.5 and 5.3 wt% CsOOCH. However, it drops off rapidly as

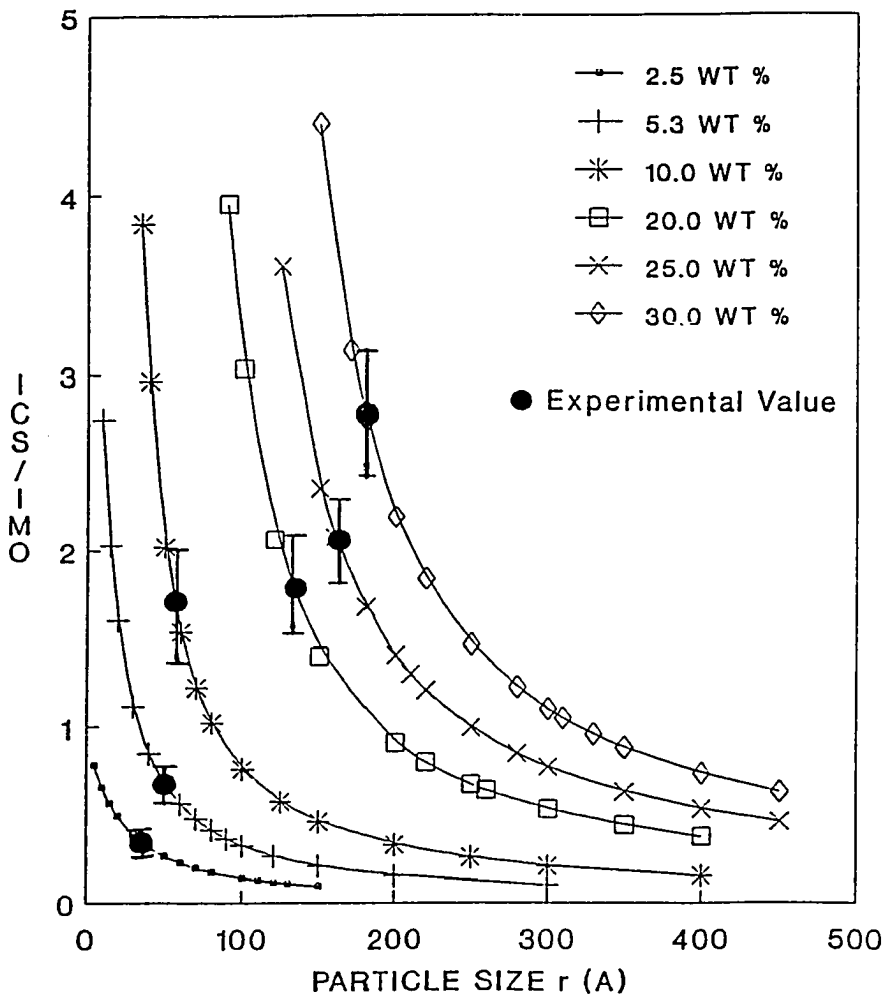

Figure 5-35 XPS intensity ratio (I_{Cs}/I_{Mo}) as a function of the cesium particle size, as determined by the "Hemispherical-Particle Model" for the Cs/MoS_2 catalysts. The cesium particle sizes corresponding to the (I_{Cs}/I_{Mo}) experimental values are given in Table 5-9 along with those found using STEM.

TABLE 5-9

Comparison Between the Particle Size Determined by STEM and the Particle Size Predicted by XPS Analysis.

Catalyst (wt% CsOOCH)	STEM Particle Radius (Å)	XPS Particle Radius (Å)
2.5	not observed	40
5.3	65	50
10.0	100	55
20.0	125	130
25.0	>500	160
30.0	>500	180

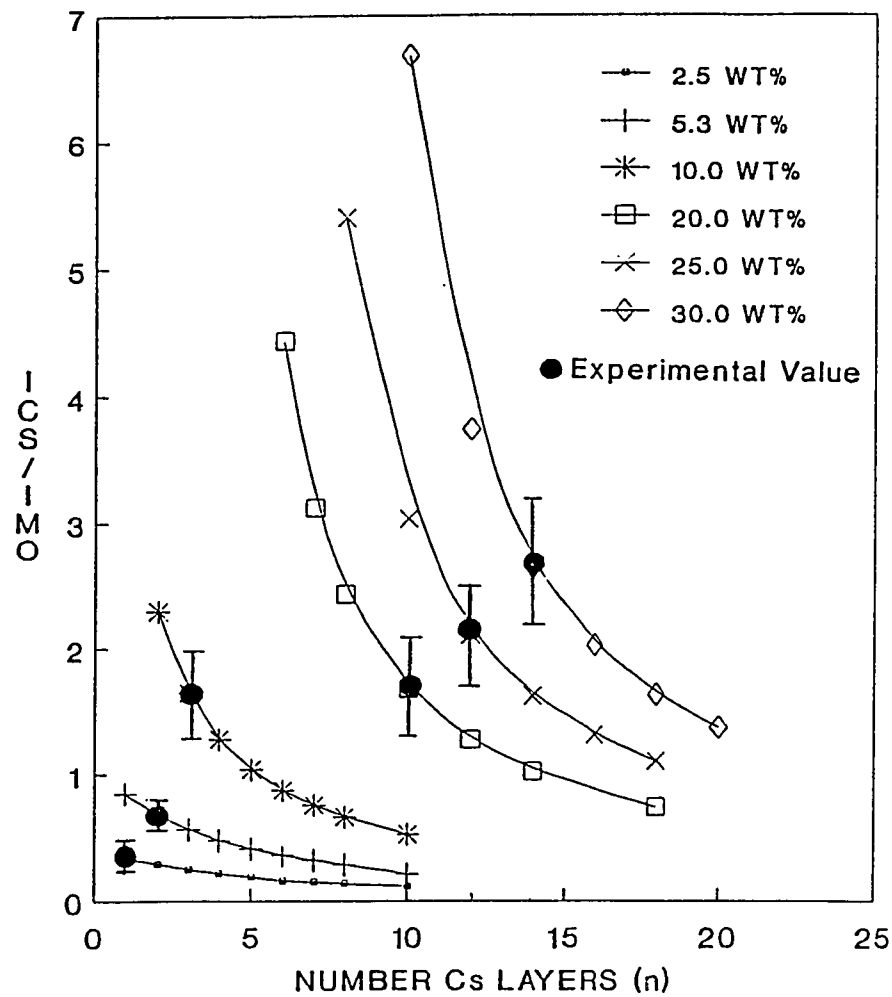

Figure 5-36 XPS intensity ratio (I_{Cs}/I_{Mo}) as a function of the number of cesium layers (n), as determined by the "Layer Model" for the Cs/MoS_2 catalysts. The number of cesium layers (n) and the MoS_2 surface coverage (f_ℓ) predicted by the "Layer Model" taking into consideration the I_{Cs}/I_{Mo} experimental value are given in Table 5-10.

the number of layers is increased in the catalysts containing >10 wt% CsOOCH.

A comparison of the experimental intensity ratios of Cs to Mo with the intensities predicted by the layer model indicates that upon increasing the amount of CsOOCH in the catalyst the number of Cs layers increases, while the surface coverage (f_ℓ) remains almost constant. These results are presented in Figure 5-37 and summarized in Table 5-10. It is difficult to rationalize these results, since one would expect that the surface coverage of MoS_2 by cesium would increase upon addition of CsOOCH to the catalyst as indicated by the decrease of the MoS_2 surface area as the cesium loading is increased.

3) "Combined Model"

This model is supported by STEM results that clearly demonstrated that the cesium is in the form of hemispherical particles as well as in the form of cesium finely dispersed and/or in the form of a film-like morphology. The Cs/Mo intensity ratio in this model is given by Equation [C-24]. To solve this equation, the values of r, χ_ρ or χ_ℓ (they are related through Equation [C-25]), and n must be known. The particle size, r, can be determined by STEM, and χ_ρ and n can be assumed or adjusted in such a way that the Cs/Mo intensity ratio approximates to the experimental value. This procedure was applied to the catalysts containing 5.3, 10.0, and 20.0 wt% CsOOCH, which showed to have a relatively narrow particle size distribution, as indicated

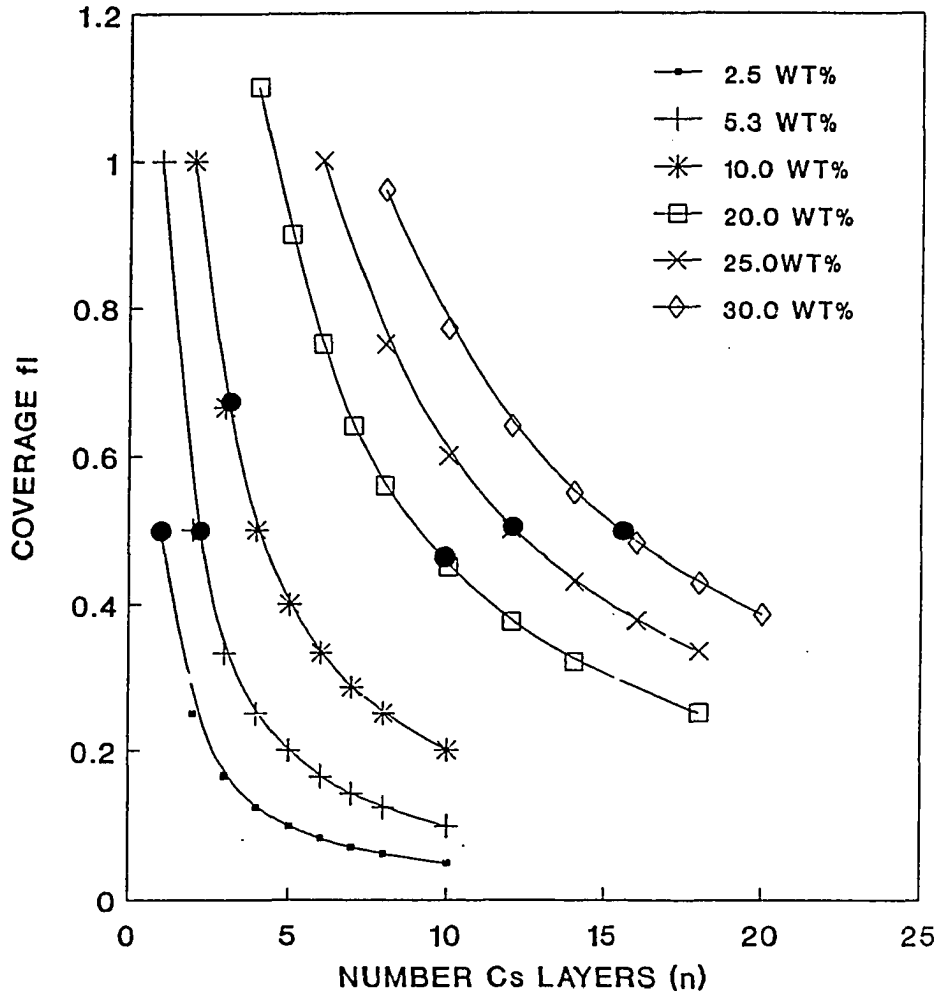

Figure 5-37 MoS_2 surface coverage (f_ℓ) as a function of the number of cesium layers (n) and cesium content in the catalyst. Dots indicate the MoS_2 surface coverage predicted by the "Layer Model" taking into consideration the I_{Cs}/I_{Mo} experimental value.

TABLE 5-10

Number of Cesium Layers (n) and the MoS_2 Surface Coverage (f_ℓ) Predicted by the Layer Model Taking into Consideration the I_{Cs}/I_{Mo} Experimental Value.

Catalyst (wt% CsOOCH)	$(I_{Cs}/I_{Mo})_{exp}$	Number of Cs Layers (n)	Surface Coverage (f_ℓ)
2.5	0.32	1	0.50
5.3	0.62	2	0.50
10.0	1.79	3	0.66
20.0	1.84	10	0.45
25.0	2.10	12	0.50
30.0	2.83	14	0.50

by STEM studies.

Table 5-11 summarizes the values predicted by the "Combined Model" of the fraction of MoS_2 surface covered by cesium particles (f_p), by cesium layers (f_ℓ), and the number of cesium layers (n). It is interesting to observe that the model finds that increasing the cesium loading from 5.3 to 10.0 wt% CsOOCH would result in an increase of the surface coverage of MoS_2 by cesium in the layer form (f_ℓ). If more cesium is added (20 wt% CsOOCH catalyst), the model predicts that the cesium would tend to agglomerate into larger particles rather than to form Cs layers. This is reflected by the fact that f_p increases and f_ℓ decreases. Note that the total surface coverage of MoS_2 by cesium (f_T) is approximately the same in the catalysts containing 10.0 and 20.0 wt% CsOOCH, but lower in the 5.3 wt% CsOOCH catalyst. It can be concluded that the "Combined Model" is a satisfactory model to predict the surface morphology of the Cs/MoS_2 catalysts, at least in the composition range between 5.3 to 20.0 wt% CsOOCH.

TABLE 5-11

Values Predicted by the Combined Model of the Fraction of MoS_2 Surface Covered by Cesium Particles (f_p), Cesium Layers (f_ℓ), and the Number of Cesium Layers (n).

Catalyst (wt% CsOOCH)	5.3	10.0	20.0
$(I_{Cs}/I_{Mo})_{exp}$	0.62	1.79	1.84
Particle Size, r (Å)[a]	65	100	135
f_p	0.10	0.12	0.38
Number of Cs Layers (n)	2	2	3
f_ℓ	0.25	0.5	0.15
$f_T = f_\ell + f_p$	0.35	0.62	0.53

[a]Determined by STEM.

APPENDIX 5.A

Determination of k Factors

There are two ways to determine k_{AB} factors, also known as Cliff-Lorimer k factors. First, k factors may be determined experimentally using standards of known composition (148,160,161) and second, k values can be calculated from first principles (162). Although it is known that the first method is currently the most accurate, Wood et al. (163) have demonstrated that the agreement between calculated and experimental k factors depends upon which theoretical models are chosen for the ionization cross-section, as well as the relative intensity factor and fluorescence yield. In the case of the Cs/MoS_2 catalysts the k factors were calculated from first principles, since no suitable standards for cesium were available.

The theoretical values of k factors were obtained by using the Goldstein et al. (162) equation

$$k_{AB} = \frac{(Qwa/A)_B}{(Qwa/A)_A} \cdot \frac{\epsilon_B}{\epsilon_A}, \qquad [A\text{-}1]$$

where Q is the ionization cross section for K, L, and M lines, w is the fluorescence yield for K, L, or M lines, a is the fraction of the total K, L, or M series intensity that is measured, A is the atomic weight and ϵ is the EDS detector efficiency. The value of these terms for Cs, S, and Mo are summarized in Table 5.A-1. Using these data, theoretical k factors were obtained and are shown in Table 5.A-2.

The ionization cross-section, Q, was obtained from the equation given by Powell (164),

$$Q = \frac{6.51 \times 10^{-20}}{E_c^2 U} n_s b_s \ell n(c_s U), \qquad [A-2]$$

where n_s is the number of electrons in a shell or subshell (e.g. n_s = 2 for a K-shell, n_s = 8 for an L-shell, and n_s = 18 for an M-shell), E_c is the ionization energy for the K-, L-, or M-shell (KeV), U is defined as the overvoltage and equal to E_o/E_c where E_o is the operating voltage of the STEM, b_s and c_s are constants for a particular shell. These constants were obtained from Brown (165) and Powell (164).

The fluorescence yield w was calculated from the Burhop (166) equation,

$$[w/(1-w)]^{1/4} = A + BZ + CZ^3, \qquad [A-3]$$

where A, B, and C are constants for a given line and Z is the atomic number. For K and L lines, constants given by Bambynek et al. (167) and Colby (168) were used. The relative intensity factor a was calculated from equations developed by Schreiber and Wims (169).

The EDS detector efficiency ϵ can be calculated using the following equation (170):

$$\epsilon_A = \{\exp[-(\mu/\rho)^A_{Be}\rho_{Be}X_{Be} - (\mu/\rho)^A_{Au}\rho_{Au}X_{Au} - (\mu/\rho)^A_{Si}\rho_{Si}X_{Si}]\} * \{1-\exp[-(\mu/\rho)^A_{Si}\rho_{Si}Y_{Si}]\}, \qquad [A-4]$$

where μ/ρ is the appropriate mass absorption coefficients of element A in Be, Au, and Si, ρ is the density of Be, Au, and Si, X is the thickness of Be window, Au surface layer, and Si dead layer, and Y_{Si} is the EDS active layer thickness.

The appropriate mass absorption coefficients (μ/ρ) for Cs, Mo and S in Be, Si, and Au were obtained from the tables of Heinrich (171). The EDS detector parameters, as suggested by Zaluzec (172), were used, i.e. $X_{Be} = 7.6 \times 10^{-4}$ cm, $X_{Au} = 2 \times 10^{-6}$ cm, $X_{Si} = 1 \times 10^{-5}$ cm, and $Y_{Si} = 0.3$ cm.

TABLE 5.A-1

Ionization Cross Sections (Q), Fluorescence Yields (w), Relative Intensity Factors (a), and Detector Efficiencies (ϵ) for Cs, S, and Mo

Element	Line	Q	w	a	ϵ
S	Kα	9.672×10^{-22}	0.076	0.939	0.794
Cs	Lα	1.272×10^{-21}	0.118	0.519	0.943
Mo	Kα	0.624×10^{-22}	0.764	0.835	0.989
Mo	Lα	3.486×10^{-21}	0.038	0.609	0.791

TABLE 5.A-2

Theoretical k factors for Cs, S, and Mo

k Factor	Value
k_{CsS}	3.08
$k_{CsMo(K\alpha)}$	0.74
$k_{CsMo(L\alpha)}$	1.22
$k_{SMo(K\alpha)}$	0.24

APPENDIX 5.B

Determination of the Minimum Detectability Limit for Cs in MoS_2

The minimum mass fraction (MMF) of an element that can be detected in a sample is influenced by factors such as nature of the sample, contamination, X-ray collection, and optimization of the instrument. A detailed description of these factors has been given by Williams (146).

The analysis requirement to detect an element is that its X-ray signal should be at least three times the standard fluctuation of the background intensity (173), i.e. $I_A \geq 3(2I_A^b)^{1/2}$. The minimum mass fraction (MMF) of cesium that can be detected in MoS_2 can be determined by the general expression given by Goldstein et al. (170),

$$C_{Cs}(MMF) = \frac{3(2I_{Cs}^b)^{1/2}}{(I_{Mo} - I_{Mo}^b)} k_{CsMo}^{-1} C_{Mo}, \qquad [B\text{-}1]$$

where I_{Cs}^b and I_{Mo}^b are the background continuum radiations in the Cs and Mo region respectively, I_{Mo} is the X-ray intensity of Mo, k_{CsMo} is the Cliff-Lorimer factor, C_{Mo} is the weight fraction of Mo of a Mo standard, and $C_{Cs}(MMF)$ is the minimum mass fraction of cesium that can be detected. For the Cs/MoS_2 catalysts, the minimum mass fraction (MMF) of cesium that can be detected was determined to be 0.24 wt% Cs (0.3 mol% Cs) when the electron microscope was operated under the conditions shown in Table 5.B-1. As indicated by Ziebold (174) the MMF

can be improved by maximizing counting time, the peak/background ratio of the element under consideration, and the counting rate. In the present study, due to the high instability of cesium under the electron beam and to avoid contamination, a relatively low counting time and low current densities were used, thus sacrificing the minimal detection limit of cesium.

TABLE 5.B-1

Estimated Detection Limit for Cs in MoS_2

STEM Operating Conditions	wt% Cs (mol% Cs)
120 keV beam LaB_6 filament <5 μa emission current 100 Å probe size 100 s counting time	0.24 ± 0.04 (0.3)

APPENDIX 5.C

Models for the Quantitative Analysis of XPS Intensities for the Cs/MoS_2 Catalysts

The objective of the quantitative XPS analysis of the Cs-doped MoS_2 catalysts was to determine the degree of dispersion and/or segregation of the cesium compound on MoS_2. The $Mo(3d_{5/2})$ XPS signal was used as an internal reference for the $Cs(3d_{5/2})$ signal.

In order to be able to obtain quantitative information from XPS intensities, a model of the morphology or geometry of the catalyst has to be known or assumed. On the basis of such a model, XPS intensities can be predicted and compared to the experimental values. A number of models have been proposed in the literature to predict XPS intensities for catalysts (154-159). In this section, XPS intensity equations will be derived to determine the degree of dispersion and/or segregation of Cs on the MoS_2 surface. These equations will be based on the model proposed by Kerkhof and Moulijn (157), that assumes that the catalyst consists of sheets of support with the promoter in-between (Figure 5.C-1). Three cases will be considered: 1)cesium is agglomerated forming hemispheric-like particles, "Hemispherical-Particles Model," 2) cesium is highly dispersed on the MoS_2 surface and/or forming film-like morphology, "Layer Model," and 3) cesium is present on the MoS_2 surface in the form of hemispherical particles as well as in a film-like morphology, "Combined Model."

Based on the electron microscopy results regarding the morphology

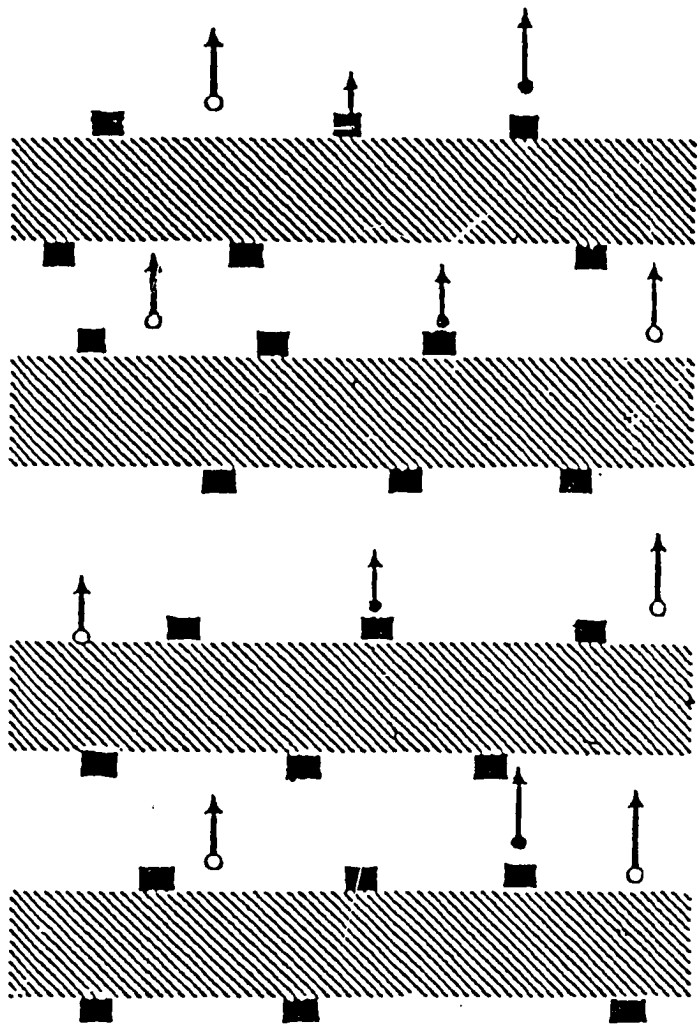

Figure 5.C-1 Model of the catalyst particle consisting of layered sheets of support with dispersed promoter (from Reference 157).

and distribution of cesium on MoS_2, three different geometric models will be considered to develop XPS intensity equations. These models are: 1) cesium is agglomerated forming hemispheric-like particles, "Hemispherical-Particles Model," 2) cesium is highly dispersed on the MoS_2 surface and/or forming a film-like morphology, "Layer Model," and 3) cesium is present on the MoS_2 surface in the form of hemispherical particles as well as in a film-like morphology, "Combined Model."

1) "Hemispherical-Particles Model"

For convenience indices i and j will designate the MoS_2 and alkali compound, respectively.

Let us assume that our Cs/MoS_2 catalyst consists of sheets of MoS_2 with hemispherical particles of cesium compound sitting on it. It can be easily shown that the thickness (t) of these MoS_2 sheets is given by:

$$t = \frac{2}{\rho_i S_o} \qquad [C\text{-}1]$$

where ρ_i is the density of MoS_2 (4.8 g/cm^3) and S_o its surface area (63 m^2/g).

Solving equation [C-1], one finds that t = 66 Å. Now, since the escape depth of an electron from MoS_2 (λ_i = 20.2 Å) has a smaller value than the thickness of a MoS_2 sheet, it can be assumed that just the top layer of MoS_2 contributes to the photoelectron intensity of MoS_2. The model for the arrangement of species i (MoS_2) and j (Cs) is

shown in Figure 5.C.2.

The total photoelectron signal of MoS_2 partially covered with cesium particles is given by:

$$I_i = I_{i1} + I_{i2} \qquad [C\text{-}2]$$

where I_{i1} is the unattenuated photoelectron signal of MoS_2, i.e. electrons coming out from MoS_2 without going through the Cs particles, and I_{i2} is the attenuated photoelectron signal of MoS_2 passing through the hemispherical Cs particles.

The unattenuated photoelectron signal of MoS_2 is given by:

$$I_{i1} = (1-f)\frac{K\sigma_i g\lambda_i n_i}{E_i}\left(1-e^{-t_i/g\lambda_i}\right) \qquad [C\text{-}3]$$

where f is the fraction of MoS_2 covered by Cs particles, K is an instrumental constant, n_i is the atomic density of MoS_2, σ_i is the photoionization cross section, λ_i is the escape depth of photoelectrons, E_i is the kinetic energy of the photoelectron, g is the escape angular factor, and t_i is the thickness of the MoS_2. In the case of a bulk homogeneous sample, i.e. bare MoS_2, $t_i \gg g\lambda_i$, thus Equation [C-3] can be reduced to

$$I_{i1} = (1-f)\frac{k\sigma_i g\lambda_i n_i}{E_i} \qquad [C\text{-}4]$$

The attenuated photoelectron signal of MoS_2 is given by

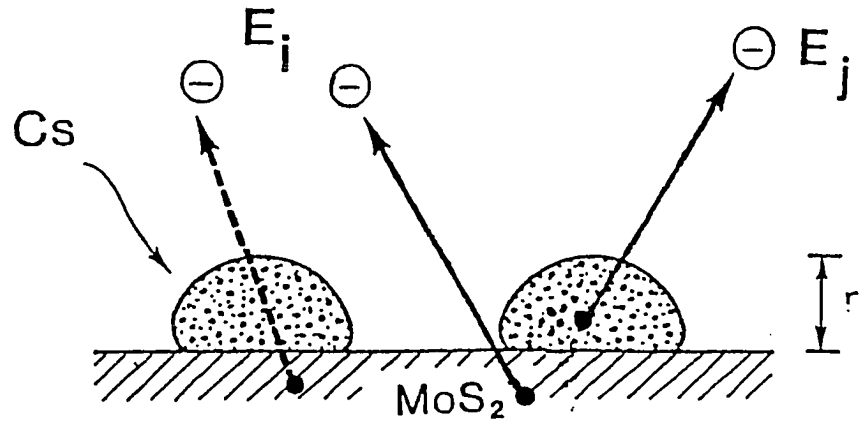

Figure 5.C-2 A schematic of the "Hemispherical-Particle Model" for Cs/MoS_2.

$$I_{i2} = \frac{fk\sigma_i g\lambda_i n_i}{E_i} e^{-r/g\lambda_{ig}} \qquad [C\text{-}5]$$

where r is the dimension of the cesium particle, λ_{ig} is the escape depth of photoelectrons from Mo passing through the cesium particle.

From Equations [C-2], [C-4], and [C-5] the total photoelectron signal of MoS_2 partially covered with cesium particles is given by

$$I_i = \frac{(1-f)k\sigma_i g\lambda_i n_i}{E_i} + \frac{fk\sigma_i g\lambda_i n_i e^{-r/g\lambda_{is}}}{E_i} \qquad [C\text{-}6]$$

The photoelectron signal of cesium particles is given by

$$I_j = \frac{fk\sigma_j g\lambda_{jnj}}{E_j} (1-e^{-r/g\lambda_j}) \qquad [C\text{-}7]$$

The intensity ratio of species i, cesium compound, to the species j, MoS_2, is given by dividing Equation [C-7] by Equation [C-6]

$$\frac{I_j}{I_i} = \frac{\sigma_j\lambda_j/E_j}{\sigma_i\lambda_i/E_i} \cdot \frac{n_j}{n_i} \cdot \frac{f(1-e^{-r/g\lambda j})}{[(1-f)+fe^{-r/g\lambda ij}]} \qquad [C\text{-}8]$$

In the present model (hemispherical cesium particles over MoS_2) the surface coverage f can be calculated from the following equation

$$f = \frac{\chi}{(1-\chi)So\rho_j} \cdot \frac{3}{2r} \qquad [C\text{-}9]$$

where χ is the cesium compound weight fraction in the catalyst, the

]other terms of the equation have already been defined. Kerkhof and Moulijn (157) proposed that the atomic density ratio (n_i/n_j) can be related to the bulk atomic ratio $(a_i/a_j)_b$ by the expression

$$(a_j/a_i)_b = \frac{n_j}{n^i} \cdot \frac{\chi}{1-\chi} \cdot \frac{\rho_i}{\rho_j} \qquad [C\text{-}10]$$

Combining Equations [C-8], [C-9], and [C-10] one obtains:

$$\frac{I_j}{I_i} = \frac{\sigma_j\lambda_j/E_j}{\sigma_i\lambda_i/E_i} \cdot \frac{a_j}{a_i}_b \cdot \frac{1}{\rho_j S_o} \cdot \frac{3}{2r} \cdot \frac{1-e^{-r/g\lambda j}}{(1-f)+fe^{-r/g\lambda ij}} \qquad [C\text{-}11]$$

The XPS intensity ratio, I_{Cs}/I_{Mo}, can be estimated by using Equation [C-11] as a function of r (f is related to r by Equation [C-9]).

2) "Layer Model"

This model is based on the assumption that the cesium is present on the MoS_2 surface in the film-like morphology. A schematic representation of this model is illustrated in Figure 5.C.3.

Following the same approach as in the previous model, the total photoelectron signal of MoS_2 partially covered with a cesium layer is given by:

$$I_i = \frac{(1-f_\ell)K\sigma_i g\lambda_i n_i}{E_i} + \frac{f_\ell K\sigma_i g\lambda_i n_i e^{-nt°\ell/\lambda i}}{E_i} \qquad [C\text{-}12]$$

where f_ℓ is the fraction of MoS_2 covered by the cesium layer, n is the number of layers, and $t°_\ell$ is the thickness of a monolayer. The first term of the right-hand side of the Equation [C-12] is the

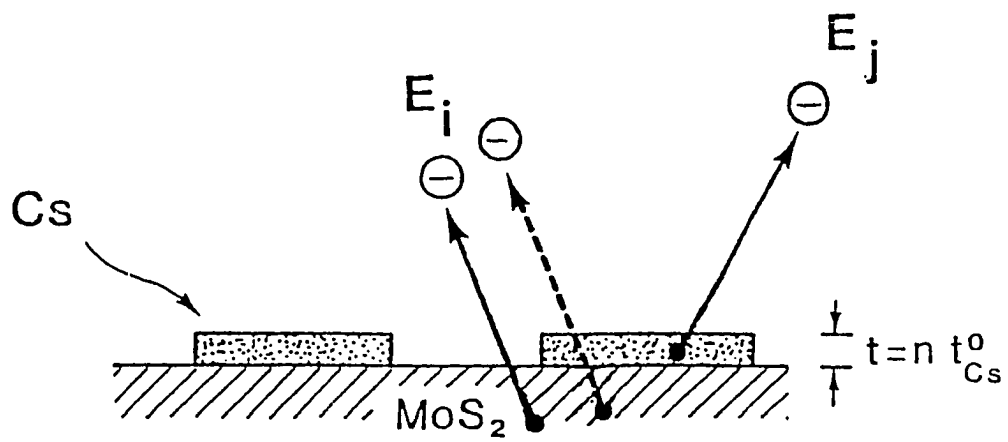

Figure 5.C-3 A schematic of the "Layer Model" for Cs/MoS_2.

photoelectron signal coming out from bare MoS_2, and the second term refers to the attenuated signal by the layer of cesium.

The total photoelectron signal of cesium is given by

$$I_j = \frac{f_\ell K \sigma_j g \lambda_j n_j}{E_j} (1-e^{-nt^\circ \ell/g\lambda j}) \qquad [C-13]$$

The XPS intensity ratio of cesium to molybdenum is obtained by dividing Equation [C-13] by [C-12]

$$\frac{I_j}{I_i} = \frac{\sigma_j \lambda_j / E_j}{\sigma_i \lambda_i / E_i} \cdot \frac{n_j}{n_i} \cdot \frac{f_\ell (1-e^{-nt^\circ \ell/g\lambda j})}{[(1-f_\ell)+f_\ell e^{-nt^\circ \ell/g\lambda ij}]} \qquad [C-14]$$

Using Equation [C-10], Equation [C-14] can be written as

$$\frac{I_j}{I_i} = \frac{\sigma_j \lambda_j / E_j}{\sigma_i \lambda_i / E_i} \cdot \frac{a_j}{a_{i\ b}} \cdot \frac{1-\chi}{\chi} \cdot \frac{\rho_j}{r_i} \cdot \frac{f_\ell (1-e^{-nt^\circ \ell/g\lambda Cs})}{[(1-f_\ell)+f_\ell e^{-nt^\circ \ell/g\lambda ij}]} \qquad [C-15]$$

This equation allows the prediction of the XPS intensity ratio, I_{Cs}/I_{Mo}, as a function of the number of layers (n) and the fraction of MoS_2 surface covered by cesium (f_ℓ). f_ℓ is a function of the CsOOCH/MoS_2 mol ratio, surface area of MoS_2, and the number of CsOOCH layers (n). f_ℓ can be determined by the following equation

$$f_\ell = X/(0.04953)(n) \qquad [C-16]$$

where X is the CsOOCH/MoS_2 mol ratio, n is the number of CsOOCH layers, and 0.04953 is the moles of CsOOCH required to cover completely ($f_\ell = 1$) with a monolayer (n = 1) a mol of MoS_2, whose

surface area is 63 m^2/g. This 0.04953 parameter was obtained as follows: the protected area of a CsOOCH molecule is $\pi r^2 = \pi(3.28 \times 10^{-10} m) = 3.3798 \times 10^{-19} m^2$, where $3.28 \times 10^{-10} m$ is the radius of the CsOOCH molecule taken from Ref. (154). The surface area of MoS_2 used in this study was determined to be 63 m^2/g, thus the total surface area per mol of MoS_2 is

$$(63\ m^2/g)(160.06\ g/mol) = 10083.78\ m^2/mol\ MoS_2.$$

The number of CsOOCH molecules needed to cover this area, assuming that the CsOOCH molecules sit next to each other, is

$$(10083 \frac{m^2}{mol MoS_2})(\frac{molecule\ CsOOCH}{3.3798 \times 10^{-19}}) = 2.983498 \times 10^{22} \frac{molecules\ of\ CsOOCH}{mol\ MoS_2}$$

expressed in mol CsOOCH/mol MoS_2, one obtains:

$$(2.93498 \times 10^{22} \frac{molecules\ of\ CsOOCH}{mol\ MoS_2} \frac{mol}{6.023 \times 10^{23}\ molecules} =$$

$$0.04953 \frac{mol\ CsOOCH}{mol\ MoS2}$$

3) "Combined Model"

This model represents the situation in which cesium is considered to be in the form of hemispherical particles as well as in a film-like morphology, i.e. a combination of the models described above.

The total photoelectron signal of MoS_2 partially covered with cesium particles and cesium in a film-like morphology is given by

$$I_i = \frac{(1-f_T)K\sigma_i g\lambda_i n_i}{E_i} + \frac{f_\ell K\sigma_i g\lambda_i n_i e^{-nt^\circ \ell/g\lambda ij}}{E_i} + \frac{f_p K\sigma_i g\lambda_i n_i e^{-r/g\lambda ij}}{E_i} \quad [C\text{-}17]$$

where f_ℓ and f_p are the fraction of MoS_2 surface covered by the cesium layer and cesium particles, respectively, f_T is the total fraction of MoS_2 covered by cesium and equal to

$$f_T = f_\ell + f_p \quad [C\text{-}18]$$

The first term of the right-hand side of Equation [C-16] refers to the unattenuated signal of MoS_2, the second term refers to the photoelectron signal attenuated by the cesium in the layer form, and the third term represents the attenuation of the signal by the cesium particles.

The total photoelectron signal of cesium is the sum of the signal coming from the cesium in the layer form plus the signal coming from the cesium particles, and is given by the following equation:

$$I_j = \frac{f_\ell K\sigma_j g\lambda_j n_{j\ell}(1-e^{-nt^\circ \ell/g\lambda j})}{E_j} + \frac{f_p K\sigma_j g\lambda_j n_{jp}(1-e^{-r/g\lambda j})}{E_j} \quad [C\text{-}19]$$

where $n_{j\ell}$ and n_{jp} are the atomic densities of cesium in the layers and particles, respectively. Dividing Equation [C-19] by [C-17], one obtains:

$$\frac{I_j}{I_i} = \frac{f_\ell A_j n_j(1-e^{-nt^\circ \ell/g\lambda j})+f_p A_j n_j(1-e^{-r/g\lambda j})}{1-f_T A_i n_i+f_\ell A_i n_i e^{-nt^\circ \ell/g\lambda ij}+f_p A_i n_i e^{-r/g\lambda ij}} \quad [C\text{-}20]$$

where:

$$A_j = \frac{\sigma_j \lambda_j}{E_j} \qquad [C\text{-}21]$$

$$A_i = \frac{\sigma_i \lambda_i}{E_i} \qquad [C\text{-}22]$$

rearranging Equation [C-20]

$$\frac{I_j}{I_i} = \frac{A_j[f_\ell(n_{j\ell}/n_i)(1-e^{-nt^\circ \ell/g\lambda j})+f_p(n_{jp}/n_i)(1-e^{-r/g\lambda j})]}{A_i[(1-f_T)+f_\ell e^{-nt^\circ \ell/g\lambda ij}+f_p e^{-r/g\lambda ij}]} \qquad [C\text{-}23]$$

combining Equations [C-10] and [C-23]

$$\frac{I_j}{I_i} = \frac{A_j[f_\ell(a_{i\ell}/a_{Mo})_b(1-\chi_\ell/\chi_\ell)(\rho_j/\rho_i)(1-e^{-nt^\circ \ell/g\lambda j})}{A_i[(1-f_T)+f_\ell e^{-nt^\circ \ell/g\lambda ij}+f_p e^{-r/g\lambda ij}]} +$$

$$+ \frac{f_p(a_{ip}/A_{Mo})_b(1-\chi_p/\chi_p(\rho_j/\rho_i)(1-e^{-r/g\lambda j})}{A_i[(1-f_T)+f_\ell e^{-nt^\circ \ell/g\lambda ij}+f_p e^{-r/g\lambda ij}]} \qquad [C\text{-}24]$$

where $(a_{Cs\ell}/a_{Mo})_b$ is the bulk atomic ratio of cesium contained in the layers and molybdenum, $(a_{Csp}/a_{Mo})_b$ is the bulk atomic ratio of cesium contained in the particles and molybdenum, χ_ℓ is the weight fraction of cesium in the layers, and χ_p is the weight fraction of cesium in the particles.

χ_ℓ and χ_p are related by

$$\chi_T = \chi_\ell + \chi_p \qquad [C\text{-}25]$$

where χ_T is the total weight fraction of cesium.

f_p is given by

$$f_p = \frac{\chi_p}{(1-\chi_T)So\rho_j} \cdot \frac{3}{2r} \qquad [C-26]$$

and f_ℓ is given by

$$f_\ell = \frac{\chi_\ell}{(0.04953)(n)} \qquad [C-27]$$

The following is the procedure to solve Equation [C-24]:

i) determine r using STEM

ii) assume a value of χ_p

iii) determine f_p using Equation [C-26]

iv) determine χ_ℓ using Equation [C-25]

v) assume a value of n and calculate f_ℓ using Equation [C-27]

vi) solve for I_{Cs}/I_{Mo}

Parameters to solve Equations [C-11], [C-15], and [C-24] are given in Table 5.C-1.

TABLE 5.C-1

XPS Data and Parameters Used for XPS Analysis

	Mo	Cs
Photoelectron Line	$3d_{5/2}$	$3d_{5/2}$
E (eV)	1024.2	528.8
σ[a]	5.77	22.93
λ[b]	20.2	30.1
t^o (Å)[c]	3.16	6.56
ρ (g/cm^3)	4.8	1.0198
S_o (m^2/g)[d]	63	
g[e]	0.75	

[a] Taken from reference (175)

[b] The escape depth, λ, was estimated from a relation given by Chang (176), $\lambda_i = 0.2\sqrt{E_i}\ t^o_i$, where t^o_i is the thickness of a monolayer.

[c] $t^o_{Mo} = 3.16$ Å was taken to be the spacing between the $(10\bar{1}0)$ planes of MoS_2 (177). $t^o_{Cs} = 6.56$ Å was considered to be the equal to the diameter of a CsOOCH molecule (154).

[d] The surface area of MoS_2 was determined to be 63 m^2/g.

[e] The escape angular factor, g, was taken from reference (156)

Chapter 6

CONCLUSIONS

The knowledge generated by this research has contributed to the understanding of the synthesis of alcohols from carbon monoxide and hydrogen over the MoS_2-based catalysts and has also provided information concerning the structure and function of the catalyst. The main features of this work are summarized below.

1. It was confirmed that the presence of the alkali promoter is indispensable for alcohol synthesis and that rather large quantities of alkali must be added to MoS_2 to shift the selectivity from hydrocarbons to alcohols. The indispensable presence of the alkali promoter in the MoS_2 catalysts for alcohol synthesis suggests that the alkali is opening a new reaction pathway by promoting the formation and/or concentration of surface species that give rise to the formation of alcohols rather than hydrocarbons.
2. The promotional effect of cesium for alcohol synthesis was greater than that shown by potassium. This superior promotional effect of cesium has been attributed to its highly basic character, which facilitates the activation of the CO molecule.
3. As the content of cesium in the catalysts was increased, the alcohol yields passed through a maximum, while the hydrocarbon formation was progressively suppressed. This

maximum was explained in terms of the bifunctionality of the catalyst, where the cesium component associatively activates CO and MoS_2 dissociatively activates H_2. The maximum activity is achieved when the CO and H_2 activating components are balanced.

4. Addition of cobalt to the alkali-doped MoS_2 catalyst promoted the $C_1 \rightarrow C_2$ homologation step that leads to ethanol as the dominant product.

5. Injection of ^{13}C-labeled CH_3OH into the synthesis gas feedstream over $CsOOCH/MoS_2$ = 20/80 wt% and $K_2CO_3/(Co/MoS_2)$ = 10/90 wt% catalysts revealed that:

   a. Linear alcohols were produced by a "classical" mechanism that proceeds via stepwise insertion of CO into alkyl-metal center bonds.

   b. Methane was a secondary product that was formed from an alkyl moiety generated from a C_1-oxygenated precursor.

   c. Methyl formate was formed from the reaction between methanol and CO. Methanol was the source of the methyl group of methyl formate, while the carbonyl group was derived from CO.

   d. Methyl acetate was formed through the Tischenko reaction, in which a methoxy anion reacts with aldehydic and/or acyl adsorbed species to produce methyl acetate.

   e. The isotope distributions observed for ethanol ($^{13}CH_3CH_2OH$) and for propanol ($^{13}CH_3CH_2CH_2OH$ and $CH_3{}^{13}CH_2CH_2OH$) over the cobalt containing alkali-doped MoS_2 catalyst were identical to those obtained in the presence of dicobalt octacarbonyl $[Co(CO)_4]_2$ homogeneous catalyst (123). These results indicate that the intermediate species involved in both homogeneous and heterogeneous systems during the synthesis of ethanol and propanol from methanol and CO/H_2 are identical.

6. The synthesis patterns over the Cs/(Co)/MoS_2 catalysts ($C_n \rightarrow C_{n+1}$ via CO insertion) are opposite to those observed with the Cs/Cu/ZnO catalyst ($C_n \rightarrow C_{n+1}$ via aldehyde coupling), and the difference between these two mechanisms is reflected in the product composition. Ethanol is the main higher alcohol produced over the Cs/(Co)/MoS_2 catalyst where CO insertion reaction dominates, and 2-methyl-1-propanol is the main higher alcohol (with ethanol a minor product) produced over the Cs/Cu/ZnO catalyst where the aldehyde coupling reaction dominates.

7. Alkali doping caused a decrease of the surface area of MoS_2. This reduction of the surface area is attributed to pore blockage by the alkali compound and not to an increase of the MoS_2 crystal size.

8. X-Ray powder diffraction studies of the Cs-doped MoS_2 catalysts indicated that the only phases present on the tested catalysts were MoS_2 and CsOOCH. No intercalation of the alkali compound into the MoS_2 lattice was detected. XRD studies also revealed that the CsOOCH compound present in the catalyst underwent dramatic changes, in particular crystal growth of the CsOOCH and phase transformation of some of the CsOOCH to Cs_2CO_3, after the catalysts were exposed to atmospheric conditions for long periods of time.

9. Analytical and transmission electron microscopy showed that the cesium compound was present on the MoS_2 surface in

a finely dispersed state as well as in the form of hemispherical particles in the catalysts containing the optimum concentration of cesium (10.0 - 20.0 wt% CsOOCH).

10. The presence of oxysulfides species and Mo^{6+} was not detected on the surface of tested catalysts.

11. Pretreatment (2%H_2/N_2, 400°C, 1h) of the catalysts induces dispersion of the cesium on the MoS_2 surface.

12. Models were developed to account for the degree of dispersion and/or segregation of cesium on the MoS_2 surface using X-ray photoelectron spectroscopy.

REFERENCES

1. Frank, M. E., and Hernandez-Robinson, A., National Meeting of the American Institute of Chemical Engineering, New Orleans, LA, April 6-19, 1986.

2. El Sawy, A., and Gray, D., DOE Contractors' Review Meeting, Pittsburgh, PA, Nov. 15-17, 1988.

3. Klier, K., in "Catalysis on the Energy Scene," (S. Kaliaguine and A. Mahay Eds.), Elsevier, Amsterdam, 1984, p. 439.

4. Abelson, P. H., American Scientist, 75 (1987) 584.

5. Di Raffaele, P., Paggini, A., and Lagana, V., French Patent, 2,482,583 (1981); assigned to Snam-Progetti.

6. Natta, G., Colombo, U., and Pasquon, I., in "Catalysis" (P. H. Emmett, Ed.), Reinhold, New York, (1957) Vol. V, p. 131.

7. Montarani, R., Aglietti, B., and Scarrosi, A., Arpel Congress on Heavy Oils, Caracas, Venezuela, Oct. 8-11, 1981.

8. Hofstadt, C. E., Kochloefl, K., and Bock, O., Eur. Patent 0034338-A2, (Aug. 26, 1981); assigned to Sü Chemie A.G.

9. Smith, K., and Anderson, R. B., Canad. J. Chem. Eng., 61 (1983) 40 and J. Catal., 85 (1984) 428.

10. Vedage, G. A., Himelfarb, P. B., Simmons, G. W., and Klier, K., ACS Symp. Ser. 279 (1985) 295.

11. Sugier, A., and Freund, E., U.S. Patent 4,122,110, (Oct. 24, 1978); assigned to Institut Francais du Petrole.

12. Chaumette, P., Courty, Ph., Durand, D., Grandvaliet, P., and Travers, C., GB Patent 2,158,730, (May 10, 1985); assigned to Institut Francais du Petrole.

13. Courty, P., Forestiere, A., Kawata, N., Ohno, T., Raimbault, C., and Yoshimoto, M., Symposium on Chemicals from Syngas and Methanol, 191st ACS National Meeting, N.Y., April 13-18, 1986.

14. Courty, P., Durand, D., Freund, E., and Sugier, A., J. Mol. Catal., 17 (1982) 241.

15. Cochran, G. A., Conway, M. M., Murchison, C. B., Pynnonen, B. W., Quarderer, Q. H., Stevens, R. R., Stowe, R. A., and Weihl, E. D.,Intern. Chem. Congr. Pac. Basin Soc., Honolulu, HI, Abstr. No. 03G35 (Dec. 1984), and Quarderer, Q. J., and Cochran, G. A., Eur. Pat. Appl. 8,410,932.5 (March 16, 1984); assigned to Dow Chemical Co.

16. Kinkade, N. E., Eur. Pat. Appl. 84116467.6 and 84116468.4 (Dec. 28, 1984); assigned to Union Carbide Corporation.

17. Stevens, R. R., Eur. Pat. Appl. 84116467.6 (Dec. 28, 1984); Conway, M. M., Murchison, C. B., and Stevens, R. R., Eur. Pat. Appl. 85109215.5 (July 23, 1985); Quarderer, G. J., Cochran, G. A., Stevens, R. R., and Murchison, C. B., Eur. Pat. Appl. 851092130.0 (July 23, 1985); Conway, M. M., Murchison, C. B., and Stevens, R. R., U.S. Patent 4,675,344 (June 23, 1987); assigned to Dow Chemical Co.

18. Youchang, X., Naasz, B. M., and Somorjai, G. A., Appl. Catal., 27 (1986) 233.

19. Dianis, W. P., Appl. Catal., 30 (1987) 99.

20. Murchison, C. B., Conway, M. M., Stevens, R. R., and Quarderer, G. J., Proc. 9th Intern. Congr. Catal., CAlgary, Canada, (1988) Vol. 2, p. 626.

21. Badische Anilin and Soda Fabrick, D.R. Patent 293,787 (1913); 295,202 (1914); 295,203 (1914); Span. Patent 20,488 (1913). U.S. Patent 1,201,850 (1914).

22. Fischer, F., and Tropsch, H., Brennstoff-Chem., 4 (1923) 276; 5 (1924) 201; 5 (1924) 217.

23. Badische Anilin and Soda Fabrick, D.R. Patent 415,686 (1923); 462,837 (1923). U.S. Patent 1,558,559 (1923); 1,569,775 (1923).

24. DuPont de Nemours, French Patent 657,124 (1928); Brit. Patent 323,240 (1928).

25. Fischer, F., and Tropsch, H., Ind. Eng. Chem., 21 (1929) 310.

26. Frolich, P. K., and Lewis, W. K., Ind. Eng. Chem., 20 (1928) 354.

27. Natta, G., Italian Patent 267,698 (1928).

28. Wenzel, W., Angew. Chem., B20 (1948) 225.

29. Paggini, A., and Sanfilippo, D., AIChE, 1986 Spring National Meeting, New Orleans, LA, April 6-10, 1986.

30. Frank, E. M., and Hernandez-Robinson, A., AIChE, 1986 Spring National Meeting, New Orleans, LA, April 6-10, 1986.

31. Hilsebein, W., presented to "1986 World Methanol Conference," Frankfurt, West Germany, Dec. 8-10, 1986.

32. Klier, K., A report prepared for the U.S. Department of Energy, October 1988, in press.

33. Mills, G. A., in "Catalysts for Fuels from Syngas," IEACR/09, ISBN 92-9029-159-1, August 1988.

34. Natta, G., in "Catalysis" (P. H. Emmett, Ed.), Reinhold, New York, (1955) Vol. III, p. 349.

35. Kung, H. H., Catal. REv. - Sci. Eng., 22 (1980) 235.

36. Klier, K., Adv. Catal., 31 (1982) 243.

37. Chinchen, G. C., Denny, P. J., Jennings, J. R., Spencer, M. S., and Waugh, K. C., Appl. Catal. 36 (1988) p. 1.

38. Bart, J. C. J., and Sneeden, R. P. A., Catal. Today, 2(1) (1987) p. 1.

39. Kiennemann, A., and Hindermann, J. P., in "Catalysis on the Energy Scene," (S. Kaliaguine and A. Mahay Eds.), Elsevier, Amsterdam, 1988, p. 181.

40. Deluzarche, A., Hindermann, J. P., Kiennemann, A., and Kieffer, R., J. Mol. Catal., 31 (1985) 225.

41. Vedage, G. A., Herman, R. G., and Klier, K., J. Catal., 95 (1985) 423.

42. Saussey, J., Lavalley, J. C., Lamotte, J., and Rais, T., J. Chem. Soc. Chem. Comm. 278 (1982).

43. Lavalley, J. C., Saussey, J., and Rais, T., J. Molec. Catal. 17 (1982) 289.

44. Takeuchi, A., and Katzer, J. R., J. Phys. Chem. 85 (1981) 937.

45. Veno, A., Onishi, T., and Tamaru, K., Trans. Faraday Soc. 67 (1971) 3585.

46. Blyholder, G., and Wyatt, W. V., J. Phys. Chem. 70, (1966) 1745.

47. Kagel, R. O., and Greenler, R. G., J. Chem. Phys. 49, (1968) 1638.

48. Soma, Y., Onishi, T., and Tamaru, K., Trans. Faraday Soc. 65 (1969) 2215.

49. Amenomiya, Y., and Tagawa, T., Proc. 8th Intern. Congr. on Catalysis, Berlin, (1984), Vol. II, p. 557.

50. Edwards, J. F., and Scrader, G. L., J. Catal. 94 (1985) 175.

51. Bogdan, C. E., Ph.D. Dissertation, Department of Chemistry, Lehigh University, 1989.

52. Ramaroson, E., Kieffer, R., and Kiennemann, Appl. Catal. 4 (1982) 281.

53. Deluzarche, A., Kieffer, A., and Muth, A., Tetrahedron Lett. 38 (1977) 3357.

54. Vedage, G. A., Pitchai, R., Herman, R. G., and Klier, K., Proc. 8th Intern. Congr. Catal., Berlin, (1984), Vol. II, p. 47.

55. Idriss, H., Hindermann, J. P., Kieffer, R., Kiennemann, A., Vallet, A., Chauvin, C., Lavalley, J. C., and Chaumette, P., submitted to J. Mol. Catal., 1986.

56. Nunan, J. G., Bogdan, C. E., Klier, K., Smith, K. J., Young, C.-W., and Herman, R. G., J. Catal. 113 (1988) 410.

57. Storch, H. H., Columbic, N., and Anderson, R. B., in "The Fischer-Tropsch and Related Synthesis," John Wiley, New York (1951).

58. Tatsumi, T., Muramatsu, A., Fukunaga, T., and Tominaga, H., Proc. 9th Intern. Congr. Catal., Calgary, Canada, (1988) Vol. 2, p. 618.

59. Heckel, H., Martin, F., and Roelen, O., Ger. Patent 902,851 (1943); assigned to Ruhrchemie A.G.

60. Sibilia, J. A., Dominguez, J. M., Herman, R. G., and Klier, K., Preprints, Div. Fuel Chem., ACS 29(5) (1984) 261.

61. Wender, I., Levine, R., and Orchin, M., J. Am. Chem. Soc., 71 (1949) 4160.

62. Pichler, H., and Schulz, H., Chem. Ing. Tech., 18 (1970) 1162.

63. Henrici-Olivé, G., Olivé, S., Angew, Chem. Int. Ed. Engl., 15 (1976) 136.

64. Biloen, P., Helle, J. N., and Sachtler, W. M. H., J. Catal., 58 (1979) 95.

65. Ponec, V., and van Barneveld, W. A., Ind. Eng. Chem. Prod. Res. Dev., 18 (1979) 268.

66. Lee, G. V. D., and Ponec, V., Catal. REv. - Sci. Eng., 29 (1987) 183.

67. Mazanec, T. J., J. Catal., 98 (1986) 115.

68. Storch, H. H., Columbic, N., and Anderson, R. B., "The Fischer-Tropsch Synthesis," Wiley, New York, (1951).

69. Anderson, R. B., in "Catalysis," (P. H. Emmett Ed.), Reinhold, New York, (1956), Vol. 4, p. 1.

70. Kummer, J. T., Podgurski, H. H., Spencer, W. D., and Emmett, P. H., J. Am. Chem. Soc., 73 (1951) 564.

71. Hall, W. K., Kokes, R. J., and Emmett, P. H., J. Am. Chem. Soc., 79 (1957) 2983; 79 (1957) 2989.

72. Frolich, P. K., and Cryder, D. S., Ind. Eng. Chem., 22 (1930) 1051.

73. Graves, G. D., Ind. Eng. Chem., 23 (1931) 1381.

74. Morgan, G. T., Hardy, D. V. N., and Procter, R. A., J. Soc. Chem. Ind. Trans. Commu., 51, (1932) 1T.

75. Taylor, R., J. Chem. Soc. (London), (1934) p. 1429; Gas World, 104 (1936) 2696.

76. Fox, J. R., Pesa, F. A., and Curatolo, B. S., J. Catal., 90 (1984) 127.

77. Döbereiner, W., Pogg. Ann., 64 (1845) 94.

78. Mross, W.-D., Catal. REv. - Sci. Eng. 25(4) (1983) 591.

79. Natta, G., and Strada, M., Giorn. Chim. Ind. Appl. 12 (1930) 13; 12 (1930) 169.

80. Dry, M. E., Shingles, T., Boshoff, L. J., Oosthuizen, G. J., J. Catal. 15 (1969) 190; 25 (1972) 99.

81. Nunan, J. G., Bogdan, C. E., Klier, K., Smith, K. J., Young, C.-W., and Herman, R. G., J. Catal., accepted.

82. Henrici-Olivé, G., and Olivé, S., in "The Chemistry of the Catalyzed Hydrogenation of Carbon Monoxide," Springer-Verlag, Berlin Heidelberg, (1984).

83. Henrici-Olivé, G., and Olivé, S., J. Mol. Catal. 16 (1982) 187.

84. Collman, J. P., Cawse, J. N., and Bramman, J. I., J. Amer. Chem. Soc. 94 (1972) 9505.

85. Collman, J. P., Finke, R. G., Cawse, J. N., and Bramman, J. I., J. Amer. Chem. Soc. 100 (1978) 4766.

86. Anh, N. T., Tetrahedron Lett., (1976) 155.

87. McLaughlin, M. M., and Gonzalez, R. D., J. Catal. 89 (1984) 392.

88. Lee, G. V. D., and Ponec, V., Catal. Rev. - Sci. Eng., 29(2&3) (1987) 183.

89. Chai, G.-Y., and Falconer, J. L., J. Catal., 93 (1985) 152.

90. Weisser, O., and Landa, S., in "Sulfide Catalysts: Their Properties and Applications," Pergamon Press, Oxford, 1973.

91. Newsome, D. S., Catal. Rev. - Sci. Eng., 21(2) (1980) 275.

92. Dickinson, R. G., and Pauling, L., J. Am. Chem. Soc. 45 (1923) 1466.

93. Tanaka, K., and Okuhara, T., J. Catal., 78 (1982) 155.

94. Stevens, G. C., and Edmonds, T., Proceedings of the Second International Conference on the Chemistry and Uses of Molybdenum, Climax Molybdenum (1976), p. 155.

95. Salmeron, M., Somorjai, G. A., Wold, A., Chianelli, R. R., and Liang, K. S., Chem. Phys. Lett., 90 (1983) 105.

96. Farras, M. H., Gellman, A. J., Somorjai, G. A., Chianelli, R. R., and Liang, K. S., Surf. Sci., 140 (1984) 181.

97. Bahl, O. P., Evans, E. L., and Thomas, J. M., Proc. Royal Soc. London Ser. A306 (1968) 53.

98. Chianelli, R. R., Ruppert, A. F., Behal, S. K., Kear, B. H., Wold, A., and Kershaw, J. Catal. 92 (1985) 56.

99. Tauster, S. J., Pecoraro, T. A., and Chianelli, R. R., J. Catal. 63 (1980) 515.

100. Voorhoeve, R. J. H., and Stuiver, J. C. M., J. Catal., 23 (1971) 228; 23 (1971) 236; 23 (1971) 243.

101. Grange, P., Catal. Rev. - Sci. Eng., 21(1) (1980) 135.

102. Furimsky, E., Catal. Rev. - Sci. Eng., 22(3) (1980) 371.

103. Ratnasamy, P., and Sivasanker, S., Catal. Rev. - Sci. Eng., 22(3) (1980) 401.

104. Chianelli, R. R., Catal. Rev. - Sci. Eng., 26(3&4) (1984) 361.

105. Topsøe, H., and Clausen, B. S., Catal. Rev. - Sci. Eng., 26(3&4) (1984) 395.

106. Concha, B. E., and Bartholomew, C. H., J. Catal., 79 (1983) 327.

107. Roxlo, C. B., Daage, M., Ruppert, A. F., and Chianelli, R. R., J. Catal., 100 (1986) 176.

108. Roxlo, C. B., Deckman, H. W., Gland, J., Cameron, S. D., and Chianelli, R. R., Science 235 (1987) 1629.

109. Anderson, A. B., Al-Saigh, Z. Y., and Hall, W. K., J. Phy. Chem. 92 (1988) 803.

110. Frety, R., and Breysse, M., in "Surface Properties and Catalysis by Non-Metals," Ed. by J. P. Bonnelle, B. Delmon, and E. Derouane, Riedel, Dordrecht, (1983) p. 379.

111. Busetto, L., Iannibello, A., Pincolini, F., and Trifiro, F., Bull. Soc. Chim. Belg. 90 (1981) 1233.

112. Dietz, W. A., J. Gas Chromatogr., 5 (1967) 68.

113. Dry, M. E., in "Catalysis," (J. R. Anderson and M. Boudart, Eds.), Springer Verlag, (1981), Vol. 1, p. 159.

114. Takeuchi, A., Katzer, J. R., and Crecely, R. W., J. Catal., 82 (1983) 474.

115. Thomas, G., Ann. Chim., 6 (1951) 367.

116. Klier, K., Zeroka, D., and Bybell, D., 189th National Meeting of the American Chemical Society, Miami Beach, FL, Abstract No. COLL-0033 (April 1985).

117. Nunan, J. G., Klier, K., Young, C.-W., Himelfarb, P. B., and Herman, R. G., J. Chem. Soc., Chem. Commun. (1986) p. 193.

118. Klier, K., Herman, R. G., Nunan, J. G., Smith, K. J., Bogdan, C. E., Young, C.-W., and Santiesteban, J. G., in "Methane Converison," (D. M. Bibby, C. D. Chang, R. F. Howe, and S. Yurchak, Eds.) Elsevier, Amsterdam, (1988) p. 109.

119. Schulz, H., C_1 Mol. Chem., 1 (1985) 231.

120. Wender, I., Friedel, R. A., and Orchin, M., Science, 113 (1951) 206.

121. Röper, M., and Loevenich, H., in "Catalysis in C_1 Chemistry," (W. Keim Ed.). D. Reidel Publishing Company, Holland, (1983) p. 105.

122. Wender, I., and Sternberg, H. W., Adv. CAtal. 9 (1957) 594.

123. Burns, G. R., J. Am. Chem. Soc. 77 (1955) 6615.

124. Sockari, S., Kitaura, K., Morokuma, K., Okhubo, K., J. Am. Chem. Soc. 105 (1983) 2280.

125. Eidus, Ya. T., Russ. Chem. Rev. (Engl. Transl.) 36 (1967) 339.

126. Araki, M., and Ponec, V., J. Catal., 44 (1976) 439.

127. Wentrcek, P. R., Wood, B. J., and Wise, H., J. Catal., 43 (1976) 363.

128. Sachtler, W. M. H., Proc. 8th Inter. Cong. Catal., Berlin, July 2-6, 1984, Springer Verlag, (1984), Vol. I, p. 151.

129. Hou, P. Y., and Wise, H., J. Catal., 93 (1985) 409.

130. Kagami, S., Naito, S., Kikuzono, Y., and Tamaru, K., J. Chem. Soc., Chem. Commun., (1983), p. 256.

131. Young, C.-W., Ph.D. Dissertation, Department of Chemical Engineering, Lehigh University, 1987.

132. Tonner, S. P., Trimm, D. L., and Wainwright, M. S., J. Mol. Catal., 18 (1983) 215.

133. Elliot, D. J., and Pennella, F., Preprints, Div. Pet. Chem., ACS, 31(1) (1986) 39.

134. Bowker, M., Houghton, H., and Waugh, K. C., J. Chem. Soc., Faraday Trans. 1, 77 (1981) 3023.

135. Foyt, D. C., and White, J. M., J. Catal., 49 (1977) 260.

136. Veno, A., Onishi, T., and Tamaru, K., J. Chem. Soc., Faraday Trans. 1, 67 (1971) 3585.

137. Satterfield, C. N., in "Heterogeneous Catalysis in Practice," McGraw-Hill, 1980.

138. Anderson, J. R., in "Structure of Metallic Catalysts," Academic Press, 1975.

139. Dombek, B. D., Contractors' Review Meeting, U.S. Department of Energy, Contract No. DE-AC22-86PC90013, Union Carbide Corp., Dec. 8-9, 1987, Pittsburgh, PA.

140. Perrichon, V., and Durupty, M. C., Appl. Catal. 42 (1988) 217.

141. Ratnasamy, P., and Leonard, A. J., J. Catal., 26 (1972) 352.

142. Ratnasamy, P., Rodrique, L., and Leonard, A. J., J. Phys. Chem. 77 (1973) 2242.

143. Chianelli, R. R., Prestridge, E. B., Pecoraro, T. A., and DeNeufville, J. P., Science, 203 (1979) 1107.

144. Chien, F. Z., Moss, S. C., Liang, K. S., and Chianelli, R. R., J. de Physique, C4 (1981) 273.

145. Guinier, A., in "X-ray Diffraction in Crystals, Imperfect Crystals, and Amorphous Bodies," Freeman, San Francisco, 1963.

146. Williams, D. B., in "Practical Analytical Electron Microscopy in Materials Science," Verlag Chemie International, Deerfield Beach, FL, 1984.

147. Joy, D. C., Romig, A. D., Jr., Goldstein, J. I., in "Principles of Analytical Electron Microscopy," Plenum Press, New York, 1986.

148. Cliff, G., and Lorimer, G. W., J. Microsc. 103 (1975) 203.

149. Gomez, A., Hernandez, P., and Jose-Yacaman, M., Surf. and Inter. Anal. 4 (1982) 120.

150. Brudnyi, A. I., and Karmadonov, A. F., Wear, 33 (1975) 243.

151. Extrapolated from values of surface tensions of KCl, NaCl, CsCl, NaI, and CsI given in CRC Handbook of Chemistry and Physics, 64th Edition, CRC Press Inc.

152. Kennou, S., Ladas, S., and Papageorgopoulos, C., Surf. Sci. 152/153 (1985) 1213.

153. Physical Electronics Industries, Inc., Reference Manual for PM I Model 548, 1975.

154. Himelfarb, P. B., Ph.D. Dissertation, Department of Material Science and Engineering, Lehigh University, 1986.

155. Defossé, C., Cocnesson, P., Rouxhet, P. G., and Delmon, B., J. Catal., 51 (1978) 269.

156. Dreling, M. J., Surf. Sci., 71 (1978) 231.

157. Kerkhof, F.P.J.M., and Moulijn, J. A., J. Phys. Chem., 83 (1979) 1612.

158. Fung, S. C., J. Catal., 58 (1979) 454.

159. Kaliaguine, S., Adnot, A., and Lemay, G., J. Phys. Chem., 91 (1987) 2886.

160. Wood, J., Williams, O. B., and Goldstein, J. I., in "Quantitative Microanalysis with High Spatial Resolution," (G. W. Lorimer, M. H. Jacobs, and P. Doig, Eds.), The Metals Society, London, Book 277, (1981) 24.

161. Morgan, A. J., Davies, T. W., and Erasmus, D. A., J. Microsc., 104 (1975) 271.

162. Goldstein, J. I., Costley, J. L., Lorimer, G. W., and Reed, S. J. B., SEM/77, Ed. by O. Johari, IITRI, Chicago, 1 (1977) 315.

163. Wood, J. E., Williams, D. B., and Goldstein, J. I., J. Microsc., 133 (1983) 255.

164. Powell, C. J., NBS Special Pub. 460, Ed. by K. F. J. Heinrich, D. E. Newbur and H. Yakowitz, (1976) 97.

165. Brown, B. D., in "Handbook of Spectroscopy," (J. W. Robinson, Ed.), C. R. Press, Cleveland, Vol. 1, (1974) 248.

166. Burhop, E. H. S., J. Phys. Radium, 16 (1955) 625.

167. Bambynek, W., Crasemann, B., Fink, R. W., Freund, H. V., Mark, H., Swift, C. D., Price, R. E., and Venugopala Rao, P., Rev. Mod. Phys., 44 (1972) 716.

168. Colby, J. W., in "Advances in X-Ray Analysis," (J. Newkirk, G. Mallett, and H. Pfeiffer, Eds.), Plenum Press, New York, Vol. 11, (1968) 287.

169. Schreiber, T. P. and Wims, A. M., X-Ray Spectrometry, 11 (1982) 41.

170. Goldstein, J. I., Williams, D. B., and Cliff, G., in "Principles of Analytical Electron Microscopy," (D. C. Joy, A.-D. Romig Jr., and J. I. Goldstein, Eds.), Plenum Press, New York, 1986, Chapter 5, 155.

171. Heinrich, K. F. J. in "The Electron Microprobe," (T. D. McKinley, K. F. J. Heinrich, and D. B. Wittry, Eds.), J. Wiley, New York, (1966) 351.

172. Zaluzec, N. J. in "Introduction to Analytical Electron Microscopy," (J. J. Hren, J. I. Goldstein, and D. C. Joy, Eds.), Plenum Press, New York, (1979) 121.

173. Romig, A. D. and Goldstein, J. I. in "Microbeam Analysis 1979," Ed. by D. E. Newbury, Pub. San Francisco Press, (1979) 124.

174. Ziebold, T. O., Anal. Chem., 39, (1967) 858.

175. Scofield, J. H., J. Electron Spectrosc. Relat. Phenom., 8 (1976) 124.

176. Chang, C. C., Surf. Sci., 48 (1975) 9.

177. JCPDS-International Center for Diffraction Data, Powder Diffraction, File Card No. 6-0097.

VITA

José Guadalupe Santiesteban Polanco was born in Parral, Chihuahua, Mexico on March 5, 1957, the third son of José Guadalupe Santiesteban and Guadalupe Polanco. He attended public schools in Parral, Chihuahua until June 1975. He entered the Chihuahua Institute of Technology, Chihuahua, Mexico, in the fall of 1975 and received a Bachelor of Science in Chemical Engineering in June 1979. In 1979, he was awarded a national prize as "One of the Best Students in Mexico, 1979". From January 1980 to December 1982, Santiesteban was awarded a National Fellowship to pursue a Master of Science in Chemical Engineering at Cd. Madero Institute of Technology, Tamaulipas, Mexico.

Mr. Santiesteban entered graduate study in Physical Chemistry at Lehigh University, Bethlehem, Pennsylvania in the fall of 1983 where he was a graduate Teaching Assistant from September 1983 to June 1984. In January 1985, he was awarded a University Fellowship at Lehigh University. From September 1984 to December 1988, he was a Research Assistant for Professor Klier at the Zettlemoyer Center for Surface Studies. During his Ph.D. program, Mr. Santiesteban co-authored several research papers dealing with heterogeneous catalysts. Mr. Santiesteban accepted employment in February 1989 as a Senior Research Chemist with Mobil Research and Development Corporation.

Mr. Santiesteban is married to Patricia Eugenia, daughter of Mr. and Mrs. José T. Cruz of Delicias, Chihuahua. Patricia and José are the parents of a son, Uriel.